Ab initio study of plasmons and electron-phonon coupling in bismuth: from free-carrier absorption towards a new method for electron energy-loss spectroscopy

Iurii Timrov

Thèse présentée pour obtenir le grade de
DOCTEUR DE L'ÉCOLE POLYTECHNIQUE
Spécialité: Physique
par

IURII TIMROV

Étude *ab initio* des plasmons et du couplage électron-phonon dans le bismuth: de la modélisation de l'absorption des porteurs libres à une nouvelle méthode pour le calcul de spectre de perte d'énergie électronique

Soutenue le 27 Mars 2013 devant le jury composé de:

Prof. Nicola MARZARI	Rapporteur
Prof. Jose Maria PITARKE	Rapporteur
Prof. Stefano BARONI	Examinateur
Prof. Peter YU	Examinateur
Prof. Luca PERFETTI	Examinateur
Dr. Lucia REINING	Examinatrice
Dr. Nathalie VAST	Directrice

Thèse préparée au Laboratoire des Solides Irradiés

Thesis presented to obtain the degree of

DOCTOR OF THE ECOLE POLYTECHNIQUE

Specialization: Physics

by

IURII TIMROV

Ab initio study of plasmons and electron-phonon coupling in bismuth: from free-carrier absorption towards a new method for electron energy-loss spectroscopy

Defended on 27 March 2013 in front of the jury:

Prof. Nicola MARZARI	Referee
Prof. Jose Maria PITARKE	Referee
Prof. Stefano BARONI	Examiner
Prof. Peter YU	Examiner
Prof. Luca PERFETTI	Examiner
Dr. Lucia REINING	Examiner
Dr. Nathalie VAST	Supervisor

Thesis prepared at the Laboratoire des Solides Irradiés

Acknowledgements

I would like to thank people with whom I have been working during my thesis.

I would first like to thank my supervisor, Nathalie Vast, for having offered me an opportunity to do this work, for total support and encouragement. Her wide knowledge and her logical way of thinking have been of great value for me. During my work with Nathalie I have greatly broadened my knowledge about condensed matter physics, and I have learned a lot about *ab initio* modelling of materials. I am also thankful to Nathalie for encouraging me to attend numerous trainings, conferences, workshops and tutorials, and I am particularly indebted to the care she has taken in the reading of this manuscript.

I thank Martine Soyer, the director of the Laboratoire des Solides Irradiés (LSI) of the École Polytechnique, for having welcomed me at LSI during the years of my PhD. I thank Nicola Marzari and Jose Pitarke to have accepted to review the manuscript and to participate in the jury of this thesis; Peter Yu, for having accepted to chair the jury; Stefano Baroni, Lucia Reining and Luca Perfetti to have accepted to be members of the jury of this thesis.

I would like to separately thank Stefano Baroni, for hospitality at SISSA (Scuola Internazionale Superiore di Studi Avanzati), for many interesting scientific discussions, and for his support and encouragement in the EELS project, which is the essential part of my thesis. I am indebted to Ralph Gebauer for having introduced me to practical aspects of the Liouville-Lanczos approach implementation, and for fruitful discussions regarding the EELS project. Also, I greatly acknowledge numerous valuable discussions with Andrea Dal Corso and Stefano de Gironcoli on various technical and conceptual issues.

I would like to thank Luca Perfetti and Jérôme Faure for many interesting discussions regarding our mutual interpretation of the time-resolved pump-probe experiments on bismuth. It was an excellent experience for me to work with such talented experimentalists, in particular I liked very much their physical intuition.

I would like to thank all old or new members of our group "Théorie: Science des matériaux", whom I have enjoyed to work with, namely Jelena Sjakste, Olivier Hardouin Dupark, Marc Hayoun, Antoine Jay, Maksim Markov, Liang Liang, Ekaterina Antoshchenkova, Emmanuel Betranhandy, Roman Raucoules, and Paola Gava for the scientific discussions, and who allowed me to fill the days with coffee breaks. I would also like to thank Lucia Reining, Francesco Sottile, Matteo Gatti and all others in the group "Theoretical spectroscopy" of LSI, for having invited me to attend scientific seminars and exciting scientific discussions. I would also like to thank our system administrator, Andrea Cucca, for getting me out of all sorts of trouble with the computers. I am thankful to Brice Arnaud, Alain Gellé, Igor Reshetnyak and all others, who I have probably forgotten to mention, for valuable scientific discussions. I am thankful to Jill Cottin for careful reading of this manuscript and making remarks about English.

I would like to separately thank my parents for their unending support and love, and

my friends all over the world.

Finally, I acknowledge the “Gaspard Monge international scholarship” from the École Polytechnique, and the financial support from the DGA and from the ANR contract “PNANO ACCATTONE”.

Résumé

Ce travail a été consacré à l'étude théorique du bismuth semi-métallique à l'aide de méthodes basées sur la théorie de la fonctionnelle de la densité (DFT). Les effets de couplage spin-orbite et d'échange et de corrélation dans l'approximation de densité locale (LDA) et de gradient généralisé (GGA) ont été approfondis de façon systématique. J'ai trouvé que les poches d'électrons et de trous au niveau de Fermi sont correctement décrites, ce qui m'a permis d'interpréter avec succès les expériences pompe-sonde dans le bismuth photoexcité menées au laboratoire des Solides Irradiés. Le calcul du couplage électron-phonon a montré la forte dépendance, par rapport au vecteur d'onde électronique, du couplage de la bande de valence la plus haute avec le phonon A_{1g} LO de centre de zone, ce qui explique l'observation de la forte dépendance en k de l'amplitude d'oscillation de l'énergie de liaison de cette même bande en photoémission résolue en temps. J'ai aussi montré que la présence d'extréma dans les bandes de valence et de conduction, où la masse des porteurs peut atteindre $18m_0$, favorise une accumulation des porteurs et conduit à une augmentation de leur fréquence plasma au cours du temps après photoexcitation, un effet qui n'a pas (encore) été observé dans d'autres matériaux. Enfin, j'ai développé une nouvelle méthode en théorie de perturbation de la fonctionnelle de la densité dépendante du temps (TDDFPT), qui permet de calculer la réponse électronique du matériau pour n'importe quelle valeur du moment transféré. Cette approche basée sur la méthode de récursion de Lanczos m'a permis de calculer les spectres de perte d'énergie électronique de Bi dans la gamme d'énergie 0-100 eV et de combler l'intervalle d'énergie entre les pertes des électrons de valence et celles des électrons de cœur. Cette méthode ouvre des perspectives considérables, comme le calcul des plasmons de surface.

Mots clés: bismuth, théorie de perturbation de la fonctionnelle de la densité dépendant du temps, méthode de récursion de Lanczos, couplage électron-phonon, fréquence plasma des porteurs libres, spectroscopie de perte d'énergie électronique.

Abstract

This work has been devoted to the theoretical study of bulk semimetallic bismuth with methods based on the density functional theory (DFT). Effects of spin-orbit coupling and of the exchange-and-correlation functionals in the local density (LDA) and generalized gradient approximation (GGA) have been systematically investigated. I have found that electron and hole pockets at the Fermi level are accurately reproduced, which has enabled me to successfully interpret the pump-probe experiments in the photoexcited bismuth performed in the Laboratoire des Solides Irradiés. The strong dependence on the electronic wave vector, of the calculated electronic coupling of the upper valence band with the zone-center A_{1g} LO phonon, explains the observation of a strongly k-dependent oscillation amplitude of the upper valence band in time-resolved photoemission experiments upon activation of the coherent A_{1g} phonon under photoexcitation. I have also shown that the presence of local extrema in the conduction and valence bands structure, where the carrier mass can be as large as $18m_0$, favours an accumulation of photoexcited carriers in these extrema and contributes to the augmentation of the plasma frequency as a function of time after the photoexcitation, an effect which has no analogy in other materials (as yet). Finally, I have developed a new *ab initio* approach in the time-dependent density functional perturbation theory (TDDFPT), which allows us to calculate the electronic response of materials for any momentum transfer. This approach based on the Lanczos recursion method has enabled me to calculate for the first time the electron energy-loss spectrum of Bi in the 0-100 eV energy range, bridging the gap between valence and core losses. This method opens the way to the routine calculation of surface plasmons.

Keywords: bismuth, time-dependent density functional perturbation theory, Lanczos recursion method, electron-phonon interaction, free-carrier plasma frequency, electron energy-loss spectroscopy.

Contents

1 Introduction **1**

I Background: state of the art **5**

2 Theory for the ground state **7**
2.1 Non-relativistic theory 8
2.1.1 Schrödinger equation 8
2.1.2 Density functional theory 9
2.2 Relativistic theory 14
2.2.1 Dirac equation 14
2.2.2 Relativistic density functional theory 17
2.3 Plane-wave pseudopotential method 22
2.3.1 Basis set 22
2.3.2 Pseudopotential approximation 25
2.4 Summary & Outlook 29

3 Time-dependent problem **31**
3.1 Time-dependent theory 32
3.1.1 Time-dependent Schrödinger equation 32
3.1.2 Time-dependent density functional theory 32
3.2 Linear response theory 36
3.2.1 Dyson-like equation 36
3.2.2 Excitation energy 38
3.2.3 Dielectric function 39
3.3 Optical absorption and electron energy-loss spectroscopy 45
3.3.1 TDDFT to explain optical absorption spectroscopy 45
3.3.2 Connection between scattering cross-section and dielectric function 47
3.3.3 TDDFT to explain EELS 52
3.4 Liouville-Lanczos approach to optical absorption spectroscopy 54
3.4.1 Formalism 55
3.4.2 Lanczos recursion method 63
3.5 Summary & Outlook 67

4 Material: bismuth **69**
4.1 Motivation for studying Bi . . . 70
4.2 Bulk properties of Bi . . . 71
4.2.1 Crystal structure . . . 71
4.2.2 Electronic structure . . . 73
4.2.3 Density of states . . . 76
4.3 Bi(111) surface . . . 77
4.3.1 Large SOC-assisted splitting of Bi(111) surface states . . . 78
4.3.2 Bi(111) Fermi surface . . . 78
4.4 Phonons in bulk Bi . . . 80
4.4.1 Phonon dispersion . . . 80
4.4.2 A_{1g} coherent phonons . . . 81
4.5 EELS and optical constants of bulk Bi . . . 83
4.6 Summary & Outlook . . . 86

II Developments, applications & results **89**

5 *Ab initio* description of Bi at equilibrium and in the photoexcited state **91**
5.1 Structural and electronic properties . . . 92
5.1.1 Computational method . . . 92
5.1.2 Lattice parameters . . . 93
5.1.3 Electronic structure within LDA & GGA . . . 96
5.1.4 Conclusions . . . 104
5.2 Interpretation of time- and angle-resolved photoemission experiment . . . 107
5.2.1 Distinction between bulk states and surface resonances . . . 107
5.2.2 Oscillation of electronic bands after the photoexcitation . . . 109
5.2.3 Computational method . . . 110
5.2.4 Determination of bulk band . . . 110
5.2.5 Analysis of electronic charge-density . . . 114
5.2.6 Dispersion of the electron-phonon coupling . . . 115
5.2.7 Origin of the shift of binding energy . . . 117
5.2.8 Conclusions . . . 118

6 Free-carrier absorption in photoexcited Bi **121**
6.1 Methodological developments for free-carrier absorption . . . 122
6.1.1 Computational method . . . 122
6.1.2 Plasma frequency . . . 122
6.1.3 Carrier velocity . . . 124
6.1.4 Effective mass . . . 130
6.1.5 Optical mass . . . 136
6.1.6 Conclusions . . . 138
6.2 Interpretation of time-resolved terahertz experiment . . . 140
6.2.1 Intraband contribution to dielectric function of Bi at equilibrium . . . 140
6.2.2 Intraband contribution to dielectric function of photoexcited Bi . . . 142

6.2.3 Theoretical interpretation of two regimes in plasma frequency . . . 144
6.2.4 A model for the temporal evolution of the plasma frequency 146
6.2.5 Conclusions 148

7 A new method to EELS & application to Bi **149**
7.1 Methodological developments 150
7.1.1 TDDFPT linear-response equations 150
7.1.2 Expression of the electronic response 153
7.1.3 Quantum Liouville equation 155
7.1.4 Electronic susceptibility 155
7.1.5 Batch representation 156
7.1.6 Use of symmetry 157
7.1.7 Extension of the formalism to metals 159
7.1.8 Relativistic case: inclusion of the spin-orbit coupling 161
7.1.9 Calculation of the dielectric function 161
7.1.10 Use of Lanczos recursion method 162
7.1.11 Conclusions 163
7.2 Test cases 164
7.2.1 Semiconductors: bulk Si 164
7.2.2 Metals: bulk Al 169
7.3 Application to Bi 174
7.3.1 Computational method 175
7.3.2 Convergence of the EEL spectrum 175
7.3.3 Comparison between LDA, GGA and experiment 177
7.3.4 Effect of the spin-orbit coupling on EEL spectrum 179
7.3.5 Real and imaginary part of the dielectric function 180
7.3.6 Plasmon dispersion 181
7.3.7 Exchange-correlation, crystal local field and anisotropy effects . . . 182
7.3.8 Comparison between $-\mathbf{Im}\left[\mathbf{1}/\boldsymbol{\epsilon}_{\mathbf{M}}(\mathbf{q})\right]$ & $\mathbf{Im}\left[\boldsymbol{\epsilon}_{\mathbf{M}}(\mathbf{q})\right]$ 185
7.3.9 Effect of the $5d$ semicore levels 185
7.4 Conclusions 186

8 General conclusions and perspectives **189**

A Bismuth **193**
A.1 Pseudopotential 193
A.2 Phase diagram 195
A.3 Restricted density of states 196

B Spectroscopy **201**
B.1 Photoemission spectroscopy 201
B.1.1 Mechanism of photoemission 201
B.1.2 Angle-resolved photoemission spectroscopy 201
B.1.3 Time-resolved ARPES 203
B.1.4 Experimental set-up 203

B.1.5 Electronic temperature after the photoexcitation of Bi 203
B.2 Terahertz spectroscopy 205
B.2.1 Time-resolved THz spectroscopy 205
B.2.2 Experimental set-up 207

C Implementation of the new method to EELS **209**
C.1 Program summary 209
C.2 Parallelization 210

D Curriculum Vitae **213**
D.1 Personal information 213
D.2 List of publications 215
D.3 High performance computing and programming 216

Nomenclature

χ	Susceptibility, or density-response function, see equation (3.15)
χ^0	Independent-particle polarizability, see equation (3.17)
ϵ	Microscopic dielectric function, see equation (3.30)
ϵ_{M}	Macroscopic dielectric function, see equation (3.33)
$\hat{\mathcal{L}}$	Liouvillian super-operator, see equation (3.98)
κ	Hartree-plus-XC kernel, see equation (3.97)
$\mathbf{G}$	Reciprocal lattice vector
$\mathbf{q}$, $\mathbf{Q}$	Momentum transfer
$\mathbf{v}_{n,\mathbf{k}}$	Carrier velocity at $\mathbf{k}$ point of n-th band, see equation (6.13)
ω_p	Plasma frequency, see equation (3.41)
Ψ	Many-body wavefunction, see equation (2.1)
ψ	Four-component single-particle wavefunction (spinor), see equation (2.20)
$\rho(\mathbf{r})$	Density matrix, see equation (3.89)
$\varepsilon_{n,\mathbf{k}}$	Kohn-Sham energy of n-th band at point $\mathbf{k}$, see equation (2.16)
$\varphi_{n,\mathbf{k}}$	Kohn-Sham wavefunction of n-th band at point $\mathbf{k}$, see equation (2.16)
f_{xc}	Exchange-correlation kernel, see equation (3.21)
f_{FD}	Fermi-Dirac distribution function, see equation (6.42)
m^*	Effective mass of carriers, see equation (6.35)
m^{op}	Optical mass of carriers, see equation (6.40)
m_0	Free-electron mass, see equation (3.40)
$n(\mathbf{r})$	Charge density, see equation (2.7)

ALDA Adiabatic Local Density Approximation

BZ Brillouin zone

DFT Density Functional Theory

DOS Density of states

EEL Electron Energy Loss

EELS Electron Energy Loss Spectroscopy

ELP Equilibrium Lattice Parameters

GGA Generalized Gradient Approximation

LDA Local Density Approximation

RPA Random Phase Approximation

SOC Spin-Orbit Coupling

TDDF(P)T Time-Dependent Density Functional (Perturbation) Theory

TDLDA Adiabatic Local Density Approximation

Chapter 1

Introduction

The general problem which has been addressed in this thesis is the *ab initio* study of the ground-state and excited-state properties of the semimetal bismuth by developing and applying new theoretical methods based on the (time-dependent) density functional theory - (TD)DFT [1, 2, 3]. This thesis has followed two main directions: (1) Theoretical developments needed for the physical interpretation of experiments carried out at the Laboratoire des Solides Irradiés on photoexcited Bi, (2) The development of a new method for the calculation of the electron energy-loss spectra, and application to Bi.

Bismuth is the material that has been extensively studied over the last 70 years, and has gained an increased interest over recent years, both on the experimental and theoretical side. This material has a lot of unique properties, *e.g.*, it has unusual electronic properties due to its semimetallic character, which involves the existence of tiny electron and hole pockets forming the Fermi surface [4]; the relativistic spin-orbit coupling effect is very large in Bi, which influences its electronic and vibrational properties [5, 6]; the effective masses of carriers at the Fermi surface may be two orders of magnitude smaller than the free-electron mass [4]; it is a prototypical element for thermoelectricity [4]; it has unique spin properties on the surface [7], to recall only some of them.

From the computational point of view bismuth is a challenging material, because (*i*) it requires the inclusion of the spin-orbit coupling in the calculations, (*ii*) the description of the electron and hole pockets at the Fermi levels requires very dense $\mathbf{k}$ point sampling of the Brillouin zone. The electronic structure of bulk Bi has been studied within the DFT [5, 8], the tight-binding model [9], empirical pseudopotential calculations [10], and in various experiments, like Shubnikov-de Haas [11], de Haas-van Alphen [12], photoemission [13], to recall only some of numerous studies. It is a challenging task to reproduce the electron and hole pockets near the Fermi level *from-first-principles*. This has been made possible in this thesis, by generating a new pseudopotential (PP) for Bi with the help of Prof. Andrea Dal Corso (SISSA, Trieste, Italy), and using such a PP for the electronic structure calculations.

Two types of experiments on Bi have been carried out by our collaborators at the Laboratoire des Solides Irradiés of the École Polytechnique, French synchrotron SOLEIL, and Max Planck Institute in Germany, namely, the time-resolved and angle-resolved photoemission experiment on Bi(111) surface (by E. Papalazarou, J. Faure, J. Mauchain,

M. Marsi, A. Taleb-Ibrahimi, I. Reshetnyak, A. van Roekeghem, and L. Perfetti), and the time-resolved terahertz experiment on Bi film of 100 nm thickness (by T. Kampfrath, J. Faure, C. R. Ast, C. Frischkorn, M. Wolf, and L. Perfetti). These two kinds of experiments needed a theoretical interpretation on the basis of the *ab initio* simulations.

In the photoemission experiment the A_{1g} coherent optical phonon mode was activated. Bismuth is a reference material for the investigation of lattice dynamics in out-of-equilibrium conditions [14]. The atomic motion following the photoexcitation of Bi is well understood nowadays: Time-resolved X-ray diffraction experiments [15] and DFT calculations [16] could accurately describe the amplitude of oscillations at high-excitation densities. However, the temporal evolution of the electronic states after photoexcitation has never been directly observed in the time-resolved (pump-probe) photoemission experiments nor studied *ab initio*. This issue will be addressed in this thesis.

This thesis also aims at understanding of the free-carrier absorption after the photoexcitation of Bi, as measured in the time-resolved terahertz experiments. I will show that the carrier dynamics of photoexcited Bi generates a Drude response that evolves over time. By performing methodological developments in order to describe the free-carrier response in Bi, I will study the Drude intraband contribution to the dielectric function of Bi, and will consider the photoinduced change of the plasma frequency. These studies have been done in collaboration with Dr. Paola Gava, at that time a postdoc at the Laboratoire des Solides Irradiés.

During the second part of my PhD, in accordance with the Gaspard Monge international program, I had to spend at least 6 weeks of my PhD work in a laboratory outside of France. I had an excellent opportunity to spend in total about 5 months of my PhD at the Scuola Internazionale Superiore di Studi Avanzati (SISSA) of Trieste (Italy) working under the supervision of Prof. Baroni, and in collaboration with Dr. Gebauer from the Abdus Salam International Centre for Theoretical Physics (ICTP) of Trieste. The goal of the research project was a methodological development of the new *ab initio* method to the electron energy-loss spectroscopy, with subsequent application to challenging materials, in particular bismuth. This project lasted 2 years.

The ability to compute electron energy-loss (EEL) spectra *from-first-principles* is of fundamental importance both to complement and help interpret experiments, and to predict properties of new materials. Thus, it is desirable to develop theoretical methods and computational techniques to obtain EEL spectra that are both accurate and scalable to systems with a large number of atoms. A commonly used state-of-the-art approach to compute EEL spectra *ab initio* is the time-dependent density functional theory (TDDFT) [3]. Current techniques based on this theory involve the computation of a multiple of single-particle empty states and the solution of the Dyson-like screening equation for the susceptibility [17]. Both operations may become very expensive, from a computational point of view, even for systems with a small number of atoms, like Bi (two atoms in the unit cell). The calculation of the EEL spectra for systems with a large number of atoms is an even more challenging problem. Hence, it is highly desirable to develop theoretical methods to solve the TDDFT equations that are scalable even to very large systems, and give access to the carrier response in extended energy range, without relying on various

approximations, *e.g.* truncation of the number of empty states, and avoid dielectric matrix inversion.

In this thesis I will present a new *ab initio* method, which overcomes all these drawbacks of the conventional TDDFT methods. The new method is an extension of the Liouville-Lanczos approach [18] from the calculation of the optical absorption spectra of finite systems (*e.g.*, molecules) to the calculation of the EEL spectra of extended systems at various transferred momenta $\mathbf{q}$. After testing the new method on prototypical examples of bulk silicon and aluminum, I will apply the Liouville-Lanczos approach to the calculation of the carrier response in bulk Bi in the energy range up to 100 eV, and thus bridge the gap between the valence-loss and core-loss contributions. I will study the single-particle and collective carrier response in Bi in the extended energy range, by calculating the valence EEL spectra at various transferred momenta $\mathbf{q}$. Numerous experimental investigations of this issue have been carried out, but no theoretical works exist confirming the origin of peaks in the experimental EEL spectrum of Bi. Thus, the new method will allow us to calculate the EEL spectra of Bi at various $\mathbf{q}$ for the first time.

This thesis is organized in two parts. Part I presents state-of-the-art methods and current knowledge about bismuth, and Part II presents my results.

Part I contains 3 chapters.

In Chapter 2 I will give an introduction to DFT and its relativistic extension. This will be needed for the consideration of Bi, in which relativistic effects are essential, in particular the spin-orbit coupling. I will also point out how the problem can be solved in practice, by using the plane-wave pseudopotential method.

In Chapter 3 I will present an extension of DFT to the time domain (TDDFT), for the description of Bi in the excited state in the linear-response regime. I will present the Liouville-Lanczos approach to the optical absorption spectra, which will be extended to electron energy-loss spectroscopy (EELS) in Chapter 7.

In Chapter 4 I will explain why Bi has been chosen as a subject of study, and what are its bulk crystal and electronic structures, surface electronic structure, vibrational properties, and EEL experimental spectra and optical dielectric function. I will stress the huge importance of the spin-orbit coupling in Bi, and its influence on all properties of this material. All of this information will be required for the discussions in Part II.

Part II contains 4 chapters.

In Chapter 5 I will present a detailed study of the theoretical equilibrium lattice parameters of Bi within the local density (LDA) and generalized gradient (GGA) approximations, and the study of the Kohn-Sham band structure, with special emphasis on a description of the electron and hole pockets. I will also discuss an interpretation of the time-resolved and angle-resolved photoemission experiment on the basis of the Kohn-Sham band structure. I will show that in the photoexcited Bi the A_{1g} coherent phonon mode leads to the oscillation of the top valence bulk electronic bands due to the electron-phonon interaction.

In Chapter 6 I will present the investigation of the low-energy carrier response in Bi.

I will present methodological developments for the free-carrier absorption, which will be needed for the interpretation of the time-resolved terahertz experiment. I will show that Bi displays a free-carrier Drude response at equilibrium and after the photoexcitation.

In Chapter 7 I will present a new method to EELS, which is an extension of the Liouville-Lanczos approach from optics to EELS at finite $\mathbf{q}$. After testing the new method on bulk silicon and aluminum, I will show the results of the EEL spectra in Bi, and study various aspects such as the effect of the exchange-and-correlation, effect of the spin-orbit coupling, plasmon dispersion, crystal local field effects, anisotropy. I will point out the advantages of the new method.

In Chapter 8 I will draw general conclusions and perspectives.

Finally, the appendices contain additional information needed for the discussions in this thesis. Appendix A describes the pseudopotential, the phase diagram, and the restricted density of states of Bi. Appendix B describes the basis of the photoemission and terahertz experiments, which will be interpreted in Secs. 5.2 and 6.2. Appendix C contains a summary of the implementation of the new method to EELS. Appendix D contains my Curriculum Vitae.

Unless otherwise stated, Gaussian units are used throughout this thesis.

Part I

Background: state of the art

Chapter 2

Theory for the ground state

Since the birth of quantum mechanics, the description of a many-body problem by solving the Schrödinger equation has been a formidable task. Many approaches exist to find an approximate solution for such a problem. Let me give examples: (*i*) the configuration interaction and the quantum Monte-Carlo approach from quantum chemistry, which aim at determining the full many-body wavefunction [19, 20], (*ii*) the dynamical mean-field theory, where the many-body problem is replaced by a single-site quantum impurity problem for an effective medium [21], (*iii*) the many-body perturbation theory, which is based on the Green's function formalism [22], and (*iv*) the density functional theory (DFT), which uses the ground-state density as a basic variable, and which reduces the complicated many-body problem to an effective single-particle problem [23]. The method of choice strongly depends on the material, the physical quantity of interest, and the required accuracy.

The solution of the many-body problem is even more difficult when relativistic effects are significant. The relativistic many-body system can be described by the Dirac equation. However, from a computational point of view, the solution of the Dirac equation for real many-body systems has remained a big challenge. Nowadays, a treatment of the relativistic spin-orbit coupling effect can be performed very accurately with different methods, in particular, within the relativistic version of DFT.

This chapter aims at giving a presentation of the density functional theory and its relativistic generalization, which I will use in the second part of the manuscript. First, I will present a non-relativistic formalism, starting from the Schrödinger equation and subsequently discussing the non-relativistic DFT. Afterwards, I will present a relativistic formalism, going from the Dirac equation to the relativistic DFT. There exist numerous textbooks for the detailed description of the theory which will be highlighted in this chapter. An interested reader can consider, *e.g.*, Refs. [24, 25, 26]. Finally, I will discuss the plane-wave pseudopotential approach to (relativistic) DFT. At the end of the chapter, I will give a summary.

2.1 Non-relativistic theory

In the framework of non-relativistic quantum mechanics, the motion of particles is governed by the Schrödinger equation. The solution of this many-body problem is a formidable task. Nevertheless, an *ab initio* description of real materials, based on the density functional theory, can be used to tackle this problem.

In this section I will discuss the Schrödinger equation, and point out what difficulties one faces when applying the Schrödinger equation to the description of a real many-body system. Afterwards, I will show how such problems can be overcome by using the density functional theory, and what is the physical idea behind it.

2.1.1 Schrödinger equation

In non-relativistic quantum mechanics, the Schrödinger equation is a mathematical tool to describe a physical system. Let us consider a system which consists of interacting electrons and nuclei. The Schrödinger equation, which was formulated by Erwin Schrödinger in 1925, of this system reads [27, 28]:

$$\hat{H}(\{\mathbf{r}_i\},\{\mathbf{R}_I\})\,\Psi(\{\mathbf{r}_i\},\{\mathbf{R}_I\}) = E\,\Psi(\{\mathbf{r}_i\},\{\mathbf{R}_I\}), \tag{2.1}$$

where $\{\mathbf{r}_i\}$ is the set of electronic coordinates, $\{\mathbf{R}_I\}$ is the set of nuclear coordinates, $\Psi(\{\mathbf{r}_i\},\{\mathbf{R}_I\})$ is the total many-body wavefunction of the system, E is the total energy of the system, and $\hat{H}$ is the Hamiltonian operator which reads:

$$\begin{aligned}\hat{H}(\{\mathbf{r}_i\},\{\mathbf{R}_I\}) &= -\frac{\hbar^2}{2m}\sum_i \boldsymbol{\nabla}_i^2 - \sum_I \frac{\hbar^2}{2M_I}\boldsymbol{\nabla}_I^2 + \frac{1}{2}\sum_{i\neq j}\frac{e^2}{|\mathbf{r}_i-\mathbf{r}_j|} \\ &\quad + \frac{1}{2}\sum_{I\neq J}\frac{Z_I Z_J e^2}{|\mathbf{R}_I-\mathbf{R}_J|} - \sum_{i,I}\frac{Z_I e^2}{|\mathbf{r}_i-\mathbf{R}_I|},\end{aligned} \tag{2.2}$$

Here, i and I are the indices of electrons and nuclei, respectively, $\mathbf{r}_i$ and $\mathbf{R}_I$ are the coordinates of electrons and nuclei, respectively, m is the electron mass, $-e$ is the electron charge, M_I and $+Z_I e$ are the mass and the charge of the I-th nucleus, respectively, and $\hbar$ is the Planck constant. In Eq. (2.2), the first term is the kinetic energy of electrons, the second term is the kinetic energy of nuclei, the third term is the electron-electron Coulomb repulsion energy, the fourth term is the nucleus-nucleus Coulomb repulsion energy, and the last term is the electron-nucleus Coulomb attraction energy.

Within the *Born-Oppenheimer* (BO) or *adiabatic* approximation [29], the motion of electrons and nuclei can be separated, because electrons are very light compared to nuclei, they move much more rapidly, and thus can follow the slower motion of nuclei [30]. Therefore, the total wavefunction $\Psi(\{\mathbf{r}_i\},\{\mathbf{R}_I\})$, can be approximated as a product of the nuclear (ionic) and electronic wavefunctions:

$$\Psi(\{\mathbf{r}_i\},\{\mathbf{R}_I\}) = \Psi_{\text{ion}}(\{\mathbf{R}_I\})\,\Psi_{\text{el}}(\{\mathbf{r}_i\},\{\mathbf{R}_I\}), \tag{2.3}$$

where $\Psi_{\rm ion}(\{\mathbf{R}_I\})$ is the nuclear wavefunction, and $\Psi_{\rm el}(\{\mathbf{r}_i\},\{\mathbf{R}_I\})$ is the electronic wavefunction which depends parametrically upon $\{\mathbf{R}_I\}$. The Schrödinger equation for the nuclei reads:

$$\left(-\sum_I \frac{\hbar^2}{2M_I}\boldsymbol{\nabla}_I^2 + E_{BO}(\{\mathbf{R}_I\})\right)\Psi_{\rm ion}(\{\mathbf{R}_I\}) = E\,\Psi_{\rm ion}(\{\mathbf{R}_I\}), \tag{2.4}$$

where E_{BO} is the ground-state energy of a system of interacting electrons moving in the field of fixed nuclei. The Schrödinger equation for the electrons reads:

$$\hat{H}_{BO}(\{\mathbf{r}_i\},\{\mathbf{R}_I\})\,\Psi_{\rm el}(\{\mathbf{r}_i\},\{\mathbf{R}_I\}) = E_{BO}(\{\mathbf{R}_I\})\,\Psi_{\rm el}(\{\mathbf{r}_i\},\{\mathbf{R}_I\}), \tag{2.5}$$

where $\hat{H}_{BO}(\{\mathbf{r}_i\},\{\mathbf{R}_I\})$ is the Hamiltonian of the electronic system, which depends also parametrically upon $\{\mathbf{R}_I\}$, and it reads:

$$\hat{H}_{BO}(\{\mathbf{r}_i\},\{\mathbf{R}_I\}) = -\frac{\hbar^2}{2m}\sum_i \boldsymbol{\nabla}_i^2 + \frac{1}{2}\sum_{i\neq j}\frac{e^2}{|\mathbf{r}_i-\mathbf{r}_j|} + V_{ext}. \tag{2.6}$$

The first term is the electronic kinetic energy, the second term is the electron-electron Coulomb repulsion energy, the third term is the potential acting on the electrons due to the nuclei, and $V_{ext} = \sum_{i,I} V_I(|\mathbf{r}_i - \mathbf{R}_I|)$. The term $E_{II} = \frac{1}{2}\sum_{I\neq J}\frac{Z_I Z_J e^2}{|\mathbf{R}_I-\mathbf{R}_J|}$ is the classical pairwise Coulomb interaction of nuclei, and it is added to the total energy of the electronic system.

For a system of N electrons, the wavefunction $\Psi_{\rm el}(\{\mathbf{r}_i\}) \equiv \Psi_{\rm el}(\mathbf{r}_1,\ldots,\mathbf{r}_N)$, depends on $3N$ spatial variables.[1] This leads to a rapid increase of the complexity of the problem with the size of the system. Already small systems, that consist only of several tens of electrons, become unfeasible. A solution of this problem is given by the density functional theory.

2.1.2 Density functional theory

In the previous paragraph I have pointed out that the solution of the Schrödinger equation for the many-body problem of interacting electrons is a tremendous task. However, the *density functional theory* (DFT) gives an elegant solution to this problem: instead of dealing with the wavefunction of $3N$ variables, $\Psi_{\rm el}(\mathbf{r}_1,\ldots,\mathbf{r}_N)$, one may consider the electronic ground-state density $n(\mathbf{r})$ of only 3 variables [23]:

$$n(\mathbf{r}) = N\int |\Psi_{\rm el}(\mathbf{r},\mathbf{r}_2,\ldots,\mathbf{r}_N)|^2\, d\mathbf{r}_2\ldots d\mathbf{r}_N. \tag{2.7}$$

The entire field of DFT is based on two fundamental mathematical theorems proved by Pierre Hohenberg and Walter Kohn [1], and the derivation of a set of equations by Walter Kohn and Lu Jey Sham [2] in the mid 60s. The main achievement of the density functional theory is a mapping of the many-body problem of interacting electrons onto a

[1] As has been pointed out above, the electronic wavefunction $\Psi_{\rm el}$ depends parametrically upon positions of the nuclei $\{\mathbf{R}_I\}$. For the sake of simplicity, we will not write explicitly this dependence in the following.

fictitious single-particle problem of non-interacting electrons in an effective local potential.

2.1.2 (a) Hohenberg-Kohn theorems

Theorem I
For any system of interacting particles in an external local potential $V_{ext}(\mathbf{r})$, the potential $V_{ext}(\mathbf{r})$ is determined uniquely, except for a constant, by the ground state particle density $n_0(\mathbf{r})$.

Theorem II
A universal functional for the energy $E_{HK}[n]$ in terms of the density $n(\mathbf{r})$ can be defined, valid for any external potential $V_{ext}(\mathbf{r})$:

$$E_{HK}[n] = F_{HK}[n] + \int V_{ext}(\mathbf{r})\, n(\mathbf{r})\, d\mathbf{r}, \tag{2.8}$$

where $F_{HK}[n]$ is a universal functional of the density which does not depend on $V_{ext}(\mathbf{r})$. For any particular $V_{ext}(\mathbf{r})$, the exact ground-state energy of the system is the global minimum value of the functional $E_{HK}[n]$, and the density $n(\mathbf{r})$ that minimizes this functional is the exact ground state density $n_0(\mathbf{r})$.

The meaning of the first theorem is that the ground-state density $n_0(\mathbf{r})$ completely determines all properties of the ground state of a given many-body system. The second theorem is a corollary of the first one, and of the variational principle of quantum mechanics. Proofs of the Hohenberg-Kohn (HK) theorems can be found in many textbooks, see, e.g., Ref. [24]. The HK theorems provide a general theoretical result, but no practical recipe is given to solve the quantum many-body problem.

2.1.2 (b) Kohn-Sham auxiliary system

A practical formulation of DFT is provided by the Kohn-Sham (KS) approach, which consists in replacing the difficult interacting many-body system by an *auxiliary system of non-interacting particles* in an effective potential, a problem that can be solved more easily [2]. The Kohn-Sham ansatz assumes that the ground-state density of the original interacting system is equal to the ground-state density of the auxiliary non-interacting system [24]. The density of the non-interacting system reads:

$$n(\mathbf{r}) = \sum_{i}^{occ} |\varphi_i(\mathbf{r})|^2, \tag{2.9}$$

where the index i runs over occupied states, and $\varphi_i(\mathbf{r})$ are the KS wavefunctions.[2] The

[2]Equation (2.9) does not include the factor 2 due to spin, nor the occupation factor which is needed for the description of metallic systems. In the general case, these factors must be included [24].

kinetic energy of the non-interacting system reads:

$$T_0 = -\frac{\hbar^2}{2m_0}\sum_i^{occ}\langle\varphi_i|\nabla^2|\varphi_i\rangle. \tag{2.10}$$

The Hartree energy, *i.e.* the classical Coulomb interaction energy of the electron density $n(\mathbf{r})$ interacting with the electrostatic potential generated by itself, reads:

$$E_H[n] = \frac{e^2}{2}\iint\frac{n(\mathbf{r})\,n(\mathbf{r}')}{|\mathbf{r}-\mathbf{r}'|}\,d\mathbf{r}\,d\mathbf{r}'. \tag{2.11}$$

The Kohn-Sham approach to the interacting many-body problem consists in rewriting the Hohenberg-Kohn expression for the ground-state energy functional (2.8) as [24]:

$$E_{KS}[n] = T_0[n] + E_H[n] + E_{\rm xc}[n] + \int V_{ext}(\mathbf{r})\,n(\mathbf{r})\,d\mathbf{r}, \tag{2.12}$$

where $E_{\rm xc}[n]$ is the exchange-correlation (XC) energy functional. The XC energy functional contains all quantum effects which are not described by $T_0[n]$ and $E_H[n]$. It accounts for the many-body effects missing in the classical description of the Hartree energy, namely the exchange energy coming from the Pauli principle, and for the correlation effects which are absent in the kinetic energy term $T_0[n]$ and $E_H[n]$ of the non-interacting system of electrons. The XC energy functional is unknown, a suitable approximation for it is necessary. This problem will be addressed in the following paragraph.

Let us apply the variational principle of Theorem II to the energy functional of Eq. (2.12), under the constraint of the orthonormalization of KS wavefunctions, $\langle\varphi_i|\varphi_j\rangle = \delta_{ij}$. Since T_0, Eq. (2.10), is explicitly expressed as a functional of the KS wavefunctions $\varphi_i(\mathbf{r})$, but all other terms in Eq. (2.12) are functionals of the density $n(\mathbf{r})$, one can vary the KS wavefunctions and use the chain rule to derive the Euler-Lagrange variational equation:

$$\frac{\delta E_{KS}}{\delta\varphi_i^*(\mathbf{r})} + \varepsilon_i\,\frac{\delta\left(1-\langle\varphi_i|\varphi_i\rangle\right)}{\delta\varphi_i^*(\mathbf{r})} = 0, \tag{2.13}$$

where ε_i are the Lagrange multipliers. The first term in Eq. (2.13) reads [see Eq. (2.12)]:

$$\frac{\delta E_{KS}}{\delta\varphi_i^*(\mathbf{r})} = \frac{\delta T_0}{\delta\varphi_i^*(\mathbf{r})} + \left[\frac{\delta E_H[n]}{\delta n(\mathbf{r})} + \frac{\delta E_{\rm xc}[n]}{\delta n(\mathbf{r})} + \frac{\delta E_{ext}[n]}{\delta n(\mathbf{r})}\right]\frac{\delta n(\mathbf{r})}{\delta\varphi_i^*(\mathbf{r})}. \tag{2.14}$$

By using Eqs. (2.9) and (2.10), one obtains:

$$\frac{\delta n(\mathbf{r})}{\delta\varphi_i^*(\mathbf{r})} = \varphi_i(\mathbf{r}), \quad \frac{\delta T_0}{\delta\varphi_i^*(\mathbf{r})} = -\frac{\hbar^2}{2m_0}\nabla^2\varphi_i(\mathbf{r}). \tag{2.15}$$

Thereby, Eqs. (2.13)-(2.15) lead to the so-called single-particle Kohn-Sham (Schrödinger-like) equations [24]:

$$\left(-\frac{\hbar^2}{2m_0}\nabla^2 + V_{KS}(\mathbf{r})\right)\varphi_i(\mathbf{r}) = \varepsilon_i\,\varphi_i(\mathbf{r}), \tag{2.16}$$

where φ_i and ε_i are the KS wavefunctions and energy values, respectively, and V_{KS} is the KS *effective* potential, which reads:

$$\begin{aligned} V_{KS}(\mathbf{r}) &= V_H(\mathbf{r}) + V_{\rm xc}(\mathbf{r}) + V_{ext}(\mathbf{r}) \\ &= e^2 \int \frac{n(\mathbf{r}')}{|\mathbf{r}-\mathbf{r}'|}\, d\mathbf{r}' + \frac{\delta E_{\rm xc}[n]}{\delta n(\mathbf{r})} + V_{ext}(\mathbf{r}), \end{aligned} \tag{2.17}$$

which is the sum of Hartree, exchange-correlation and external potentials [see Eq. (2.14)]. The KS equations are independent of any approximation to the XC functional, and would lead to the exact ground-state density and energy of the interacting many-body system, if the *exact* XC functional were known, which is not the case [24]. In practice, Eqs. (2.9), (2.16) and (2.17) are solved *self-consistently* by iterations [24].

2.1.2 (c) Physical meaning of Kohn-Sham energy values

Kohn-Sham energy values ε_i of a fictitious non-interacting system have no physical meaning. Only the energy of the highest occupied KS state corresponds to the exact ionization energy of the system [31]. The time-independent DFT is a *ground state* theory, and thus it is not allowed, strictly speaking, to describe the excited states of the system. The Kohn-Sham energy values ε_i must be distinguished from the quasiparticle energy values, which can be obtained by using Green's function techniques [17], of the system which is measured, *e.g.* in photoemission experiments [22]. Nevertheless, there are many systems where the quasiparticle corrections to the KS energy values are quite small, and thus the latter can be used as a first approximation to the quasiparticle band structure, except a gap (see the discussion in Sec. 5.1.3).

I will make a detailed comparison of the KS energy values with available experiments on bismuth in Sec. 5.1.3.

2.1.2 (d) Exchange-correlation functional

So far, all of the DFT equations have been formally exact. But one still has to find an explicit form for the XC functional $E_{\rm xc}[n]$. In fact, the *exact* form of the XC functional is unknown [24]. The success of DFT is due to the fact that $E_{\rm xc}[n]$ can be reasonably approximated. There is a number of approximate functionals that have been found to give good results in a large variety of physical problems. One useful classification of functionals has been given by John Perdew and co-workers [32].[3] In this paragraph I will briefly overview the functionals that I have used for the results described in part II of this manuscript.

The simplest approximation to the true XC functional is the *local density approximation* (LDA), which assumes that the XC energy of the real system behaves locally as that

[3]For a review of XC functionals see, *e.g.*, Ref. [24].

of a uniform electron gas [32]. The XC functional in this case can be expressed as:

$$E_{\rm xc}^{LDA}[n] = \int \varepsilon_{\rm xc}^{hom}(n(\mathbf{r}))\, n(\mathbf{r})\, d\mathbf{r}, \tag{2.18}$$

where $\varepsilon_{\rm xc}^{hom}(n)$ is the XC energy per electron of the electron gas with a homogeneous density n. The exchange contribution can be evaluated analytically [24], while the correlation part is obtained by parameterizing the results of Monte Carlo simulations of Ceperley-Alder [33]. The most widely used LDA functional is the Perdew-Zunger functional (PZ81) [34]. The LDA is exact in the limit of high density or slowly varying density distributions; in fact, experience has shown that accurate results can be obtained well beyond this expected range of validity [25]. Typically LDA yields a good accuracy in reproducing experimental structural and vibrational properties of strongly bound systems; it usually overestimates the values of the bonding energy and underestimates bond lengths [25].

The next approximation to the XC functional is the *generalized gradient approximation* (GGA). The physical idea behind the GGA is that the real electron densities are not uniform, and an inclusion of information about its spatial variation can create a functional with greater flexibility to describe real materials [32]. In GGA, the XC functional is expressed using both the local electron density $n(\mathbf{r})$, and the gradient of the electron density $\nabla n(\mathbf{r})$:

$$E_{\rm xc}^{GGA}[n] = \int \varepsilon_{\rm xc}(n(\mathbf{r}), \nabla n(\mathbf{r}))\, n(\mathbf{r})\, d\mathbf{r}. \tag{2.19}$$

Since there are many ways in which information from the gradient of the electron density can be included in the GGA functional, there is a large number of GGA functionals. Two of the most widely used GGA functionals in calculations for solids are the Perdew-Wang functional (PW91) [35] and the Perdew-Burke-Ernzerhof functional (PBE) [36]. The GGA functionals usually overestimate bond lengths.

There are many other types of XC functionals, *e.g. meta-GGA*, which include the information from $n(\mathbf{r})$, $\nabla n(\mathbf{r})$, and $\nabla^2 n(\mathbf{r})$; *hybrid-GGA*, which describe exchange using a mixture of the exact-exchange and GGA-exchange functional, etc. [24]. The choice of the XC functional depends on the system and properties which are studied.

In this thesis I will use the LDA functional with Ceperley-Alder parametrization [33], and the GGA functional with Perdew-Burke-Ernzerhof parametrization [36]. In Sec. 5.1.2 I will discuss the lattice parameters and bond length in bismuth, within the LDA and GGA.

2.1.2 (e) Generalization of DFT

I would like to point out that Hohenberg, Kohn and Sham's formulation of DFT was performed for non-relativistic time-independent zero-temperature case. However, after the great success of this theory, DFT was generalized. In Sec. 2.2.2 I will discuss the generalization of DFT to the relativistic case, and in Sec. 3.1.2 I will present the time-dependent DFT. The DFT was also generalized to systems at finite temperatures [37], however, I will not discuss it in this thesis. Finally, there has also been developed a density

functional *perturbation* theory (DFPT) [38, 39, 40, 41], for the description of vibrational properties of materials (phonons). Sections 3.4 and 7.1 are closely related to DFPT [40].

2.2 Relativistic theory

The preceding discussion of Sec. 2.1 was based on the non-relativistic quantum mechanics, where the spin of an electron and the relativistic effects were neglected. However, spin plays an important role in a determination of a wide variety of properties of materials, and thus without a proper account of it the theory would be incomplete. Moreover, when the system under study consists of heavy atoms, relativistic effects become essential. The coupling of the spin to the orbital momentum of an electron, the *spin-orbit coupling*, should be taken into account for a correct description of the relativistic system. In some systems, *e.g.* semimetal bismuth (see Chapter 4), the spin-orbit coupling is extremely large, and it is crucial for the correct description of electronic and vibrational properties of the material.

In this section, I will give an introduction to the relativistic formalism of the many-body electronic problem. First, I will discuss the relativistic Dirac equation, and afterwards I will present a relativistic generalization of the density functional theory.

2.2.1 Dirac equation

2.2.1 (a) General theory

The relativistic system is described by the Dirac equation, invented by Paul Dirac in 1928, which generalizes the Schrödinger equation in a relativistically covariant form [42, 43]:

$$\hat{H}_D\,\psi(\mathbf{r}) = E\,\psi(\mathbf{r}), \tag{2.20}$$

where $\hat{H}_D$ is the Dirac Hamiltonian, $\psi(\mathbf{r})$ is the four-component single-particle wavefunction (spinor) that describes spin-$\frac{1}{2}$ particles, and E is the energy of this particle. The Dirac Hamiltonian for an electron moving in an effective scalar potential V (as opposed to a vector potential), reads:

$$\hat{H}_D = c\,(\boldsymbol{\alpha}\cdot\mathbf{p}) + \boldsymbol{\beta}\,mc^2 + V I_4, \tag{2.21}$$

where c is the speed of light, m is the electron mass, $\mathbf{p} = -i\hbar\boldsymbol{\nabla}$ is the momentum operator, and I_4 is the 4×4 identity matrix. The components α_i of the 4×4 matrix $\boldsymbol{\alpha}$ read:

$$\alpha_i = \begin{pmatrix} 0 & \sigma_i \\ \sigma_i & 0 \end{pmatrix}, \tag{2.22}$$

where σ_i are the 2×2 Pauli matrices:

$$\sigma_1 = \begin{pmatrix} 0 & 1 \\ 1 & 0 \end{pmatrix}, \quad \sigma_2 = \begin{pmatrix} 0 & -i \\ i & 0 \end{pmatrix}, \quad \sigma_3 = \begin{pmatrix} 1 & 0 \\ 0 & -1 \end{pmatrix}. \tag{2.23}$$

The 4×4 matrix $\boldsymbol{\beta}$ reads:

$$\boldsymbol{\beta} = \begin{pmatrix} I_2 & 0 \\ 0 & -I_2 \end{pmatrix}, \tag{2.24}$$

where I_2 is the 2×2 identity matrix. The four-component spinor $\psi(\mathbf{r})$, appearing in the Dirac equation (2.20), can be written in terms of two two-component spinors:

$$\psi(\mathbf{r}) = \begin{pmatrix} \psi^A(\mathbf{r}) \\ \psi^B(\mathbf{r}) \end{pmatrix}, \tag{2.25}$$

where in the case of electrons (solutions of Eq. (2.20) having a positive energy), ψ^A is the *large* component, and ψ^B is the *small* component. The Dirac equation (2.20) becomes a *set of coupled equations* for ψ^A and ψ^B, namely [24]:

$$c\,(\boldsymbol{\sigma}\cdot\mathbf{p})\,\psi^B = \left(E - V - mc^2\right)\psi^A, \tag{2.26}$$

$$c\,(\boldsymbol{\sigma}\cdot\mathbf{p})\,\psi^A = \left(E - V + mc^2\right)\psi^B. \tag{2.27}$$

Relativistic effects[4] originate deep inside the atomic core, so it is sufficient to solve the relativistic equations in a spherical atomic geometry. In the case of a spherical potential $V(r)$, one can make use of a conservation of parity and total angular momentum [24]. The total angular momentum reads:

$$\mathbf{J} = \mathbf{L} + \mathbf{S}, \tag{2.28}$$

where $\mathbf{L}$ is the orbital angular momentum, $\mathbf{S} = \hbar\,\boldsymbol{\Sigma}/2$ is the spin angular momentum, and $\boldsymbol{\Sigma}$ reads:

$$\boldsymbol{\Sigma} = \begin{pmatrix} \boldsymbol{\sigma} & 0 \\ 0 & \boldsymbol{\sigma} \end{pmatrix}. \tag{2.29}$$

The spinor $\psi(\mathbf{r})$ can be expressed in terms of radial and angular-spin functions [$\mathbf{r} = (r, \theta, \varphi)$]:

$$\psi_{njlm}(\mathbf{r}) = \begin{pmatrix} \psi^A_{njlm}(\mathbf{r}) \\ \psi^B_{njlm}(\mathbf{r}) \end{pmatrix} = \begin{pmatrix} g_{nj}(r)\,\phi_{jlm}(\theta,\varphi) \\ i f_{nj}(r)\,\phi_{jlm}(\theta,\varphi) \end{pmatrix}, \tag{2.30}$$

where n, j, l, and m are the quantum numbers, which characterize the quantum state of the electron: n is the principal quantum number, l is the azimuthal quantum number (angular momentum), m is the magnetic quantum number (projection of angular momentum), and j is the total angular momentum. Equation (2.30) defines two functions with the same quantum numbers n, j and m, but opposite parity for the two possible values $l = j \pm \frac{1}{2}$. The two-component angular-spin functions $\phi_{jlm}(\theta,\varphi)$ are the eigenfunctions of the total angular momentum j, and can be written explicitly as [24]:

$$\phi_{jlm} = \sqrt{\frac{l + \frac{1}{2} \pm m}{2l+1}}\, Y_l^{m-\frac{1}{2}} \begin{pmatrix} 1 \\ 0 \end{pmatrix} \pm \sqrt{\frac{l + \frac{1}{2} \mp m}{2l+1}}\, Y_l^{m+\frac{1}{2}} \begin{pmatrix} 0 \\ 1 \end{pmatrix}, \tag{2.31}$$

[4]Relativistic effects are the spin-orbit coupling, the mass-velocity, and the Darwin correction. These effects will be defined in the following discussion.

where the upper sign is for $j = l + \frac{1}{2}$, and the lower sign is for $j = l - \frac{1}{2}$. Here, $Y_l^{m\pm\frac{1}{2}}(\theta, \varphi)$ are the spherical harmonics, and $\begin{pmatrix} 1 \\ 0 \end{pmatrix}$, $\begin{pmatrix} 0 \\ 1 \end{pmatrix}$ are the Pauli spinors. The resulting equations for the radial functions $g(r)$ and $f(r)$ are simplified if one defines the energy as:

$$E' = E - mc^2, \tag{2.32}$$

and the *mass-velocity*, which is the radially varying mass, as:

$$M(r) = m + \frac{E' - V(r)}{2c^2}, \tag{2.33}$$

and using the quantum number κ,

$$\begin{aligned} &\text{if } l = j + \frac{1}{2}, \qquad \text{then } \kappa = j + \frac{1}{2} = l, \\ &\text{if } l = j - \frac{1}{2}, \qquad \text{then } \kappa = -\left(j + \frac{1}{2}\right) = -(l+1). \end{aligned} \tag{2.34}$$

Note that $\kappa(\kappa+1) = l(l+1)$ in either case. Thereby, the coupled equations (2.26), (2.27) can be written in the form of radial equations [24]:

$$\begin{aligned} -\frac{\hbar^2}{2M}\frac{1}{r^2}\frac{d}{dr}\left[r^2\frac{dg_{n\kappa}}{dr}\right] + \left[V + \frac{\hbar^2}{2M}\frac{l(l+1)}{r^2}\right] g_{n\kappa} \\ -\frac{\hbar^2}{4M^2c^2}\frac{dV}{dr}\frac{dg_{n\kappa}}{dr} - \frac{\hbar^2}{4M^2c^2}\frac{dV}{dr}\frac{1+\kappa}{r}g_{n\kappa} \;\; = \;\; E' g_{n\kappa}\,, \end{aligned} \tag{2.35}$$

and

$$\frac{df_{n\kappa}}{dr} = \frac{1}{\hbar c}\left(V - E'\right) g_{n\kappa} + \frac{\kappa - 1}{r} f_{n\kappa}. \tag{2.36}$$

For valence[5] electrons, *i.e.* small E', outside of the core region, *i.e.* small $V(r)$, one can rewrite Eq. (2.36) as [44]:

$$f_{n\kappa} = \frac{\hbar}{2Mc}\left[\frac{dg_{n\kappa}}{dr} + \frac{1+\kappa}{r} g_{n\kappa}\right]. \tag{2.37}$$

These are the general equations for a spherical potential. No approximations have been made so far. Equation (2.35) is the same as an ordinary radial Schrödinger equation [24], except that the mass M is a function of the radius, and there are two added terms on the left-hand side, which are, the *Darwin term*, $\frac{dV}{dr}\frac{dg}{dr}$, and the last term is the *spin-orbit coupling*. The latter is due to the fact that

$$\mathbf{L} \cdot \boldsymbol{\sigma}\, \phi_{\kappa m} = -\hbar\,(1+\kappa)\,\phi_{\kappa m}, \tag{2.38}$$

where $\phi_{\kappa m}$ is the appropriate ϕ_{jlm} determined by the quantum number κ [see Eq. (2.34)].

[5]The discussion about a partition of an atom on valence and core regions will be given in Sec. 2.3.2.

2.2.1 (b) Scalar-relativistic approximation and spin-orbit coupling

If the spin-orbit coupling in the system is weak, then the corresponding term can be neglected in the radial equations for g and f, Eqs. (2.35) and (2.37). Afterwards, the spin-orbit coupling can be treated variationally or by the perturbation theory [24]. Thereby, Eqs. (2.35) and (2.37) can be written in terms of the approximate functions $\tilde{g}_{nl}$ and $\tilde{f}_{nl}$ as [24]:

$$-\frac{\hbar^2}{2M}\frac{1}{r^2}\frac{d}{dr}\left[r^2\frac{d\tilde{g}_{nl}}{dr}\right]+\left[V+\frac{\hbar^2}{2M}\frac{l(l+1)}{r^2}\right]\tilde{g}_{nl}-\frac{\hbar^2}{4M^2c^2}\frac{dV}{dr}\frac{d\tilde{g}_{n\kappa}}{dr}=E'\tilde{g}_{nl}\,, \tag{2.39}$$

and

$$\tilde{f}_{nl}=\frac{\hbar}{2Mc}\frac{d\tilde{g}_{nl}}{dr}, \tag{2.40}$$

with the normalization condition:

$$\int\left(\tilde{g}_{nl}^2+\tilde{f}_{nl}^2\right)r^2\,dr=1. \tag{2.41}$$

Equation (2.39) is the *scalar-relativistic radial equation*, which can be solved with the same techniques as the usual non-relativistic equation. By expanding the mass-velocity $M(r)$ [see Eq. (2.33)] in series in Eq. (2.39), one will obtain the Pauli equation [45]. The Pauli equation is the non-relativistic limit of the Dirac equation, and it can be used when electrons are slow enough so that relativistic effects can be neglected.

When the relativistic spin-orbit coupling effect is neglected, all electronic states are at least twofold degenerate. The spin-orbit coupling term can be included variationally (perturbatively) following the approach of MacDonald *et al.* [46], with the corresponding Hamiltonian:

$$\hat{H}^{\mathrm{so}}=\frac{\hbar^2}{2M^2c^2}\frac{1}{r}\frac{dV}{dr}\begin{pmatrix}(\mathbf{L}\cdot\boldsymbol{\sigma})\;I_2\\ 0\end{pmatrix}. \tag{2.42}$$

The matrix elements of $\hat{H}^{\mathrm{so}}$ are computed in the basis used by a particular method, and then they are added to the Hamiltonian matrix in the variational procedure. In more refined calculations, the spin-orbit coupling is treated *self-consistently* (see Sec. 2.2.2). The inclusion of the spin-orbit coupling effect lifts the degeneracy of the formerly spin-degenerate bands. In the calculations of solids, relativistic effects can be included indirectly through pseudopotentials, by generating them using relativistic atomic calculations. This has been done in the present work (see Sec. 2.3.2).

2.2.2 Relativistic density functional theory

One fundamental limitation of the DFT formalism presented in Sec. 2.1.2 is that it is based on non-relativistic quantum theory, and hence it will not give an accurate description of a system in which relativistic effects are significant. A few years after the proposal of DFT, a relativistic extension able to deal with both non-magnetic and magnetic systems was proposed [47, 48]. The basic variables of the relativistic DFT are the charge and the vector-current densities [48]. In this thesis I will not consider the general theory

[49, 50, 51], but a simplified version [47, 48, 52], in which the dependence of the total energy on the orbital part of the vector-current is neglected.

Before proceeding to the generalization of the non-relativistic DFT to the relativistic case, I would like to point out that the relativistic effects can be treated by using an *ab initio* scalar-relativistic *zeroth-order regular approximation* (ZORA) [53]. It has been introduced in the quantum chemistry community for atomic and molecular electronic structure calculations, which take into account relativistic effects. It is worth noting that the ZORA approach has been applied almost exclusively within the framework of DFT [53]. I will not discuss the ZORA approach in the following. An interested reader is referred to, *e.g.*, Ref. [53].

2.2.2 (a) Dirac-Hohenberg-Kohn theorems

Rajagopal and Callaway have shown [48] that the two Hohenberg-Kohn theorems (see Sec. 2.1.2) can be generalized by including the relativistic effects. This leads to the so-called *Dirac-Hohenberg-Kohn* (DHK) *theorems*. A proof of the DHK theorems is performed in exactly the same way as the proof of Hohenberg-Kohn theorems within the non-relativistic formalism [47].

The Dirac-Hohenberg-Kohn energy functional E_{DHK}, can be written using the Gordon decomposition as a functional dependent on the density $n(\mathbf{r})$ and the magnetization $\mathbf{m}(\mathbf{r})$, $E_{DHK}[n(\mathbf{r}), \mathbf{m}(\mathbf{r})]$, [48]. In the Gordon decomposition a three-dimensional current is represented as the sum of the orbit-current and the magnetization. The first term is usually neglected because in most cases it is small in comparison to the second one. A general theory, based on a quantum electrodynamics (QED) formalism, can be found in Refs. [49, 50, 51]. One can prove that the ground-state energy is a unique functional of the ground-state density and magnetization density, provided the system is not subject to an external magnetic field [49]. This means that the system can be completely described by its density and magnetization density.

2.2.2 (b) Dirac-Kohn-Sham equations

Similarly to the non-relativistic DFT, the interacting relativistic many-body electronic system can be replaced by an auxiliary relativistic system of non-interacting electrons. Therefore, let us start by defining the *spin density*, $n_{\eta_1,\eta_2}(\mathbf{r})$, of the non-interacting system as [54]:

$$n_{\eta_1,\eta_2}(\mathbf{r}) = \sum_i \psi^*_{i,\eta_1}(\mathbf{r})\psi_{i,\eta_2}(\mathbf{r}), \tag{2.43}$$

where $\psi_{i,\eta}(\mathbf{r})$ are the four-component one-electron spinors, the index i runs over the occupied states, and the indices η_1 and η_2 run over the four spinor components. Then, one can define the electron density, $n(\mathbf{r})$, and the magnetization density, $\mathbf{m}(\mathbf{r})$, of the

non-interacting system as [54]:[6]

$$n(\mathbf{r}) = \sum_{\eta} n_{\eta,\eta}(\mathbf{r}) = \sum_{i,\eta} |\psi_{i,\eta}(\mathbf{r})|^2, \tag{2.44}$$

$$\begin{aligned} \mathbf{m}_k(\mathbf{r}) &= \mu_B \hbar \sum_{\eta_1,\eta_2} n_{\eta_1,\eta_2}(\mathbf{r}) \left(\boldsymbol{\beta}\boldsymbol{\Sigma}_k\right)^{\eta_1,\eta_2} \\ &= \mu_B \hbar \sum_{i,\eta_1,\eta_2} \psi^*_{i,\eta_1}(\mathbf{r}) \left(\boldsymbol{\beta}\boldsymbol{\Sigma}_k\right)^{\eta_1,\eta_2} \psi_{i,\eta_2}(\mathbf{r}), \end{aligned} \tag{2.45}$$

where the index k runs over 3 components of the vector-matrix, μ_B is the Bohr magneton, $\hbar\,\boldsymbol{\Sigma}/2$ is the spin angular momentum [see Eq. (2.29)], and $\boldsymbol{\beta}$ is the 4×4 matrix defined in Eq. (2.24). The Dirac kinetic energy T_0 of the non-interacting relativistic system reads [54]:

$$T_0 = \sum_{i,\eta_1,\eta_2} \langle \Psi_{i,\eta_1} | T_D^{\eta_1,\eta_2} | \Psi_{i,\eta_2} \rangle, \tag{2.46}$$

where $T_D^{\eta_1,\eta_2}$ are the components of the Dirac kinetic energy operator, which can be written in terms of the momentum operator $\mathbf{p} = -i\hbar\boldsymbol{\nabla}$, and the 4×4 matrices $\boldsymbol{\alpha}$ and $\boldsymbol{\beta}$ [see Eqs. (2.22)-(2.24)]. By subtracting the electron rest energy, mc^2, [see Eq. (2.32)], one obtains [see Eq. (2.21)]:

$$\hat{T}_D = c\,(\boldsymbol{\alpha} \cdot \mathbf{p}) + (\boldsymbol{\beta} - I_4)\,mc^2. \tag{2.47}$$

Thereby, the Dirac-Kohn-Sham (DKS) energy functional, E_{DKS}, of the interacting relativistic many-body electronic system in the external potential, $V_{ext}(\mathbf{r})$, can be expressed as [cf. Eq. (2.12)]:

$$E_{DKS}[n, \mathbf{m}] = T_0[n] + E_H[n] + E_{\rm xc}[n, \mathbf{m}] + \int V_{ext}(\mathbf{r})\, n(\mathbf{r})\, d\mathbf{r}, \tag{2.48}$$

where $E_H[n]$ is the Hartree energy functional [see Eq. (2.11)], and $E_{\rm xc}[n, \mathbf{m}]$ is the exchange-correlation (XC) energy functional which depends on both the electron density $n(\mathbf{r})$ and the magnetization density $\mathbf{m}(\mathbf{r})$. The minimization of the energy functional, E_{DKS}, according to the DHK Theorem II leads to the Dirac-type relativistic Kohn-Sham single-particle equations, so-called, *Dirac-Kohn-Sham* (DKS) *equations* [54]:

$$\sum_{\eta_2} \Big[T_D^{\eta_1,\eta_2} + V_{DKS}(\mathbf{r})\,\delta^{\eta_1,\eta_2} - \mu_B \hbar\, \mathbf{B}_{\rm xc}(\mathbf{r}) \cdot \left(\boldsymbol{\beta}\boldsymbol{\Sigma}\right)^{\eta_1,\eta_2} \Big] \psi_{i,\eta_2}(\mathbf{r}) = \varepsilon_i \psi_{i,\eta_1}(\mathbf{r}), \tag{2.49}$$

where $\psi_{i,\eta}$ and ε_i are the DKS spinors and energy values, respectively, and V_{DKS} is the DKS effective potential which reads [cf. Eq. (2.17)]:

$$\begin{aligned} V_{DKS}(\mathbf{r}) &= V_H(\mathbf{r}) + V_{\rm xc}(\mathbf{r}) + V_{ext}(\mathbf{r}) \\ &= e^2 \int \frac{n(\mathbf{r}')}{|\mathbf{r} - \mathbf{r}'|}\, d\mathbf{r} + \frac{\delta E_{\rm xc}[n, \mathbf{m}]}{\delta n(\mathbf{r})} + V_{ext}(\mathbf{r}), \end{aligned} \tag{2.50}$$

[6] The spin density $n_{\eta_1,\eta_2}(\mathbf{r})$ on one hand, or the electron density $n(\mathbf{r})$ and the magnetization density $\mathbf{m}(\mathbf{r})$ on the other hand, can be considered as equivalent variables [54].

and $\mathbf{B}_{\rm xc}$ is the exchange-correlation magnetic field, which reads:

$$\mathbf{B}_{\rm xc}(\mathbf{r}) = -\frac{\delta E_{\rm xc}[n,\mathbf{m}]}{\delta \mathbf{m}(\mathbf{r})}. \tag{2.51}$$

There are several differences between the non-relativistic and relativistic formulations of DFT, namely:

(*i*) There is a replacement of the single-particle Schrödinger-like equation (2.16), by a single-particle Dirac-like equation (2.49);

(*ii*) The sums over the occupied states i in Eqs. (2.43) - (2.46) must be over positive-energy states only.

(*iii*) The XC functional, $E_{\rm xc}[n,\mathbf{m}]$, contains relativistic effects in addition to the many-body exchange and correlation effects of the non-relativistic formalism. These additional effects are the retardation of the Coulomb interaction between the electrons, and the magnetic interaction between moving electrons [47].

The DKS equations (2.49) can be rewritten by introducing the *large* and the *small* components of the four-component spinors $\psi_{i,\eta}$ [see Eq. (2.25)]:

$$\psi_{i\eta}(\mathbf{r}) = \begin{pmatrix} \psi^A_{i,\sigma}(\mathbf{r}) \\ \\ \psi^B_{i,\sigma}(\mathbf{r}) \end{pmatrix}, \tag{2.52}$$

where $\psi^A_{i\sigma}$ and $\psi^B_{i\sigma}$ are the large and the small two-component spinors, respectively, the index η runs over the four spinor components, and the index σ runs over the two spinor components. Therefore, Eq. (2.49) becomes a set of coupled equations [cf. Eqs. (2.26) - (2.27)] [54]:

$$\begin{aligned} \sum_{\sigma_2} c\,\left(\boldsymbol{\sigma}^{\sigma_1,\sigma_2}\cdot\mathbf{p}\right)\,\psi^B_{i,\sigma_2}(\mathbf{r}) &= \left(\varepsilon_i - V_{DKS}(\mathbf{r})\right)\delta^{\sigma_1,\sigma_2}\psi^A_{i,\sigma_1}(\mathbf{r}) \\ &\quad +\mu_B\hbar\sum_{\sigma_2}\left(\mathbf{B}_{\rm xc}(\mathbf{r})\cdot\boldsymbol{\sigma}^{\sigma_1,\sigma_2}\right)\psi^A_{i,\sigma_2}(\mathbf{r}), \end{aligned} \tag{2.53}$$

$$\begin{aligned} \sum_{\sigma_2} c\,\left(\boldsymbol{\sigma}^{\sigma_1,\sigma_2}\cdot\mathbf{p}\right)\,\psi^A_{i,\sigma_2}(\mathbf{r}) &= \left(\varepsilon_i - V_{DKS}(\mathbf{r}) + 2mc^2\right)\delta^{\sigma_1,\sigma_2}\psi^B_{i,\sigma_1}(\mathbf{r}) \\ &\quad -\mu_B\hbar\sum_{\sigma_2}\left(\mathbf{B}_{\rm xc}(\mathbf{r})\cdot\boldsymbol{\sigma}^{\sigma_1,\sigma_2}\right)\psi^B_{i,\sigma_2}(\mathbf{r}). \end{aligned} \tag{2.54}$$

Equations (2.53) and (2.54) are exact, no approximations have been made so far. They are solved *self-consistently* in an iterative way. All relativistic effects, *i.e.* the spin-orbit coupling, the mass-velocity, and the Darwin contribution, are contained in these equations.

2.2.2 (c) Non-relativistic limit: Pauli equations

When the electron speed is much smaller than the speed of light c, the Dirac-type Kohn-Sham equations (2.53) and (2.54) can be approximated by the *Pauli-type Kohn-Sham equations* [54]:[7]

$$\sum_{\sigma_2}\left[\left(\frac{\mathbf{p}^2}{2m}+V_{DKS}(\mathbf{r})\right)\delta^{\sigma_1,\sigma_2}-\mu_B\hbar\left(\mathbf{B}_{\mathrm{xc}}(\mathbf{r})\cdot\boldsymbol{\sigma}^{\sigma_1,\sigma_2}\right)\right]\psi^A_{i,\sigma_2}(\mathbf{r})=\varepsilon_i\psi^A_{i,\sigma_1}(\mathbf{r}), \tag{2.55}$$

and

$$\psi^B_{i,\sigma_1}(\mathbf{r})\approx\sum_{\sigma_2}\frac{\boldsymbol{\sigma}^{\sigma_1,\sigma_2}\cdot\mathbf{p}}{2c}\,\psi^A_{i,\sigma_2}(\mathbf{r}). \tag{2.56}$$

Equations (2.55) and (2.56) have an error of the order $(\mathrm{v}/c)^2$, where v is the electron velocity [54]. In the regions far from the nuclei, *i.e.* for valence electrons (see Sec. 2.3.2), the Pauli-type Kohn-Sham equation (2.55) is quite a good approximation of fully relativistic Dirac-type Kohn-Sham equations (2.53) and (2.54) [54] in some materials, *e.g.* light elements. However, the spin-orbit coupling may be essential, *e.g.* for heavy elements like bismuth (see Chapter 4). Therefore, it has to be included in the calculations.

2.2.2 (d) Perturbative and self-consistent treatment of the spin-orbit coupling

The relativistic effects up to order α^2, where α is the fine-structure constant, can be included in electronic structure calculations by solving non-relativistic Kohn-Sham equations, like Pauli-type Kohn-Sham equations for two-component spinors (2.55), with pseudopotentials (see Sec. 2.3.2) tailored to reproduce the solutions of fully relativistic Dirac-type Kohn-Sham equations (2.53) and (2.54) [44, 55]. The spin-orbit coupling (SOC) can be treated either perturbatively or self-consistently [56]. In the perturbative approach, the SOC is included to first order through a second variational step on the scalar-relativistic zeroth order wavefunctions. Examples of the perturbative treatment of the SOC are Refs. [57, 58, 59]. In contrast, in the self-consistent approach, the SOC is treated on equal footing with other relativistic effects, *i.e.* the mass-velocity and the Darwin contribution. The self-consistency is achieved for the full Hamiltonian, including the SOC term [see Eq. (2.42)], when solving the Pauli-type Kohn-Sham equations (2.39). Examples of the self-consistent treatment of the SOC are Refs. [60, 61, 62]. The fully self-consistent treatment of the SOC leads to only minor corrections in the case of semiconductors, but it is of greater importance when dealing with metals [62].

In this work the self-consistent treatment of the SOC has been used.

[7] The Pauli-type Kohn-Sham equations can be obtained directly from the minimization of the non-relativistic energy-functional, Eq. (2.12), written for two-component spinors [54].

2.2.2 (e) Exchange-correlation functional

In principle, the relativistic DFT provides a method for calculating the charge density, the magnetization, and the ground-state energy exactly. In practice, however, an approximation must be made for the exchange-correlation functional, $E_{\rm xc}$, as in the non-relativistic case. Only the exchange contribution to the relativistic extension of LDA (RLDA), Ref. [63, 47], and GGA (RGGA), Ref. [64], has been investigated so far. The exact contribution from the correlation of electrons is not known even in the non-relativistic formalism. Practice shows that one can still use the XC functionals in their non-relativistic form for relativistic calculations, because the differences between the results obtained by using one form or another are small. This has been demonstrated on single atoms [65] and on periodic solids, like gold and platinum [66, 55].

2.3 Plane-wave pseudopotential method

In Secs. 2.1.2 and 2.2.2 I have presented non-relativistic and relativistic formulation of the density functional theory, respectively. These theories are based on the solution of the (Dirac-type) Kohn-Sham equations, Eqs. (2.16) and (2.49). In practice, in order to solve these equations, one has to choose a basis set, suitable for the system under study, in order to expand the Kohn-Sham wavefunctions. In particular, for the description of solids, the plane wave basis set is a good choice, since the plane waves have the periodicity of solids. However, the electronic wavefunctions become rapidly oscillating functions near atomic nuclei, and thus a large number of plane waves would be required to describe such oscillations. Nevertheless, by using a pseudopotential approximation, such a problem can be overcome. The use of plane waves basis sets with pseudopotentials constitutes the *plane-wave pseudopotential method*. A detailed description of such a method is given, *e.g.*, in Refs. [24, 25, 67]. In this thesis, I will present the results obtained by using the `QUANTUM ESPRESSO` package [68], which is based on the plane-wave pseudopotential method.

In Sec. 2.3.1 I will discuss different basis sets which can be used for the expansion of the Kohn-Sham wavefunctions. In particular, I will present a formulation of the Kohn-Sham equations in the basis of plane waves. In Sec. 2.3.2 I will show what is the pseudopotential approximation, and how the spin-orbit coupling can be treated with pseudopotentials.

2.3.1 Basis set

2.3.1 (a) Choice of the basis set

The basic step of the DFT calculations is an evaluation of the Kohn-Sham Hamiltonian $\hat{H}_{KS}$. In order to solve the KS equations [see Eq. (2.16)], $\hat{H}_{KS}\,\varphi(\mathbf{r}) = \varepsilon\,\varphi(\mathbf{r})$, one has to expand the Kohn-Sham wavefunctions, φ, in some suitable basis set $\{\phi_i\}$ as:

$$\varphi(\mathbf{r}) = \sum_i c_i \phi_i(\mathbf{r}), \tag{2.57}$$

where c_i are the coefficients of the expansion. For an orthonormal basis set, one has to solve a set of equations:

$$\sum_i \left(\langle \phi_j | \hat{H}_{KS} | \phi_i \rangle - \varepsilon \, \delta_{ij} \right) c_i = 0. \tag{2.58}$$

Most popular basis sets are:

(i) *Localized* basis sets:
- Linear Combinations of Atomic Orbitals (LCAO) [69]
- Gaussian-type Orbitals (GTO) [70]
- Linearized Muffin-Tin Orbitals (LMTO) [71]

(ii) *Delocalized* basis sets:
- Plane Waves (PW) [40]

(iii) *Mixed* basis sets:
- Linearized Augmented Plane Waves (LAPW) [72]
- Projector Augmented Plane Waves (PAW) [73]

Spatially localized functions are extremely useful to deal with the quantum chemistry of isolated molecules, because their wavefunctions decay to zero far away from the molecule. Instead, if one is interested in a bulk material, such as atoms in the solid, the spatially localized functions can still be used to describe each atom, and these functions must be added to describe the overall material [25]. But this is certainly not the only possibility. A good alternative is to use periodic functions, *e.g.* plane waves, to describe the wavefunctions which are also spatially periodic.

What are the advantages and disadvantages of localized and delocalized (plane-wave) basis sets? The advantages of localized basis sets are: (i) the convergence with respect to the size of the basis set is fast, just a few functions per atom are needed, and (ii) finite systems, *e.g.* molecules, can be treated easily. However, there are several disadvantages: (i) it is difficult to evaluate the convergence quality, as there is no systematic way to improve the convergence, (ii) localized basis sets are difficult to use, because of the need to compute two- and three-center integrals, and (iii) it is difficult to calculate forces on atoms, as there is a Pulay term.[8] In contrast, PW basis sets have the following advantages: (i) it is easy to evaluate the convergence quality by just increasing the kinetic-energy cutoff, (ii) it is easy to use a Fourier transform, and (iii) it is easy to calculate forces on atoms, as there is no Pulay term. However, PW basis sets have some disadvantages: (i) the convergence with respect to the size of the PW basis set is slow, because many more plane waves are needed than localized functions, and (ii) there is a need to use a supercell for the description of finite systems.

In this thesis I will consider a bulk material bismuth (see Chapter 2), therefore the PW basis set will be used. In the following, I will give a brief description of the problem in the framework of the PW basis set.

[8] *Pulay forces* appear when evaluating derivatives of the localized basis set functions with respect to atomic positions. Pulay forces do not appear when a PW basis set is used.

2.3.1 (b) Plane-wave basis set

According to the Bloch theorem [74], an electron moving in the effective potential $V_{KS}(\mathbf{r})$ [see Eqs. (2.17)], which has the periodicity of the crystal, $V_{KS}(\mathbf{r}+\mathbf{R}) = V_{KS}(\mathbf{r})$, where $\mathbf{R}$ is the radius-vector of the unit cell, can be described by a wavefunction of the form:

$$\varphi_{n,\mathbf{k}}(\mathbf{r}) = e^{i\mathbf{k}\cdot\mathbf{r}}\, u_{n,\mathbf{k}}(\mathbf{r}), \tag{2.59}$$

where n is the energy band index, $\mathbf{k}$ is the point in the Brillouin zone, $e^{i\mathbf{k}\cdot\mathbf{r}}$ is the phase factor, and $u_{n,\mathbf{k}}(\mathbf{r})$ is the function which has the periodicity of the crystal, $u_{n,\mathbf{k}}(\mathbf{r}+\mathbf{R}) = u_{n,\mathbf{k}}(\mathbf{r})$. The periodicity of $u_{n,\mathbf{k}}(\mathbf{r})$ means that it can be expanded in terms of a set of plane waves:

$$u_{n,\mathbf{k}}(\mathbf{r}) = \sum_{\mathbf{G}} c_{n,\mathbf{k}+\mathbf{G}}\, e^{i\mathbf{G}\cdot\mathbf{r}}, \tag{2.60}$$

where the summation is over vectors defined by $\mathbf{G} = m_1\mathbf{b}_1 + m_2\mathbf{b}_2 + m_3\mathbf{b}_3$, where m_1, m_2, m_3 are integer numbers, and $\mathbf{b}_1$, $\mathbf{b}_2$, $\mathbf{b}_3$ are the reciprocal lattice vectors, and $c_{n,\mathbf{k}+\mathbf{G}}$ are the coefficients of the expansion. Combining Eqs. (2.59) and (2.60), gives:

$$\varphi_{n,\mathbf{k}}(\mathbf{r}) = \sum_{\mathbf{G}} c_{n,\mathbf{k}+\mathbf{G}}\, e^{i(\mathbf{k}+\mathbf{G})\cdot\mathbf{r}}. \tag{2.61}$$

According to Eq. (2.61), evaluating the solution at even one single $\mathbf{k}$ point involves a summation over an infinite number of possible values of $\mathbf{G}$. However, the plane waves $e^{i(\mathbf{k}+\mathbf{G})\cdot\mathbf{r}}$ have a simple interpretation as solutions of the Schrödinger equation: they are solutions of the non-interacting problem with the kinetic energy $T = \hbar^2/(2m_0)\times\,|\mathbf{k}+\mathbf{G}|^2$. As a result, the infinite sum over $\mathbf{G}$ in Eq. (2.61) is usually truncated, to include only solutions with kinetic energy values less than some value E_{cut}, the so-called *cutoff energy*:

$$\frac{\hbar^2}{2m_0}|\mathbf{k}+\mathbf{G}|^2 \le E_{cut}, \quad E_{cut} = \frac{\hbar^2}{2m_0}G_{cut}^2. \tag{2.62}$$

Therefore, the infinite sum then reduces to the finite sum:

$$\varphi_{n,\mathbf{k}}(\mathbf{r}) = \sum_{|\mathbf{k}+\mathbf{G}|\le G_{cut}} c_{n,\mathbf{k}+\mathbf{G}}\, e^{i(\mathbf{k}+\mathbf{G})\cdot\mathbf{r}}. \tag{2.63}$$

The above expression includes slightly different number of terms for different values of $\mathbf{k}$. In a PW basis set, the eigenvalue problem of Eq. (2.58) takes the form:

$$\sum_{\mathbf{G}'} \left(\langle \mathbf{k}+\mathbf{G}|\hat{H}_{KS}|\mathbf{k}+\mathbf{G}'\rangle - \varepsilon_{n,\mathbf{k}}\,\delta_{\mathbf{G},\mathbf{G}'} \right) c_{n,\mathbf{k}+\mathbf{G}'} = 0, \tag{2.64}$$

where matrix elements of the Hamiltonian read:

$$\langle \mathbf{k}+\mathbf{G}|\hat{H}_{KS}|\mathbf{k}+\mathbf{G}'\rangle = \frac{\hbar^2}{2m_0}|\mathbf{k}+\mathbf{G}|^2\,\delta_{\mathbf{G},\mathbf{G}'} + V_{KS}(\mathbf{G}-\mathbf{G}'), \tag{2.65}$$

and

$$V_{KS}(\mathbf{G}-\mathbf{G}') = \langle \mathbf{k}+\mathbf{G}|V_{KS}|\mathbf{k}+\mathbf{G}'\rangle. \tag{2.66}$$

In order to obtain the eigenvalues $\varepsilon_{n,\mathbf{k}}$ and the coefficients $c_{n,\mathbf{k}+\mathbf{G}}$ (eigenfunctions) of Eq. (2.64), one has to diagonalize the matrix composed of the elements $\langle \mathbf{k}+\mathbf{G}|\hat{H}_{KS}|\mathbf{k}+\mathbf{G}'\rangle$.

In the PW basis set the Kohn-Sham equations can be solved very efficiently. However, it is worth noting that the electronic wavefunctions become rapidly oscillating functions when approaching the nuclei. Therefore, a very large number of plane waves is required to describe such oscillations. Nevertheless, this problem can be overcome by using the pseudopotential approximation.

2.3.2 Pseudopotential approximation

2.3.2 (a) Division of an atom into core and valence regions

The *pseudopotential* (PP) *approximation* is based on the fact that chemical properties of materials mainly depend on the valence electrons, whereas the tightly bound core electrons are hardly influenced by the environment [24, 75]. Within the *frozen core approximation*, one assumes that the core electrons and the corresponding density are independent of the external perturbation and of the chemical environment of the atom. They can be determined from an all-electron calculation for a single atom. In the DFT calculation, only the valence electrons can be taken into account explicitly, while the core electrons are included in the ionic potential [75].[9]

Any linear functional of the density, *e.g.* the Hartree functional, can be separated into a functional that depends only on the core electron density, and a functional that depends only on the valence electron density. For nonlinear functionals, *e.g.* the exchange-correlation functional, this is only possible when the core and valence densities are spatially separated. This is roughly fulfilled when the core states form a closed shell. Otherwise, one should use a nonlinear core correction, proposed by Louie *et al.* [76].

Although the core electrons screen the nuclear charge, the ionic potential still has a Coulomb singularity at the nucleus (see Fig. 2.1). Hence, due to the steep ionic potential, the valence wavefunctions strongly oscillate in the core region [24]. Consequently, if a plane-wave basis set is used to expand the electronic wavefunctions, a very large number of plane waves would be needed. An extremely large number of plane waves would be required to perform an all-electron calculation - a computationally demanding task. The PP approximation allows the electronic wavefunctions to be expanded using a much smaller number of plane-wave basis states. Moreover, the PP approximation has also other advantages: (*i*) a removal of the core electrons means that fewer electronic wavefunctions have to be calculated, (*ii*) the total energy of the valence electron system is typically one thousand times smaller than the total energy of the all-electron system, and thus the accuracy required to determine energy differences between ionic configurations in a PP calculation is much smaller than the accuracy required in the all-electron calculation [75].

Since the binding properties of materials are independent of the exact form of the wavefunctions close to the nucleus, one can introduce a *pseudo-ion*, which has the same

[9] In the full-potential *all-electron* calculations both valence and core electrons are treated explicitly. The core density is recomputed in the spherical symmetry.

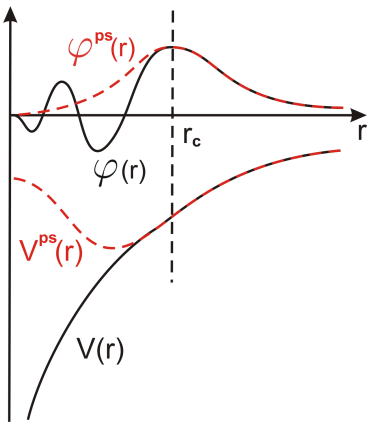

Figure 2.1: Schematic illustration of the replacement of the true potential $V(r)$ and true electronic wavefunction $\varphi(r)$ by a fictitious pseudopotential $V^{\rm ps}(r)$ and pseudo-wavefunction $\varphi^{\rm ps}(r)$, respectively. For $r > r_c$, the PPs and wavefunctions become identical. This is the basic idea of the PP approximation. According to Ref. [75].

chemical properties as the real one, but whose *pseudo-wavefunctions* are smooth inside a small sphere with radius r_c around the ion (see Fig. 2.1). Therefore, one starts from an all-electron calculation of a single atom, and replaces the real ionic potential by a pseudopotential V^{ps}, so that the following quantities remain unchanged [24]: (i) the Kohn-Sham energy values, (ii) the Kohn-Sham wavefunctions outside of the cutoff radius r_c, (iii) the total charge density inside of the sphere (norm conservation), and (iv) the scattering properties (or phase shifts). Such pseudopotentials are called *norm-conserving* (NC) *pseudopotentials*, and they were first proposed by Hamann, Schlüter and Chiang [77]. Thus, when one solves the Kohn-Sham equations (2.16), instead of using the true ionic potential, which was designated as V_{ext} [see Eq. (2.17)], one can use the pseudopotential $V^{\rm ps}$. Norm-conserving PPs are *transferable*, i.e. they reproduce the scattering properties of the true potential in a wide range of energy; and they are relatively *smooth* [24].

The limitation of NC-PPs is that they are still *hard*, i.e. they require large plane-wave basis sets, which results in large requirements of the computational (CPU) time and the memory (RAM). The *ultrasoft* (US) *pseudopotentials* were devised to overcome such a problem [78]. US-PPs require substantially lower energy cutoff than NC-PPs. Moreover, US-PPs are directly produced in the separable form [78]. Another frozen core approach is the *projector augmented-wave* (PAW) *method*, originally introduced by Blöchl [73] and later adapted for plane-wave calculations by Kresse and Joubert [79]. NC and US pseudopotentials are approximations of the PAW method [24]. It has been shown that well-constructed US-PPs and the PAW method give results that are essentially identical in many cases, and which are in good agreement with all-electron calculations [24]. I will not discuss the principles of the US-PPs and PAW method, because in this thesis I will use NC-PPs.

2.3.2 (b) Semilocal and separable forms of PP

Originally, NC-PPs were proposed in the *semilocal* (SL) form, *i.e.* the radial part of the PP is local, and the angular part is non-local, so that there is a different PP for each

atomic angular momentum l [24]:

$$V_{\rm SL}^{\rm ps}(\mathbf{r},\mathbf{r}') = \sum_{l,m} Y_{lm}^*(\theta,\varphi) V_l(r) \delta(r-r') Y_{lm}(\theta',\varphi'), \tag{2.67}$$

where l and m are the angular momentum and its projection, respectively, $\mathbf{r} = (r,\theta,\varphi)$ is the radius-vector in spherical coordinates, $Y_{lm}(\theta,\varphi)$ are the spherical harmonics, and $V_l(r)$ are PPs for each angular momentum l. One can separate the ionic PP into a local l-independent part and l-dependent part as $V_l(r) = V_{\rm loc}(r) + \delta V_l(r)$. Here, $V_{\rm loc}(r) \simeq -Z_{\rm v}e^2/r$ for large r, where $Z_{\rm v}$ is the number of valence electrons, and $\delta V_l(r) = 0$ for $r > r_c$ (see Fig. 2.1). All the long-range effects of the Coulomb potential are included in the local potential $V_{\rm loc}(r)$ [24]. Hence, by using the property of spherical harmonics, $\sum_{l,m} Y_{lm}^*(\theta,\varphi) Y_{lm}(\theta',\varphi') = \delta(\theta-\theta')\delta(\varphi-\varphi')$, one can rewrite Eq. (2.67) as:

$$V_{\rm SL}^{\rm ps}(\mathbf{r},\mathbf{r}') = V_{\rm loc}(r)\delta(\mathbf{r}-\mathbf{r}') + \sum_{l,m} Y_{lm}^*(\theta,\varphi)\delta V_l(r)\delta(r-r')Y_{lm}(\theta',\varphi'). \tag{2.68}$$

Kleinman and Bylander [80] realized that PPs can be recast in a *separable* fully nonlocal (NL) form, which is computationally much more efficient then semilocal form. Each PP is projected onto the atomic reference pseudo-wavefunctions, $\varphi_{lm}^{\rm ps}(\mathbf{r}) = \chi_l^{\rm ps}(r) \times Y_{lm}(\theta,\varphi)$, and thus the PP reads:

$$V_{\rm NL}^{\rm ps} = V_{\rm loc} + \sum_{l,m} \frac{|\varphi_{lm}^{\rm ps}\delta V_l\rangle\langle\delta V_l \varphi_{lm}^{\rm ps}|}{\langle\varphi_{lm}^{\rm ps}|\delta V_l|\varphi_{lm}^{\rm ps}\rangle}. \tag{2.69}$$

By construction, the original PPs and the projected PPs have the same eigenvalues and eigenvectors on the reference states $\varphi_{lm}^{\rm ps}(\mathbf{r})$. However, the separable form may fail in some cases due to the appearance of spurious *ghost states* [81]. Nevertheless, Gonze *et al.* have found how to overcome such a problem [81, 82]. It is worth noting that for semilocal PPs the ghost states do not appear [24].

2.3.2 (c) Scalar-relativistic and fully-relativistic PPs

In the relativistic case, the total ionic pseudopotential reads [60]:

$$\begin{aligned} V^{\rm ps}(\mathbf{r},\mathbf{r}') &= \sum_{j=l-\frac{1}{2}}^{l+\frac{1}{2}} \sum_{l,m} |\phi_{j,l,m}(\theta,\varphi)\rangle V_{l,j}(r,r') \langle\phi_{j,l,m}(\theta,\varphi)| \\ &= \sum_{l,m} |\phi_{j=l-\frac{1}{2},l,m}(\theta,\varphi)\rangle V_{l,j=l-\frac{1}{2}}(r,r') \langle\phi_{j=l-\frac{1}{2},l,m}(\theta,\varphi)| \\ &+ \sum_{l,m} |\phi_{j=l+\frac{1}{2},l,m}(\theta,\varphi)\rangle V_{l,j=l+\frac{1}{2}}(r,r') \langle\phi_{j=l+\frac{1}{2},l,m}(\theta,\varphi)|, \end{aligned} \tag{2.70}$$

where $\phi_{j,l,m}(\theta,\varphi)$ are the two-component angular-spin functions [see Eq. (2.31)], and $V_{l,j=l\pm\frac{1}{2}}$ are the pseudopotentials for each of the valence states $|l, j = l \pm \frac{1}{2}\rangle$ of orbital

angular momentum l and total angular momentum $j = l \pm \frac{1}{2}$ of the atom. The potentials corresponding to states $|l, j = l - \frac{1}{2}\rangle$ and $|l, j = l + \frac{1}{2}\rangle$ are combined to define j-weighted average to obtain the *scalar-relativistic* (SR) nonlocal pseudopotentials $\overline{V}_l(r, r')$ [83]:

$$\overline{V}_l(r, r') = \frac{1}{2l+1}\left[l V_{l,j=l-\frac{1}{2}}(r, r') + (l+1) V_{l,j=l+\frac{1}{2}}(r, r') \right]. \tag{2.71}$$

The weighting accounts for the relative degeneracies of the $|l, j = l - \frac{1}{2}\rangle$ and $|l, j = l + \frac{1}{2}\rangle$ states. The SR-PP contains all scalar parts of the relativistic PP, *i.e.* the mass-velocity and the Darwin contribution (see Sec. 2.2.1), and it does not include the spin-orbit coupling term, which distinguishes different $|l, j = l \pm \frac{1}{2}\rangle$ states. Therefore, in the calculations with SR-PPs, eigenvalues for l are not split. The spin-orbit PP (weighted difference), $\Delta V_l^{so}(r, r')$, is defined as [83]:

$$V_l^{\mathrm{so}}(r, r') = \frac{2}{2l+1}\left[V_{l,j=l+\frac{1}{2}}(r, r') - V_{l,j=l-\frac{1}{2}}(r, r') \right]. \tag{2.72}$$

The total ionic *fully-relativistic* (FR) pseudopotential is then written as:

$$V^{\mathrm{ps}}(\mathbf{r}, \mathbf{r}') = \sum_{j=l-\frac{1}{2}}^{l+\frac{1}{2}} \sum_{l,m} |\phi_{j,l,m}(\theta, \varphi)\rangle \left[\overline{V}_l(r, r') + V_l^{\mathrm{so}}(r, r')\, \mathbf{L} \cdot \mathbf{S} \right] \langle \phi_{j,l,m}(\theta, \varphi)|, \tag{2.73}$$

where $\mathbf{L}$ is the orbital angular momentum, $\mathbf{S}$ is the spin angular momentum [see Eq. (2.29)], and the term $\mathbf{L} \cdot \mathbf{S}$ accounts for different j states. The FR NC-PPs were first introduced by Kleinman [44], and by Bachelet and Schlüter [84]. The disadvantage of the originally proposed FR NC-PPs was that, while SR-PP, Eq. (2.71), can be replaced by a fully separable potential of the Kleinman-Bylander form [80] [see Eq. (2.69)], the spin-orbit PP, Eq. (2.72), cannot. Hence, one must calculate and store a huge number of additional integrals in the process of calculating the matrix elements of the spin-orbit coupling operator. This problem has been solved by Hemstreet, Fong and Nelson [57], who represented both the scalar-relativistic and spin-orbit contributions to the ionic PPs in fully separable form.[10]

The major contribution of the spin-orbit coupling to the energy of valence electrons comes from the core region [24]. The rigid core of the PP approximation is fully relativistic, and thus the Dirac equation must be solved inside the core region. However, the wavefunctions describing the valence electrons outside the core region can be accurately described by retaining only the large component of the Dirac spinor [see Eq. (2.25)] [44]. The radial two-component spinor satisfies the Pauli-like Kohn-Sham equation (2.55) outside the core, which contains all relativistic effects to order α^2, where α is the fine structure constant [44, 54].

In this thesis I will use fully-relativistic norm-conserving pseudopotentials (FR NC-PPs) in fully separable (Kleinman-Bylander) form (see Appendix A.1), with the self-consistent treatment of the spin-orbit coupling.

[10] Very recently, fully-relativistic US-PPs [55] and fully-relativistic PAW method [54] have been introduced by Andrea Dal Corso.

2.4 Summary & Outlook

In this chapter, the calculation of the ground state has been addressed in the framework of non-relativistic and relativistic quantum mechanics. Instead of solving the many-body Schrödinger equation (or Dirac equation in the relativistic case), the ground-state properties can be obtained from a minimization of a density functional for the total energy within the (relativistic) density functional theory. Using the density as a basic variable results in a tremendous computational simplification compared to approaches which deal directly with many-body wavefunctions. The density functional is constructed by mapping the interacting system to a fictitious system of independent electrons. The latter constitutes an effective single-particle problem, which is much easier to solve than the many-body problem of interacting electrons. Such a mapping is exact, and it results in a set of self-consistent (Dirac-type) Kohn-Sham equations, which can be solved numerically by iterations. In practice, when the (relativistic) DFT is used, one has to make an approximation for the exchange-correlation potential, and often pseudopotentials are used to reduce the numerical workload.

A special attention has been paid in this chapter to the description of the relativistic effects, in particular the spin-orbit coupling. In the calculations of solids, relativistic effects can be included indirectly through pseudopotentials, by generating them using relativistic atomic calculations. Afterwards, when solving the Pauli-type Kohn-Sham equations for the valence states, the spin-orbit coupling can be treated either perturbatively or self-consistently.

In this thesis I will consider the semimetal bismuth, in which relativistic effects are very large due to heavy atoms ($Z = 83$). The spin-orbit coupling is huge in this material, and thus it has to be included in calculations for the accurate description of electronic, vibrational and other properties. Due to the spin-orbit coupling, bismuth is a challenging material from the computational point of view. As will be shown in the following, this effect leads to extremely large changes in the bulk and surface electronic states, as well as in the dispersion of phonon modes in this material. In particular, the spin-orbit coupling is of crucial importance for the interpretation of the time-resolved terahertz and photoemission experiments on bismuth, as will be shown in Secs. 6.2 and 5.2. Also, it has a large effect on the electron energy-loss spectra of bismuth, as will be demonstrated in Sec. 7. In this thesis I will present the *ab initio* results on bismuth obtained by including the spin-orbit coupling effect in the calculations in a self-consistent way, by using fully-relativistic norm-conserving pseudopotentials in the fully separable form (see Appendix A.1).

Chapter 3

Time-dependent problem

The description of the many-body problem in the ground state is an important issue, which allows for an understanding of various materials. However, one is often interested in the description of the many-body system in the excited state. There exist many approaches to find an approximate solution for the time-dependent many-body problem. I will mention some of them: (*i*) The *GW* approximation within the many-body perturbation theory, which is based on a set of Green's function equations [85]. It is used to solve the quasiparticle problem, when a charge is added or subtracted from the system. (*ii*) The Bethe-Salpeter approach within the many-body perturbation theory, which is based on the solution of the Bethe-Salpeter screened equation [86]. It is used on top of the *GW* method, and it includes the electron-hole interaction. (*iii*) Time-dependent density functional theory (TDDFT), which is an extension of the ground-state DFT to deal with time-dependent external perturbations in terms of the time-dependent density [3]. TDDFT in principle is able to describe neutral excitations. It is exact, provided the time-dependent exchange-correlation potential is known, which is not the case nowadays, and hence one usually uses approximations, *e.g.* the adiabatic approximation.

In this chapter I will discuss TDDFT within the linear response. DFT is a ground-state theory, thus not, strictly speaking, applicable to the calculation of excitation energies or other excited-state properties - instead, one can use TDDFT. Clearly, the presence of a time-dependent external perturbation drives the system away from its stationary ground-state, and hence one can use TDDFT to calculate the excitation properties of the system.

In Sec. 3.1 I will show how the time-dependent many-body problem can be formulated within the TDDFT instead of dealing with the time-dependent Schrödinger equation. In Sec. 3.2 I will present a linear response formulation of TDDFT, and discuss the explanation of the optical absorption and electron energy-loss spectroscopy with the help of the Dyson-like screening equation. In Sec. 3.4 I will present an alternative efficient Liouville-Lanczos approach to the calculation of optical absorption spectra of finite systems.

3.1 Time-dependent theory

3.1.1 Time-dependent Schrödinger equation

As in the static case, let us consider the Born-Oppenheimer approximation, which assumes that the motion of electrons and nuclei can be separated, because light electrons move much faster than heavy nuclei (see Sec. 2.1.1). The evolution of a non-relativistic interacting many-electron system is governed by the time-dependent Schrödinger equation [27]:

$$i\hbar\frac{\partial}{\partial t}\Psi_{\rm el}(\{\mathbf{r}_i\},t) = \hat{H}(\{\mathbf{r}_i\},t)\,\Psi_{\rm el}(\{\mathbf{r}_i\},t), \tag{3.1}$$

where $i = \overline{1,N}$, N is the number of electrons, $\{\mathbf{r}_i\}$ is the set of electronic coordinates, t is the time, $\Psi_{\rm el}$ is the many-body electronic wavefunction, and $\hat{H}$ is the Hamiltonian operator which reads:

$$\hat{H}(\{\mathbf{r}_i\},t) = -\frac{\hbar^2}{2m_0}\sum_i \boldsymbol{\nabla}_i^2 + \frac{1}{2}\sum_{i\neq j}\frac{e^2}{|\mathbf{r}_i-\mathbf{r}_j|} + \sum_i V_{ext}(\mathbf{r}_i,t), \tag{3.2}$$

where m_0 is the free-electron mass, $-e$ is the electron charge, and $V_{ext}(\mathbf{r}_i,t)$ is the time-dependent external potential. The only difference between the time-dependent Hamiltonian, Eq. (3.2), and the static one, Eq. (2.6), is that the external potential V_{ext} depends on time in the former case.[1]

Before the time-dependent perturbation is "switched on" at $t = t_0$, the electronic system is initially at rest in a static potential $V_{ext}(\mathbf{r}_i,t_0)$. The initial state at time t_0 is described by the stationary ground-state wavefunction $\Psi_{\rm el}(\{\mathbf{r}_i\},t_0) = \Psi_{\rm el}(\{\mathbf{r}_i\})e^{-iE_0t_0/\hbar}$, where E_0 is the ground-state energy [see Eq. (2.5), where $E_{BO} = E_0$].

The solution of the time-dependent Schrödinger equation for the many-electron system, Eq. (3.1), is even more complex than the solution of the static (time-independent) Schrödinger equation, Eq. (2.5). Therefore, by analogy to the static case, instead of considering the electronic wavefunction of $3N+1$ variables, $\Psi_{\rm el}(\mathbf{r}_1,\mathbf{r}_2,...,\mathbf{r}_N,t)$, one can consider the electronic density, $n(\mathbf{r},t)$, which is the function of only 4 variables, and which reads:

$$n(\mathbf{r},t) = N\int |\Psi_{\rm el}(\mathbf{r},\mathbf{r}_2,\ldots,\mathbf{r}_N,t)|^2\,d\mathbf{r}_2\ldots d\mathbf{r}_N. \tag{3.3}$$

After the great success of static density functional theory in the description of the many-body systems, Runge and Gross extended this theory to the time domain. In the next section I will give a brief introduction to such a theory.

3.1.2 Time-dependent density functional theory

As we have seen in Sec. 2.1.2, the density functional theory is based on the existence of an exact mapping between the density and the external potential. This has been proven

[1] In Eq. (3.2) I do not include the term $E_{II} = \frac{1}{2}\sum_{I\neq J}\frac{Z_IZ_Je^2}{|\mathbf{R}_I-\mathbf{R}_J|}$, which describes the classical interaction between the nuclei, which is just a constant energy (parameter) for the electronic system, due to the Born-Oppenheimer approximation.

by relying on the Rayleigh-Ritz minimization principle of the total energy. However, a straightforward extension of this idea to the time-dependent domain is not possible. The minimization principle of the total energy does not hold because the total energy is no longer a conserved quantity. The solution of this problem was found by Erich Runge and Eberhard K. U. Gross in the mid 80s [3], who developed a mathematical formulation of the time-dependent density functional theory (TDDFT). Analogous to the static DFT, the time-dependent density $n(\mathbf{r}, t)$ can be introduced as a basic variable by means of a one-to-one correspondence between the density $n(\mathbf{r}, t)$ and the external potential $V_{ext}(\mathbf{r}, t)$.

3.1.2 (a) Runge-Gross theorems

Theorem I

For any system of interacting particles in an external time-dependent potential $V_{ext}(\mathbf{r}, t)$, which can be expanded in Taylor series with respect to time, and given an initial state $\Psi(\mathbf{r}, t_0) = \Psi_0(\mathbf{r})$, there is a one-to-one correspondence between $V_{ext}(\mathbf{r}, t)$ and the time-dependent density $n(\mathbf{r}, t)$, apart from a trivial function of time.

Similarly to the ground-state DFT, Theorem I states that from the knowledge of the density $n(\mathbf{r}, t)$ alone it is possible to deduce the external potential $V_{ext}(\mathbf{r}, t)$ and hence the many-body wavefunction $\Psi(\mathbf{r}, t)$, which in turn determines every observable of the system. Therefore, all observables can ultimately be regarded as functionals of the density. It is important to notice that, differently from DFT, in this case it is necessary to set an initial condition, since we are following an evolution in time.

As I have pointed out in the beginning of this section, in TDDFT the variational principle cannot be formulated in terms of the energy as in Eq. (2.8). Alternatively, there exists a quantity analogous to the energy, the quantum-mechanical action functional, which is defined in Theorem II.

Theorem II

A quantum-mechanical action functional

$$\mathcal{A}[n] = \int_{t_0}^{t_1} dt \, \langle \Psi(t) | i\hbar \frac{\partial}{\partial t} - \hat{H}(t) | \Psi(t) \rangle, \tag{3.4}$$

becomes stationary at the exact time-dependent density $n_0(\mathbf{r}, t)$ which corresponds to the external potential $V_0(\mathbf{r}, t)$, given the initial state $\Psi_0(\mathbf{r})$ at t_0:

$$\left. \frac{\delta \mathcal{A}[n]}{\delta n(\mathbf{r}, t)} \right|_{n_0} = 0. \tag{3.5}$$

Theorem II means that it is possible to solve the time-dependent problem by searching for the stationary point of the action $\mathcal{A}$. In contrast to the energy in the static case, the stationary point is not necessarily a minimum. Furthermore, the value of the action itself does not provide any relevant additional information, since for the true density $\mathcal{A}[n_0] = 0$.

Actually, the definition of the action functional $\mathcal{A}$, Eq. (3.4), has some problems. Namely, the exchange-correlation potential deduced from the action is not causal, and the endpoints at t_0 and t_1 are not independent. These problems could be solved as proposed by van Leeuwen [87] by using the time-contour formalism of Keldysh.

3.1.2 (b) Time-dependent Kohn-Sham equations

As in the static DFT, the action functional $\mathcal{A}$ can be decomposed on the components, much in the same way as it has been done for the energy functional [see Eq. (2.12)]:

$$\mathcal{A}[n] = \mathcal{T}_0[n] + \mathcal{A}_H[n] + \mathcal{A}_{\rm xc}[n] - \int_{t_0}^{t_1} dt \int d\mathbf{r}\, V_{ext}(\mathbf{r},t) n(\mathbf{r},t), \tag{3.6}$$

where

$$\mathcal{A}_H[n] = -\frac{e^2}{2} \int_{t_0}^{t_1} dt \iint \frac{n(\mathbf{r},t)\, n(\mathbf{r}',t)}{|\mathbf{r}-\mathbf{r}'|}\, d\mathbf{r}\, d\mathbf{r}'. \tag{3.7}$$

In order to approximate the unknown action functional $\mathcal{A}$, Gross and Kohn [88] have introduced an auxiliary fictitious system of non-interacting particles that satisfy the time-dependent Kohn-Sham equations [89]:

$$i\hbar \frac{\partial}{\partial t} \varphi_i(\mathbf{r},t) = \left(-\frac{\hbar^2}{2m_0} \nabla^2 + V_{KS}(\mathbf{r},t) \right) \varphi_i(\mathbf{r},t), \tag{3.8}$$

where $\varphi_i(\mathbf{r},t)$ and $V_{KS}(\mathbf{r},t)$ are the time-dependent Kohn-Sham wavefunction and potential, respectively. The density of the non-interacting system reads:

$$n(\mathbf{r},t) = \sum_i^N |\varphi_i(\mathbf{r},t)|^2, \tag{3.9}$$

where N is the number of occupied states. The effective potential $V_{KS}(\mathbf{r},t)$ has such a form that the density of the non-interacting system is equal to the density of the real system of interacting electrons. The existence of the potential $V_{KS}(\mathbf{r},t)$ for any density $n(\mathbf{r},t)$ can be inferred from the Runge-Gross Theorem I, and has been rigorously proved by van Leeuwen [90]. Thus, by using the decomposition of the action functional Eq. (3.6) and the variational principle stated in Theorem II, we obtain

$$\begin{aligned} V_{KS}(\mathbf{r},t) &= V_H(\mathbf{r},t) + V_{\rm xc}(\mathbf{r},t) + V_{ext}(\mathbf{r},t) \\ &= e^2 \int \frac{n(\mathbf{r}',t)}{|\mathbf{r}-\mathbf{r}'|}\, d\mathbf{r}' + \frac{\delta \mathcal{A}_{\rm xc}[n]}{\delta n(\mathbf{r},t)} + V_{ext}(\mathbf{r},t), \end{aligned} \tag{3.10}$$

where $V_H(\mathbf{r},t)$ is the time-dependent Hartree potential, $V_{ext}(\mathbf{r},t)$ is the time-dependent external potential, and $V_{\rm xc}(\mathbf{r},t)$ is the time-dependent exchange-correlation (XC) potential which is unknown. Equation (3.10) defines the time-dependent XC potential. However, in practice, this quantity has to be approximated.

3.1.2 (c) Adiabatic approximation

As in the ground-state DFT, the time-dependent Kohn-Sham equations (3.8) require a suitable approximation for the XC potential in order to be applied in practice. In the time-dependent case, the XC potential is time-dependent and depends on density $n(\mathbf{r}, t)$ at all past times, and thus it is absolutely nontrivial and even more difficult than in the static case to find an expression for it. Therefore, most calculations simply use one of the established XC functionals of static density functional theory. The most popular choice is the *adiabatic local-density approximation* (ALDA), which is obtained by evaluating the standard LDA potential with the time-dependent density $n(\mathbf{r}, t)$:

$$V_{\mathrm{xc}}^{\mathrm{ALDA}}[n](\mathbf{r}, t) = V_{\mathrm{xc}}^{\mathrm{LDA}}(n(\mathbf{r}, t)). \tag{3.11}$$

The ALDA potential is local both in time and space. In fact, all other ground-state XC functionals like GGA, hybrid or any other can yield a corresponding adiabatic approximation. However, it is worth to note that the adiabatic approach is a drastic simplification, and *a priori* only justified for systems with a weak time-dependence which are always close to the equilibrium. In the limit of an external potential that varies slowly in time, the adiabatic approximation becomes exact if the true XC ground-state functional is known. In practice, the results are also affected by the faults of the ground-state approximations, such as the lack of spatial non-locality of LDA or GGA. Nevertheless, despite the simplicity of the adiabatic approach, it could give accurate results in many systems [17].

There are several known failures of the adiabatic approximation, due to either lack of the memory effects or spatial non-locality. Among them I mention the optical properties of solids and long conjugated molecules, double excitations, and charge-transfer excitations. These drawbacks and the attempts to solve them are reviewed in Ref. [91]. Nowadays, the design of specific approximations for the time-dependent XC potentials in TDDFT is still at an early stage [92].

In this thesis, all my applications of TDDFT will be done with the adiabatic approximation.

3.1.2 (c) Generalization of TDDFT

Before going to the next section, I would like to point out that Runge, Gross and Kohn's formulation of TDDFT was done for *non-relativistic* systems at *zero temperature*. The TDDFT was generalized to relativistic systems and to systems at finite temperature. I will not present here the corresponding theories, but just give an idea and references for further reading.

The TDDFT formalism for systems at finite temperature in thermal equilibrium was developed in Refs. [93, 94]. The theory states the following: *"For a system of fixed number of particles which satisfies the second law of thermodynamics, there is a one-to-one mapping between the time-dependent density $n(\mathbf{r}, t)$ and the time-dependent external potential $V_{ext}(\mathbf{r}, t)$ (i) if the system under consideration is at thermal equilibrium and (ii) if corresponding to this equilibrium state there is a unique minimum in the Helmholtz free energy F"* [93].

The relativistic formulation of TDDFT is given in Ref. [95]. In fact, the theory was developed not by generalizing the TDDFT to the relativistic case, but by generalizing the relativistic static DFT to the time domain (see Sec. 2.2.2). Several recent examples of the applications of the relativistic TDDFT can be found, *e.g.*, in Refs. [96, 97, 98, 99].

3.2 Linear response theory

3.2.1 Dyson-like equation

Let us assume that the time-dependent external potential is weak, and that it can be presented in the form:

$$V_{ext}(\mathbf{r},t) = V^0_{ext}(\mathbf{r}) + V'_{ext}(\mathbf{r},t), \tag{3.12}$$

where $V^0_{ext}(\mathbf{r})$ is the static external potential of the unperturbed system, and $V'_{ext}(\mathbf{r},t)$ is the time-dependent perturbation. Therefore, the density $n(\mathbf{r},t)$ can be expanded in Taylor series with respect to the perturbation $V'_{ext}(\mathbf{r},t)$:

$$n(\mathbf{r},t) = n^0(\mathbf{r}) + n'(\mathbf{r},t) + n''(\mathbf{r},t) + \dots, \tag{3.13}$$

where $n^0(\mathbf{r})$ is the density of the unperturbed system, $n'(\mathbf{r},t)$ is the first order time-dependent density-response, $n''(\mathbf{r},t)$ is the second order time-dependent density-response etc. Let us consider a *linear-response theory*, by taking into account only the first order density-response and by neglecting higher order terms.[2] The first order correction reads [92]:

$$n'(\mathbf{r},t) = \int_{-\infty}^{\infty} dt' \int d\mathbf{r}'\, \chi(\mathbf{r},\mathbf{r}',t-t')V'_{ext}(\mathbf{r}',t'), \tag{3.14}$$

where χ is the linear density-response function,[3] which is defined as:

$$\chi(\mathbf{r},\mathbf{r}',t-t') = \left.\frac{\delta n(\mathbf{r},t)}{\delta V_{ext}(\mathbf{r}',t')}\right|_{V_{ext}(\mathbf{r}',t')=V^0_{ext}(\mathbf{r}')}. \tag{3.15}$$

The causality principle requires that $\chi(\mathbf{r},\mathbf{r}',t-t') = 0$ for $t < t'$, because the density at time t cannot be affected by later variations of the potential [92].

3.2.1 (a) Dyson-like equation in real space

In order to calculate the susceptibility χ in practice, one makes use of the fact that the density of the real system is equal to the density of the non-interacting Kohn-Sham system (see Sec. 3.1.2). Since the latter is described by the effective potential $V_{KS}(\mathbf{r},t)$, one starts by applying the chain rule for functional derivatives:

$$\chi(\mathbf{r},\mathbf{r}',t-t') = \int_{-\infty}^{\infty} dt' \int d\mathbf{r}''\, \frac{\delta n(\mathbf{r},t)}{\delta V_{KS}(\mathbf{r}'',t'')} \frac{\delta V_{KS}(\mathbf{r}'',t'')}{\delta V_{ext}(\mathbf{r}',t')}. \tag{3.16}$$

[2] If one is interested in nonlinear phenomena, then it is necessary to consider a *time-dependent higher-order (nonlinear) response*, by calculating the higher order terms in the Taylor expansion, Eq. (3.13) (see, *e.g.* Ref. [89]).

[3] The linear density-response function χ is also called the *susceptibility* or *reducible polarizability*.

The first term on the right-hand side corresponds to the linear density-response function of the non-interacting Kohn-Sham system, $\delta n/\delta V_{KS} = \chi^0$, since the effective potential, V_{KS}, plays the role of the "external potential" of the Kohn-Sham system [92].[4] It can be calculated explicitly from the time-dependent perturbation theory, and it reads in the frequency representation as [100]:

$$\chi^0(\mathbf{r},\mathbf{r}',\omega) = \sum_{i,j}(f_j - f_i)\frac{\varphi_i^0(\mathbf{r})\varphi_j^{0*}(\mathbf{r})\varphi_j^0(\mathbf{r}')\varphi_i^{0*}(\mathbf{r}')}{\hbar\omega - (\varepsilon_i - \varepsilon_j) + i\eta}, \tag{3.17}$$

where f_i are the occupation numbers, $\varphi_i^0(\mathbf{r})$ are the unperturbed Kohn-Sham states, ε_i are the unperturbed Kohn-Sham energies, and the index i splits in the periodic system into a band index n and a wavevector $\mathbf{k}$, $i = \{n, \mathbf{k}\}$, and $\eta \to +0$ is the positive infinitesimal. In order to evaluate the second term in Eq. (3.16), let us decompose the Kohn-Sham potential given by Eq. (3.10). As a result, one will obtain:

$$\frac{\delta V_{KS}(\mathbf{r},t)}{\delta V_{ext}(\mathbf{r}',t')} = \frac{\delta V_H(\mathbf{r},t)}{\delta V_{ext}(\mathbf{r}',t')} + \frac{\delta V_{\mathrm{xc}}(\mathbf{r},t)}{\delta V_{ext}(\mathbf{r}',t')} + \delta(\mathbf{r}-\mathbf{r}')\delta(t-t'). \tag{3.18}$$

Since both the Hartree and exchange-correlation potentials are functionals of the density, one can apply the chain rule once again and rewrite these two contributions as:

$$\frac{\delta V_H(\mathbf{r},t)}{\delta V_{ext}(\mathbf{r}',t')} = \int_{-\infty}^{\infty} dt'' \int d\mathbf{r}'' \, \frac{\delta V_H(\mathbf{r},t)}{\delta n(\mathbf{r}'',t'')}\frac{\delta n(\mathbf{r}'',t'')}{\delta V_{ext}(\mathbf{r}',t')}, \tag{3.19}$$

and analogously for $\delta V_{\mathrm{xc}}/\delta V_{ext}$. The first term on the right-hand side of Eq. (3.19) can be calculated by using the definition of the Hartree potential [see Eq. (3.10)]:

$$\frac{\delta V_H(\mathbf{r},t)}{\delta n(\mathbf{r}'',t'')} = \frac{e^2}{|\mathbf{r}-\mathbf{r}''|}\,\delta(t-t''), \tag{3.20}$$

and the second term in Eq. (3.19) can be easily recognized as the linear density-response function, $\delta n/\delta V_{ext} = \chi$. The second term in Eq. (3.18) contains the so-called *exchange-correlation kernel*, which reads [92, 100]:

$$f_{\mathrm{xc}}(\mathbf{r},\mathbf{r}',t-t') \equiv \left.\frac{\delta V_{\mathrm{xc}}(\mathbf{r},t)}{\delta n(\mathbf{r}',t')}\right|_{n(\mathbf{r}',t')=n^0(\mathbf{r}')}. \tag{3.21}$$

After gathering all terms together, and performing a Fourier transformation to the frequency domain, one obtains the final integral equation, which is called the *Dyson-like screening equation*, which reads [101]:

$$\chi(\mathbf{r},\mathbf{r}',\omega) = \chi^0(\mathbf{r},\mathbf{r}',\omega) + \int d\mathbf{r}'' \int d\mathbf{r}''' \, \chi^0(\mathbf{r},\mathbf{r}'',\omega)\left(\frac{e^2}{|\mathbf{r}''-\mathbf{r}'''|} + f_{\mathrm{xc}}(\mathbf{r}'',\mathbf{r}''',\omega)\right)\chi(\mathbf{r}''',\mathbf{r}',\omega). \tag{3.22}$$

[4] The linear density-response function χ^0 is also called the *independent-particle polarizability*.

3.2.1 (b) Dyson-like equation in reciprocal space

Let us rewrite the Dyson-like equation (3.22) in the reciprocal space. To this end, let us make use of the Fourier transformation [102]:

$$\chi^0(\mathbf{r},\mathbf{r}',\omega) = \frac{1}{\Omega}\sum_{\mathbf{q}}^{\mathrm{BZ}}\sum_{\mathbf{G},\mathbf{G}'} e^{i(\mathbf{q}+\mathbf{G})\cdot\mathbf{r}}\,\chi^0_{\mathbf{G},\mathbf{G}'}(\mathbf{q},\omega)\,e^{-i(\mathbf{q}+\mathbf{G}')\cdot\mathbf{r}'}, \tag{3.23}$$

where Ω is the crystal volume, $\mathbf{G}$ and $\mathbf{G}'$ are the reciprocal lattice vectors, and $\mathbf{q}$ is the wavevector in the Brillouin zone (BZ). Hence, the Fourier coefficients $\chi^0_{\mathbf{G},\mathbf{G}'}(\mathbf{q},\omega) = \chi^0(\mathbf{q}+\mathbf{G},\mathbf{q}+\mathbf{G}',\omega)$ read [103, 104]:

$$\begin{aligned}\chi^0_{\mathbf{G},\mathbf{G}'}(\mathbf{q},\omega) &= \frac{1}{\Omega}\sum_{\mathbf{k}}^{\mathrm{BZ}}\sum_{n,n'}\frac{f_{n,\mathbf{k}}-f_{n',\mathbf{k}+\mathbf{q}}}{\hbar\omega+\varepsilon_{n,\mathbf{k}}-\varepsilon_{n',\mathbf{k}+\mathbf{q}}+i\eta}\\ &\times \langle\varphi^0_{n,\mathbf{k}}|e^{-i(\mathbf{q}+\mathbf{G})\cdot\mathbf{r}}|\varphi^0_{n',\mathbf{k}+\mathbf{q}}\rangle\,\langle\varphi^0_{n',\mathbf{k}+\mathbf{q}}|e^{i(\mathbf{q}+\mathbf{G}')\cdot\mathbf{r}'}|\varphi^0_{n,\mathbf{k}}\rangle,\end{aligned} \tag{3.24}$$

where

$$\langle\varphi^0_{n,\mathbf{k}}|e^{-i(\mathbf{q}+\mathbf{G})\cdot\mathbf{r}}|\varphi^0_{n',\mathbf{k}+\mathbf{q}}\rangle = \int \varphi^{0\,*}_{n,\mathbf{k}}(\mathbf{r})\,e^{-i(\mathbf{q}+\mathbf{G})\cdot\mathbf{r}}\,\varphi^0_{n',\mathbf{k}+\mathbf{q}}(\mathbf{r})\,d\mathbf{r}. \tag{3.25}$$

Therefore, the Dyson-like equation reads [105, 106]:

$$\chi_{\mathbf{G},\mathbf{G}'}(\mathbf{q},\omega) = \chi^0_{\mathbf{G},\mathbf{G}'}(\mathbf{q},\omega) + \sum_{\mathbf{G}_1,\mathbf{G}_2}\chi^0_{\mathbf{G},\mathbf{G}_1}(\mathbf{q},\omega)\Big[v_{\mathbf{G}_1}(\mathbf{q})\delta_{\mathbf{G}_1,\mathbf{G}_2} + f^{\mathrm{xc}}_{\mathbf{G}_1,\mathbf{G}_2}(\mathbf{q},\omega)\Big]\chi_{\mathbf{G}_2,\mathbf{G}'}(\mathbf{q},\omega), \tag{3.26}$$

where $v_{\mathbf{G}}(\mathbf{q}) = 4\pi e^2/|\mathbf{q}+\mathbf{G}|^2$ is the Fourier transform of the Coulomb potential, and $f^{\mathrm{xc}}_{\mathbf{G},\mathbf{G}'}(\mathbf{q},\omega)$ is the Fourier transform of the exchange-correlation kernel.

3.2.2 Excitation energy

The independent-particle polarizability χ_0 as a function of ω has poles at the Kohn-Sham energy differences, $\varepsilon_i - \varepsilon_j$, as can be seen from the denominator of Eq. (3.17). However, these Kohn-Sham excitation energy differences, $\varepsilon_i - \varepsilon_j$, are not identical to the *true* ones, because the interpretation of the one-particle Kohn-Sham energy ε_i as quasiparticle energy is not formally justified. This leads to the well-known problem of the underestimation of transition energy differences, in particular when one considers the excitations from the valence bands to the conduction bands in semiconductors or insulators. Indeed, the "bandgap problem" in DFT underestimates the gaps between the valence and conduction bands by 30-50 % [24].

In the framework of TDDFT, the relevant information about the excited states is contained in the screened susceptibility $\chi(\mathbf{r},\mathbf{r}',\omega)$: the true excitation energy differences are its poles. The susceptibility χ can be written in the Lehmann representation [107]:

$$\chi(\mathbf{r},\mathbf{r}',\omega) = \sum_{f\neq i}\left(\frac{\langle\Psi_i|\hat{n}(\mathbf{r})|\Psi_f\rangle\langle\Psi_f|\hat{n}(\mathbf{r}')|\Psi_i\rangle}{\hbar\omega-(E_f-E_i)+i\eta} - \frac{\langle\Psi_i|\hat{n}(\mathbf{r}')|\Psi_f\rangle\langle\Psi_f|\hat{n}(\mathbf{r})|\Psi_i\rangle}{\hbar\omega+(E_f-E_i)+i\eta}\right), \tag{3.27}$$

where $\hat{n}(\mathbf{r}) = \sum_l \delta(\mathbf{r} - \mathbf{r}_l)$ is the density operator, l runs over all electrons, $|\Psi_i\rangle$, E_i and $|\Psi_f\rangle$, E_f denote exact initial (ground) state and final (excited) state and corresponding energy values of the many-body electronic system, respectively, and $\eta \to +0$ is the positive infinitesimal. Using the transformation (3.23), one can determine the Fourier coefficients $\chi_{\mathbf{G},\mathbf{G}'}(\mathbf{q},\omega)$ [107]:

$$\chi_{\mathbf{G},\mathbf{G}'}(\mathbf{q},\omega) = \sum_{f\neq i} \left(\frac{\langle\Psi_i|\hat{n}^*_{\mathbf{q}+\mathbf{G}}|\Psi_f\rangle\langle\Psi_f|\hat{n}_{\mathbf{q}+\mathbf{G}'}|\Psi_i\rangle}{\hbar\omega - (E_f - E_i) + i\eta} - \frac{\langle\Psi_i|\hat{n}_{\mathbf{q}+\mathbf{G}'}|\Psi_f\rangle\langle\Psi_f|\hat{n}^*_{\mathbf{q}+\mathbf{G}}|\Psi_i\rangle}{\hbar\omega + (E_f - E_i) + i\eta} \right), \tag{3.28}$$

where $\hat{n}_{\mathbf{q}+\mathbf{G}} = \sum_l e^{i(\mathbf{q}+\mathbf{G})\cdot\mathbf{r}_l}$. From Eq. (3.27) it can be seen that the poles of $\chi(\mathbf{r},\mathbf{r}',\omega)$ correspond to *exact* excitation energy differences, $E_f - E_i$. Moreover, all quantities on the right-hand side of Eq. (3.27) depend only on the Hamiltonian of the unperturbed system. Hence, by virtue of the Hohenberg-Kohn theorem, the susceptibility χ is a functional of the *static* ground-state density [92]. The form of Eq. (3.27) is valid for finite systems with discrete eigenvalues. Since the energy values E_i of the many-body electronic system are real, the poles of $\chi(\mathbf{r},\mathbf{r}',\omega)$ appear at real energy values. However, for extended systems the spectrum is continuous, and thus the sum in Eq. (3.27) turns into an integral that gives rise to a branch cut along the real energy axis. Therefore, the infinitely close-lying resonances merge into broad structures that can be identified with elementary quasiparticles, such as plasmons or excitons [92]. Since these structures have a certain width, they are described by poles in the complex plane with a real part, which corresponds to the energy of the excitation, and an imaginary part, whose inverse is proportional to the excitation lifetime.

From a practical point of view, the Lehmann representation of the susceptibility χ, Eqs. (3.27) and (3.28), is not convenient, because a knowledge of the many-body electronic wavefunctions, Ψ_i and Ψ_f, and energy values, E_i and E_f, is needed. Instead, in practice one usually solves the Dyson-like equation (3.26).

In the second part of this thesis, I will present a new *ab initio* approach, other than the Dyson-like equation (3.26), to obtain the susceptibility, χ, Eq. (3.15).

3.2.3 Dielectric function

3.2.3 (a) Definition

The linear response theory can be applied to study the response of an electronic system to a weak time-dependent perturbation $V_{ext}(\mathbf{r},t)$. Due to the external perturbation, the system is polarized, and the total potential becomes the sum of the external potential and the induced potential: $V_{tot} = V_{ext} + V_{ind}$. The basic quantity that gives information about the screening of the system at the level of the linear response is the *microscopic dielectric function*, ϵ, which relates the total potential V_{tot} to the applied potential V_{ext} [92]:

$$V_{tot}(\mathbf{r},t) = \int_{-\infty}^{\infty} dt' \int d\mathbf{r}'\, \epsilon^{-1}(\mathbf{r},\mathbf{r}',t-t')\, V_{ext}(\mathbf{r}',t'). \tag{3.29}$$

Therefore, the microscopic dielectric function ϵ and the susceptibility χ are related by the relation:

$$\epsilon^{-1}(\mathbf{r},\mathbf{r}',t-t') = \delta(\mathbf{r}-\mathbf{r}')\,\delta(t-t') + \int d\mathbf{r}''\, v(\mathbf{r}-\mathbf{r}'')\,\chi(\mathbf{r}'',\mathbf{r}',t-t'), \tag{3.30}$$

where $v(\mathbf{r}-\mathbf{r}'') = e^2/|\mathbf{r}-\mathbf{r}''|$ is the Coulomb potential. For periodic systems, the most natural way to deal with spatial periodicity is to apply a Fourier transform [108]:

$$\epsilon^{-1}(\mathbf{r},\mathbf{r}',\omega) = \frac{1}{\Omega}\sum_{\mathbf{q}}^{\mathrm{BZ}}\sum_{\mathbf{G},\mathbf{G}'} e^{i(\mathbf{q}+\mathbf{G})\cdot\mathbf{r}}\,\epsilon^{-1}_{\mathbf{G},\mathbf{G}'}(\mathbf{q},\omega)\,e^{-i(\mathbf{q}+\mathbf{G}')\cdot\mathbf{r}'}, \tag{3.31}$$

where Ω is the crystal volume, $\mathbf{G}$ and $\mathbf{G}'$ are the reciprocal lattice vectors, and $\mathbf{q}$ is the wavevector in the Brillouin zone (BZ). Thus, one can rewrite Eq. (3.30) in the reciprocal space as [100]:

$$\epsilon^{-1}_{\mathbf{G},\mathbf{G}'}(\mathbf{q},\omega) = \delta_{\mathbf{G},\mathbf{G}'} + v_{\mathbf{G}}(\mathbf{q})\,\chi_{\mathbf{G},\mathbf{G}'}(\mathbf{q},\omega), \tag{3.32}$$

where $v_{\mathbf{G}}(\mathbf{q}) = 4\pi e^2/|\mathbf{q}+\mathbf{G}|^2$ is the Fourier transform of the Coulomb potential. Note, we have also used a Fourier transform to move from time to frequency domain.

Once the microscopic dielectric function is known, measurable quantities need to be obtained. Let us define the function:

$$\epsilon_{\mathrm{M}}(\mathbf{Q},\omega) = \frac{1}{\epsilon^{-1}_{\mathbf{G},\mathbf{G}}(\mathbf{q},\omega)}, \tag{3.33}$$

where $\mathbf{Q} = \mathbf{q}+\mathbf{G}$. Notice, if the wavevector $\mathbf{Q}$ is in the *first* Brillouin zone, then $\mathbf{G} = 0$, and therefore $\mathbf{Q} = \mathbf{q}$. In the limit when $\mathbf{q} \to 0$, one can define a *macroscopic dielectric function*, which reads:

$$\epsilon_{\mathrm{M}}(\omega) = \lim_{\mathbf{q}\to 0}\epsilon_{\mathrm{M}}(\mathbf{q},\omega) = \lim_{\mathbf{q}\to 0}\frac{1}{\left[\epsilon^{-1}_{\mathbf{G},\mathbf{G}'}(\mathbf{q},\omega)\right]_{\mathbf{G},\mathbf{G}'=0}}. \tag{3.34}$$

In the following I will show how the dielectric function $\epsilon_{\mathrm{M}}(\mathbf{Q},\omega)$ is related to different spectroscopies, namely to the optical absorption spectrum and electron energy-loss spectrum. In general, for anisotropic systems, the microscopic and macroscopic dielectric functions depend on the direction of the wavevector $\mathbf{q}$, *i.e.* on the polarization of the incoming radiation. Therefore, both of them are described by a *dielectric tensor*, instead of simple scalar functions [92].

3.2.3 (b) Random Phase Approximation without Local Field Effects

The *local field effects* (LFE) are related to fluctuations of a polarization of the system on the atomic scale [17]. In the Dyson-like equation (3.26), the LFE arise from the $\mathbf{G} \neq 0$ components of the Coulomb potential $v_{\mathbf{G}}(\mathbf{q}) = 4\pi e^2/|\mathbf{q}+\mathbf{G}|^2$ [109], and from the off-diagonal elements of the independent-particle polarizability $\chi^0_{\mathbf{G},\mathbf{G}'}(\mathbf{q},\omega)$, provided that one uses the *random phase approximation* (RPA), *i.e.* neglecting the exchange-correlation

effects, $f_{\rm xc} = 0$. Therefore, given that $\mathbf{q} \in 1\text{BZ}$, neglecting the LFE implies including only the long-range part of the Coulomb potential, $v_{\mathbf{G}=0}(\mathbf{q})$, and keeping only the head of the independent-particle polarizability, $\chi^0_{\mathbf{G}=0,\mathbf{G}'=0}$. The Dyson equation is then simplified, and one obtains the head of the susceptibility χ:

$$\chi_{\mathbf{G}=0,\mathbf{G}'=0} = \frac{\chi^0_{\mathbf{G}=0,\mathbf{G}'=0}}{1 - v_{\mathbf{G}=0}\chi^0_{\mathbf{G}=0,\mathbf{G}'=0}}. \tag{3.35}$$

This being said, the head of the *inverse* microscopic dielectric tensor reads:

$$\epsilon^{-1}_{\mathbf{G}=0,\mathbf{G}'=0}(\mathbf{q},\omega) = 1 + v_{\mathbf{G}=0}(\mathbf{q})\,\chi_{\mathbf{G}=0,\mathbf{G}'=0}(\mathbf{q},\omega), \tag{3.36}$$

and the head of the *direct* microscopic dielectric tensor reads:

$$\epsilon_{\mathbf{G}=0,\mathbf{G}'=0}(\mathbf{q},\omega) = 1 - v_{\mathbf{G}=0}(\mathbf{q})\,\chi^0_{\mathbf{G}=0,\mathbf{G}'=0}(\mathbf{q},\omega). \tag{3.37}$$

In the past, most calculations had been performed at the level of RPA without LFE [110, 111]. Since then, crystal local-field effects (CLFE) and exchange-correlation (XC) effects have been studied. I will discuss both effects in Secs. 3.2.3(d) and 3.2.3(e).

3.2.3 (c) Intraband and interband contributions

Within the RPA without LFE, from Eqs. (3.37) and (3.24), in the limit when $\mathbf{q} \to 0$, to first order in the perturbation theory, one obtains [112, 113, 114]:

$$\lim_{\mathbf{q}\to 0} \epsilon_{\mathbf{G}=0,\mathbf{G}'=0}(\mathbf{q},\omega) = \epsilon_{intra}(\omega) + \epsilon_{inter}(\omega), \tag{3.38}$$

where the *intraband* contribution reads:

$$\epsilon_{intra}(\omega) = 1 - \frac{\omega_p^2}{\omega(\omega + i\gamma)}, \tag{3.39}$$

and the *interband* contribution reads:

$$\epsilon_{inter}(\omega) = \frac{2e^2\hbar^2}{\pi^2 m_0^2} \int d\mathbf{k} \sum_{n,n'}{}' \frac{f_{n,\mathbf{k}}\ |\langle\varphi_{n',\mathbf{k}}|\mathbf{p}|\varphi_{n,\mathbf{k}}\rangle|^2}{(\varepsilon_{n',\mathbf{k}} - \varepsilon_{n,\mathbf{k}})\left[(\varepsilon_{n',\mathbf{k}} - \varepsilon_{n,\mathbf{k}})^2 - (\hbar\omega + i\hbar\Gamma_{n,n'})^2\right]}. \tag{3.40}$$

where m_0 is the free-electron mass, $-e$ is the electron charge, $\Gamma_{n,n'}$ is the interband scattering rate between bands n and n', $f_{n,\mathbf{k}} \equiv f_{FD}(\varepsilon_{n,\mathbf{k}}) = \{1+\exp[(\varepsilon_{n,\mathbf{k}}-\varepsilon_F)/(k_BT)]\}^{-1}$ is the Fermi-Dirac distribution function, $\mathbf{p} = -i\hbar\nabla$ is the momentum operator, and the prime in the sum of Eq. (3.40) means that the term $n = n'$ is not included. It is not necessary to distinguish explicitly here between the longitudinal and transverse dielectric function since at least within the RPA the two are equal at long wavelengths [103]. In the non-isotropic case, one has to consider a tensor of the dielectric function [115].

Equation (3.39) represents the Drude model [74], where ω_p is the Drude plasma frequency:

$$\omega_p^2 = \frac{4\pi e^2 n}{m_0}, \tag{3.41}$$

where $n = N/V$ is the electron density, $\gamma \equiv 1/\tau$ is the intraband scattering rate, τ is the relaxation time. The Drude model provides accurate results for free-electron-like metals (*e.g.* aluminum), whereas there may be deviations from the Drude behavior in non-free-electron-like materials. Therefore, there exist various generalizations of the Drude model [116, 117, 118, 119, 120]. In this thesis, in Sec. 6.2 I will use the generalization of the Drude model to the system, in which there are two types of carriers (electrons and holes) [118, 120]:

$$\epsilon_{intra}(\omega) = 1 - \frac{\omega_{p,1}^2}{\omega\left(\omega + i/\tau_1\right)} - \frac{\omega_{p,2}^2}{\omega\left(\omega + i/\tau_2\right)}, \tag{3.42}$$

where $\omega_{p,1}$ and τ_1 are the plasma frequency and the relaxation time of the first type of carriers (electrons), and $\omega_{p,2}$ and τ_2 are the plasma frequency and the relaxation time of the second type of carriers (holes). Some two-carrier models presume that $\tau_1 \approx \tau_2$.

If the plasma frequency of Eq. (3.41) is smaller than the interband threshold, $\hbar\omega_p \ll (\varepsilon_{n,\mathbf{k}} - \varepsilon_{n,\mathbf{k}'})$, then the full dielectric function of Eq. (3.38) will read:

$$\epsilon(\omega) = \epsilon_\infty - \frac{\omega_p^2}{\omega\left(\omega + i\gamma\right)}, \tag{3.43}$$

where ϵ_∞ is the contribution to the dielectric function from everything except the Drude term [121]. In metals, the onset of interband absorption is associated with transitions from the Fermi level to the next higher empty band, or with transitions from a lower lying occupied band to the Fermi level [113].

At finite value of $\mathbf{q}$, one can still divide χ^0 [see Eq. (3.37)] into intraband and interband contributions, and obtain the corresponding dielectric function [122].

The description of the interband contribution, ϵ_{inter}, is sufficient for insulators and intrinsic semiconductors at equilibrium (see Fig. 3.1). Metals, semimetals, doped semiconductors or thermally excited semiconductors, and photoexcited materials might have a number of non-vanishing electrons (and holes) at the energy of chemical potential (Fermi surface in the case of metals or semimetals), which present the intraband contribution, ϵ_{intra}, at very small energy values (tens to hundreds of meV), as well as the interband contribution, ϵ_{inter} (see Fig. 3.1).

Let us distinguish between two energy regions, the first one for small energy values (from tens of meV to hundreds of meV), and the second one for large energy values (from several eV to tens of eV). Let us consider the second energy range. As can be seen in Fig. 3.1, there is a peak in ϵ_2 due to the interband transition when ϵ_1 crosses zero with a negative slope, whereas the plasmon peak in the loss function $-\mathrm{Im}(1/\epsilon)$ occurs when ϵ_1 crosses zero with a positive slope, and it corresponds to a collective excitation [110]. If one considers the free-electron-like metal, then the plasmon peak can be accurately described by the Drude model, otherwise one has to use a more accurate description, like TDDFT (see Sec. 3.1.2). In addition, there might be peaks due to interband transitions that appear both in ϵ_2 and $-\mathrm{Im}(1/\epsilon)$ at the same energy (see Fig. 3.1). Such peaks may occur when ϵ_1 has a negative slope but does not cross zero.

At small energy values (tens and hundreds of meV), some materials, *e.g.* semimetal bismuth (see Chapter 4), show free-electron-like behaviour (see Ref. [123] and Chapter 6).

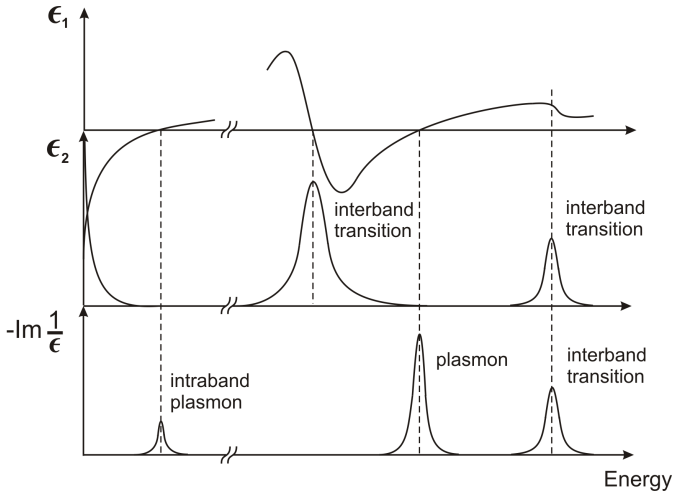

Figure 3.1: Schematic illustration of $\epsilon_1 = \mathrm{Re}\,\epsilon(\omega)$, $\epsilon_2 = \mathrm{Im}\,\epsilon(\omega)$, and $-\mathrm{Im}[1/\epsilon(\omega)]$. For ϵ_2, the low energy part represents the intraband contribution, ϵ_{intra}, described by the Drude model [123, 121], and the higher energy part represents the interband contribution, ϵ_{inter}, [110, 124].

Therefore, the dielectric function in this energy range can be described by the Drude model [see Eq. (3.39)].

3.2.3 (d) Crystal Local Field Effects

The *crystal local field effects* (CLFE) arise whenever the system under consideration is nonhomogeneous on the microscopic scale. In this case, for example, an external spatially constant perturbing field will induce fluctuations on the scale of interatomic distances in the material, giving rise to additional internal microscopic fields [17].

With respect to the previous paragraph, the Dyson-like equation (3.26) is now a matrix equation. The inclusion of the CLFE implies that $\mathbf{G} \neq 0$ components of the Coulomb potential are taken into account, and the full integral $\mathbf{G}\mathbf{G}'$-matrix equation (3.26) is solved (but for the fact that $f_{\mathrm{xc}} = 0$), which implies a matrix inversion. Hence, the inverse microscopic dielectric tensor is given by Eq. (3.32).

Another way to describe the CLFE is to start from the microscopic dielectric tensor and to consider its off-diagonal elements, $\epsilon_{\mathbf{G},\mathbf{G}'}(\mathbf{q},\omega)$. In the inversion, which yields $\epsilon^{-1}_{\mathbf{G},\mathbf{G}'}(\mathbf{q},\omega)$, the CLFE *mix* transitions of different energy. If the inhomogeneity of the system is small, then the off-diagonal elements of the microscopic dielectric tensor $\epsilon_{\mathbf{G},\mathbf{G}'}(\mathbf{q},\omega)$ are also small, and therefore they can be neglected. Only one diagonal matrix element would be considered in this case: the head of the matrix, if $\mathbf{q} \in$ 1BZ. And when one would make the inversion of the tensor $\epsilon_{\mathbf{G},\mathbf{G}'}(\mathbf{q},\omega)$, there would be no mixing. But one may wonder, when the CLFE are more important and when they are less important, and thus can be neglected? It is a general rule that the CLFE become stronger as the wavevector $\mathbf{q}$ increases, since then the wavelength of the excitation becomes smaller, and

thus one samples the local inhomogeneities of the electronic system [17]. The RPA with CLFE yields results of reasonable accuracy for a wide range of systems, and it is still widely employed in actual calculations [17, 100] (but not for optics of extended systems).

3.2.3 (e) The $f_{\rm xc}$ contribution

The exchange-correlation (XC) kernel $f_{\rm xc}$ is a complex quantity that contains all non-trivial many-body effects [17]. Its exact analytical expression is unknown. Most of present approximations of $f_{\rm xc}$ have a vanishing $\mathbf{G} = 0$ component. For this reason, their contribution is also called *exchange-correlation local field effects* (XCLFE) [125]. Similarly to the CLFE, the XCLFE arise from the $\mathbf{G}, \mathbf{G}' \neq 0$ components of the exchange-correlation kernel $f^{\rm xc}_{\mathbf{G},\mathbf{G}'}(\mathbf{q},\omega)$, and from the off-diagonal components of $\chi^0_{\mathbf{G},\mathbf{G}'}(\mathbf{q},\omega)$.

In the adiabatic approximation (ALDA, or TDLDA), the XC kernel is instantaneous, *i.e.* its Fourier transform is frequency independent, but it can be non-local in space:

$$f_{\rm xc}(\mathbf{r},\mathbf{r}',t,t') = f_{\rm xc}(\mathbf{r},\mathbf{r}')\,\delta(t-t'), \tag{3.44}$$

where $f_{\rm xc}(\mathbf{r},\mathbf{r}')$ is the functional derivative of the ground-state XC potential, calculated at the ground-state charge density, $n^0(\mathbf{r})$ [see Eq. (3.21)]:

$$f_{\rm xc}(\mathbf{r},\mathbf{r}') = \left.\frac{\delta V_{\rm xc}(n(\mathbf{r}),\mathbf{r})}{\delta n(\mathbf{r}')}\right|_{n=n^0(\mathbf{r})}. \tag{3.45}$$

In the adiabatic local-density approximation, the XC kernel reads [88]:

$$\begin{aligned} f_{\rm xc}^{\rm TDLDA}(\mathbf{r},\mathbf{r}') &= \delta(\mathbf{r}-\mathbf{r}')\left.\frac{\delta V_{\rm xc}(n(\mathbf{r}),\mathbf{r})}{\delta n(\mathbf{r}')}\right|_{n=n^0(\mathbf{r})} = \\ &= \delta(\mathbf{r}-\mathbf{r}')\,\frac{d^2}{dn^2}\left[n\,\varepsilon_{\rm xc}^{hom}(n)\right]_{n=n^0(\mathbf{r})}, \end{aligned} \tag{3.46}$$

where $\varepsilon_{\rm xc}^{hom}$ is the energy of the homogeneous electron gas per unit volume. By construction, the TDLDA kernel is local both in time and space. Memory effects or the influence of the charge distribution at a distant point are not included, *e.g.* for the Van-der-Waals interaction [88]. In the reciprocal space, the TDLDA kernel reads:

$$f^{\rm xc}_{\mathbf{G},\mathbf{G}'} = \int d\mathbf{r}\, e^{-i(\mathbf{G}-\mathbf{G}')\cdot\mathbf{r}}\ \left.\frac{\delta V_{\rm xc}[n]}{\delta n}\right|_{n=n^0(\mathbf{r})}. \tag{3.47}$$

It is evident that the TDLDA retains all of the problems already present in the LDA. The most important of them for neutral finite systems is the incorrect asymptotic behaviour of the LDA potential (exponential decay instead of $-1/r$), and, for infinite systems, its local dependence on the density [92]. These drawbacks are not corrected by using GGA nor meta-GGA functionals.

The behaviour of different approximations depends strongly on the spectroscopy and on the dimensionality of the physical system. I will discuss this issue in more detail for the optical absorption and electron energy-loss spectra of finite and extended systems.

3.3 Optical absorption and electron energy-loss spectroscopy

3.3.1 TDDFT to explain optical absorption spectroscopy

The *optical absorption spectroscopy* describes an absorption of the electromagnetic radiation, due to its interaction with a sample. The intensity of the absorption varies as a function of the frequency, and this variation is described by the absorption spectrum. The basic quantity for the description of the absorption spectrum is the imaginary part of the macroscopic dielectric function, $\mathrm{Im}\left[\epsilon_{\mathrm{M}}(\omega)\right]$ [112, 103, 104], where $\epsilon_{\mathrm{M}}(\omega)$ is given by Eq. (3.34). From the knowledge of $\epsilon_{\mathrm{M}}(\omega)$, one can determine the *absorption coefficient*, which is essentially $I(\omega) \propto \omega\,\mathrm{Im}\left[\epsilon_{\mathrm{M}}(\omega)\right]$ [126].

3.3.1 (a) Dyson-like equation with modified Coulomb potential

The imaginary part of the macroscopic dielectric function can be written in the form [17, 92]:

$$\mathrm{Im}\left[\epsilon_{\mathrm{M}}(\omega)\right] = -\lim_{\mathbf{q}\to 0} v_{\mathbf{G}}(\mathbf{q})\,\mathrm{Im}\left[\overline{\chi}_{\mathbf{G},\mathbf{G}}(\mathbf{q},\omega)\right], \tag{3.48}$$

where $\overline{\chi}$ is the *modified density-response function*, which satisfies the Dyson-like screening equation:[5]

$$\overline{\chi} = \chi^0 + \chi^0\left(\overline{v} + f_{\mathrm{xc}}\right)\overline{\chi}. \tag{3.49}$$

Here χ^0 is the independent-particle polarizability [see Eq. (3.24)], f_{xc} is the exchange-correlation kernel, and $\overline{v}$ is the *modified Coulomb potential* which reads [17, 92]:

$$\overline{v}_{\mathbf{G}} = \begin{cases} v_{\mathbf{G}}\,, & \text{if } \mathbf{G} \neq 0 \\ 0\,, & \text{if } \mathbf{G} = 0\,. \end{cases} \tag{3.50}$$

From Eq. (3.50) it is seen that $\overline{v}_{\mathbf{G}}$ does not contain the long-range part of the Coulomb potential, *i.e.* when $\mathbf{G} = 0$. This makes a drastic difference with respect to the electron energy-loss spectroscopy, which does contain the long-range part (see Sec. 3.3.3). Within the RPA ($f_{\mathrm{xc}} = 0$), and by neglecting the CLFE ($v_{\mathbf{G}}$, when $\mathbf{G} \neq 0$), one obtains $\overline{\chi} = \chi^0$ - the *independent particle approximation*. The basic ingredients to obtain the absorption spectrum are the Kohn-Sham wavefunctions and energy values, which enter the expression of the independent-particle polarizability χ^0 [see Eq. (3.17)]. They are usually obtained from a ground-state DFT calculation, using some approximation for the exchange-correlation potential.

[5] The Dyson-like equation (3.49) is written in the compact form. Note that all quantities are $\mathbf{G}\mathbf{G}'$-matrices.

3.3.1 (b) Discussion

How good is the TDDFT approach for the calculation of the optical absorption spectra? In order to answer this question, let us distinguish between finite and extended systems. The absorption spectra of finite systems, calculated within the RPA or TDLDA, are, in general, in good agreement with experimental data [17, 92]. However, there are many exceptions, most of which are related to the incorrect tail of the LDA or GGA exchange-correlation potential at large r (exponential decay instead of $-1/r$). For example, the failure in reproducing Rydberg series in the atom within TDDFT [127] is related to this drawback.

In view of the excellent quality of the results obtained within TDDFT for finite systems, one could perhaps expect that the same would occur for extended systems. However, this is not the case [109]. The inability of TDDFT in reproducing the absorption spectra is found in a wide range of semiconductors (Si, Ge, GaAs, etc.) and wide-band gap semiconductors or insulators (diamond, MgO, SiO_2, etc.) [17]. The reasons for the failure of TDDFT are: (1) The poles of $\overline{\chi}$, obtained from Eq. (3.49), are not at correct (true) energy values, and (2) TDDFT does not describe the *excitonic effects*, which are related to the interaction between an excited electron and its associated hole (electron-hole interaction).[6] However, these two problems can be overcome within the many-body perturbation theory [17].

3.3.1 (c) Beyond TDDFT

One may wonder, is there a method beyond TDDFT that can describe optical properties of extended systems? A good level of approximation is the *GW* approximation [85], in the framework of the many-body perturbation theory [85].[7] Using this approach, one can calculate electron addition and removal (quasiparticle) energy values through self-energy corrections to the DFT Kohn-Sham energy values, hence taking properly into account the electron-electron interaction, and thus having poles at proper excitation energy values. This solves the first above mentioned problem of TDDFT. Nevertheless, even when doing so, the excitonic effects are still neglected, while they might be important.

A good agreement of the theoretical absorption spectrum with the experimental one can be obtained by solving the many-body Bethe-Salpeter equation (BSE) on top of the *GW* method [86, 129], though at the price of very large computational effort.[8] In

[6] Recently, there have been proposed a class of exchange-correlation kernels that turned out to reproduce the optical absorption spectra [92, 128].

[7] The *GW* approximation consists of solving an equation similar to the DFT Kohn-Sham system of equations, in which the local exchange-correlation potential $V_{\rm xc}(\mathbf{r})$ is replaced by a non-local and dynamical self-energy operator $\Sigma(\omega, \mathbf{r}, \mathbf{r}')$: $\hat{H}_{KS}\varphi_i(\mathbf{r}) - V_{\rm xc}(\mathbf{r})\varphi_i(\mathbf{r}) + \int d\mathbf{r}'\, \Sigma(\omega, \mathbf{r}, \mathbf{r}')\varphi_i(\mathbf{r}') = \varepsilon_i^{\rm QP}\varphi_i(\mathbf{r})$, where $\Sigma \approx iGW$ is evaluated at quasiparticle energies $\omega = \varepsilon_i^{\rm QP}$.

[8] The BSE is an integral equation that can be written symbolically as: $L = L_0 + L_0 K L$, where L and L_0 are the four-point screened and free-particle correlation functions, respectively, and K is the electron-hole interaction kernel. If K is approximated by the Coulomb potential, the BSE can be rewritten analytically leading to the Dyson-like equation.

this framework, the quasiparticle energy values are computed at the *GW* level, and the electron-hole interaction is explicitly computed within the many-body Green's function theory. Thus, this solves the second aforementioned problem of TDDFT.

3.3.1 (d) f-sum rule

The $\mathrm{Im}\left[\epsilon_{\mathrm{M}}(\omega)\right]$ satisfies the Thomas-Reiche-Kuhn (or f-sum) rule, which reads [130]:

$$\int_0^\infty \mathrm{Im}\left[\epsilon_{\mathrm{M}}(\omega)\right]\omega d\omega = \frac{\pi}{2}\,\omega_p^2, \tag{3.51}$$

where ω_p is the Drude plasma frequency [see Eq. (3.41)].

3.3.2 Connection between scattering cross-section and dielectric function

Electron energy-loss spectroscopy (EELS) is a technique that measures the change in kinetic energy of electrons after they have interacted with the material sample [131]. EELS gives information about the composition, electronic structure and optical properties of materials.

3.3.2 (a) EELS experiment

A typical angular-resolved EELS[9] experiment is illustrated in Fig. 3.2. An electron with a momentum $\mathbf{k}_i$ is incident to the sample, where it is inelastically scattered and where it looses some energy. The electron is scattered into a small solid-angle element $d\Omega$, and it has a momentum $\mathbf{k}_f$, which is smaller than its initial momentum, $|\mathbf{k}_f| < |\mathbf{k}_i|$. Thus, the incident electron transfers some energy and momentum to electrons of the atoms of the sample. As a consequence, there may occur single-electron excitations and collective excitations. In the latter case, the energy of the incident electron is transferred to many electrons of the target simultaneously, which results in their *collective oscillation*. Such a cooperative motion of electrons is due to their mutual interaction. The collective oscillations of the valence electrons closely resemble the electronic plasma oscillations observed in gaseous discharges [111]. Therefore, one can define a *plasmon* as the quantum of elementary excitation associated with a high-frequency collective motion.

Nowadays, EELS experiments can be carried out with a spatial resolution of ~ 0.1 nm, and the energy resolution typically of 1 eV, but it can be reduced down to ~ 0.1 eV if an electron-beam monochromator is used [131].

The main goal of the EELS experiment is to measure a double-differential cross section $d^2\sigma/(d\Omega d\omega)$, which is given by the removal rate of electrons from the incoming beam due to scattering into a solid angle range $[\Omega, \Omega + d\Omega]$ and an energy-transfer range $[\hbar\omega, \hbar\omega + \hbar d\omega]$.

[9] Angular-resolved EELS provides the same information as inelastic X-ray scattering experiments [131].

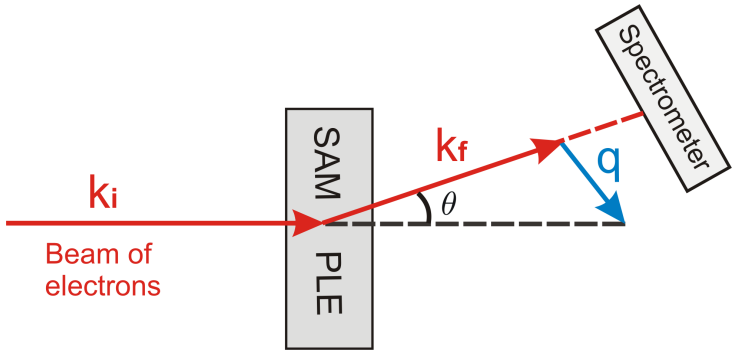

Figure 3.2: Schematic illustration of the angular-resolved EELS experiment. An incident electron with a momentum $\mathbf{k}_i$ inelastically scatters in the sample, and thus looses energy. After the scattering it has a momentum $\mathbf{k}_f = \mathbf{k}_i - \mathbf{q}$, where $\mathbf{q}$ is the momentum transfer. According to Ref. [135].

The EELS technique can be divided into the *valence-loss* and *core-loss* EELS. The former measures single-particle and collective excitations of valence electrons, whereas the latter measures single-particle excitations of core electrons (see also Refs. [132, 133]).[10] The dividing line between the valence-loss and core-loss EELS is somewhat ill-defined, and is in the vicinity of ~ 50 eV [131]. So far, TDDFT calculations (see Sec. 3.3.3) have been applied to study the valence-loss EELS. I will show in Chapter 7 that a new method, developed in this thesis, bridging the gap between the valence-loss and core-loss EELS, in the range 50 - 100 eV.

3.3.2 (b) Theory of EELS

There are three ways to describe the interaction of an incident electron with matter [131]: (*i*) Classical description: collision of a particle with a target (Bohr impact theory), (*ii*) Interaction of an electromagnetic field with a dielectric (Fermi dielectric theory), and (*ii*) Quantum mechanical interaction between the incident electron and the target represented by its potential (Bethe transition-rate theory). In this section I will consider the Bethe theory, which takes into account a quantum mechanical nature of the target in order to describe dynamic effects in the scattering.

Differential cross section

The differential cross section for the scattering of the incident electron from the sample reads:

$$d\sigma = \frac{1}{J_i} \sum_f dw_{fi}, \tag{3.52}$$

[10] Because of the strong binding of core electrons to the nucleus, collective effects are less important than for valence electrons [131].

where the indexes i and j stand for *initial* and *final* states, respectively, $\sum_f$ is the summation over *all* final states, $J_i = \hbar k_i/m_0$ is the current of incoming electrons, m_0 is the free-electron mass, and dw_{fi} is the probability per unit time that the system makes a transition from the initial to any of the final states compatible with the observation conditions of the outcoming electrons, *e.g.* their energy and direction of propagation. Let us assume that the initial and final states can have the form:

$$\Phi_i(\mathbf{r}, \{\mathbf{r}_l\}) = e^{i\mathbf{k}_i\cdot\mathbf{r}}\, \Psi_i(\{\mathbf{r}_l\}), \tag{3.53}$$

$$\Phi_f(\mathbf{r}, \{\mathbf{r}_l\}) = e^{i\mathbf{k}_f\cdot\mathbf{r}}\, \Psi_f(\{\mathbf{r}_l\}), \tag{3.54}$$

where $\mathbf{r}$ is the coordinate of the scattering electron, $\{\mathbf{r}_l\}$ is the set of coordinates of the electrons of the target, and Ψ_i and Ψ_f are the many-body ground- and excited-state electronic wavefunctions of the target, respectively. According to standard quantum mechanics [27], the transition probability dw_{fi} in Eq. (3.52) is given by the Fermi golden rule:

$$dw_{fi} = \frac{2\pi}{\hbar} |\langle \Phi_f | \hat{V} | \Phi_i \rangle|^2\, \delta(E'_f - E'_i)\, d\nu_f, \tag{3.55}$$

where $\hat{V}$ is the Coulomb interaction potential between the incident electron and the target atom, which in coordinate representation reads:

$$V(\mathbf{r}, \{\mathbf{r}_l\}) = \sum_l \frac{e^2}{|\mathbf{r} - \mathbf{r}_l|} - \frac{Ze^2}{|\mathbf{r}|}, \tag{3.56}$$

where the first term describes the electrostatic repulsion between the incident electron and the atomic electrons l, and the second term describes the electrostatic attraction between the incident electron and the nucleus of charge $+Ze$. Furthermore, E'_i and E'_f in Eq. (3.55) are the energy values of the initial and final states, respectively, which read:

$$E'_i = E_i + \frac{\hbar^2 k_i^2}{2m_0}, \qquad E'_f = E_f + \frac{\hbar^2 k_f^2}{2m_0}, \tag{3.57}$$

where E_i and E_f are the energy values of the target before and after the interaction with the incident electron, respectively. Finally, ν_f in Eq. (3.55) are the (continuous) quantum numbers of the final states, such as the energy and propagation direction of the scattering electron, as well as any internal degrees of freedom of the target. The differential $d\nu_f$ reads:

$$d\nu_f = \frac{d\mathbf{k}_f}{(2\pi)^3} = \frac{1}{(2\pi)^3} k_f^2 dk_f d\Omega = \frac{m_0}{(2\pi)^3\hbar^2} k_f d\varepsilon d\Omega, \tag{3.58}$$

where $\varepsilon = \hbar\omega = \hbar^2(k_f^2 - k_i^2)/(2m_0)$ is the amount of energy transferred from the incident electron to the target,[11] and $d\Omega$ is the solid angle in which the electron is scattered. The matrix element in Eq. (3.55) reads:

$$\langle \Phi_f | \hat{V} | \Phi_i \rangle = \int d\{\mathbf{r}_l\}\, \Psi_f^*(\{\mathbf{r}_l\})\, \Psi_i(\{\mathbf{r}_l\}) \int d\mathbf{r}\, e^{i\mathbf{q}\cdot\mathbf{r}} \left[\sum_l \frac{e^2}{|\mathbf{r} - \mathbf{r}_l|} - \frac{Ze^2}{|\mathbf{r}|} \right], \tag{3.59}$$

[11] I have used the differential of the transferred energy $d\varepsilon$, rather than that of the final-state momentum dk_f for later notational convenience.

where $\mathbf{q} = \mathbf{k}_i - \mathbf{k}_f$ is the momentum transfer.[12] The evaluation of integrals gives:

$$\int \frac{e^{i\mathbf{q}\cdot\mathbf{r}}}{|\mathbf{r}-\mathbf{r}_l|}\, d\mathbf{r} = \frac{4\pi}{q^2}\, e^{i\mathbf{q}\cdot\mathbf{r}_l}, \qquad \int \frac{e^{i\mathbf{q}\cdot\mathbf{r}}}{|\mathbf{r}|}\, d\mathbf{r} = 0. \tag{3.60}$$

Therefore, Eq. (3.59) can be rewritten in the form:

$$\langle \Phi_f | \hat{V} | \Phi_i \rangle = \frac{4\pi e^2}{q^2}\, \langle \Psi_f | \hat{n}_{\mathbf{q}} | \Psi_i \rangle, \tag{3.61}$$

where $\hat{n}_{\mathbf{q}} = \sum_l e^{i\mathbf{q}\cdot\mathbf{r}_l}$ is the Fourier transform of the density operator. Finally, the double-differential cross section of Eq. (3.52) reads:

$$\frac{d^2\sigma}{d\Omega d\varepsilon} = A\, S(\mathbf{q},\omega), \tag{3.62}$$

where

$$A = \left(\frac{4\pi e^2}{q^2}\right)^2 \frac{m_0^2}{4\pi^2\hbar^5}\, \frac{k_f}{k_i}, \tag{3.63}$$

and

$$S(\mathbf{q},\omega) = \sum_f |\langle \Psi_f | \hat{n}_{\mathbf{q}} | \Psi_i \rangle|^2\, \delta\left(\frac{E_f - E_i}{\hbar} - \omega\right). \tag{3.64}$$

Such a separation of two factors in the double-differential cross section is quite general [134], and it is a consequence of the use of momentum and energy transfer as independent variables.[13] [14] The first factor, A, is called the *probe factor* which describes the properties of the incident electron, and the second factor, $S(\mathbf{q},\omega)$, is called the *dynamic structure factor* which describes the target. The ratio k_f/k_i in Eq. (3.63) is ensuring that the incoming electron current is the same as the outgoing one. This ratio is close to unity, provided the energy loss is much smaller than the energy of the incident electron.[15]

[12] In general case the momentum transfer can be out of the first Brillouin zone (1BZ), *i.e.* $\mathbf{Q} = \mathbf{q} + \mathbf{G} = \mathbf{k}_i - \mathbf{k}_f$, where $\mathbf{G}$ is the reciprocal lattice vector, and $\mathbf{q} \in$ 1BZ. For the sake of simplicity and without loss of generality, let us assume that the momentum transfer is in the 1BZ, thus $\mathbf{G} = 0$ and $\mathbf{Q} = \mathbf{q} = \mathbf{k}_i - \mathbf{k}_f$.

[13] Equations (3.62)-(3.64) coincide with Eqs. (2)-(4) of Ref. [134] upon a substitution $W(q) = \left(4\pi e^2/q^2\right)^2$, which is the Coulomb interaction between the incident electron and the target, and $p_{n0} = \delta_{n_0,0}$, since the target is initially in its ground state.

[14] In the dipole approximation, $e^{i\mathbf{q}\cdot\mathbf{r}_l} \approx 1 + i\,\mathbf{q}\cdot\mathbf{r}_l$, which assumes that the region of overlap between final and initial states of the electron making the transition is smaller than $1/q$, one has that $d^2\sigma/(d\Omega d\varepsilon) \propto |\langle \Psi_f | \mathbf{r} | \Psi_i \rangle|^2$. The matrix element $|\langle \Psi_f | \mathbf{r} | \Psi_i \rangle|$ is the same as the matrix element for optical dipole transitions.

[15] For small energy losses ≤ 100 eV and an energy value of the incoming electron of 10 keV, the factor k_f/k_i is frequency independent, and $k_f/k_i \approx 1$.

Connection with the dielectric theory

The diagonal matrix element of the susceptibility in the Lehmann representation $\chi(\mathbf{q},\omega) \equiv \chi_{00}(\mathbf{q},\omega)$ reads [see Eq. (3.28)]:[16]

$$\chi(\mathbf{q},\omega) = \sum_f |\langle\Psi_f|\hat{n}_{\mathbf{q}}|\Psi_i\rangle|^2 \left(\frac{1}{\hbar\omega - (E_f - E_i) + i\eta} - \frac{1}{\hbar\omega + (E_f - E_i) + i\eta}\right), \quad (3.65)$$

where $\eta \to +0$ is the positive infinitesimal. Using the relation:

$$\lim_{\eta\to+0} \frac{1}{x + i\eta} = \mathcal{P}\left(\frac{1}{x}\right) - i\pi\delta(x), \quad (3.66)$$

one obtains:

$$\mathrm{Im}[\chi(\mathbf{q},\omega)] = -\pi \sum_f |\langle\Psi_f|\hat{n}_{\mathbf{q}}|\Psi_i\rangle|^2 \Big[\delta(\hbar\omega - (E_f - E_i)) - \delta(\hbar\omega + (E_f - E_i))\Big]. \quad (3.67)$$

For positive frequencies, one has therefore [135]:

$$S(\mathbf{q},\omega) = -\frac{\hbar}{\pi}\,\mathrm{Im}[\chi(\mathbf{q},\omega)]. \quad (3.68)$$

This is the so-called *fluctuation-dissipation theorem* [134, 110, 136]. It relates the density fluctuations due to electronic correlations which is described by $S(\mathbf{q},\omega)$ with the dissipation of energy in the system described by $\mathrm{Im}[\chi(\mathbf{q},\omega)]$ [135]. Finally, by making use of Eqs. (3.32) and (3.33) one can rewrite the double-differential cross section as:

$$\frac{d^2\sigma}{d\Omega d\varepsilon} = -\frac{1}{(\pi e a_0)^2}\,\frac{1}{q^2}\,\mathrm{Im}\left[\frac{1}{\epsilon_{\mathrm{M}}(\mathbf{q},\omega)}\right], \quad (3.69)$$

where $a_0 = \hbar^2/(m_0 e^2)$ is the Bohr radius, $-e$ is the electron charge, m_0 is the free-electron mass, and ϵ_{M} is the dielectric function. This formula is the main conclusion of this section.[17] Therefore, a measurement of the angular distribution of inelastically scattered incident electrons is a direct measurement of the imaginary part of the inverse dielectric function of the solid, at the frequency and momentum of the energy transfer to the electrons of the solid.

[16] For simplicity and without loss of generality I have chosen $\mathbf{G} = \mathbf{G}' = 0$. In the general case, one has to consider $\mathbf{G} = \mathbf{G}'$ which are different from zero.

[17] In Eq. (3.69) I have assumed that the momentum transfer $\mathbf{q}$ is inside the first Brillouin zone (1BZ). In the general case, one has instead $\mathbf{Q} = \mathbf{q} + \mathbf{G}$, where $\mathbf{G}$ is the reciprocal lattice vector, and $\mathbf{q} \in$ 1BZ.

3.3.3 TDDFT to explain EELS

3.3.3 (a) Dyson-like equation for EELS

The basic quantity for the description of EELS is the *loss function*, which reads:

$$-\mathrm{Im}\left[\frac{1}{\epsilon_{\mathrm{M}}(\mathbf{Q},\omega)}\right] = -\mathrm{Im}\left[\epsilon^{-1}_{\mathbf{G},\mathbf{G}}(\mathbf{q},\omega)\right], \tag{3.70}$$

where $\mathbf{Q} = \mathbf{q} + \mathbf{G}$, $\mathbf{q}$ is the momentum transfer, $\mathbf{G}$ is the reciprocal lattice vector, ϵ_{M} is the dielectric tensor defined by Eq. (3.33), and $\epsilon^{-1}_{\mathbf{G},\mathbf{G}'}$ is the microscopic dielectric tensor defined by Eq. (3.32). From Eq. (3.32) it follows that the loss function is related to the susceptibility χ as:

$$-\mathrm{Im}\left[\epsilon^{-1}_{\mathbf{G},\mathbf{G}}(\mathbf{q},\omega)\right] = -v_{\mathbf{G}}(\mathbf{q})\,\mathrm{Im}\left[\chi_{\mathbf{G},\mathbf{G}'}(\mathbf{q},\omega)\right], \tag{3.71}$$

where the susceptibility χ can be obtained by solving the Dyson-like screening equation (3.26):[18]

$$\chi = \chi^0 + \chi^0\,(v + f_{\mathrm{xc}})\,\chi. \tag{3.72}$$

Here χ^0 is the independent-particle polarizability [see Eq. (3.24)], f_{xc} is the exchange-correlation kernel, and v is the *full* Coulomb potential. The Coulomb potential v in Eq. (3.72) contains the long-range part, *i.e.* $\mathbf{G} = 0$ term, at variance with the optical absorption case, which does not contain this term (see Sec. 3.3.1). This makes the difference between EELS and absorption spectroscopy [109]. Whenever this contribution is negligible, both spectra should be equivalent, *e.g.* for finite systems [92].[19] In the case of EELS, the electron-hole interaction (which is long-range) has a weak influence on the plasmon resonance (because there is already a strong Coulomb long-range term $v_{\mathbf{G}=0}$ in Eq. (3.72)), whereas it is crucial in optical spectra.

As in the case of absorption spectroscopy, the basic ingredients to calculate EELS are the Kohn-Sham wavefunctions and energy values that enter the expression of the independent-particle polarizability χ^0 [see Eq. (3.17)], and which are usually obtained from a ground-state DFT calculation.

3.3.3 (b) Discussion

How good is TDDFT for the calculation of EELS? In the case of absorption spectroscopy, we have seen that TDDFT works well for finite systems and it fails for extended systems within RPA and TDLDA. What about EELS?

The TDDFT works well for the calculation of EELS in *finite* systems, as in the case of absorption spectroscopy [109]. In fact, EELS at vanishing momentum transfer $\mathbf{q} \to 0$ and

[18] The Dyson-like equation (3.26) is written in the compact form. Note that all quantities are $\mathbf{G}\mathbf{G}'$-matrices.

[19] Sottile *et al.* [109] have demonstrated on the example of bulk silicon, that one can go smoothly from EELS at $\mathbf{q} \to 0$ to the absorption spectrum by "switching off" the long-range component of the Coulomb potential v_0 (see also Fig. 5 in Ref. [92]).

absorption spectra are equivalent for finite systems [109]. This is because the long-range part of the Coulomb potential is not significant for finite systems. Since this term is not present in the absorption spectrum and it has a small effect in the case of EELS for finite systems, the two spectroscopies give the same result.

The TDDFT works also well for the calculation of EELS in *extended* systems, in contrast to the absorption spectrum [17]. In the case of EELS, it is a common finding that the inclusion of exchange-correlation corrections in the scheme of TDLDA beyond the RPA has a small effect at small values of transferred momenta $\mathbf{q}$, as was demonstrated, *e.g.*, for graphite and TiO_2 [109, 137]. However, at large $\mathbf{q}$, TDLDA can give sizable improvement with respect to RPA [138].

3.3.3 (c) Beyond TDDFT

One may wonder, is there a method that can give the electron energy-loss spectrum of extended systems even better than TDDFT? Olevano and Reining [139] (see also Ref. [17]) have shown on the example of silicon, that the Bethe-Salpeter approach on top of the *GW* method give slightly better agreement with the experimental data than TDLDA, for vanishing momentum transfer. However, since the full BSE calculation is still very expensive from the computational point of view, the use of TDLDA (or even RPA) is ofter well justified. It is worth noting that the *GW* + Bethe-Salpeter results are superior to TDLDA results in those parts of the electron energy-loss spectra that are dominated by interband transitions, *i.e.* by the structures in the imaginary part of the dielectric function which might be not well reproduced in TDLDA [17].

3.3.3 (d) Comparison between $-\mathbf{Im}\,[1/\boldsymbol{\epsilon}_{\mathbf{M}}(\mathbf{Q},\boldsymbol{\omega})]$ & $\mathbf{Im}\,[\boldsymbol{\epsilon}_{\mathbf{M}}(\mathbf{Q},\boldsymbol{\omega})]$

Let us make a point about the comparison of two functions, namely, $-\mathrm{Im}\,[1/\epsilon_{\mathrm{M}}(\mathbf{Q},\omega)]$ and $\mathrm{Im}\,[\epsilon_{\mathrm{M}}(\mathbf{Q},\omega)]$. Recently, Weissker *et al.* [140] have shown on the example of silicon, that these functions are different for small momentum transfer $\mathbf{Q}$, whereas they become equivalent when $\mathbf{Q}$ increases. This is due to the fact that for small $\mathbf{Q}$ the long-range component of the kernel $(v + f_{\mathrm{xc}})$ is important [see Eq. (3.72)], and thus the two functions are different [140]. Instead, for large $\mathbf{Q}$ the short-range effects dominate and the screening that causes the difference between $-\mathrm{Im}\,[1/\epsilon_{\mathrm{M}}(\mathbf{Q},\omega)]$ and $\mathrm{Im}\,[\epsilon_{\mathrm{M}}(\mathbf{Q},\omega)]$ becomes less relevant, until finally the two functions become identical [140].

3.3.3 (e) *f*-sum rule

The $-\mathrm{Im}\,[1/\epsilon_{\mathrm{M}}(\mathbf{Q},\omega)]$, satisfies the Thomas-Reiche-Kuhn (or f-sum) rule, which reads [130]:

$$-\int_0^\infty \mathrm{Im}\left[\frac{1}{\epsilon_{\mathrm{M}}(\mathbf{Q},\omega)}\right]\omega d\omega = \frac{\pi}{2}\,\omega_p^2, \tag{3.73}$$

where ω_p is the Drude plasma frequency [see Eq. (3.41)]. Equation (3.73) holds for $\mathbf{Q} \neq 0$,

and $\mathbf{Q} \to 0$. Interestingly, the f-sum rule for both $-\mathrm{Im}\,[1/\epsilon_{\mathrm{M}}(\mathbf{Q},\omega)]$ and $\mathrm{Im}\,[\epsilon_{\mathrm{M}}(\mathbf{Q},\omega)]$ (see Sec. 3.3.1 for $\mathbf{Q} \to 0$) yield the same result, $\pi\omega_p^2/2$, and this result is independent of $\mathbf{Q}$. It should not be concluded that the functions $-\mathrm{Im}\,[1/\epsilon_{\mathrm{M}}(\mathbf{Q},\omega)]$ and $\mathrm{Im}\,[\epsilon_{\mathrm{M}}(\mathbf{Q},\omega)]$ are identical (but for large $\mathbf{Q}$).

3.4 Liouville-Lanczos approach to optical absorption spectroscopy

In this section I will discuss the calculation of the optical absorption spectra of *finite* systems (molecules, clusters) within the linear-response time-dependent density functional *perturbation* theory (TDDFPT).

The TDDFT equations in the linear-response regime can be cast in numerous different forms. In most current implementations, the Dyson-like integral equation (3.26) is solved (see Sec. 3.2). This is an expensive operation both from a computational and memory-requirement point of view. The first expensive task, is the calculation of the empty states of the ground-state Kohn-Sham (KS) Hamiltonian in order to determine the independent-particle polarizability χ^0 [see Eq. (3.17)]. In practice, one truncates the sum over empty states, and thus limits the applicability of this approach to a lower energy range.[20] [21] The second expensive task, is the solution of the Dyson-like equation (3.26), which requires multiplications and inversions of large matrices. Moreover, this procedure must be repeated for each value of frequency. In practice, because of its unfavourable scaling, such an approach is applicable only for systems containing relatively small number of atoms.

Alternatively, optical absorption spectra can be calculated by propagating the full time-dependent KS equations in real time [143, 144]. This description decreases storage requirements; it allows the entire frequency-dependent dielectric function to be calculated at once, and the scaling with the number of atoms is quite favourable [145]. This approach scales numerically as ground-state DFT calculations, and it also allows the calculation of nonlinear optical properties. Due to this, the real-time propagation approach has recently gained popularity in conjunction with the use of real-space grids [146]. The main limitation of such an approach is that a stable integration of the time-dependent KS equations requires a time step as small as $\approx 10^{-3}$ fs in typical pseudopotential applications, and the typical number of time-steps can be as large as $\approx 10^4$ [145].

Another alternative approach is based on Ghosh and Dhara's linear-response time-dependent density functional formalism [147, 148]. This approach uses an iterative scheme in real space, in which the density and potential are updated in each cycle, thus avoiding

[20] Very recently, Berger *et al.* [141, 142] have proposed a method for the calculation of electronic excitations by reformulating spectral sum-over-states expressions so that only occupied states appear, and all empty states are replaced by one effective energy. Such a method speeds up the calculations by more than one order of magnitude. Though, such a method cannot be applied for calculation of spectra.

[21] One can also raise a question about the validity of the description of empty states at high energy, in particular when pseudopotentials are used, and also with linear methods involving the choice of energy values to build the basis wavefunctions, like (FP)LMTO and (FP)LAPW [45].

the explicit calculation of the Kohn-Sham response kernels [148].

Finally, recently there has been proposed a new efficient approach, the so-called *Liouville-Lanczos approach*, to calculate optical absorption spectra of finite systems in the frequency domain, thus avoiding the explicit integration of the time-dependent Kohn-Sham equations [149, 18].[22] This method does not require the calculation of empty states, nor time-consuming matrix operations, in contrast to the conventional TDDFT approach described in Sec. 3.2 [145, 153, 154]. In the Liouville-Lanczos approach, the susceptibility χ is expressed as an off-diagonal matrix element of the resolvent of the Liouvillian superoperator, which is evaluated using a Lanczos recursion method [149], as will be discussed in Secs. 3.4.1 and 3.4.2. The distinctive feature of the new approach is that it allows the calculation of the full spectrum of a system over a broad frequency range; most importantly, the full spectrum is obtained *at once* without repeating time-consuming operations for different frequencies [18]. The computational effort of such an approach is of the same order as that of time-independent density functional perturbation theory [40], or of the iterative diagonalization of a ground-state KS Hamiltonian, or of a Car-Parrinello molecular dynamics [155]. The Liouville-Lanczos approach can be readily applied to systems with a large number (hundreds) of atoms (see, *e.g.*, Refs. [156, 157, 158]).[23] Note, such large systems can also be treated by conventional TDDFT approach, though with considerably higher computational cost.

In the following, I will describe in detail the Liouville-Lanczos formalism. In Chapter 7 I will extend this approach to the electron energy-loss spectroscopy for extended systems.

3.4.1 Formalism

The formalism starts from Casida's linear-response formulation of TDDFT [159, 160]. Before this thesis, the formalism has been published by Rocca *et al.* [18] for optical absorption spectra of molecules, *i.e.* for zero momentum transfer, $\mathbf{q} = 0$, using supercells and Γ point sampling of the Brillouin zone. In the following, I will closely follow Refs. [145, 18, 154] for the explanation of the Liouville-Lanczos approach.

3.4.1 (a) Linearized time-dependent Kohn-Sham equations

The time-dependent Kohn-Sham (KS) equations of TDDFT read [see Eq. (3.8)]:

$$i\hbar \frac{\partial \varphi_v(\mathbf{r},t)}{\partial t} = \hat{H}_{KS}(\mathbf{r},t)\,\varphi_v(\mathbf{r},t), \tag{3.74}$$

where v is the dummy index, $\varphi_v(\mathbf{r},t)$ are the KS eigenstates, and $\hat{H}_{KS}(\mathbf{r},t)$ is the KS

[22] Very recently, the Liouville-Lanczos approach has been applied within the many-body perturbation theory to the calculation of optical absorption spectra of finite and extended systems by solving the Bethe-Salpeter equation [150, 151, 152].

[23] For example, Malcioglu *et al.* Ref. [158] have successfully applied the Liouville-Lanczos approach to calculate the absorption spectrum of the solvated Cya molecule: $C_{21}H_{21}O_{11}Cl$ surrounded by 95 water molecules H_2O. Thus, in total there were 339 atoms (938 electrons).

Hamiltonian which reads:

$$\hat{H}_{KS}(\mathbf{r},t) = -\frac{\hbar^2}{2m_0}\nabla^2 + V_{ext}(\mathbf{r},t) + V_{H\mathrm{xc}}(\mathbf{r},t), \tag{3.75}$$

where $V_{ext}(\mathbf{r},t)$ is the time-dependent external potential, and $V_{H\mathrm{xc}}(\mathbf{r},t)$ is the time-dependent Hartree plus exchange-correlation (XC) potential [see Eq. (3.10)]. If the external perturbation is weak, it can be linearized [see Eq. (3.12)]:

$$V_{ext}(\mathbf{r},t) = V^0_{ext}(\mathbf{r}) + V'_{ext}(\mathbf{r},t), \tag{3.76}$$

where $V^0_{ext}(\mathbf{r})$ is the static external potential of the unperturbed system, and $V'_{ext}(\mathbf{r},t)$ is the time-dependent perturbation. Thus, the Hartree-plus-XC potential can also be linearized:

$$V_{H\mathrm{xc}}(\mathbf{r},t) = V^0_{H\mathrm{xc}}(\mathbf{r}) + V'_{H\mathrm{xc}}(\mathbf{r},t), \tag{3.77}$$

where $V^0_{H\mathrm{xc}}(\mathbf{r})$ is the static Hartree-plus-XC potential of the unperturbed system, and $V'_{H\mathrm{xc}}(\mathbf{r},t)$ is the time-dependent Hartree-plus-XC potential induced due to the external perturbing potential $V'_{ext}(\mathbf{r},t)$ (through the density response). Therefore, the KS Hamiltonian, Eq. (3.75), reads:

$$\hat{H}_{KS}(\mathbf{r},t) = \hat{H}^0(\mathbf{r}) + V'(\mathbf{r},t), \tag{3.78}$$

where

$$\hat{H}^0(\mathbf{r}) = -\frac{\hbar^2}{2m_0}\nabla^2 + V^0_{ext}(\mathbf{r}) + V^0_{H\mathrm{xc}}(\mathbf{r}), \tag{3.79}$$

and

$$V'(\mathbf{r},t) = V'_{ext}(\mathbf{r},t) + V'_{H\mathrm{xc}}(\mathbf{r},t), \tag{3.80}$$

where $\hat{H}^0$ is the Hamiltonian of the unperturbed system, whose solution is given by the static KS equation [see Eq. (2.16)]:

$$\hat{H}^0(\mathbf{r})\,\varphi^0_v(\mathbf{r}) = \varepsilon_v\,\varphi^0_v(\mathbf{r}), \tag{3.81}$$

where $\varphi^0_v(\mathbf{r})$ and ε_v are the KS wavefunctions and energy values of the unperturbed system, respectively.

The KS wavefunctions $\varphi_v(\mathbf{r},t)$ of Eq. (3.74), can be presented in the form:

$$\varphi_v(\mathbf{r},t) = e^{-i\varepsilon_v t/\hbar}\left[\varphi^0_v(\mathbf{r}) + \varphi'_v(\mathbf{r},t)\right], \tag{3.82}$$

where $\varphi'_v(\mathbf{r},t)$ are the *orbital response functions*, which can be chosen to be orthogonal to all of the unperturbed occupied orbitals $\{\varphi^0_v\}$, *i.e.* $\langle\varphi'_{v'}|\varphi^0_v\rangle = 0$, $\forall\,(v,v')$ [18]. Let us also assume that the KS states $\varphi_v(\mathbf{r},t)$ satisfy the initial conditions: $\varphi_v(\mathbf{r},0) = \varphi^0_v(\mathbf{r})$, therefore $\varphi'_v(\mathbf{r},0) = 0$.

Thereby, to first order in the perturbation, the time-dependent KS equations (3.74) can be cast into the form [18]:

$$i\hbar\frac{\partial\varphi'_v(\mathbf{r},t)}{\partial t} = (\hat{H}^0 - \varepsilon_v)\varphi'_v(\mathbf{r},t) + \left[V'_{ext}(\mathbf{r},t) + V'_{H\mathrm{xc}}(\mathbf{r},t)\right]\varphi^0_v(\mathbf{r}). \tag{3.83}$$

A similar expression can also be written for the complex-conjugate problem:

$$-i\hbar\frac{\partial\varphi_v'^*(\mathbf{r},t)}{\partial t} = (\hat{H}^0 - \varepsilon_v)\varphi_v'^*(\mathbf{r},t) + \left[V'_{ext}(\mathbf{r},t) + V'_{H\mathrm{xc}}(\mathbf{r},t)\right]\varphi_v^{0*}(\mathbf{r}). \tag{3.84}$$

Here I have used the fact that some operators and functions are real, due to time-reversal symmetry, namely $\hat{H}^{0*} = \hat{H}^0$, $V'^*_{ext}(\mathbf{r},t) = V'_{ext}(\mathbf{r},t)$, $V'^*_{H\mathrm{xc}}(\mathbf{r},t) = V'_{H\mathrm{xc}}(\mathbf{r},t)$, and $\varepsilon_v^* = \varepsilon_v$.

Let us Fourier analyze Eqs. (3.83) and (3.84). By definition, the Fourier transformation reads:

$$\varphi'_v(\mathbf{r},t) = \int_{-\infty}^{\infty}\tilde{\varphi}'_v(\mathbf{r},\omega)e^{-i\omega t}d\omega, \tag{3.85}$$

$$\varphi_v'^*(\mathbf{r},t) = \int_{-\infty}^{\infty}\tilde{\varphi}_v'^*(\mathbf{r},-\omega)e^{-i\omega t}d\omega. \tag{3.86}$$

Hence, in the frequency domain, Eqs. (3.83) and (3.84) read [145]:

$$(\hat{H}^0 - \varepsilon_v - \hbar\omega)\tilde{\varphi}'_v(\mathbf{r},\omega) + \hat{P}_c\tilde{V}'_{H\mathrm{xc}}(\mathbf{r},\omega)\varphi_v^0(\mathbf{r}) = -\hat{P}_c\tilde{V}'_{ext}(\mathbf{r},\omega)\varphi_v^0(\mathbf{r}), \tag{3.87}$$

$$(\hat{H}^0 - \varepsilon_v + \hbar\omega)\tilde{\varphi}_v'^*(\mathbf{r},-\omega) + \hat{P}_c\tilde{V}'_{H\mathrm{xc}}(\mathbf{r},\omega)\varphi_v^0(\mathbf{r}) = -\hat{P}_c\tilde{V}'_{ext}(\mathbf{r},\omega)\varphi_v^0(\mathbf{r}). \tag{3.88}$$

Equations (3.87) and (3.88) have the same form but for the sign of the frequency, $\pm\hbar\omega$, which is the only difference. A projector on empty states, $\hat{P}_c = \sum_c |\varphi_c^0\rangle\langle\varphi_c^0|$, where the summation runs only over empty states, has been applied in Eqs. (3.87) and (3.88).[24] In order to avoid the summation over empty states, one can present the projector on empty states as $\hat{P}_c = 1 - \hat{P}_v$, where $\hat{P}_v = \sum_v |\varphi_v^0\rangle\langle\varphi_v^0|$ is the projector on occupied states, and the summation runs only over occupied states v. [25] One can do so, because the following relation holds: $\hat{P}_v + \hat{P}_c = \sum_i |\varphi_i^0\rangle\langle\varphi_i^0| = 1$, where i runs over *all* states. The use of the projector on empty states $\hat{P}_c$ is a common practise of the static density functional perturbation theory (DFPT) [40]. Since the orbital response functions $\{\varphi'_v\}$ have been chosen to be orthogonal to the unperturbed occupied orbitals $\{\varphi_v^0\}$, the action of the projector operator $\hat{P}_c$ on the first term on the left-hand side of Eqs. (3.87) and (3.88) will give zero.

3.4.1 (b) Quantum Liouville equation

In classical mechanics, the Liouville equation describes an evolution in time of the probability density in phase space [27]. In quantum mechanics, the *quantum* Liouville equation dictates that:

$$i\hbar\,\frac{d\hat{\rho}(\mathbf{r},t)}{dt} = \left[\hat{H}_{KS}(\mathbf{r},t), \hat{\rho}(\mathbf{r},t)\right], \tag{3.89}$$

where $\hat{\rho}(\mathbf{r},t)$ is the reduced one-electron KS *density-matrix*, whose kernel reads:

$$\rho(\mathbf{r},\mathbf{r}';t) = 2\sum_v \varphi_v(\mathbf{r},t)\,\varphi_v^*(\mathbf{r}',t), \tag{3.90}$$

[24] The dummy index c stands for "conduction" bands, *i.e.* empty states.
[25] The dummy index v stands for "valence" bands, *i.e.* occupied states.

and the square brackets indicate a commutator. Note, we consider a non-spin-polarized case, therefore the definition (3.90) contains a factor of 2 due to spin degeneracy. Equation (3.89) is the equivalent of the time-dependent KS equation (3.74) [18]. Linearization of Eq. (3.89) with respect to the external perturbation leads to:

$$i\hbar \frac{d\hat{\rho}'(\mathbf{r},t)}{dt} = [\hat{H}^0, \hat{\rho}'(\mathbf{r},t)] + \left[V'_{H\mathrm{xc}}(\mathbf{r},t), \hat{\rho}^0(\mathbf{r})\right] + \left[V'_{ext}(\mathbf{r},t), \hat{\rho}^0(\mathbf{r})\right], \tag{3.91}$$

where $\hat{\rho}^0(\mathbf{r})$ is the unperturbed density-matrix, and $\hat{\rho}'(\mathbf{r},t) = \hat{\rho}(\mathbf{r},t) - \hat{\rho}^0(\mathbf{r})$ is the response density-matrix. Let us linearize also the density-matrix kernel Eq. (3.90), by using Eq. (3.82). One will obtain:

$$\rho'(\mathbf{r},\mathbf{r}';t) = 2\sum_v \left[\varphi'_v(\mathbf{r},t)\varphi_v^{0\,*}(\mathbf{r}') + \varphi_v'^{\,*}(\mathbf{r}',t)\varphi_v^0(\mathbf{r})\right], \tag{3.92}$$

whose Fourier transform reads:

$$\tilde{\rho}'(\mathbf{r},\mathbf{r}';\omega) = 2\sum_v \left[\varphi'_v(\mathbf{r},\omega)\varphi_v^{0\,*}(\mathbf{r}') + \varphi_v'^{\,*}(\mathbf{r}',-\omega)\varphi_v^0(\mathbf{r})\right]. \tag{3.93}$$

Therefore, the Fourier transform of the linearized response charge-density, $\tilde{n}'(\mathbf{r},\omega) = \tilde{\rho}'(\mathbf{r},\mathbf{r};\omega)$, reads:

$$\tilde{n}'(\mathbf{r},\omega) = 2\sum_v \left[\tilde{\varphi}'_v(\mathbf{r},\omega)\varphi_v^{0\,*}(\mathbf{r}) + \tilde{\varphi}_v'^{\,*}(\mathbf{r},-\omega)\varphi_v^0(\mathbf{r})\right], \tag{3.94}$$

and the following relation holds: $\tilde{n}'^{\,*}(\mathbf{r},\omega) = \tilde{n}'(\mathbf{r},-\omega)$.

The Hartree-plus-XC potential $V'_{H\mathrm{xc}}(\mathbf{r},t)$ is linearly induced by the response charge-density $n'(\mathbf{r},t)$, and it reads:

$$V'_{H\mathrm{xc}}(\mathbf{r},t) = \iint \left[\frac{e^2}{|\mathbf{r}-\mathbf{r}'|}\delta(t-t') + f_{\mathrm{xc}}(\mathbf{r},\mathbf{r}',t,t')\right] n'(\mathbf{r}',t')\, d\mathbf{r}'\, dt', \tag{3.95}$$

where f_{xc} is the exchange-correlation kernel defined in Eq. (3.21). In the adiabatic approximation [see Eq. (3.44)], Eq. (3.95) can be rewritten in the form:

$$V'_{H\mathrm{xc}}(\mathbf{r},t) = \int \kappa(\mathbf{r},\mathbf{r}')\, n'(\mathbf{r}',t)\, d\mathbf{r}', \tag{3.96}$$

where $\kappa(\mathbf{r},\mathbf{r}')$ is the Hartree-plus-XC kernel which reads:

$$\kappa(\mathbf{r},\mathbf{r}') = \frac{e^2}{|\mathbf{r}-\mathbf{r}'|} + f_{\mathrm{xc}}(\mathbf{r},\mathbf{r}'), \tag{3.97}$$

where $f_{\mathrm{xc}}(\mathbf{r},\mathbf{r}')$ is the XC kernel which is defined in Eq. (3.45). By inserting Eq. (3.96) into Eq. (3.91), the linearized quantum Liouville equation is cast into the form [18]:

$$i\hbar \frac{d\hat{\rho}'(\mathbf{r},t)}{dt} = \hat{\mathcal{L}} \cdot \hat{\rho}'(\mathbf{r},t) + \left[V'_{ext}(\mathbf{r},t), \hat{\rho}^0(\mathbf{r})\right], \tag{3.98}$$

where the action of the *Liouvillian superoperator*[26] $\hat{\mathcal{L}}$ onto $\hat{\rho}'$ is defined as:

$$\hat{\mathcal{L}} \cdot \hat{\rho}' = [\hat{H}^0, \hat{\rho}'] + \left[V'_{H\mathrm{xc}}[\hat{\rho}'], \hat{\rho}^0\right]. \tag{3.99}$$

By Fourier analyzing the quantum Liouville equation (3.98) in time, one obtains:

$$(\hbar\omega - \hat{\mathcal{L}}) \cdot \hat{\tilde{\rho}}'(\mathbf{r}, \omega) = [\tilde{V}'_{ext}(\mathbf{r}, \omega), \hat{\rho}^0(\mathbf{r})], \tag{3.100}$$

The solution of Eq. (3.100) can be formally written as:

$$\hat{\tilde{\rho}}'(\mathbf{r}, \omega) = (\hbar\omega - \hat{\mathcal{L}})^{-1} \cdot [\tilde{V}'_{ext}(\mathbf{r}, \omega), \hat{\rho}^0(\mathbf{r})]. \tag{3.101}$$

In the absence of any external perturbations, *i.e.* $\tilde{V}'_{ext}(\mathbf{r}, \omega) = 0$, Eq. (3.100) becomes an eigenvalue equation for $\hat{\tilde{\rho}}'(\mathbf{r}, \omega)$, whose eigen-pairs describe *free oscillations* of the system, *i.e.* excited states [159]. Eigenvalues correspond to excitation energy values, whereas eigenvectors can be used to calculate transition oscillator strength, and the response of system properties to any generic external perturbation [18].

3.4.1 (c) Optical properties: dipole dynamical polarizability

The expectation value of any one-electron operator can be expressed as the trace of its product with the one-electron density-matrix. Therefore, the Fourier transform of the dipole which is linearly induced by the external perturbation reads:

$$\mathbf{d}(\omega) = \mathrm{Tr}[\hat{\mathbf{r}}\, \hat{\tilde{\rho}}'(\mathbf{r}, \omega)], \tag{3.102}$$

where $\hat{\mathbf{r}}$ is the quantum-mechanical position operator, and $\hat{\tilde{\rho}}'(\mathbf{r}, \omega)$ is the solution of the quantum Liouville equation (3.101). Let us suppose that the external perturbation is a homogeneous electric field:

$$\tilde{V}'_{ext}(\mathbf{r}, \omega) = -e\, \mathbf{E}(\omega) \cdot \mathbf{r}, \tag{3.103}$$

where $-e$ is the electron charge, and $\mathbf{E}(\omega)$ is the Fourier transform of the amplitude of the electric field. The dipole given by Eq. (3.102) reads:

$$d_i(\omega) = \sum_j \alpha_{ij}(\omega) E_j(\omega), \tag{3.104}$$

where $\alpha_{ij}(\omega)$ is the *dynamical polarizability tensor of the dipole*, which reads:

$$\alpha_{ij}(\omega) = -e\, \mathrm{Tr}\left(\hat{r}_i\, (\hbar\omega - \hat{\mathcal{L}})^{-1} \cdot [\hat{r}_j, \hat{\rho}^0]\right). \tag{3.105}$$

Traces of products of operators can be considered as scalar products defined in the linear space of quantum mechanical operators.[27] Therefore, Eq. (3.105) can be formally written as:

$$\alpha_{ij}(\omega) = -e\, \langle \hat{r}_i | (\hbar\omega - \hat{\mathcal{L}})^{-1} \cdot \hat{s}_j \rangle, \tag{3.106}$$

[26] *Superoperator* is a linear operator acting on a vector space of linear operators.

[27] For example, if $\hat{A}$ and $\hat{B}$ are two general one-electron operators, then the scalar product can be defined as: $\langle \hat{A} | \hat{B} \rangle \equiv \mathrm{Tr}(\hat{A}^\dagger \hat{B})$.

where $\hat{s}_j = [\hat{r}_j, \hat{\rho}^0]$. From Eq. (3.106) one can conclude, that the dynamical polarizability can be expressed as the off-diagonal matrix element of the resolvent[28] of the Liouvillian super-operator [18]. This statement can be extended in a straightforward way to the dynamic linear response of any observable to any local one-electron perturbation. It is worth noting that the operators $\hat{r}_i$ and $\hat{s}_j$, which enter the definition of the scalar product in Eq. (3.106), are orthogonal. Indeed, since $\hat{r}_i$ is Hermitian and $\hat{s}_j$ is anti-Hermitian, the scalar product of one Hermitian and one anti-Hermitian operators vanishes, $\langle \hat{r}_i | \hat{s}_j \rangle = 0$.

Lastly, I would like to point out that the absorption coefficient is related to the dynamical polarizability as: $I(\omega) \propto \omega \, \mathrm{Tr}[\alpha_{ij}(\omega)]$.

3.4.1 (d) Batch representation

As can be seen from Eq. (3.93), the response density-matrix at any given frequency ω is *uniquely* determined by the two sets of response orbitals:

$$\mathbf{x} = \{x_v(\mathbf{r})\} = \{\tilde{\varphi}'_v(\mathbf{r}, \omega)\}, \tag{3.107}$$

$$\mathbf{y} = \{y_v(\mathbf{r})\} = \{\tilde{\varphi}'^*_v(\mathbf{r}, -\omega)\}, \tag{3.108}$$

which are so-called *batches* [18]. This term has been introduced in Ref. [149]. Also, as I have pointed out earlier, the response orbitals $\{\tilde{\varphi}'_v\}$ can be chosen to be orthogonal to the KS occupied-state manifold $\{\varphi^0_v\}$. For this reason, the response density-matrix kernel of Eq. (3.93) has vanishing matrix elements between pairs of occupied and unoccupied states. Namely, $\langle \varphi^0_v | \hat{\rho}' | \varphi^0_{v'} \rangle = 0$, $\forall\,(v, v')$, where v and v' denote occupied (*valence*) states, and $\langle \varphi^0_c | \hat{\rho}' | \varphi^0_{c'} \rangle = 0$, $\forall\,(c, c')$, where c and c' denote empty (*conduction*) states [18]. Hence, the response density-matrix has the block structure:

$$\hat{\rho}' \longrightarrow \begin{pmatrix} 0 & \rho'_{vc} \\ \rho'_{cv} & 0 \end{pmatrix}. \tag{3.109}$$

This block structure allows us to represent conveniently the operators appearing in Eqs. (3.99) and (3.105). A detailed discussion about this issue can be found in Refs. [18, 154].

From now on, let us assume that the unperturbed system is time-reversal invariant, so that the unperturbed KS orbitals $\varphi^0_v(\mathbf{r})$ can be assumed to be real.[29] Therefore, the response charge-density, Eq. (3.94), in the batch representation reads:

$$\tilde{n}'(\mathbf{r}, \omega) = 2 \sum_v \varphi^0_v(\mathbf{r}) \left[\tilde{\varphi}'_v(\mathbf{r}, \omega) + \tilde{\varphi}'^*_v(\mathbf{r}, -\omega) \right] = 2 \sum_v \varphi^0_v(\mathbf{r}) \left[x_v(\mathbf{r}) + y_v(\mathbf{r}) \right]. \tag{3.110}$$

[28] Given a linear operator $\hat{A}$, the resolvent is defined as $R(z) = (\hat{A} - z\hat{I})^{-1}$, where $\hat{I}$ is the identity operator, and z is the complex number. In the current context, the resolvent of the linear Liouvillian superoperator $\hat{\mathcal{L}}$ is defined as $(\hbar\omega - \hat{\mathcal{L}})^{-1}$, where ω is the frequency, with the real part which corresponds to the excitation energy values and the complex part which corresponds to the broadening of the spectrum.

[29] Such an assumption can be made because we are considering optical absorption spectra of finite systems. In order to perform an *ab initio* calculation of a finite system within the plane-wave pseudopotential framework (see Sec. 2.3), one uses a supercell scheme and samples the Brillouin zone only with the Γ point. The wavefunctions at the Γ point are real, $\varphi^{0\,*}_v(\mathbf{r}) = \varphi^0_v(\mathbf{r})$, and I use this fact in the following derivations.

The batch representation of the product of the Liouvillian superoperator with the response density-matrix, Eq. (3.99), or equivalently the left-hand side of Eqs. (3.87) and (3.88) but for the $\hbar\omega$ term, can be written in the matrix form [18]:

$$\hat{\mathcal{L}} \begin{pmatrix} \mathbf{x} \\ \mathbf{y} \end{pmatrix} = \begin{pmatrix} \hat{\mathcal{D}} + \hat{\mathcal{K}} & \hat{\mathcal{K}} \\ -\hat{\mathcal{K}} & -\hat{\mathcal{D}} - \hat{\mathcal{K}} \end{pmatrix} \begin{pmatrix} \mathbf{x} \\ \mathbf{y} \end{pmatrix}, \tag{3.111}$$

where the action of the $\hat{\mathcal{D}}$ and $\hat{\mathcal{K}}$ super-operators on batches of orbitals is defined as:

$$\hat{\mathcal{D}} \cdot x_v(\mathbf{r}) = (\hat{H}^0 - \varepsilon_v)\, x_v(\mathbf{r}), \tag{3.112}$$

and

$$\hat{\mathcal{K}} \cdot x_v(\mathbf{r}) = 2\hat{P}_c \sum_{v'} \int K_{vv'}(\mathbf{r}, \mathbf{r}')\, x_{v'}(\mathbf{r}')\, d\mathbf{r}', \tag{3.113}$$

where the kernel $K_{vv'}(\mathbf{r}, \mathbf{r}')$ reads:

$$K_{vv'}(\mathbf{r}, \mathbf{r}') = \kappa(\mathbf{r}, \mathbf{r}')\, \varphi^0_v(\mathbf{r})\, \varphi^0_{v'}(\mathbf{r}'), \tag{3.114}$$

where $\kappa(\mathbf{r}, \mathbf{r}')$ is the Hartree-plus-XC kernel defined in Eq. (3.97). According to Eqs. (3.111)-(3.113), the calculation of the product of the Liouvillian with a general one-electron operator in the batch representation only requires operating on a number of one-electron orbitals equal to the number of occupied KS states, *without the need to calculate any empty states* [18]. Also, I would like to point out, that in practice the calculation of Eq. (3.113) is performed by calculating first the Hartree-plus-XC potential $\tilde{V}'_{H\text{xc}}$ [see Eq. (3.96)], then by applying it to each unperturbed occupied KS orbital, $\tilde{V}'_{H\text{xc}}\, \varphi^0_v$, and afterwords by applying the projector on empty states, $\hat{P}_c\, \tilde{V}'_{H\text{xc}}\, \varphi^0_v$ [see the second term on the left-hand side in Eqs. (3.87) and (3.88)].

According to Tsiper [161], it is convenient to perform a 45° rotation in the space of batches and define:

$$q_v(\mathbf{r}) = \frac{1}{2}\, [\tilde{\varphi}'_v(\mathbf{r}, \omega) + \tilde{\varphi}'^*_v(\mathbf{r}, -\omega)]\,, \tag{3.115}$$

$$p_v(\mathbf{r}) = \frac{1}{2}\, [\tilde{\varphi}'_v(\mathbf{r}, \omega) - \tilde{\varphi}'^*_v(\mathbf{r}, -\omega)]\,. \tag{3.116}$$

Equations (3.115) and (3.116) define the *standard batch representation* (SBR) of the density-matrix response, $\mathbf{q} = \{q_v(\mathbf{r})\}$ and $\mathbf{p} = \{p_v(\mathbf{r})\}$. The $q_v(\mathbf{r})$ and $p_v(\mathbf{r})$ are called the *upper* (or q-like) and the *lower* (or p-like) components of the SBR [154]. The SBR of the response charge-density, Eq. (3.110), therefore reads:

$$\tilde{n}'(\mathbf{r}, \omega) = 4 \sum_{v} \varphi^0_v(\mathbf{r}) q_v(\mathbf{r}). \tag{3.117}$$

The SBR of the Liouvillian super-operator, Eq. (3.111), reads:

$$\hat{\mathcal{L}} = \begin{pmatrix} 0 & \hat{\mathcal{D}} \\ \hat{\mathcal{D}} + 2\hat{\mathcal{K}} & 0 \end{pmatrix}, \tag{3.118}$$

and the SBR of the quantum Liouville equation (3.100) reads:

$$\begin{pmatrix} \hbar\omega & -\hat{\mathcal{D}} \\ -\hat{\mathcal{D}} - 2\hat{\mathcal{K}} & \hbar\omega \end{pmatrix} \begin{pmatrix} \mathbf{q} \\ \mathbf{p} \end{pmatrix} = \begin{pmatrix} 0 \\ \{\hat{P}_c \, \tilde{V}'_{ext}(\mathbf{r},\omega) \, \varphi_v^0(\mathbf{r})\} \end{pmatrix}. \tag{3.119}$$

General one-electron quantum mechanical operators can also be presented in the standard batch representation. The SBR of a general operator is defined as [154]:

$$\hat{A} \xrightarrow{\text{SBR}} \begin{pmatrix} \{a_v^q\} \\ \{a_v^p\} \end{pmatrix}, \tag{3.120}$$

where the orbitals $a_v^q(\mathbf{r})$ and $a_v^p(\mathbf{r})$ are defined as:

$$a_v^q(\mathbf{r}) = \frac{1}{2} \left[\hat{P}_c \, \hat{A} \, \varphi_v^0(\mathbf{r}) + (\hat{P}_c \, \hat{A}^\dagger \, \varphi_v^0(\mathbf{r}))^* \right], \tag{3.121}$$

$$a_v^p(\mathbf{r}) = \frac{1}{2} \left[\hat{P}_c \, \hat{A} \, \varphi_v^0(\mathbf{r}) - (\hat{P}_c \, \hat{A}^\dagger \, \varphi_v^0(\mathbf{r}))^* \right]. \tag{3.122}$$

If $\hat{A}$ is a Hermitian operator, then its SBR is given by

$$\hat{A} = \hat{A}^\dagger \xrightarrow{\text{SBR}} \begin{pmatrix} \{\hat{P}_c \, \hat{A} \, \varphi_v^0(\mathbf{r})\} \\ 0 \end{pmatrix}. \tag{3.123}$$

Armed with foregoing considerations, let us express the dynamical polarizability $\alpha_{ij}(\omega)$, Eq. (3.106), in the SBR. According to definitions (3.120)-(3.122), the operators $\hat{r}_i$ and $[\hat{r}_j, \hat{\rho^0}]$, appearing in Eq. (3.106), in the SBR read [154]:

$$\hat{r}_i \xrightarrow{\text{SBR}} \begin{pmatrix} \{\hat{P}_c \, \hat{r}_i \, \varphi_v^0(\mathbf{r})\} \\ 0 \end{pmatrix}, \tag{3.124}$$

and

$$[\hat{r}_j, \hat{\rho^0}] \xrightarrow{\text{SBR}} \begin{pmatrix} 0 \\ \{\hat{P}_c \, \hat{r}_j \, \varphi_v^0(\mathbf{r})\} \end{pmatrix}. \tag{3.125}$$

Therefore, the dynamical polarizability $\alpha_{ij}(\omega)$ in the SBR reads (see Eq. (2.40) in Ref. [162]):

$$\alpha_{ij}(\omega) = -e \left\langle (\{\hat{P}_c \, \hat{r}_i \, \varphi_v^0\}, 0) \middle| (\hbar\omega \hat{I} - \hat{\mathcal{L}})^{-1} \cdot (0, \{\hat{P}_c \, \hat{r}_j \, \varphi_v^0\}) \right\rangle, \tag{3.126}$$

or, equivalently [see Eq. (3.119)],

$$\alpha_{ij}(\omega) = \left\langle (\{\hat{P}_c \, \hat{r}_i \, \varphi_v^0\}, 0) \middle| \begin{pmatrix} \hbar\omega & -\hat{\mathcal{D}} \\ -\hat{\mathcal{D}} - 2\hat{\mathcal{K}} & \hbar\omega \end{pmatrix}^{-1} \begin{pmatrix} 0 \\ \{\hat{P}_c \, \hat{r}_j \, \varphi_v^0\} \end{pmatrix} \right\rangle. \tag{3.127}$$

Such a matrix element can be efficiently calculated using the Lanczos recursion method (see Sec. 3.4.2).

3.4.1 (e) Dipole operator in periodic boundary conditions

On the right-hand side of Eq. (3.119), there is a term $\hat{P}_c\,\tilde{V}'_{ext}(\mathbf{r},\omega)\,\varphi_v^0(\mathbf{r})$. In the case when the external perturbation is the electric field, Eq. (3.103), one has to compute hence $\hat{P}_c\,\hat{\mathbf{r}}\,\varphi_v^0(\mathbf{r})$. However, the quantum mechanical position operator $\hat{\mathbf{r}}$ is ill-defined in the periodic boundary conditions, used in plane-wave implementation. Nevertheless, since $\hat{P}_c\,\hat{\mathbf{r}}\,\varphi_v^0(\mathbf{r}) = \sum_c |\varphi_c^0\rangle\langle\varphi_c^0|\hat{\mathbf{r}}|\varphi_v^0\rangle$, one can make use of the relation:

$$\langle\varphi_c^0|\hat{\mathbf{r}}|\varphi_v^0\rangle = \frac{\langle\varphi_c^0|[\hat{H}^0,\hat{\mathbf{r}}]|\varphi_v^0\rangle}{\varepsilon_c - \varepsilon_v}, \tag{3.128}$$

where the matrix element $\langle\varphi_c^0|[\hat{H}^0,\hat{\mathbf{r}}]|\varphi_v^0\rangle$ is well defined in periodic boundary conditions [154]. If the potential in the unperturbed Hamiltonian $\hat{H}^0$ is local, then $[\hat{H}^0,\hat{\mathbf{r}}] = -i\hbar\hat{\mathbf{p}}/m$, where $\hat{\mathbf{p}}$ is the momentum operator, and m is the electron mass. However, if the potential acting on electrons has also a non-local part, which is the case for many pseudopotentials, then an additional term must be added to the momentum operator [163].[30]

In the summary of this section, in order to calculate optical absorption spectra of finite systems, one has to determine the dynamical polarizability Eq. (3.106). All operators which are present in Eq. (3.106) can be conveniently presented in the batch representation, introduced in Ref. [149], which allows us to avoid explicit calculation of unoccupied Kohn-Sham states. In the next section I will present a numerical algorithm, which allows us to calculate an off-diagonal matrix element of the resolvent of the Liouvillian superoperator, like the one in Eq. (3.106).

3.4.2 Lanczos recursion method

3.4.2 (a) The algorithm

According to the discussion in the previous section, the dynamical polarizability $\alpha_{ij}(\omega)$ can be expressed as an off-diagonal matrix element of the resolvent of the Liouvillian superoperator, Eq. (3.106). In this section I will briefly present how such a matrix element can be efficiently calculated using the Lanczos recursion method, which is a generalization of the recursion method by Haydock, Heine, and Kelly [164].

At first sight, it may seem that the calculation of the dynamical polarizability from the resolvent of the Liouvillian would require an inversion of $(\omega - \hat{\mathcal{L}})$ for each value of the frequency ω, which is a very demanding task as the system size and the number of frequencies increase. However, a specially tailored iterative method, the so-called *Lanczos biorthogonalization algorithm* [18, 165, 166], can be used, which allows to perform the calculation only *once for all frequencies*.

Let us define two two-component Lanczos vectors:

$$\mathbf{V}_i = \begin{pmatrix} q_v^i \\ p_v^i \end{pmatrix}, \quad \text{and} \quad \mathbf{U}_i = \begin{pmatrix} \tilde{q}_v^i \\ \tilde{p}_v^i \end{pmatrix}, \tag{3.129}$$

[30] Notice, the electron velocity reads $\mathbf{v} = (i/\hbar)\langle\varphi_v^0|[\hat{H}^0,\hat{\mathbf{r}}]|\varphi_v^0\rangle$, which is the *diagonal* matrix element of the commutator. Instead, here we are interested in the *off-diagonal* matrix element of the commutator Eq. (3.128). In Sec. 6.1.3 I will discussion in detail practical aspects of an *ab initio* calculation of such matrix elements.

where index i denotes the number of the Lanczos iteration, v is the band index, q_v^i and $\tilde{q}_v^i$ are the *upper* (or q-like) components of the SBR, and p_v^i and $\tilde{p}_v^i$ are the *lower* (or p-like) components of the SBR. Further, let us define the starting Lanczos vectors $\mathbf{V}_1$ and $\mathbf{U}_1$ according to the right-hand side of Eq. (3.119):

$$\mathbf{V}_1 = \mathbf{U}_1 = \begin{pmatrix} 0 \\ \hat{P}_c\,\hat{\mathbf{r}}\,\varphi_v^0(\mathbf{r}) \end{pmatrix}. \tag{3.130}$$

The scalar product of the starting Lanczos vectors $\mathbf{V}_1$ and $\mathbf{U}_1$ must be equal to 1 [167], hence they have to be normalized: $\mathbf{V'}_1 = \mathbf{V}_1/\langle \mathbf{U}_1|\mathbf{V}_1\rangle$, and $\mathbf{U'}_1 = \mathbf{U}_1/\langle \mathbf{U}_1|\mathbf{V}_1\rangle$, so that $\langle \mathbf{U'}_1|\mathbf{V'}_1\rangle = 1$.

The rule to build the Lanczos recursion chain reads [165]:

$$\beta_{i+1}\,\mathbf{V}_{i+1} = \hat{\mathcal{L}}\,\mathbf{V}_i - \gamma_i\,\mathbf{V}_{i-1}, \tag{3.131}$$

$$\gamma_{i+1}\,\mathbf{U}_{i+1} = \hat{\mathcal{L}}^T\,\mathbf{U}_i - \beta_i\,\mathbf{U}_{i-1}, \tag{3.132}$$

where the index i runs from 1 to N (N being the maximal number of Lanczos iterations), $\mathbf{V}_0 = \mathbf{U}_0 = 0$, and β_i and γ_i are the Lanczos coefficients (real numbers). Since the diagonal elements of the Liouvillian $\hat{\mathcal{L}}$ are zero in the SBR, Eq. (3.118), an application of $\hat{\mathcal{L}}$ (or $\hat{\mathcal{L}}^T$) to Lanczos vectors $\mathbf{V}_i$ and $\mathbf{U}_i$ will bring a q-part to a p-part of the new vector, and a p-part to a q-part. Therefore, the $\mathbf{V}_i$ and $\mathbf{U}_i$ vectors will always have either the p-part zero and q-part non-zero, or vice-versa. Which part is zero in a given iteration depends on whether the iteration is even or odd.

The Lanczos coefficients are defined so that they must fulfill the orthonormality condition of the Lanczos vectors: $\langle \mathbf{U}_{i+1}|\mathbf{V}_{i+1}\rangle = 1$. Therefore, according to Saad [165]:

$$\beta_{i+1} = \sqrt{|\langle \hat{\mathcal{L}}\,\mathbf{V}_i - \gamma_i\,\mathbf{V}_{i-1}|\hat{\mathcal{L}}^T\,\mathbf{U}_i - \beta_i\,\mathbf{U}_{i-1}\rangle|}\,, \tag{3.133}$$

$$\gamma_{i+1} = \beta_{i+1}\ \mathrm{sign}\left(\langle \hat{\mathcal{L}}\,\mathbf{V}_i - \gamma_i\,\mathbf{V}_{i-1}|\hat{\mathcal{L}}^T\,\mathbf{U}_i - \beta_i\,\mathbf{U}_{i-1}\rangle\right), \tag{3.134}$$

and $\beta_1 = \gamma_1 = 0$. By solving the system (3.131) - (3.132) in an iterative way, two matrices of Lanczos vectors are generated: $\overline{\mathbf{V}}^N = [\mathbf{V}_1, \mathbf{V}_2, \ldots, \mathbf{V}_N]$, and $\overline{\mathbf{U}}^N = [\mathbf{U}_1, \mathbf{U}_2, \ldots, \mathbf{U}_N]$. In the basis of the Lanczos vectors $\{\mathbf{V}_i\}$ and $\{\mathbf{U}_i\}$, the Liouvillian $\hat{\mathcal{L}}$ has a tridiagonal form [167]:

$$\left(\overline{\mathbf{U}}^N\right)^T \hat{\mathcal{L}}\ \overline{\mathbf{V}}^N = \hat{T}^N, \tag{3.135}$$

where $\hat{T}^N$ is the tridiagonal matrix which reads:

$$\hat{T}^N = \begin{pmatrix} 0 & \gamma_2 & 0 & \ldots & 0 \\ \beta_2 & 0 & \gamma_3 & 0 & 0 \\ 0 & \beta_3 & 0 & \ddots & 0 \\ \vdots & 0 & \ddots & \ddots & \gamma_N \\ 0 & \ldots & 0 & \beta_N & 0 \end{pmatrix}. \tag{3.136}$$

It is worth noting that the diagonal matrix elements in Eq. (3.136) vanish because of the special (off-diagonal) structure of the Liouvillian $\hat{\mathcal{L}}$ in the SBR, Eq. (3.118),[31] and of the starting Lanczos vectors $\mathbf{V}_1$ and $\mathbf{U}_1$, Eq. (3.130). This is the reason why the diagonal matrix elements $\alpha_i = \langle \mathbf{U}_i | \hat{\mathcal{L}} \mathbf{V}_i \rangle$, which in the general case must be present in Eqs. (3.131) - (3.132), are equal to zero [18, 154].

It can be shown (see Eqs. (71)-(77) of Ref. [18]) that within the Lanczos recursive scheme the matrix element of the form Eq. (3.106) can be cast into the form [154]:

$$\alpha(\omega) \simeq -e \left\langle \boldsymbol{\zeta}^N | (\hbar\omega \hat{I} - \hat{T}^N)^{-1} \cdot \mathbf{e}_1^N \right\rangle, \tag{3.137}$$

where $\alpha(\omega)$ is the dynamical polarizability, $-e$ is the electron charge, N is the maximal number of Lanczos iterations, $\hat{I}$ is the $N \times N$ identity matrix, $\mathbf{e}_1^N = (1, 0, \ldots, 0)$ is the unit vector in N-dimensional space, and $\boldsymbol{\zeta}^N = (\zeta_1, \zeta_2, \ldots, \zeta_N)$ is the vector composed of the coefficients ζ_i which are defined as:

$$\zeta_i = \left\langle (\hat{P}_c \, \hat{\mathbf{r}} \, \varphi_v^0(\mathbf{r}), 0) | \mathbf{V}_i \right\rangle, \tag{3.138}$$

where the index i denotes the number of the Lanczos iteration. The right-hand side of the scalar product in Eq. (3.137) is determined by solving, for a given value of ω, the following equation:

$$\left(\hbar\omega \hat{I} - \hat{T}^N \right) \cdot \boldsymbol{\eta}^N = \mathbf{e}_1^N, \tag{3.139}$$

and, therefore, the dynamical polarizability $\alpha(\omega)$ can be calculated as:

$$\alpha(\omega) = -e \, \langle \boldsymbol{\zeta}^N | \boldsymbol{\eta}^N \rangle. \tag{3.140}$$

The coefficients ζ_i, Eq. (3.138), are calculated *on the fly* during the Lanczos recursion. Since the Lanczos vectors $\mathbf{V}_i$ have either q-part zero and p-part non-zero, or p-part zero and q-part non-zero depending on whether the iteration is even or odd, the coefficients ζ_i can be either zero or non-zero. More specifically, when the iteration is odd then $\zeta_i = 0$, and when the iteration is even then $\zeta_i \neq 0$.

In practice, the procedure outlined above is performed in two steps. In the first step, which is also the most time consuming, one generates the tridiagonal matrix $\hat{T}^N$, Eq. (3.136), and the $\boldsymbol{\zeta}^N$ array, Eq. (3.138). In the second step, the dynamical polarizability $\alpha(\omega)$ is calculated from Eq. (3.140) upon the solution of Eq. (3.139), for different frequencies ω.[32] Because of the tridiagonal form and the small dimension of the matrix $\hat{T}^N$, the second step computationally costs much less than the first step, and this is one of the big advantages of the method.

[31] This is why the rotation of batches on 45° is convenient, Eqs. (3.115) and (3.116).

[32] In practice a small imaginary part σ is added to the frequency argument, $\omega \to \omega + i\sigma$, in order to regularize the spectrum [18]. Setting σ to a non-zero value amounts to convolute the theoretical spectrum with a Lorentzian, or, alternatively, to broaden each individual spectral line. The optimal value of σ is slightly larger than the minimum separation between discrete peaks, and depends in principle on the details of the system being studied.

3.4.2 (b) Extrapolation of the Lanczos recursion chain

A careful inspection of the convergence of the calculated spectrum with respect to the number of Lanczos iterations allows the formulation of a simple extrapolation scheme that drastically enhances the numerical performance of the Liouville-Lanczos method [18]. The components of the $\boldsymbol{\zeta}^N$ array, Eq. (3.138), decrease rather rapidly when the number of Lanczos iterations increases, so that only a relatively small number of components have to be explicitly calculated [18]. However, a much larger number of β_i and γ_i coefficients is necessary in order to converge the solution of Eq. (3.139). When the number of Lanczos iterations is large enough, β_i and γ_i coefficients oscillate around two distinct values for odd and even iterations, whose average is approximatively equal to half of the kinetic-energy cutoff (in a plane-wave implementation, see Sec. 2.3.1), and whose difference is approximatively twice as large as the optical gap [18, 154].

Thereby, the extrapolation can be performed in the following way. Let us suppose that N Lanczos iterations have been performed, and that a regime where further components of the $\boldsymbol{\zeta}^N$ array are negligible have been attained, and the Lanczos coefficients β_i and γ_i display a bimodal behaviour. Subsequently, a much larger tridiagonal system can be solved, for $N' \gg N$, Eq. (3.139), where the missing components of $\boldsymbol{\zeta}^{N'}$ are set to zero, and the missing values of β_i and γ_i are set to the average of the values which have been actually calculated, $\langle\beta_i\rangle$ and $\langle\gamma_i\rangle$.[33] Moreover, using distinct averages for odd and even iterations, $\langle\beta_i\rangle_{\text{odd}}$ and $\langle\beta_i\rangle_{\text{even}}$, may actually slightly improve the accuracy of the extrapolation - the, so-called, *biconstant extrapolation*.

3.4.2 (c) Feautures of the Liouville-Lanczos approach

- The higher the plane-wave kinetic-energy cutoff, the more Lanczos iterations are necessary to converge the absorption spectrum [149]. This is related to the condition number of the problem, which is defined as a ratio of the total spectral width of the Liouvillian to the typical energy level spacing one need to resolve (typically fractions of 1 eV). At high energy values, the Hamiltonian (and therefore the Liouvillian) is determined in a PW basis set by the kinetic energy, and the maximum energy is (roughly) the highest kinetic energy possible. Therefore, the higher the kinetic-energy cutoff, the larger the condition number, and the worse the spectrum is converged. Hence, the increase of the number of Lanczos iterations is needed to converge the spectrum. The dependence between the number of Lanczos iterations and the kinetic-energy cutoff is *linear*, *e.g.* the increase of the kinetic-energy cutoff by a factor of two requires the increase of the number of Lanczos iterations also by the factor of two.

- The numerical instabilities, which may occur during the Lanczos recursion, have little effect on the final absorption spectrum [18, 167].

[33] Notice that $\gamma_i = \pm|\beta_i|$. It very rarely occurs that γ_i and β_i have a different sign. Thus, extrapolating them to the same positive value, $\langle\gamma_i\rangle \simeq \langle\beta_i\rangle$, does not affect the accuracy of the extrapolation [18].

- The Tamm-Dancoff approximation[34] reduces the computational effort of the Liouville-Lanczos approach. Though, one has to check whether such an approximation is sufficient for the description of the absorption spectrum of the system being studied.

- If the exchange-correlation kernel f_{xc} is frequency independent, as in the adiabatic approximation, Eq. (3.45), the tridiagonal representation of the Liouvillian $\hat{\mathcal{L}}$, Eq. (3.135), is also independent of frequency, and thus *one single Lanczos chain* allows for the calculation of the absorption spectrum at *all* frequencies via Eq. (3.137).

- If the exchange-correlation kernel f_{xc} is frequency dependent, the situation is not as simple. It is possible to make a linearization of the f_{xc} kernel within selected frequency windows, which will result in a manageable scheme based on a single Lanczos chain per window [149].

- The Liouville-Lanczos approach can also be applied with *non-local* kernels, such as those occuring with hybrid functionals, once the action of the exchange operator onto a molecular orbital is properly implemented for ground-state calculations [149].

- A remarkable feature of the Liouville-Lanczos approach is that the f-sum rule is satisfied exactly when truncating the Lanczos recursion to any number of iterations [169]. However, this is only the case when using *local* pseudopotentials. When *non-local* pseudopotentials are used, violations of the f-sum rule occur. Experience shows [154], that such violations are rather small, though larger for ultrasoft ($< 8\%$) than for norm-conserving ($\sim 1\%$) pseudopotentials.

3.5 Summary & Outlook

In this chapter, the time-dependent problem has been addressed in the framework of non-relativistic quantum mechanics. Excitation properties, like the linear response to an external perturbation, can be accessed in the framework of the time-dependent density functional theory (TDDFT). It is based on the same ideas as static density functional theory (see Chapter 2), but the time evolution of the density is formally given by the stationary solution of a quantum-mechanical action functional, and can be calculated from the time-dependent Kohn-Sham equations.

I have presented a conventional linear-response formalism to TDDFT. Within this formalism, the microscopic and macroscopic dielectric tensors can be obtained in the following way: First, the independent-particle polarizability χ^0 of the Kohn-Sham particles is calculated; second, one solves the Dyson-like screening equation for the susceptibility χ; and finally, one determines micro- and macroscopic dielectric tensors. The knowledge of these quantities allows for a determination of optical absorption spectra in finite systems and electron energy-loss spectra in finite and extended systems. I have pointed out that

[34]The Tamm-Dancoff approximation (TDA) consists in neglecting the non-Hermitian components of the Liouvillian, thus enforcing to it a Hermiticity [168]. It has been shown that the use of the TDA does not change the overall absorption spectrum much (this is not the case for EELS) [18]. The convergence of TDA calculations is much faster than when using the full non-Hermitian form of the Liouvillian [149].

the crystal local field effects and exchange-correlation effects may be very important for both spectroscopies, depending on the system under study. In addition, I have discussed the principles of EELS experiments, what physics behind it, and what is the relation to the dielectric theory.

Finally, I have discussed a new very efficient approach to the calculation of absorption spectra of finite systems - Liouville-Lanczos approach. This approach does not require the calculation of any unoccupied Kohn-Sham states, nor time-consuming matrix operations. The absorption spectrum can be obtained from a dynamical polarizability, which is evaluated using a Lanczos recursion method. The Liouville-Lanczos approach opens the way to the study of systems which are too large to be treated with conventional techniques, *i.e.* the solution of the Dyson-like equation. Moreover, very recently, this new approach has been extended to the calculation of absorption spectra of finite and extended systems by solving the Bethe-Salpeter equation [150, 151, 152].

In Chapter 7 of this thesis, I will extend the Liouville-Lanczos approach from the case of optical absorption of finite systems ($\mathbf{q} = 0$) to the case of EELS of extended systems ($\mathbf{q} \neq 0$). In particular, I will make an extension of the implementation based on the use of supercells and Γ point sampling of the Brillouin zone and real unperturbed KS wavefunctions, to the general case of the use of primitive unit cells with generic $\mathbf{k}$ points sampling of the Brillouin zone and complex unperturbed KS wavefunctions. Such an extension of the method would allow us to make calculations of EELS for systems containing hundreds of atoms, which is a computationally demanding task for the conventional TDDFT methods (see Sec. 3.2). Moreover, such a new method for EELS would also allow us to fill the gap between 50 and 100 eV between the valence-loss and core-loss EELS, which is hardly accessible by conventional techniques. Furthermore, I will extend the method to metals, and introduce the relativistic effect of the spin-orbit coupling (see Sec. 2.2), which would allow the study of EELS of systems where relativistic effects are important, like in bismuth (see Chapter 4).

Chapter 4

Material: bismuth

In this chapter I will describe the material which I have studied during my thesis - semimetal bismuth. Owing to semimetals, and especially to bismuth, many of the sophisticated experimental techniques and various effects have been discovered. For example, the quantum oscillatory techniques like de Haas-van Alphen and Shubnikov-de Haas, and a property like thermoelectricity, have been indeed first discovered on bismuth [4]. This is not surprising, because its particular properties facilitate the observation of such effects. In recent years, there has been an increasing interest in Bi, both from the experimental and theoretical side, and considerable progress has been made [7].

Nevertheless, Bi still remains rather challenging for both experiments and calculations. Very high energy resolution and low temperatures are required in order to experimentally resolve tiny features of Bi, like its extremely small Fermi surface and small effective masses of carriers. From the theoretical point of view, Bi requires inclusion of relativistic effects (spin-orbit coupling) due to its heavy atoms, and a very dense $\mathbf{k}$ point sampling of the Brillouin zone is needed to accurately describe tiny details like the electron and hole pockets forming the Fermi surface.

This chapter is organized as follows. In Sec. 4.1 I will explain my motivation for studying bismuth. In Sec. 4.2 I will discuss the bulk properties of Bi, like its crystalline structure, electronic structure and the density of states. I will put a stress on the importance of the spin-orbit coupling effect, in particular, for the description of the electron and hole pockets. In Sec. 4.3 I will discuss the Bi(111) surface, and I will show the crucial role of the spin-orbit coupling effect in the description of surface states. In Sec. 4.4 I will present the phonon dispersion in Bi, again by pointing out the effect of the spin-orbit coupling, and also I will describe the generation mechanism of the A_{1g} coherent phonon in bulk Bi. In Sec. 4.5 I will discuss the electron-energy loss spectrum of Bi. Finally, at the end of the chapter I will give a summary.

4.1 Motivation for studying Bi

Bismuth is the semimetal which has an atomic number $Z = 83$ in Mendeleev's periodic table of elements. This is one of the materials which have been extensively studied over the past 70 years because it has a number of unique properties:

- Very low density of carriers (electrons and holes) $n = p = 2.7 \times 10^{17}$ cm^{-3} [4], and high carrier mobility, $\mu_n = 12\,838$ and $\mu_p = 5\,986$ cm^2/(V s) at 300 K [170].
- Extremely small Fermi surface volume and small anisotropic effective mass of carriers ($\sim 10^{-2} m_0$), which lead to a long de Broglie wavelength of around $\lambda = 120$ Å [7].
- Bi has carriers with a very long mean free path, ≈ 1 mm at low temperatures [7], which is advantageous for electronic transport, as it can be measured on the macroscopic scale. The later property makes Bi a very attractive material for thermoelectric applications [4].
- Bi is the most diamagnetic element, with the volume magnetic susceptibility $\chi_v = -1.66 \times 10^{-4}$ (unitless) [171].
- Bi has the highest Hall effect, with the Hall coefficient $R = -171$ (unitless) at 0.07 Gauss [172].
- Bi has low thermal conductivity, $\kappa = 0.1$ W/(m K) at 200 K [4], due to heavy mass ions.
- Bi has a low melting temperature of $T = 271$ °C [4].
- Bi is a reference material for the investigation of lattice dynamics in out-of-equilibrium conditions. Indeed, a photoexcitation of this material induces coherent phonons of large amplitude of oscillation [15].
- Core electrons may move at a speed close to light velocity in the interior of Bi atom, and thus a purely nonrelativistic theoretical description of Bi is not sufficient [82].
- The spin-orbit coupling effect in Bi is extremely large for valence electrons, which influences all its properties, like electronic [82], vibrational [6].

Recently, much attention has been directed toward the electronic structure and transport properties of Bi nanostructures [7]. For instance, there is a potential importance of Bi nanowires and nanowire arrays in thermoelectric applications. For purposes of cooling or power generation, the thermoelectric figure of merit ZT has to be maximized [4], but for conventional materials the achievable values of ZT are reached. It has been proposed that the limits of ZT could be overcome by using nanowires instead of bulk crystals [173], and that Bi would be a promising material for such nanowires [174]. These ideas are supported by recent experimental results [175, 176].

Moreover, there is a lot of interest in the electronic structure and superconducting properties of small Bi clusters. Bulk Bi at ambient conditions is not superconducting (see Appendix A.2). However, Weitzel and Micklitz have reported the observation of superconductivity in granular films of rhombohedral Bi clusters [177]. Depending on the cluster size, the critical temperature of superconductivity T_c can reach values as high as several Kelvins.

There is an increased interest also in metallic Bi surfaces, because they have unique spin properties [7]. One of the practical applications of Bi surfaces could be a construction of spin-sources or spin-filters for the field of *spintronics*, which is a novel type of electronics based on a spin degree of freedom in addition to the charge [7].

Bismuth is a semimetal like graphite, and it is one of the elements on which are based topological insulators Bi_2Te_3 and Bi_2Se_3 [178, 179]. Both, graphite-originated systems (e.g. graphene, carbon nanotubes, etc. [180]) and topological insulators, have gained enormous attention among scientists over the past years, due to their unique properties and a potential importance in nanoelectronics. Therefore, it is important to understand in detail properties of bismuth, which would allow us to make parallels with aforementioned systems and to give new insights into the understanding of their properties. For instance, the main problem of the carbon nanotubes research is related to the preparation of samples. However, these technical problems can be overcome for Bi nanowires. Recently, it has been possible to grow Bi nanowires with a precise diameter size as well as crystalline quality [181]. Therefore, a comparative investigation of Bi nanowires may reveal optical and transport effects due to the 1D confinement of the electronic wavefunctions.

In this thesis I will present an *ab initio* study of bulk Bi. Although bulk Bi has been extensively studied, both experimentally and theoretically, there are still many unrevealed issues in this unusual material. In Secs. 5.2 and 6.2 I will present a theoretical interpretation of the time-resolved photoemission and terahertz experiments, relying on the *ab initio* calculations within the density functional theory. In Sec. 7.3 I will present the first *ab initio* study of the electron energy-loss spectra of bulk Bi, as well as new findings related to this issue.

4.2 Bulk properties of Bi

Bismuth has a complex phase diagram, as discussed in the Appendix A.2. In this section, I will present the crystal and electronic structure of bulk Bi in the rhombohedral phase. I will discuss the peculiarity of the band structure of Bi, and about the density of states, in particular, near the Fermi level.

4.2.1 Crystal structure

Most of the properties that distinguish the group-V semimetals from the less exotic isotropic metals or semiconductors are due to their particular crystallographic structure. Bismuth is the heaviest element among the group-V semimetals. Like As and Sb, it crystallizes in the $A7$ rhombohedral structure [see Fig. 4.1(a)], with two atoms in the primitive

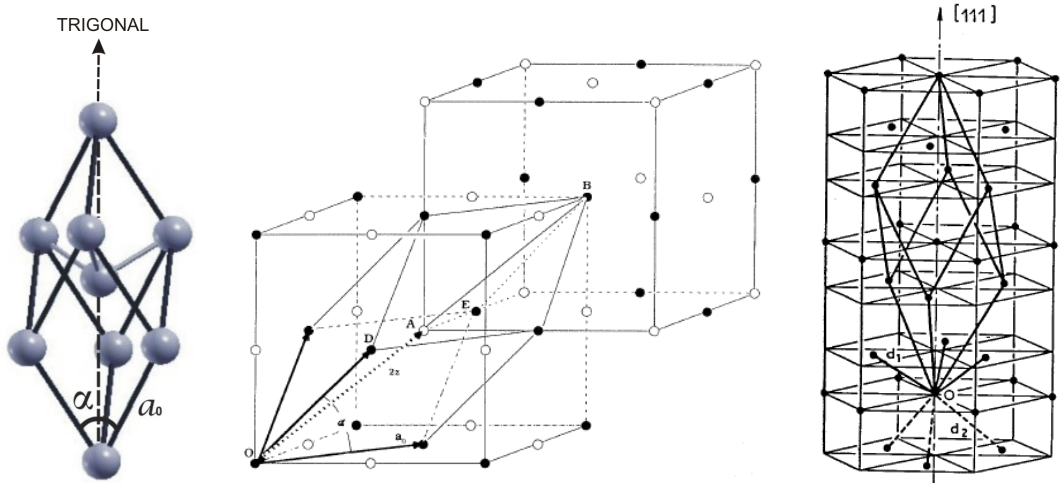

(a) (b) (c)

Figure 4.1: (a) $A7$ rhombohedral unit cell of Bi. (b) Illustration of the formation of the $A7$ rhombohedral unit cell by two interpenetrating *fcc* sublattices. Two independent distortions have to be applied: a slight displacement of the *fcc* sublattices along a body diagonal, which remains a trigonal axis of symmetry, and a small shear of the rhombohedral angle α. From Ref. [186]. (c) Puckered bilayers of Bi atoms. From Ref. [13].

unit cell. It can be obtained from the simple cubic structure formed by two interpenetrating face-centered cubic (*fcc*) sublattices, by applying two independent distortions: (*i*) a strain of the unit cell along the [111] direction, *i.e.* along the trigonal axis, and (*ii*) an internal displacement of the atoms of the two *fcc* sublattices towards each other along the [111] direction [see Fig. 4.1(b)]. Such a distortion from the cubic structure to $A7$ structure is stabilized by the *Peierls-Jones mechanism* [see Ref. [182], and chapter 5 in Ref. [183]], because the $A7$ structure is energetically more favorable [184]. Alternatively, the structure of bismuth can be described as hexagonal with six atoms *per* unit cell, or as a pseudocubic structure with one atom *per* unit cell. More details on the crystal structure of Bi can be found in Refs. [7, 185].

Each atom has three equidistant nearest-neighbour atoms and three equidistant next-nearest neighbours slightly further away. This results in puckered bilayers of atoms perpendicular to the [111] direction, in which each atom is covalently bonded to its three nearest neighbours [see Fig. 4.1(c)]. The next-nearest neighbours are in the adjacent bilayer, and a bonding within each bilayer is much stronger than the inter-bilayer bonding. As Bi is brittle at room temperature, Bi crystals are easily cleaved along the (111) plane, *i.e.* along the basal plane, which is perpendicular to the [111] direction.

What is the symmetry of the $A7$ rhombohedral structure? The twelve symmetry elements are the trigonal axis, binary axis, bisectrix axis, mirror planes and the inversion symmetry [187, 188]. Since the trigonal axis has a threefold symmetry, the binary and bisectrix axes and the mirror plane exist three times.

The simplest description of the Bi structure is obtained when using the $A7$ rhom-

bohedral Bravais lattice with two atoms in the primitive unit cell. Three parameters completely determine the unit cell and atomic positions: the length a_0 of the rhombohedral edge, the rhombohedral angle α, and the internal parameter u describing atomic positions along the trigonal axis: (u, u, u) and $(-u, -u, -u)$. From X-ray diffraction measurements at $T = 4.2$ K [189] the following parameters for the unit cell of Bi were found: $a_0 = 4.7236$ Å, $\alpha = 57.35°$, and $u = 0.234$ (in units of a_0). [1] The Brillouin zone (BZ) of bismuth is shown in Fig. 4.3(a).

In the hexagonal lattice system, the crystal structure is described by the parameters a_{hex}, c and u. To recall, the transformation from the rhombohedral lattice parameters to the hexagonal ones is done by means of the equations [190]: $a_{hex} = 2\,a_0 \sin(\alpha/2)$, $c = \sqrt{3}\,a_0\sqrt{1 + 2\cos\alpha}$. The experimental values are $a_{hex} = 4.5330$ Å, $c = 11.797$ Å[189].

In Sec. 5.1.2 I will make a comparison between the equilibrium theoretical lattice parameters obtained in this thesis by using DFT within LDA and GGA approximations, and experimental lattice parameters.

4.2.2 Electronic structure

The electronic configuration of the neutral Bi atom is [Xe]$4f^{14}5d^{10}6s^26p^3$. The external (valence) electrons are $6s^26p^3$, plus a complete $5d$ semicore shell. The lower lying electrons together with the nucleus form a core. The $6s$ and $6p$ levels form energy bands in the solid, while $5d$-electrons and core-electron energy levels remain practically unchanged. The $5d$ semicore electrons can be either included in the core, or in the valence region. In some of the anterior studies the $5d$-electrons were included in the core region [186, 5, 191, 9, 8], and some authors included them in the valence region [192]. It is worth noting that the inclusion of semicore states in the valence region influences the exchange energy, which shows up in the transferability tests of pseudopotentials (see Appendix A.1). For this reason, in this thesis I will include the $5d$-electrons in the valence region.

Figure 4.2.2 shows the Kohn-Sham band structure of bulk bismuth, including the effect of spin-orbit coupling (SOC). The high-symmetry directions in the bulk Brillouin zone can be seen in Fig. 4.3(a). There are several features in the band structure of Bi:

(*i*) two $6s$ valence bands are well separated from the three $6p$ valence bands, and disperse around -10 eV,

(*ii*) three lowest conduction $6p$ bands are separated from the higher lying conduction bands,

(*iii*) ten $5d$ levels lie very deeply, below -20 eV, and are split due to the SOC; and more peculiarly,

(*iv*) the highest valence band crosses the Fermi level at the T point, and thus creates the hole pocket,

(*v*) the lowest conduction band crosses the Fermi level at the L point, and thus creates the electron pocket,

(*vi*) in the full BZ there are three electron pockets (at three L points) and one hole pocket (at point T) [see Fig. 4.3(b)],

[1] The comparison of the experimental lattice parameters with the theoretical ones will be given in Sec. 5.1.2.

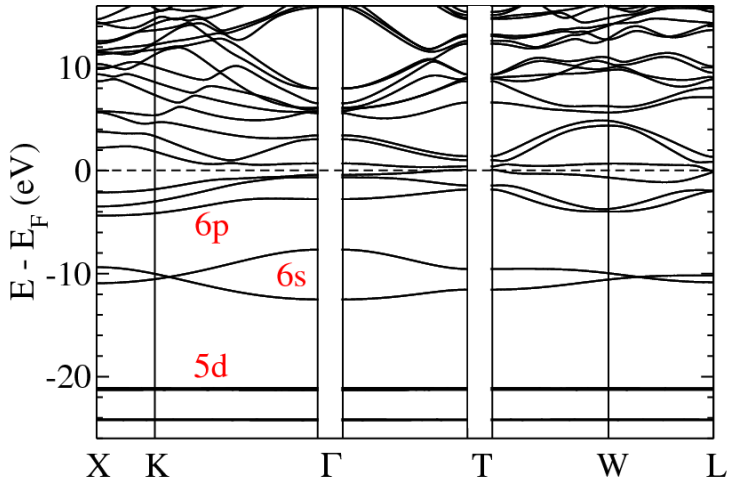

Figure 4.2: Kohn-Sham band structure of Bi including spin-orbit coupling, obtained within DFT-GGA (see Sec. 5.1 for more details). Fermi level is at zero energy. (Unpublished)

(*vii*) there is an extremely small overlap between the highest valence band and the lowest conduction band.

The effect of the spin-orbit coupling causes a very large splitting of energy bands, as can be seen in Figs. 4.4(a) and 4.4(b), by comparing two calculations performed with and without the SOC. Namely, there is a large splitting of the 6*p* levels due to the SOC, in particular, at the Γ point the splitting is as large as 1.5 eV [5]. The 6*s* levels do not split, because the orbital momentum is zero ($L = 0$). Also there is a large splitting of the 5*d* semicore levels, as illustrated in Fig. 4.4(b). A similar observation of the splitting of the 5*d* levels due to the SOC has been observed in metallic Pb, in which the SOC effect is also very large [56]. Without the SOC, the details of the band structure near the Fermi level change dramatically [see Fig. 4.4(a)]:

(*i*) the highest valence band does not cross the Fermi level at the T point, and thus there is no hole pocket,

(*ii*) there is an artificial crossing of the bands at the Fermi level along the T - W direction, and thus the material becomes metallic,

(*iii*) the electron pockets at the L points are still present, even when the SOC is "switched off", though they are modified.

Unique electronic properties of bulk Bi are directly related to its crystalline *A*7 structure. Namely, the Peierls distortion lowers the conduction band at the L point, slightly causing a negative indirect band gap with the band maximum at the T point. Shick *et al.* [8] have studied from *ab initio* the effects of two structural distortions, yielding to the *A*7 structure (see Sec. 4.2.1), on the electronic structure of Bi. It has been shown that the increase of the internal displacement u along the [111] direction towards the value of 0.25, which corresponds to undistorted simple-cubic structure, causes the semimetal-to-metal transition; and the increase of the rhombohedral angle α towards the value of 60°,

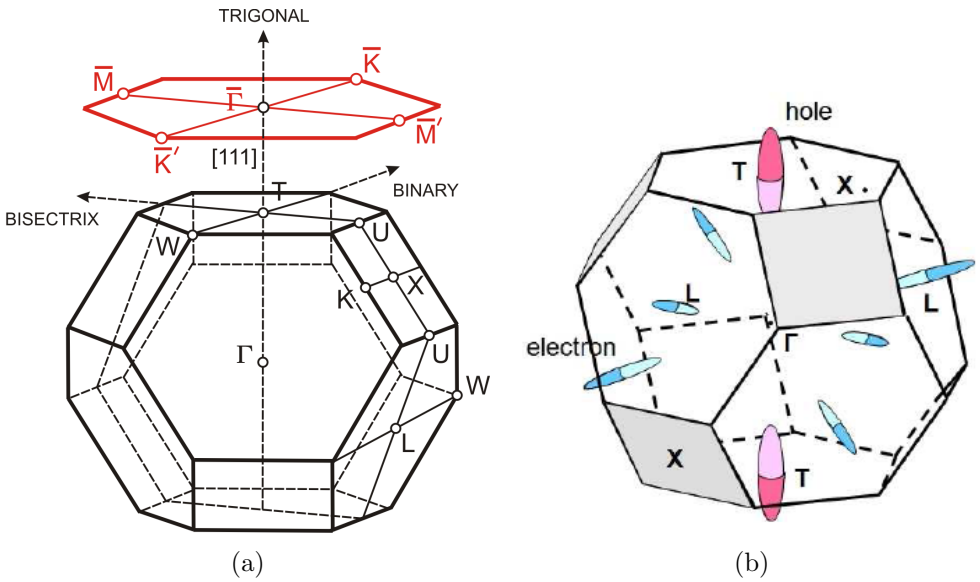

Figure 4.3: (a) Bulk (black) and surface (red) Brillouin zone with usual notation for symmetry points, Refs. [188, 7]. The principal crystallographic axes (trigonal, binary, and bisectrix) are indicated according to Ref. [193]. (b) Fermi surface of bulk Bi, which consists of hole pockets at the T points, and electron pockets at the L points. The pockets have been enlarged for clarity, in reality they are very small (volume of each ellipsoid is $\sim 10^{-5}$ the volume of the bulk BZ [4]). From Ref. [194].

which also corresponds to undistorted simple-cubic structure, causes the semimetal-to-semiconductor transition [8]. The latter can be used to induce a semiconducting behaviour of Bi films, and to control their thermoelectric properties [8].

The electronic band structure of Bi has been extensively studied over the past 70 years by different theoretical methods and in different experiments. Among theoretical methods I mention:

(*i*) The tight-binding calculations [195, 196, 191, 9].

(*ii*) The empirical pseudopotential calculations [10].

The above mentioned approaches rely on a fit with experimental data.

(*iii*) The studies based on DFT with pseudopotentials [186, 5], where the occupancy of valence states was fixed before including the spin-orbit coupling.

(*iv*) The *ab initio* all-electron DFT studies [8].

In particular, a big effort has been made to describe accurately the electron and hole pockets. Even though a considerable progress has been made, further attempts to improve the theoretical description of the subtleties in the band structure of Bi are desirable. In this thesis, I will present an *ab initio* study of the electronic structure of Bi. I will make a detailed comparison of the Kohn-Sham band structure obtained in this work with previous theoretical calculations and experiments in Sec. 5.1.3. Particular attention will be paid to the description of the electron and hole pockets.

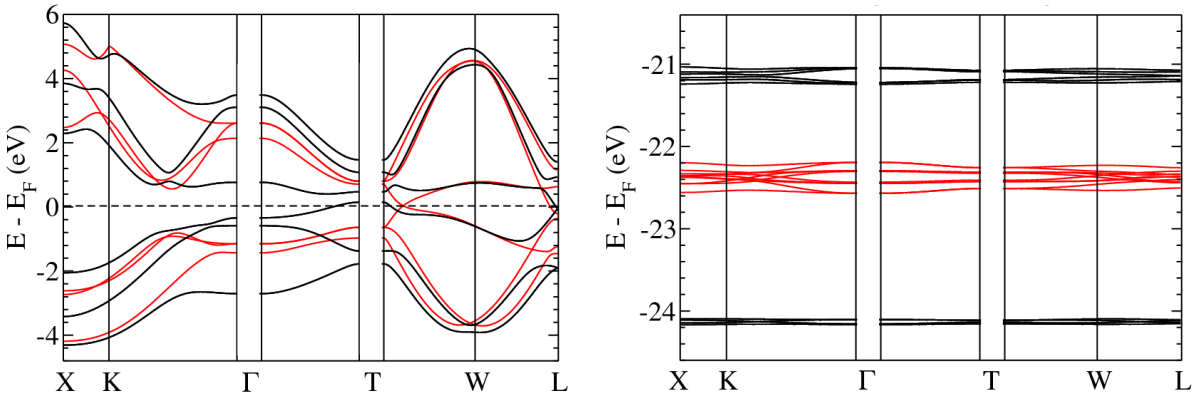

(a) (b)

Figure 4.4: Comparison of the Kohn-Sham band structure of Bi with SOC (black lines) and without SOC (red lines), obtained within DFT-GGA (see Sec. 5.1 for more details). (a) Splitting of the $6p$ levels. (b) Splitting of the $5d$ levels. Fermi level is at zero energy. (Unpublished)

4.2.3 Density of states

The electronic density of states (DOS) of bulk bismuth with and without the spin-orbit coupling is illustrated in Figs. 4.5(a) and 4.5(b). The first study of the SOC effect on the DOS has been made by Gonze *et al.* [5]. In Fig. 4.5(a) it can be seen that there are two structures at about -9.5 and -11 eV, which are due to $6s$ states. When the SOC is included, these two structures do not change, because there is no splitting of the $6s$ states. However, the DOS in the range from 0 to -4.5 eV changes drastically when the SOC is included, which is due to a splitting of the $6p$ states [5]. Thus, this is one of the direct consequences of the relativistic behavior of electrons. Above the Fermi level, *i.e.* for energy values larger than 0 eV, there is also a big change of the DOS when the SOC is included, for the same reason - splitting of the levels.

In this thesis, I am interested in the DOS near the Fermi level (see Sec. 6). Therefore, in Fig. 4.5(b) I present such a DOS. As can be seen, the SOC has a very large effect. Moreover, the DOS is very small at the Fermi level, which means that bismuth is not superconducting in the rhombohedral phase at zero pressure (see Appendix A.2). Such a small DOS at the Fermi level is due to the smallness of the volume spanned by the Fermi surface, which is formed by tiny electron and hole pockets [see Fig. 4.3(b)].

When the SOC is not included, Bi is metallic as there is an artificial crossing of bands at the Fermi level [see Fig. 4.4(a)]. The DOS without SOC is still small at the Fermi level, though larger than the DOS with SOC.

In the Appendix A.3 I present the *ab initio* calculation of the *restricted* DOS near the Fermi level. It will be needed in Sec. 6.1 for a study of free-carrier absorption in Bi.

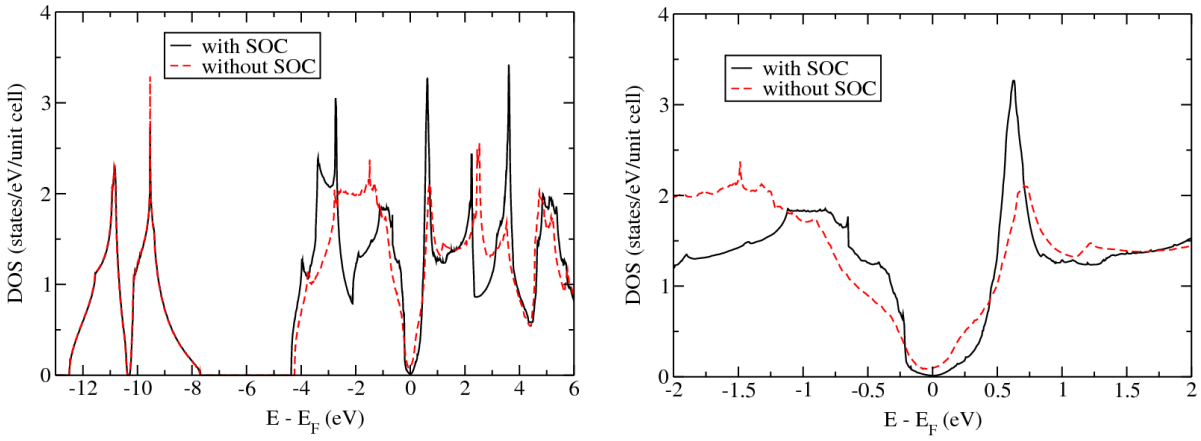

Figure 4.5: (a) Density of states (DOS) of bulk bismuth with and without spin-orbit coupling (SOC). (b) The same as (a) but near the Fermi level. The DOS was calculated within DFT-GGA, by using a tetrahedron method [197] and $30 \times 30 \times 30$ uniform $\mathbf{k}$ point mesh centered at the Γ point (see Sec. 5.1.1 for more details). The separate contributions from the electron and hole pockets is given in Figs. A.4(a) and A.4(b) in Appendix A.3. (Unpublished)

4.3 Bi(111) surface

Properties of surfaces can be very different from those of the corresponding bulk material [7]. The importance of surfaces increases for smaller structures, and this has considerable practical interest, in particular for nanotechnology. Bismuth is a striking example of the difference between bulk and surface material properties [7]. Namely, while the bulk is a semimetal the surface is a metal due to an existence of electronic surface states crossing the Fermi level [198]. This means that the surface carrier density is also much higher than the corresponding bulk value. Hence, Bi surfaces may probably be superconducting [177, 7].

In this section I will briefly talk about the Bi(111) surface. This discussion will be needed for the interpretation of the time- and angle-resolved photoemission experiments in Sec. 5.2. In this thesis I will not present the *ab initio* calculations on surfaces of bismuth (I will present the calculations only on the bulk Bi), therefore I will not discuss the surface geometric structure. The reader interested in this issue is referred to the review on Bi surfaces by Hofmann [7], which contains also a discussion about the Bi(110) and Bi(100) surfaces. Bi(111) is by far the most important Bi surface for practical applications. It is the natural cleavage plane of Bi crystals, and it is the preferred direction of epitaxial growth [7]. Moreover, Bi(111) is the only surface of Bi for which many angle-resolved photoemission spectroscopy studies have been performed.

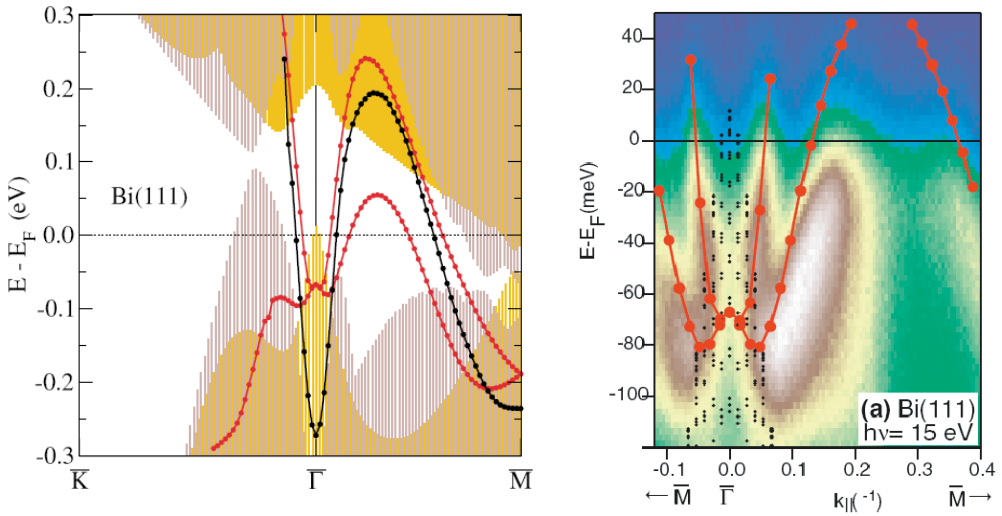

(a) (b)

Figure 4.6: (a) Surface states of Bi(111) surface calculated within *ab initio* one-step photoemission theory, without (black) and with (red) spin-orbit coupling. The shaded areas show the projection of bulk bands obtained without (violet) and with (yellow) spin-orbit coupling and their superposition. From Ref. [198]. (b) Calculated (from *ab initio*) and measured (in photoemission experiments) electronic structure near the $\overline{\Gamma}$ point of the surface Brillouin zone (see Fig. 4.3(a)). The small black dots are the projected bulk band structure, the red circles are the calculated surface state energies with spin-orbit coupling, the red line is a guide for the eye. The photoemission intensity is linearly scaled from dark blue (minimum) to white (maximum). From Ref. [198].

4.3.1 Large SOC-assisted splitting of Bi(111) surface states

In Sec. 4.2.2 we have seen that in bulk Bi there is a large splitting of energy levels due to the spin-orbit coupling (SOC). It turns out that the effect of SOC is also large at the surface. Figure 4.6(a) shows the electronic structure of Bi(111) surface, and the projected on this surface bulk band structure, calculated with and without SOC (from Ref. [198]). When the SOC is not included, there is a parabolic surface state which is located around $\overline{\Gamma}$. This surface state gives rise to a hexagonal electron-like Fermi surface element [198]. When the SOC is included, there is a large splitting of the surface state in all directions, and only at the $\overline{\Gamma}$ and $\overline{\mathrm{M}}$ points the degeneracy is left (there is no degeneracy at $\overline{\mathrm{K}}$). Around $\overline{\Gamma}$ this SOC-assisted surface state is degenerate with bulk states, and thus shows less clear surface character [198].

4.3.2 Bi(111) Fermi surface

The inclusion of the spin-orbit coupling leads to radical changes of the Bi(111) Fermi surface [see Fig. 4.6(a)]:

(i) the radius of the electron pocket Fermi surface is smaller by 30% compared to the

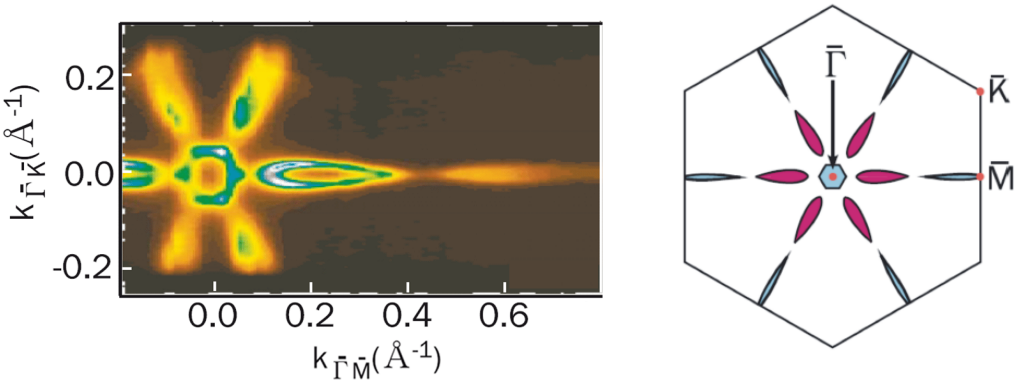

(a) (b)

Figure 4.7: (a) Intensity map at the Fermi level of Bi(111) surface. From Ref. [200]. (b) Schematic illustration of the Fermi surface of Bi(111) in the surface Brillouin zone [see Fig. 4.3(a)]. Electron pockets are colored in light blue and hole pockets in purple. From Ref. [200].

non-relativistic calculation [198],

(*ii*) in the $\overline{\Gamma}$ - $\overline{\mathrm{M}}$ symmetry directions, hole pockets are formed,[2]

(*iii*) the splitting of the surface states due to SOC is strongly anisotropic: it is ≈ 0.2 eV in the $\overline{\Gamma}$ - $\overline{\mathrm{M}}$ direction and even more along $\overline{\Gamma}$ - $\overline{\mathrm{K}}$,

(*iv*) the splitting of the surface states gives an explanation of the fact that Bi(111) is metallic.

The proof of the large splitting of the surface states due to SOC is obtained when the calculations are compared to the experimental findings, as shown in Fig. 4.6(b) (from Ref. [198]). There is a remarkable agreement between measurements in photoemission experiments with *ab initio* calculations only if the spin-orbit coupling is taken into account [198].

In angle-resolved photoemission experiments [199, 201, 200] it was observed that there are two features in the Bi(111) Fermi surface near the $\overline{\Gamma}$ point: an inner ring, which is actually a hexagon, and six narrow lobes in the $\overline{\Gamma}$ - $\overline{\mathrm{M}}$ directions, as shown in Figs. 4.7(a) and 4.7(b). The inner hexagon encloses occupied states and the lobes enclose empty states, as can be seen in Fig. 4.6(a). Therefore, these Fermi surface elements have been called the *electron pocket* and *hole pocket*, respectively [199]. Probing this electronic structure over a wider range of photon energies has shown that both the electron and hole pockets are surface states [7]. From Fig. 4.7(b) it can be seen that along the $\overline{\Gamma}$ - $\overline{\mathrm{M}}$ directions there are also cigar-shaped electron pockets. Their existence has been confirmed experimentally and theoretically [202, 200].

For rhombohedral systems, like bismuth, bulk features are expected to show a three-fold symmetry around the trigonal axis. However, the rotational symmetry of the ovals around the trigonal axis is six-fold, as can be seen in Figs. 4.7(a) and 4.7(b), indicating

[2]Interestingly, the hole pockets both in the bulk and on the surface are caused by SOC (see Sec. 4.2.2).

the two-dimensional nature [199, 201].

Finally, I would like to point out that due to the breakdown of the inversion symmetry at the surface, in contrast to the bulk, there is a large spin-polarization of the surface states. Very recently this fact has been confirmed by spin- and angle-resolved photoemission experiments and *ab initio* one-step photoemission calculations [203, 204, 205].

4.4 Phonons in bulk Bi

In Secs. 4.2.2 and 4.3 we have seen that the spin-orbit coupling (SOC) effect is very important for the description of the bulk and surface electronic states. In this section I will point out that the SOC has a large effect also on the phonon dispersion in bulk Bi. Also, I will discuss the A_{1g} coherent phonons and a mechanism of their generation. Discussions of this section will be needed for the interpretation of the time- and angle-resolved photoemission experiments in Sec. 5.2.

4.4.1 Phonon dispersion

Since in the $A7$ crystal structure there are two atoms in the primitive unit cell (see Sec. 4.2.1), there are six phonon branches, which are divided into three acoustic and three optical phonon branches [6, 206]. Along the Γ - T direction of the bulk Brillouin zone [see Fig. 4.3(a)], which coincides with the trigonal axis, the phonon dispersion curves can be classified as E_g or A_{1g}, according to whether their displacements are perpendicular or parallel to the trigonal axis, respectively. For the acoustic or optical A_{1g} phonon modes, the atoms move in the direction parallel to the trigonal axis. For the other two acoustic or optical E_g phonon modes, the atoms move in the perpendicular plane with respect to this axis. In the simple-cubic structure ($u = 0.25$) the A_{1g} and E_g phonon modes are degenerate, but the degeneracy is removed in the $A7$ structure due to the Peierls distortion (see Sec. 4.2.1).

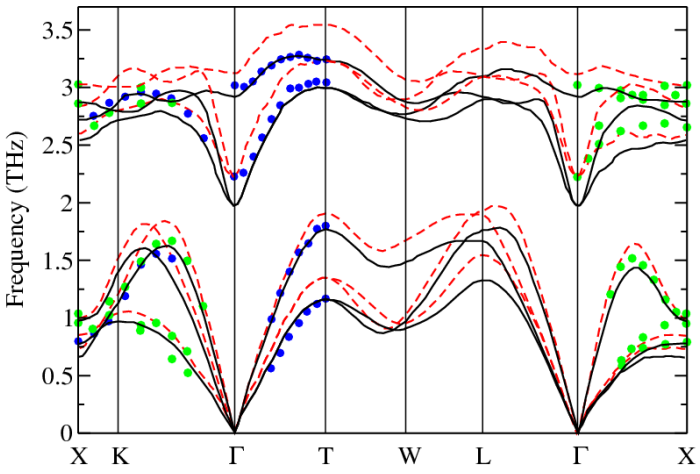

Figure 4.8: Phonon dispersion of Bi calculated from *ab initio* [6] with (solid black curves) and without (dashed red curves) spin-orbit coupling effect, and measured in experiments: blue dots from Ref. [207], and green dots from Ref. [208]. Reproduced after Ref. [6].

Figure 4.8 shows the comparison of the phonon dispersion of Bi calculated from *ab initio* [6] with and without spin-orbit coupling effect, and measured in experiments [207, 208]. It can be seen that the effect of SOC is very large. Without SOC the disagreement is on the order of 10 % for many phonon branches when compared to the experimental data [6]. However, the agreement is excellent when the SOC is included. The major effect due to the SOC is a *softening* of all of the phonon branches.

At the Γ point the optical phonons are split by the crystal symmetry. Usually the mode at zone center has the highest frequency since (for 2 atoms per primitive cell) one of the mode is a *breathing mode* in which the bonds are stretched. However, in bismuth the highest frequency phonon does not occur at Γ but instead along the Γ - T direction. The maximum overbending is 1.8 meV when SOC is included, 1.5 meV when SOC is not included, and 1.1 meV as determined from the experiment (see Fig. 4.8). The overbending is not peculiar to bismuth, it has been also observed in diamond. The maximum overbending in diamond is along the Γ - X direction, with the experimental value of 1.5 meV [211], and the theoretical value of 1.8 meV [209, 210]. The origin of the overbending is sufficiently large interatomic force constants between second-nearest neighbors [209, 210].

4.4.2 A_{1g} coherent phonons

In Sec. 4.2.1 I have shown that bismuth crystallizes in the $A7$ rhombohedral structure which is a Peierls distortion of the simple-cubic lattice. Hence, due to the distorted nature of the ground state, atomic positions are extremely sensitive to external perturbations [15, 212]. Because of the strong electron-phonon interaction in Bi, the lattice configuration is sensitive to the population distribution of electrons within the conduction bands [15]. This conjecture has been verified experimentally by suddenly changing the occupation number of the electrons via the absorption of a femtosecond laser pulse [213, 214, 14]. The photoexcitation of electrons changes the equilibrium positions of the atoms, and then these atoms oscillate coherently[3] with large amplitudes around their new quasi-equilibrium positions [see Fig. 4.9(a)], a mechanism known as the *displacive excitation of coherent phonons*[4] (DECP) [213]. In this kind of experiment, the fully-symmetric A_{1g} zone-center longitudinal-optical coherent phonon mode is generated [15]. According to the DECP theory, an excitation of the coherent phonon mode with only the A_{1g} symmetry is possible [213]. The A_{1g} is a "breathing mode" because it corresponds to the beating of the two atoms in the primitive unit cell against each other [see Fig. 4.1(a)]. The A_{1g} coherent phonon mode does not lower the symmetry of the lattice. The atomic separation is $2uc$ along the trigonal axis (see Sec. 4.2.1), thus u is the A_{1g} phonon coordinate [16].

Further insights into the understanding of the A_{1g} coherent phonon generation in Bi can be gained by considering the laser-induced evolution of the potential energy surface along the direction of the Peierls distortion. Such a potential energy surface has been mapped by time-resolved X-ray diffraction experiments for excitation carrier densities $n < 2\,\%$ [15], and calculated using a constrained density functional theory for densities

[3] *Coherent oscillation* means in-phase atomic oscillation.

[4] *Coherent states* are superpositions of states with different number of phonons [215].

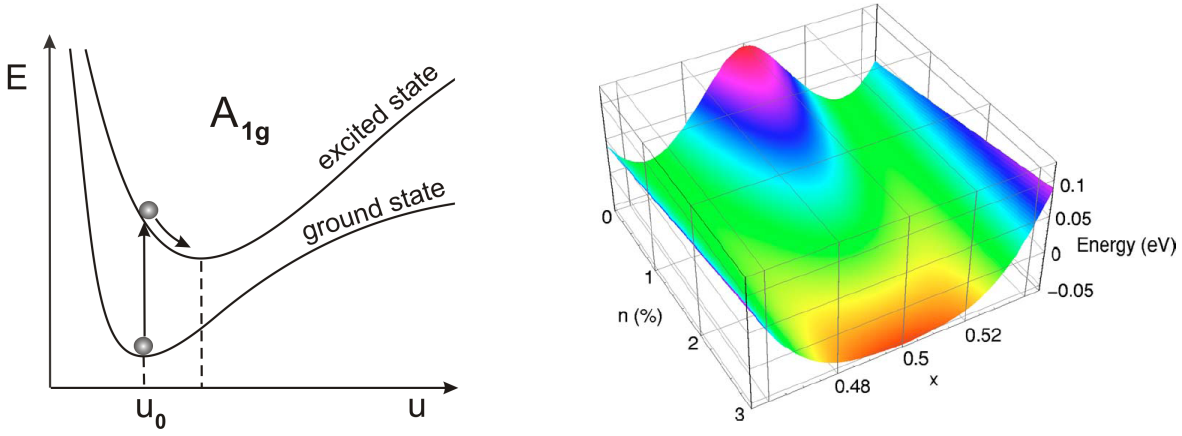

(a) (b)

Figure 4.9: (a) Schematic illustration of the displacive excitation of the A_{1g} phonon mode. The photoexcitation of electrons changes the potential energy surface of the lattice, and therefore atoms change their equilibrium positions from $u_0^{exp} \approx 0.234$ toward a hypothetical cubic phase with $u = 0.25$. (b) Potential energy surface (adjusted) in Bi. Here, $x = 2u$, where u is the A_{1g} phonon coordinate and the internal parameter describing the $A7$ rhombohedral structure [see Fig. 4.1(a)]. For each value of the photoexcited carrier density n, the energy for $x_0 = 2u_0 = 0.468$ (the ground-state equilibrium position) was subtracted for illustrative purposes. From Ref. [216].

$n \leq 3\,\%$ [216]. The calculated potential energy surface from Ref. [216] is shown in Fig. 4.9(b). In the absence of damping, oscillations at constant n occur along the [111] direction, *i.e.* along $x = 2u$, between locations where the adjusted energy is zero. At the excitation carrier density of $n \simeq 1\,\%$ there is a shift of the potential energy surface minima, and the Peierls barrier (central peak) decreases. The atoms are initially at the equilibrium position of the electronic ground state $x_0 = 2u_0$, and therefore experience a net force along the A_{1g} mode coordinate due to the increase of the potential energy gradient [216]. The overall result is the launching of atomic motions by the aforementioned displacive excitation mechanism. When the excitation level reaches the value of $n \simeq 2\,\%$, the Peierls barrier completely flattens. Therefore, as the excitation density increases, the equilibrium position shifts toward $x = 0.5$ ($u = 0.25$), which corresponds to the hypothetical cubic phase, with an accompanying loss of the Peierls distortion. However, in reality, material displays a non-thermal melting before the symmetric phase can be attained [217].

Experimentally, the A_{1g} coherent vibrational mode has been observed indirectly by measuring time-dependent optical reflectivity [218, 214, 14, 216], and directly by time-resolved X-ray diffraction measurements [212, 15]. Theoretically, the A_{1g} atomic motion following the photoexcitation of bismuth has been studied in Refs. [16, 194] by using a thermodynamic model based on the two-temperature approach and density-functional theory, and in Refs. [216, 219] by performing *ab initio* density-functional theory calculations.

Lastly, the observations in photoexcited bismuth have revealed that the vibrational

frequency of the A_{1g} mode is not constant: it red-shifts from the equilibrium value of 2.92 THz to 2.45 THz at the fluence of 7.6 mJ/cm^2 under high-intensity excitations [14], indicating a softening of the phonon mode. After the initial softening, the oscillation frequency blue-shifts back toward the equilibrium value as the oscillation amplitude and carrier density decay [14, 216]. The mechanism responsible for this time-dependent vibrational frequency shift has been controversial. Hase and coworkers concluded that the shift is due to an amplitude-dependent frequency caused by anharmonicity of the interatomic potential [14]. Fahy and Reis suggested an alternative explanation based on the *electronic softening*[5] of the potential and the subsequent dynamics of photoexcited carriers [220]. Optical coherent control experiments and constrained density functional theory calculations demonstrated that the observed phonon frequency variation is dominated by electronic effects, and that the anharmonicity in the interatomic potential plays a negligible role [216].

In Sec. 5.2 I will present an interpretation of the time- and angle-resolved photoemission experiment on Bi, in which an A_{1g} coherent phonon mode was generated.

4.5 EELS and optical constants of bulk Bi

In this section I will highlight briefly what is known in the literature about the electron energy-loss (EEL) spectrum of bismuth.

The EEL spectrum of bulk Bi was studied experimentally about half a century ago by several authors [221, 222, 223, 224, 225, 226, 227]. Only over the last decade, when the technical and scientific development of the EEL spectroscopy (EELS) instrumentation became rapid, EELS experiments were carried out on Bi nanoparticles [228, 229, 230], Bi nanowires [231, 232], and Bi nanorods [233]. However, until today, there have been no *ab initio* studies of the EEL spectra of bulk Bi nor of Bi nanostructures, because this material is challenging from the computational point of view. In this thesis I will deal with the EELS of bulk Bi, and thus in this section I will present old experimental data on bulk Bi. In Sec. 7.3 I will present the first *ab initio* calculations of the EEL spectra of bulk Bi, by using the newly developed method of this thesis.

Figure 4.10(a) shows Wehenkel and Gauthe's experimental electron energy-loss spectrum at vanishing momentum transfer ($\mathbf{q} \to 0$) of Bi films with 230 Å thickness [227]. As can be seen, there are several contributions to the spectrum. The main contribution comes from the volume loss, which contains a main plasmon peak at 14 eV, a shoulder at $E < 10$ eV, two peaks between 20 and 30 eV, and a faint broad structure between 40 and 100 eV. The total experimental spectrum also contains a contribution due to the electron energy-loss at the surface, which displays a rather sharp peak at about 11 eV, and is also partially responsible for the slope change observed near 5 eV. The main peak of the surface loss spectrum cannot be seen on the experimental spectrum in Fig. 4.10(a) because of the superposition of a predominant volume contribution. However, in other experiments the surface plasmon peak was resolved, at around 10 eV [221, 226]. And,

[5] *Electronic softening* is the effect which consists in a weakening of the interatomic restoring forces due to excitation of electrons from valence bands to conduction bands.

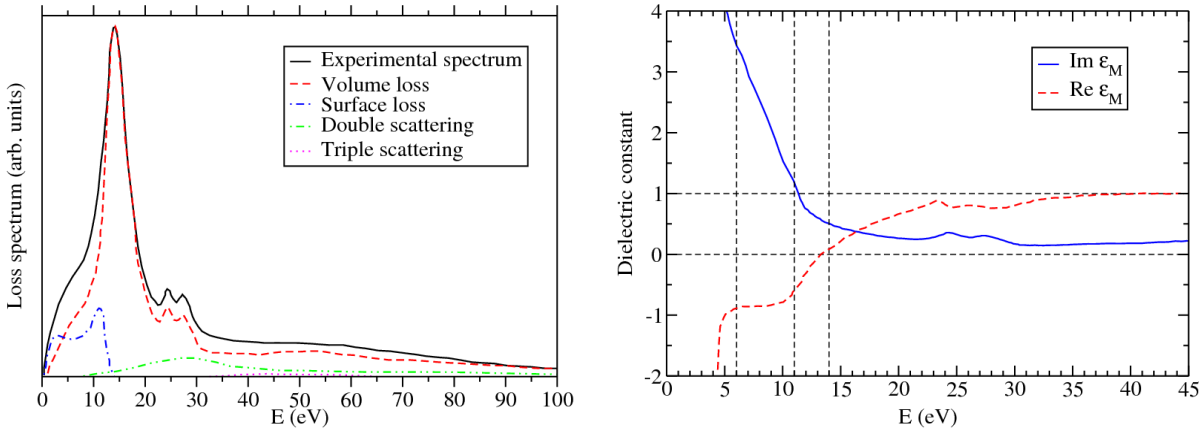

(a) (b)

Figure 4.10: (a) Experimental electron energy-loss spectrum at vanishing momentum transfer ($\mathbf{q} \to 0$) of 230 Å thick Bi films. Reproduced after Ref. [227]. (b) Real and imaginary parts of the macroscopic dielectric constant, obtained from the loss spectrum by applying Kramers-Kronig transformation. Reproduced after Ref. [227].

finally, in the total experimental spectrum there are contributions due to the double and triple scattering, which are present because the Bi film, used in the experiments, was rather thick [227].

Let us consider in more detail the volume loss spectrum. In order to interpret the features in the loss spectrum, let us consider the real and imaginary parts of the macroscopic dielectric constant, which are depicted in Fig. 4.10(b). They can be obtained from the knowledge of the loss function, $-\mathrm{Im}[1/\epsilon_\mathrm{M}]$, by applying Kramers-Kronig transformation, which was done by Wehenkel and Gauthe [227]. Figure 4.10(b) shows that the volume plasmon condition, $\mathrm{Re}[\epsilon_\mathrm{M}] = 0$, is satisfied at $E = \hbar\omega_p = 13.95$ eV, and the corresponding $\mathrm{Im}[\epsilon_\mathrm{M}]$ is 0.5. Thus, the classical resonance condition, $\mathrm{Re}[\epsilon_\mathrm{M}] = \mathrm{Im}[\epsilon_\mathrm{M}] = 0$, is not strictly satisfied [227].[6] Further, the two peaks observed in the volume loss spectrum at 24.45 and 27.3 eV [227], are also present in the absorption spectrum, *i.e.* in $\mathrm{Im}[\epsilon_\mathrm{M}]$. Moreover, Hunter *et al.* [234] have found minima in the transmittance of Bi films at photon energies of 24.6 and 27.6 eV. Therefore, these two peaks were attributed to excitations of electrons from O_4 and O_5 subshells,[7] *i.e.* from the $5d$ levels [236, 223, 227] [see Fig. 4.2.2]. Finally, the broad feature in the volume loss function with a maximum at about 50 eV [see Fig. 4.10(a)] was also observed in the optical absorption coefficient [227], and was reported in the optical work by Hunter *et al.* [234]. This faint structure corresponds to the excitations from the $5d$ levels to higher conduction bands,[8] as was also confirmed

[6] Wehenkel and Gauthe reported [227] that the surface plasmon condition, $\mathrm{Re}[\epsilon_\mathrm{M}] = -1$, is fulfilled at 6 eV. However, $\mathrm{Im}[\epsilon_\mathrm{M}] = 3.5$ at 6 eV, which is too large. Thus the main surface plasmon occurs at 11 eV, where $\mathrm{Re}[\epsilon_\mathrm{M}] = -0.75$ and $\mathrm{Im}[\epsilon_\mathrm{M}] = 1.15$ [227].

[7] The photoemission data on Bi indicates that the binding energy values of the O_4 and O_5 subshells relative to the Fermi level, which is taken to be zero, are 26.5 ± 0.5 and 24.4 ± 0.6 eV, respectively [235].

[8] The next atomic levels, which lie below the $5d$ levels, are $5p$ levels (O_3 subshell) with a binding energy

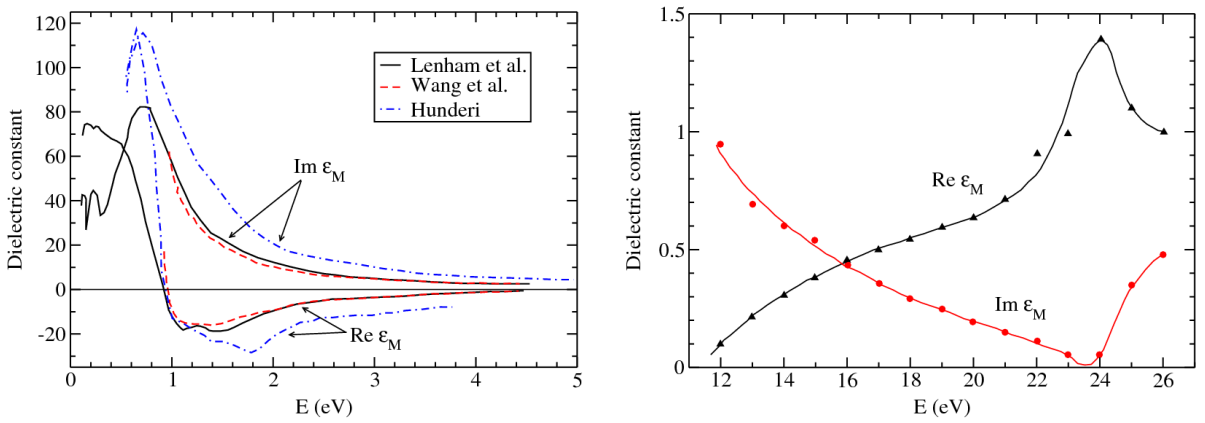

Figure 4.11: Real and imaginary parts of the macroscopic dielectric constant, measured by (a) Lenham *et al.* Ref. [239], Wang *et al.* Ref. [240], Hunderi Ref. [241], and (b) Toots and Marton, Ref. [242].

by the theoretical calculations of the $5d$ subshell photoionization cross-section maximum [237].

I would like to point out that there are two other peaks in the volume loss spectrum, at $\sim$ 5.5 and 29 eV, which are not present in Fig. 4.10(a), but were observed in other experimental works. The first peak was reported in Refs. [222, 225, 226, 224], and it is seen as a shoulder at about 5 eV in Fig. 4.10(a). Moreover, the measurements of Cardona and Greenaway show an optical absorption peak at 5.3 eV, which corresponds to the zero optical transmittance [238]. Therefore, this peak can be attributed to $6p \rightarrow 6p$ interband transitions (from occupied to empty levels) [see Fig. 4.4(a)]. The second peak of 29 eV was reported in Refs. [221, 226, 225], but the origin of this peak has not been revealed. Notice, in Ref. [227] the authors have pointed out that Bi_2O_3 has a pronounced loss peak at exactly 29 eV.

Lastly, I discuss the experimental data on optical dielectric constants in bismuth, which were determined without relying on the knowledge of the loss function nor using the Kramers-Kronig transformation. The available experimental data is depicted in Figs. 4.11(a) and 4.11(b). In Fig. 4.11(a) it is seen that there is an absorption peak at about 0.7 eV, though the real part of the dielectric constant is zero only at 0.9 eV. The energy range which is covered in Fig. 4.11(a) cannot help us to interpret any feature in the loss function in Fig. 4.10(a). In Fig. 4.11(b) one can see that there is a rise in $\mathrm{Im}[\epsilon_\mathrm{M}]$ between 24 and 26 eV, which corresponds to aforementioned excitations from the $5d$ levels. Notice, the data of Toots *et al.* [242] shows that $\mathrm{Re}[\epsilon_\mathrm{M}] = 0.3$ and $\mathrm{Im}[\epsilon_\mathrm{M}] = 0.6$ at 14 eV, where the volume plasmon peak was observed. Unfortunately, there is no experimental data on the dielectric constant in the energy range $5 < E < 12$ eV, where there are features in the loss function: a peak at $\sim$ 5.5 eV due to interband transitions, and a

of 92.8 $\pm$ 0.6 eV [235]. Therefore, the broad feature in the volume loss spectrum at about 50 eV cannot be attributed to the excitations from the $5p$ levels.

surface plasmon peak at ~ 11 eV.

Ab initio calculations of EEL spectra of Bi are desirable for the confirmation of origin of peaks in the loss function, and to give new insights in the understanding of unrevealed features in the spectrum. I will address this question in Sec. 7, by performing first *ab initio* calculations of EEL spectra of bulk Bi, by using a new theoretical approach developed in this thesis in Sec. 7.1.

4.6 Summary & Outlook

In this chapter, I have given a description of the semimetal bismuth and its various properties, and I have described problems which I will tackle in the second part of this manuscript.

Bulk Bi crystallizes in the $A7$ rhombohedral structure, which is a Peierls distortion of the simple cubic lattice. This leads to unique electronic properties, namely, there is a weak overlap between the lowest conduction band at the L point and the highest valence band at the T point. The effect of the spin-orbit coupling (SOC) is extremely large, and it leads to large splitting of bulk electronic states. The SOC is responsible for the semimetallic character of bulk Bi. The Fermi surface, which consists of the hole pocket at the T point and three electron pockets at equivalent L points, is exceedingly small. Owing to this fact, the density of electronic states at the Fermi level is also very small, which prevents an occurrence of superconductivity in bulk Bi. In Sec. 5.1 I will present an *ab initio* study of the crystal and electronic structure of bulk Bi. I will pay particular attention to the description of electron and hole pockets, and make a comparison with previous theoretical and experimental studies. In Sec. 6.1 I will investigate free-carrier absorption in bulk Bi on the basis of the Kohn-Sham band structure, which will be needed for an interpretation of the time-resolved terahertz experiment on Bi in Sec. 6.2.

In contrast to the bulk, the surface of Bi is metallic. The effect of the SOC on the surface states is huge, as it is in the bulk. There is a large splitting of the surface states due to the SOC, which results in the Fermi surface which consists of the electron pocket at the $\overline{\Gamma}$ point, six cigar-shaped hole pockets and six cigar-shaped electron pockets located along the $\overline{\Gamma}$ - $\overline{\mathrm{M}}$ and $\overline{\Gamma}$ - $\overline{\mathrm{M}}'$ directions, which are connected by 60° rotation. In Sec. 5.2 I will interpret the time- and angle-resolved photoemission experiment on Bi(111) surface, where the surface states, surface resonances and bulk states are observed. Knowledge of the difference between bulk and surface states, like their symmetry and polarization, will be essential for the interpretation of the experiment.

I have also discussed the phonons in bulk Bi. The SOC is equally important for the correct description of the phonon dispersion, much like it is important for the correct description of the above mentioned bulk and surface electronic states. Due to the distorted nature of the ground state, Bi is extremely sensitive to external perturbations. For example, a photoexcitation of electrons gives rise to appearance of A_{1g} coherent phonons with a very large amplitude of oscillation. In Sec. 5.2 I will address the time- and angle-resolved photoemission experiment on Bi(111) surface, in the sense of a birth of A_{1g} coherent phonons and their coupling to electronic states.

Finally, I have discussed the electron energy-loss (EEL) spectrum and optical dielectric

properties of bulk Bi. I have presented the available experimental data, and the interpretation of different features in the spectrum. I have pointed out that until today there have been no *ab initio* studies of EEL spectra of Bi, and that such a study would be desirable. In Chapter 7 I will address this question by using a new efficient *ab initio* approach to EELS within the time-dependent density functional perturbation theory, which will be described in Sec. 7.1. In particular, this new approach will allow us to examine the effect of the SOC on EEL spectra, the plasmon dispersion, and the anisotropy of EEL spectra.

Part II

Developments, applications & results

Chapter 5

Ab initio description of Bi at equilibrium and in the photoexcited state

In this chapter I will present an *ab initio* DFT study of bulk bismuth within the LDA and GGA including the spin-orbit coupling. This chapter is divided into two parts.

In the first part, Sec. 5.1, I will study Bi at equilibrium. I will compare the theoretical equilibrium lattice parameters of Bi within the LDA and GGA, between themselves and with the experimental ones. Particular attention will be given to the study of the influence of the spin-orbit coupling on the lattice parameters. I will also present a detailed comparison of the Kohn-Sham band structure of Bi within the LDA and GGA including the spin-orbit coupling with anterior theoretical and experimental studies. Special attention will be given to the description of the electron and hole pockets at the Fermi level.

In the second part, Sec. 5.2, I will study Bi in the photoexcited state by using the ground-state DFT. Strictly speaking, the ground-state theory should not be applied to a study of the system in the excited state (see Chapter 3). However, my analysis will be based on the valence Kohn-Sham energy levels near the Fermi level, which are in remarkable agreement with the experimental electronic structure of Bi, according to Sec. 5.1, and thus the method is justified. I will present an interpretation of the time- and angle-resolved photoemission experiment on Bi(111) surface.

5.1 Structural and electronic properties

In this section I will present a detailed analysis of the theoretical equilibrium lattice parameters and Kohn-Sham band structure of bulk Bi. Special attention will be given to the discussion the effect of the spin-orbit coupling (SOC). The SOC has been included in the *ab initio* DFT calculations, because it is crucial for the comparison of the Kohn-Sham band structure with the experimental data. Although the electronic band structure of Bi has been extensively studied during the last 70 years, both experimentally and theoretically, until today there has been no comparison of the local density approximation (LDA) and generalized gradient approximation (GGA) in Bi. Therefore, I will present such a study, also by making a comparison with anterior DFT and tight-binding calculations, and various experiments such as Shubnikov-de Haas, de Haas-van Alphen, photoemission.

In Sec. 5.1.1 I will present the computational details of the DFT studies. In Sec. 5.1.2 I will make a comparison of the theoretical equilibrium lattice parameters of Bi, within the LDA and GGA, with and without spin-orbit coupling, as obtained in this work and other theoretical and experimental studies. Finally, in Sec. 5.1.3 I will make a detailed analysis of the Kohn-Sham band structure of Bi. Particular attention will be given to the description of the electron and hole pockets, and the effect of the spin-orbit coupling.

5.1.1 Computational method

I have performed *ab initio* DFT calculations with the `QUANTUM ESPRESSO` package [68], by solving self-consistently the Kohn-Sham equations, as described in Sec. 2.1.2. The total energy has been calculated by finding its convergence towards an absolute minimum. I have used the Broyden-Fletcher-Goldfarb-Shanno quasi-Newton algorithm and damped (Verlet) dynamics for structural relaxation [243], which allowed me to obtain theoretical equilibrium lattice parameters within the LDA and GGA (see Sec. 5.1.2). The calculations have been performed by using the norm-conserving pseudopotentials described in Appendix A.1, including the $5d$ semicore levels in the valence region.

The calculations have been converged with respect to all of the parameters. The Kohn-Sham wavefunctions were expanded in plane waves (see Sec. 2.3.1) up to a kinetic-energy cutoff of 150 Ry, which corresponds to about 14 700 plane waves. The use of such a high kinetic-energy cutoff is needed due to the inclusion of the $5d$ semicore states in the valence region. These semicore states are more localized than the valence states, and thus more plane waves are needed for their description. I have used the Methfessel-Paxton smearing method [244] with a broadening parameter of 0.02 Ry.

Special attention has been paid to the $\mathbf{k}$ points sampling of the Brillouin zone (BZ), which is important for the description of the electron and hole pockets (see Sec. 4.2.2). I have used a uniform $20 \times 20 \times 20$ $\mathbf{k}$ points mesh centered at the Γ point, which yields 781 $\mathbf{k}$ points in the irreducible BZ. Special care has been given to the convergence of the Fermi energy E_F: it has been obtained independently by a calculation with the improved tetrahedron method of Ref. [197], using a $50 \times 50 \times 50$ uniform $\mathbf{k}$ point mesh centered at the Γ point, yielding 11076 $\mathbf{k}$ points in the irreducible BZ. Afterwards, the $5d$ energy

levels have been aligned in the two calculations. A precision of ± 5 meV on the Fermi energy was reached.

In the calculations, the spin-orbit coupling has been included self-consistently, as described in Sec. 2.2.2. The convergence parameters were the same in both calculations, with and without SOC, and they have been described above. The calculations with SOC were twice as long as those without SOC, due to the use of two-component spinors while solving Pauli-type Kohn-Sham equations (see Sec. 2.2.2), instead of one-component Kohn-Sham wavefunctions. This doubles the number of plane waves. In Sec. 5.1.2 I will present theoretical lattice parameters optimized both with and without SOC, in order to figure out the effect of SOC. In Sec. 5.1.3 I will present the Kohn-Sham band structure including SOC, since the SOC is crucial for the comparison with experiments [see also Fig. 4.4(a)].

5.1.2 Lattice parameters

Most of the *ab initio* calculations of Bi have been performed within the LDA at experimental lattice parameters (see, *e.g.*, Refs. [5, 8, 16]), and there is only one study in which theoretical equilibrium lattice parameters within the LDA have been used [6]. No calculations within the GGA have been performed so far (except our own publication, Ref. [245]). In the following, I will present a detailed analysis of the theoretical equilibrium lattice parameters (ELP) of Bi, within the LDA and GGA. Special attention will be given to the effect of the spin-orbit coupling, and the effect of the inclusion of the $5d$ semicore levels in the valence region. I will also make a comparison with findings on the metallic Pb ($Z = 82$) and metallic Tl ($Z = 81$), in which the SOC is also large as in the semimetallic Bi ($Z = 83$).

The theoretical lattice parameters of Bi have been determined in Refs. [6, 194], within the LDA, with and without SOC (see Table 5.1). However, in both references the authors used the same pseudopotential, namely Hartwigsen-Goedecker-Hutter type [246], which does not include the $5d$ semicore levels in the valence region. Transferability tests of my pseudopotentials (PP) described in Appendix A.1 have shown that the inclusion of the $5d$ semicore levels in the valence region is necessary. A similar conclusion was reached for Pb [247, 248, 249], namely, although $5d$ semicore levels are low in energy, their inclusion in the valence region significantly changes the lattice parameter, by $\sim 1\%$ within the LDA,[1] and leads to better agreement with the experimental lattice parameter. Therefore, given the fact that the PPs of this work are different from those of Refs. [6, 194], and the lack of reliability to the PPs of Refs. [6, 194] when maintaining the $5d$ levels in the core region, I will not make a direct comparison of the theoretical equilibrium lattice parameters obtained in this thesis with those of Refs. [6, 194].

Table 5.1 shows the comparison of the theoretical equilibrium lattice parameters of Bi, as obtained in this work within the LDA and GGA, with and without spin-orbit coupling, including the $5d$ semicore electrons in the valence region, with the experimental lattice parameters [189]. Let us discuss first the lattice parameter a_0, which is the length of the edge of the rhombohedral unit cell (see Sec. 4.2.1), and afterwards the volume V of the

[1] The spin-orbit coupling has been found to make a negligible effect on the lattice parameters in Pb, namely 0.1% within the LDA [248, 249, 250].

primitive unit cell.

Within the LDA, a_0 is underestimated with respect to the experimental value by 1.6% (without SOC) and 0.5% (with SOC). Thus, the SOC has a large effect, it changes the lattice parameter a_0 by 1.1%. In fact, the same effect of the SOC in Bi has been also found in Refs. [6, 194], even when the $5d$ levels were maintained in the core region. In contrast, in Pb the SOC has a negligible effect, 0.1% [248, 249, 250], but in Tl the effect is bigger, 0.7% [250]. The reason for such a difference between Bi on one hand, and Pb and Tl on the hand, is the following. In Bi there are much more electronic occupied bands ($6p$ valence bands) which are drastically affected by the SOC [see Fig. 4.4(a)], whereas in Pb and Tl the SOC leads to much smaller changes in the dispersion of the occupied bands with respect to Bi [56, 250, 248], as most of the $6p$ states in Pb and Tl are above the Fermi level. Hence, since the electronic distribution has an influence on the equilibration of the atomic positions, especially in Bi which is extremely sensitive to it, the SOC leads to big changes in the lattice parameter a_0 in Bi.

In contrast, within the GGA, the parameter a_0 is overestimated by 3.8% (without SOC) and 4.2% (with SOC), which is slightly higher than what is expected from the GGA [24]. I ascribe such unusual behaviour of the GGA to the inclusion of the $5d$ semicore states in the valence region (see Appendix A.1). Within the GGA, the SOC leads to smaller changes in a_0, 0.4%, compared to the LDA. Another difference between LDA and GGA is that, when including the SOC, a_0 becomes closer to the experimental value within the LDA, whereas it becomes farther from the experimental value within the GGA.

As for the volume of a primitive unit cell, when the SOC is not included, the LDA volume is underestimated by 3.9%, whereas when the SOC is included, the LDA volume is overestimated by 0.02%. Such unusual behaviour of the LDA when the SOC is included, is probably due to the inclusion of the $5d$ levels in the valence region. The combination of these two effects ($5d$ + SOC) yields to such unexpected behaviour of the LDA. I did not check this conjecture explicitly, because without the $5d$ semicore levels in the valence region, the pseudopotential is not transferable enough, and thus not justifiable for the utilization, and not expected to give reliable results. In contrast, the GGA volume is overestimated both with and without the inclusion of the SOC. Namely, it is overestimated by 8.2% (without SOC) and 10.4% (with SOC), which is a lot, and which is not expected from the GGA. This is again ascribed to the inclusion of the $5d$ levels in the valence region. Thus, the SOC changes the volume of the primitive unit cell by $\sim 4\,\%$ within LDA, and $\sim 2\,\%$ within GGA.

As has been pointed out in Sec. 2.1.2(d), the bond length within the LDA is expected to be underestimated, and within the GGA, overestimated. In Table 5.1 I report the bond length in Bi. As can be seen, the bond length within the LDA without SOC is indeed underestimated by 0.3%, though it is overestimated by 0.9% when the SOC is included. The latter is not expected from the LDA, and is attributed to the inclusion of the $5d$ levels in the valence region. Within the GGA, the bond length is indeed overestimated, however, more than what is usually expected. Namely, the bong length is overestimated by 7.9% (without SOC) and 8.3% (with SOC). I ascribe such an unusual behaviour of the GGA again to the $5d$ levels.

	Expt.[a]	This work				Other works			
		LDA		GGA		Ref.[b] (LDA)		Ref.[c] (LDA)	
		no SOC	with SOC	no SOC	with SOC	no SOC	with SOC	no SOC	with SOC
a_0 (a.u.)	8.9263	8.7825	8.8800	9.2690	9.3025	8.7938	8.8719	8.7920	8.8711
$\Delta a_0/a_0^{exp}$ (%)	-	−1.6	−0.5	3.8	4.2	−1.5	−0.6	−1.5	−0.6
α (deg)	57.35	57.72	58.00	56.01	56.36	57.48	57.58	57.48	57.57
u	0.23407	0.23617	0.23559	0.23279	0.23197	0.23553	0.23408	0.23554	0.23410
V (a.u.)^3	472.25	453.96	472.36	511.09	521.28	452.99	466.31	452.70	466.07
$\Delta V/V^{exp}$ (%)	-	−3.9	0.02	8.2	10.4	−4.1	−1.3	−4.1	−1.3
a_{NN} (a.u.)	5.7871	5.7714	5.8370	6.2432	6.2703	5.7421	5.7652	5.7416	5.7646
$a_{\mathrm{NN}}/a_{\mathrm{NN}}^{exp}$ (%)	-	−0.3	0.9	7.9	8.3	−0.8	−0.4	−0.8	−0.4

[a] Experimental data from Ref. [189], obtained at $T = 4.2$ K.

[b] Theoretical data from Ref. [194].

[c] Theoretical data from Ref. [6].

Table 5.1: Comparison of the crystallographic parameters of the rhombohedral unit cell of Bi, as obtained in this work from *ab initio* DFT calculations within the LDA and GGA, with and without spin-orbit coupling (SOC), and measured in experiments [189]. The last four columns represent the DFT results of Refs. [6, 194]. Here, a_0 is the length of the edge of the rhombohedral unit cell, α is the rhombohedral angle, u is the internal parameter of the unit cell, $V = a_0^3\sqrt{2\cos^3\alpha - 3\cos^2\alpha + 1}$ is the volume of the primitive unit cell, and a_{NN} is the nearest-neighbour (NN) distance (or bond length). See Sec. 4.2 for more details about the crystallographic structure of Bi. In this work the $5d$ electrons have been included in the valence region in order to make the pseudopotentials transferable (see Appendix A.1), whereas in Refs. [6, 194] they were maintained in the core region. Therefore, due to the assumption of the lack of the transferability of the pseudopotentials of Refs. [6, 194], I will not make a direct comparison of the lattice parameters obtained in this work with those of Refs. [6, 194]. (Unpublished)

In the next section, I will show that both the LDA and GGA give a rather accurate description of the electronic band structure of bulk Bi, in particular the electron and hole pockets are described fairly good. Moreover, although the GGA lattice parameters and the GGA volume quite largely deviate from the experimental values, the calculations of the Kohn-Sham band structure within the GGA provide a slightly better agreement with experiment rather than the calculations within the LDA. In the rest of the second part of the thesis, most of the results will be presented both within the LDA and GGA. Both approximations describe the same physics, and thus they should give qualitatively similar results. Hence, in the following chapters I will make systematic comparisons between these two approximations.

5.1.3 Electronic structure within LDA & GGA

Figure 5.1(a) shows the Kohn-Sham band structure obtained within the GGA at the GGA equilibrium lattice parameters including the SOC, along some high-symmetry directions in the Brillouin zone. The symmetry of bands at the high symmetry points X, Γ, T and L are indicated, in agreement with Ref. [9]. The subtleties of the band structure around the Fermi level, *i.e.* the electron and hole pockets, are shown in Fig. 5.1(b). I reproduce the hole pocket at the T point and the electron pocket at the L point, in agreement with previous DFT calculations [5, 8] and with various experiments (see Table 5.2).

In anterior DFT studies of the band structure of Bi, a lot of effort has been made in order to describe the electron and hole pockets. For example, Gonze *et al.* [5] have performed DFT calculations including the SOC by treating the charge density of Bi as of a semiconductor, and by adding to it the experimental number of electrons at the L point and of holes at the T point. The charge density was treated non-self-consistently, since there was an adjustment to the experimental data. Hence, these calculations cannot be considered as fully *ab initio*. Another DFT calculation has been performed by Shick *et al.* [8], who used the relativistic version of the full-potential linear muffin-tin orbital-plane wave method [71]. In contrast, Liu and Allen [9] have developed a third-neighbor tight-binding model including the spin-orbit coupling. The parameters of their model were fitted to the experimental data, and thus their model describes the electron and hole pockets much better, than the two aforementioned DFT studies.

A detailed comparison of the *ab initio* DFT study of Bi including SOC performed in this thesis with other theoretical and experimental studies is summarized in Tables 5.2 and 5.3. I present the DFT calculations within two approximations, LDA and GGA, in order to compare the quality of their description of the band structure of Bi. The effect of the spin-orbit coupling on energy bands is so big (see Sec. 4.2.2), that it was necessary to include SOC in the calculations for the comparison with the experimental data. The LDA and GGA calculations have been performed at their respective equilibrium lattice parameters (see Table 5.1). I would also like to point out that in the anterior DFT studies [5, 8], the authors used the LDA at the experimental lattice parameters. Moreover, up to today, there have been no studies of Bi within the GGA, since it severely overestimates the lattice parameters with respect to the experimental ones (see Table 5.1). Thus, since the details of the electronic band structure depend strongly on the lattice parameters,

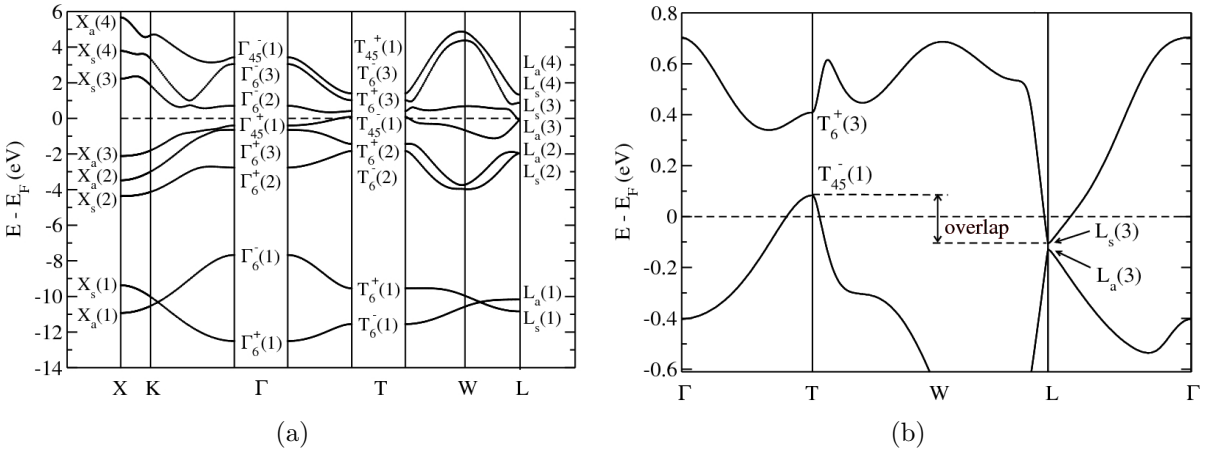

(a) (b)

Figure 5.1: (a) Kohn-Sham band structure of Bi including the spin-orbit coupling, calculated within the GGA at the GGA equilibrium lattice parameters. Symmetry of bands are indicated according to Ref. [9]. From Ref. [245]. (b) Zoom on the band structure near the Fermi level. The hole pocket at the T point, and the electron pocket at the L point are reproduced. The Fermi level is taken to be equal to zero. (Unpublished)

the GGA has never been used. However, in the following I will show, on the basis of Table 5.2, that the GGA provides a very good description of the band structure, in some cases describing some energy levels or their differences even better than the LDA.

One may wonder if we can describe tiny electron and hole pockets in Bi by DFT? What is the accuracy of DFT calculations? The accuracy of DFT calculations is limited by the exchange-correlation and pseudopotential approximations, and is ~ 0.03 eV within the LDA or greater [251], while the electron and hole pockets in Bi are of the order of ~ 0.01 eV. Therefore, their description within the DFT can be made only with a precision not better than 0.03 eV. Nevertheless, we will see in the following, that the DFT can still give a fairly good description of the electron and hole pockets despite the relatively large error bar of the *ab initio* calculations.

Band Energy	Theory (this work)				Theory (previous works)			Expt.[d]
	Theor. ELP		Expt. LP		Ref.[a]	Ref.[b]	Ref.[c]	
	LDA	GGA	LDA	GGA				
$L_s(3)$	-0.0148	-0.0959	-0.0139	-0.0161	-0.068	-0.018	-0.0267	-0.0266[e], -0.0276[f]
$L_a(3)$	-0.1267	-0.1195	-0.1222	-0.1092		-0.28	-0.0403	-0.0416[e], -0.0429[f]
$L_a(3) - L_s(3)$	-0.112	-0.024	-0.108	-0.093		-0.262	-0.014	-0.011 – -0.015
$T_{45}^-(1)$	0.097	0.092	0.112	0.096	0.095	0.023	0.011	
$T_6^+(3)$	0.217	0.417	0.315	0.330		0.49	0.381	
$T_6^+(3) - T_{45}^-(1)$	0.120	0.326	0.203	0.234		0.467	0.370	0.18 – 0.41
$T_{45}^-(1) - L_s(3)$	0.112	0.188	0.127	0.114	0.163	0.041	0.038	0.036 – 0.039
$\Gamma_6^-(1) - \Gamma_6^+(1)$	5.65	4.82	5.70	5.75	5.61	5.73	5.91	4.7 – 5.9
$\Gamma_{45}^+(1) - \Gamma_6^+(3)$	0.15	0.25	0.21	0.21	0.23	0.19	0.31	0.18 – 0.35
$\Gamma_6^-(2) - \Gamma_{45}^+(1)$	1.48	1.11	1.41	1.47		1.72	1.07	0.72 – 0.81
$\Gamma_6^-(2) - \Gamma_6^+(3)$	1.62	1.35	1.63	1.68		1.91	1.37	0.65 – 0.71
$T_6^+(1) - T_6^-(1)$	1.72	2.01	1.95	1.95	1.94	1.88	1.11	1.18 – 1.90
$T_6^+(2) - T_{45}^-(1)$	1.60	-1.52	1.57	1.50	-2.08	-1.30	-1.13	
$T_6^-(3) - T_{45}^-(1)$	0.78	0.94	0.92	0.94		1.09	0.94	0.80 – 0.88
$L_a(1) - L_s(1)$	0.57	0.67	0.65	0.65		0.72	0.36	
$L_a(2) - L_s(3)$	-1.84	-1.86	-1.90	-1.87		-1.97	-1.64	-1.92 – -2.10
$L_s(4) - L_a(3)$	0.89	1.00	0.95	0.94		1.04	0.84	1.05 – 1.15
$L_s(4) - L_s(3)$	0.78	0.97	0.84	0.85		0.78	0.83	

[a] Shick *et al.*, Ref. [8].
[b] Gonze *et al.*, Ref. [5], cited in Ref. [191].
[c] Liu *et al.*, Ref. [9].
[d] See Table 5.3.
[e] Isaacson *et al.*, Ref. [252].
[f] Smith *et al.*, Ref. [253].

Table 5.2: Energy levels (eV) as obtained in this work from DFT within the LDA and GGA [245], using the respective theoretical equilibrium lattice parameters (Theor. ELP) including spin-orbit coupling (SOC), and the experimental ones (Expt. LP) [189] (see Table 5.1); from other DFT calculations within the LDA at experimental LP including SOC [8, 5], from tight-binding calculations [9], and from experiments (see Table 5.3). Extension of the table published in Ref. [245].

Label	Band Energy (eV)	T (K)	Refs.	Year	Type of the experiment
$L_a(3) - L_s(3)$	-0.015 ± 0.002	4.2	[254]	1963	Infrared magnetoreflection
	-0.015		[252]	1969	Alfvén-Wave propagation
	-0.011 ± 0.001	4.2	[12]	1970	Magnetoreflection, de Haas-van Alphen studies
	-0.0136	4.2	[255]	1974	Analysis of magnetoreflection data
	-0.012	2-10	[11]	1974	Shubnikov-de Haas (SdH) quantum oscillations
$T_6^+(3) - T_{45}^-(1)$	0.180, 0.194	4.2	[256]	1976	Far-infrared magnetospectroscopy
	0.250 ± 0.050		[252]	1969	Alfvén-Wave propagation
	0.207	4.2	[257]	1969	Galvanomagnetic studies (SdH and Hall effect)
	0.407 ± 0.005	4.2	[258]	1993	Infrared magnetotransmission studies
	0.200 ± 0.008	110	[259, 260]	1993	High-Resolution EELS
$T_{45}^-(1) - L_s(3)$	0.0385	1.4	[253]	1964	Shubnikov-de Haas quantum oscillations
	0.03820 ± 0.00015		[252]	1969	Alfvén-Wave propagation
	0.036	2-10	[11]	1974	Shubnikov-de Haas quantum oscillations
	0.0375	4.2	[256]	1976	Far-infrared magnetospectroscopy
$\Gamma_6^-(1) - \Gamma_6^+(1)$	5.9		[261]	1973	Photoemission (X-ray radiation)
	4.7	20–300	[13]	1997	Photoemission (Synchrotron radiation)
$\Gamma_{45}^+(1) - \Gamma_6^+(3)$	0.35	20–300	[13]	1997	Photoemission (Synchrotron radiation)
	0.18	50	[262]	2004	Photoemission (Synchrotron radiation)
$\Gamma_6^-(2) - \Gamma_{45}^+(1)$	0.81 ± 0.02	300	[240]	1970	Piezoreflectance
	0.78 / 0.72	10/300	[241]	1975	Ellipsometry
$\Gamma_6^-(2) - \Gamma_6^+(3)$	0.69 ± 0.02	300	[240]	1970	Piezoreflectance
	0.71 / 0.65	10/300	[241]	1975	Ellipsometry
$T_6^+(1) - T_6^-(1)$	1.18		[261]	1973	Photoemission (X-ray radiation)
	1.9	20–300	[13]	1997	Photoemission (Synchrotron radiation)
$T_6^-(3) - T_{45}^-(1)$	0.88 / 0.80	10/300	[241]	1975	Ellipsometry
$L_a(2) - L_s(3)$	-1.92 ± 0.02	300	[240]	1970	Piezoreflectance
	-2.10/-2.10	10/300	[241]	1975	Ellipsometry
$L_s(4) - L_a(3)$	1.15 ± 0.02	300	[240]	1970	Piezoreflectance
	1.20 / 1.05	10/300	[241]	1975	Ellipsometry

Table 5.3: Experimental data on energy levels (eV) at various temperatures. The temperature effects are significant in the description of the electron and hole pockets in Bi [263, 255]. The accuracy on a single level in Ref. [261] was 0.55 eV, in Ref. [13] was 0.25 eV, and in Ref. [262] was 0.04 eV. (Unpublished)

When comparing *ab initio* DFT Kohn-Sham energy bands with the experimental data, special attention has to be paid to which experiment we are comparing them with. Let us distinguish between two groups of experiments, which are listed in Table 5.3, namely: (*i*) photoemission experiments, and (*ii*) all other experiments, like Shubnikov-de Haas effect, de Haas-van Alphen effect, etc.[2] When considering the photoemission experiments, the quasiparticle corrections may be large, and thus Kohn-Sham energy bands may generally differ significantly from the experimentally measured ones [17]. In contrast, the Kohn-Sham energy bands can be safely compared with the experiments like the Shubnikov-de Haas or others (see Table 5.3).

5.1.3 (a) Comparison of Kohn-Sham energy levels with Shubnikov-de Haas and de Haas-van Alphen experiments

(*i*) The energy difference of the two highest occupied bands at the L point is $E[L_a(3)] - E[L_s(3)]$ [see Fig. 5.1(b)], and it covers the energy range -11 – -15 meV according to various experiments (see Table 5.3). The GGA at the GGA equilibrium lattice parameters (ELP) gives -24 meV, and it is the closest value to the experimental one, because the LDA at the LDA-ELP gives -112 meV, and the LDA at the experimental LP gives -108 meV. With respect to the previous theoretical studies, the GGA value of -24 meV is much closer to the experimental one than the value of -262 meV from the DFT calculations of Gonze *et al.* [5]. The tight-binding calculations of Liu and Allen [9] give -14 meV, which is in extremely good agreement with the experimental value, due to the fit with the experimental data.

(*ii*) The electron pocket at the L point is defined by the depth of the $L_s(3)$ level. The experimental value is $\sim$ -27 meV (see Table 5.2). The $L_s(3)$ level is almost equally well reproduced within the LDA and GGA at the experimental LP and within the LDA at the LDA-ELP, $\sim$ -15 meV, which is not very far from the experimental value, while the GGA at the GGA-ELP gives -96 meV. Gonze *et al.* [5] obtained -18 meV, while Liu and Allen [9] obtained again an extremely good value of $\sim$ -27 meV.

(*iii*) The energy difference of the two lowest unoccupied bands at the T point is $E[T_6^+(3)] - E[T_{45}^-(1)]$ [see Fig. 5.1(b)], and it covers the energy range 180 – 410 meV according to various experiments (see Table 5.3). The GGA at the GGA-ELP gives 326 meV, which is inside the experimental energy range; the LDA at the LDA-ELP gives 120 meV, which underestimates the gap and is outside the experimental energy range; the LDA and GGA at the experimental LP give 203 and 234 meV, respectively, which are very close to the lower border of the experimental energy range. It is well known that both the LDA and GGA underestimate gaps in semiconductors [24]. Thus, it is not expected that the gap at the T point is well reproduced within

[2] *Shubnikov-de Haas* and *de Haas-van Alphen effects* describe oscillations in the conductivity and magnetization of a material, respectively, that occur at low temperatures in the presence of very intense magnetic fields.

either the LDA or GGA. The DFT calculations of Gonze *et al.* [5] give the value of 467 meV, which is too large and is outside the experimental energy range, and the tight-binding calculations of Liu and Allen give 370 meV, which is inside the experimental energy range.

(*iv*) The hole pocket at the T point is defined by the height of the $T_{45}^{-}(1)$ level. This level is unoccupied, and there is no experimental data in the literature. The energy of the $T_{45}^{-}(1)$ level is almost equal in each case of my calculations, and cover the energy range 92 – 112 meV, and is much larger than the values obtained in anterior theoretical studies. Namely, the DFT calculations of Gonze *et al.* [5] give 23 meV, and the tight-binding calculations of Liu and Allen [9] give 11 meV. However, the *ab initio* DFT calculations of Shick *et al.* [8] give 95 meV, which is very close to the values obtained in my calculations.

(*v*) The overlap energy is $E[T_{45}^{-}(1)]-E[L_s(3)]$, and it is greatly overestimated in all cases with respect to the experimental values which cover the energy range 36 – 39 meV. Namely, within the LDA at the LDA-ELP I obtain 112 meV, within the GGA at the GGA-ELP I obtain 188 meV, and within the LDA and GGA at the experimental LP I obtain 127 meV and 114 meV, respectively. The DFT calculations of Shick *et al.* [8] give the value of the overlap of 163 meV, which is also far from the experimental energy range. The calculations of Gonze *et al.* [5], and Liu and Allen [9], both fitted onto the experimental data, give extremely good values of 41 meV and 38 meV, respectively.

5.1.3 (b) Comparison of Kohn-Sham energy levels with photoemission experiments

In photoemission experiments, the electronic band structure is subject to many-body effects incorporated in the electronic self-energy $\Sigma(\omega)$ [17]. The self-energy is usually evaluated within the *GW* approximation [85], which is based on an expansion in terms of the dynamically screened Coulomb interaction. The application of the *GW* method to compute self-energy corrections on top of *ab initio* DFT results has become a well-established and standard technique, giving energy levels generally in close agreement with experiments [264]. The gaps between occupied and empty states generally increase by a substantial amount with respect to those obtained in the Kohn-Sham formulation of DFT, reaching agreement with experimental results [264]. However, due to the high complexity and large computational requirements of *ab initio* calculations of Σ [17], the experimental band structure measured by photoemission of electrons is often compared with the results of (simpler) calculations performed within the DFT. The consequences of this approach, in which the LDA or GGA exchange-correlation potentials can be considered as approximations to the self-energy Σ, must, however, be considered with a great care. *A priori*, it is not clear to which extent and over which energy range the quasiparticle corrections will affect the Kohn-Sham band structure of the system as semimetal Bi. In general, they can lead to a reduced band width and cause dispersion deviations near the Fermi level [262]. Up to today there have been no *GW* studies of Bi, because

it is very challenging material. Such calculations would be desirable in order to estimate the quasiparticle corrections in Bi. In the following I show, that both DFT-LDA and DFT-GGA descriptions of the band structure of Bi are in fairly close agreement with the photoemission data:

(*i*) The energy difference of two $6s$ levels at the Γ point, $E[\Gamma_6^-(1)] - E[\Gamma_6^+(1)]$, [see Fig. 5.1(a)] was measured in the photoemission experiments by Ley *et al.* [261], and they obtained the value of 5.9 eV with a precision of 0.55 eV on a single level; and more recently the photoemission experiment by Jezequel *et al.* [13] yielded 4.7 eV with a higher precision on a single level of 0.25 eV. From my DFT calculations I have found that within the GGA at the GGA-ELP I obtain a value of 4.82 eV, which is very close to the measurement by Jezequel *et al.* The other cases of my DFT calculations give values in the range 5.65 – 5.75 which are closer to less precise experimental data by Ley *et al.* The DFT calculations by Shick *et al.* [8] give 5.61 eV, the DFT calculations by Gonze *et al.* [5] give 5.73 eV, and the tight-binding calculations by Liu and Allen [9] give 5.91 eV, which are all close to the measurement by Ley *et al.* rather than to the data of Jezequel *et al.* However, the experimental data of Jezequel *et al.* should be considered as being more reliable, since the resolution on a single level in their photoemission experiments was higher by a factor of ~ 2 with respect to experiment of Ley *et al.*. Therefore, the GGA at the GGA-ELP provides the closest results to the experimental ones.

(*ii*) The energy difference $E[\Gamma_{45}^+(1)] - E[\Gamma_6^+(3)]$ was measured in the photoemission experiments by Jezequel *et al.* [13], and they obtained a value of 0.35 eV, and more recently by Ast and Höchst [262], who obtained a value of 0.18 eV. My *ab initio* calculations within the GGA at the GGA-ELP give 0.25 eV, which is between the two experimental values, and thus can be considered to be satisfactory. The LDA at the LDA-ELP gives 0.15 eV, slightly smaller than the value obtained by Ast and Höchst; and the LDA and GGA at the experimental LP both give 0.21 eV, which is again between the two experimental values. The DFT calculations by Shick *et al.* [8] give 0.23 eV, Gonze *et al.* [5] obtained 0.19 eV, and Liu and Allen [9] obtained 0.31 eV, which are all between the two experimental values, and thus can be considered to be satisfactory as well.

(*iii*) The energy difference $E[T_6^+(1)] - E[T_6^-(1)]$ was measured in the photoemission experiments by Ley *et al.* [261], and they obtained the value of 1.18 eV, whereas Jezequel *et al.* [13] obtained the value of 1.90 eV. All our values are very close to the measurement by Jezequel *et al.*, and they cover the range 1.72 – 2.01 eV. The *ab initio* DFT calculations by Shick *et al.* [8] give 1.94 eV, and the DFT calculations by Gonze *et al.* [5] give 1.88 eV, which are both close to the data by Jezequel *et al.* In contrast, the tight-binding calculations by Liu and Allen [9] give the value of 1.11 eV, which is close to the less precise experimental data by Ley *et al.* It is worth noting, that Liu and Allen applied the tight-binding approach in order to describe the details of the band structure near the Fermi level, and thus the dispersion of bands far from the Fermi level, *e.g.* $T_6^+(1)$ and $T_6^-(1)$ levels, might be

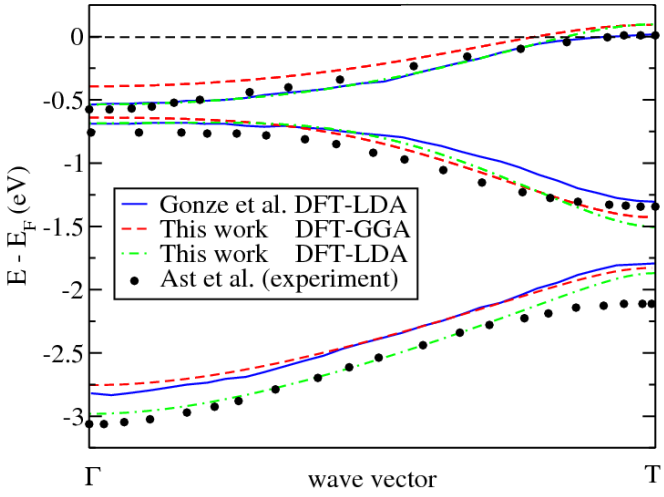

Figure 5.2: Comparison of the band structure of Bi along the Γ-T direction in the Brillouin zone, as computed in this work within the DFT-GGA at the GGA-ELP (red dashed lines), the DFT-LDA at the LDA-ELP (green dot-dashed lines), anterior DFT-LDA studies at the experimental LP by Gonze *et al.* Ref. [5] (blue solid lines), and as mesured in the photoemission experiment of Ref. [262] (black dots). The Fermi level is taken to be equal to zero. (Unpublished)

unsatisfactory (see Fig. 2 of Ref. [7]). Therefore, the theoretical data by Liu and Allen for the energy difference $E[T_6^+(1)] - E[T_6^-(1)]$ should not be considered as being reliable.

Figure 5.2 shows the comparison of the band structure of bismuth along the Γ-T direction in the BZ, as computed in this work within the LDA and GGA, anterior calculations by Gonze *et al.* within the LDA [5], and as measured in the photoemission experiment of Ref. [262]. The absolute values of the Kohn-Sham energies of this work within the DFT (both LDA and GGA) are in better agreement with experimental binding energies then calculations by Shick *et al.* using DFT-LDA [8], and the calculations by Liu and Allen using the tight-binding model [9] (see Fig. 7(d) of Ref. [262]).

It might seem very surprising that the DFT calculations provide a close agreement with photoemission experiments in bulk Bi. This is, probably, an indication of the fact that DFT Kohn-Sham energy bands are reasonable approximations to the full quasiparticle band structure of Bi. In fact, quasiparticle corrections are expected to be less important in metals than in semiconductors, as has been observed for metallic β-Sn [265]. Therefore, for further discussions in this thesis, I will use the DFT Kohn-Sham energy bands.

5.1.3 (c) Effect of lattice parameters on Kohn-Sham energy levels

Once we are convinced of the quality of the DFT Kohn-Sham description of the energy bands in Bi from the comparison with various experiments, let us make a point about

the effect of lattice parameters on the Kohn-Sham energy levels. As it has been shown above and illustrated in Fig. 5.3(a), the electronic band structure, and, in particular, the electron and hole pockets, are very sensitive to the lattice parameters. In the vicinity of the Fermi level, covering the energy range from -1.5 to 1.5 eV, the dispersion of Kohn-Sham levels differ quite significantly within the LDA and GGA at their respective theoretical parameters, as shown in Fig. 5.3(b). However, if the LDA and GGA are used with the same LP, then the energy bands are almost identical. This is illustrated, *e.g.*, in Figs. 5.3(c) and 5.3(d), where the LDA and GGA are both used at the experimental LP. Moreover, if we compare the LDA and GGA both at the LDA (or GGA) ELP, then we will see that both approximations give again almost identical band structures (not shown). This indicates that the LDA and GGA describe the same physics. It means that one has to apply some pressure in order to adjust the LDA band structure at the LDA-ELP to the GGA band structure at the GGA-ELP. Such a shift in pressure has been found to be necessary in a semiconductor like Ge [266].

Finally, in Fig. 5.3(e) I compare the LDA band structure calculated at the LDA-ELP and experimental LP. The dispersion of bands is qualitatively similar, but quantitatively there are some small differences. Namely, the valence bands behave very similarly, whereas the conduction bands are shifted down when calculated at theoretical LP with respect to the calculation at the experimental LP. Figure 5.3(f) shows similar comparison for the GGA: the GGA band structure calculated at the GGA-ELP and experimental LP. The difference between the calculations at the theoretical and experimental LP is more pronounced in GGA, than in LDA. This is due to the fact that GGA-ELP differ more from the experimental LP, than LDA-ELP do (see Table 5.1).

5.1.4 Conclusions

In this section I have presented a detailed analysis of the theoretical equilibrium lattice parameters and the Kohn-Sham band structure of Bi within the local density and generalized gradient approximations. It turns out, that the lattice parameters are strongly influenced by the spin-orbit coupling. Namely, if the SOC is included, the volume of the unit cell increases by as much as $\sim 4\,\%$ within the LDA, and $\sim 2\,\%$ within the GGA. Moreover, the $5d$ semicore levels, which were treated as valence states, have a drastic effect on the volume of the primitive unit cell: The LDA volume is overestimated by 0.02 % when the SOC is included, and the GGA volume is greatly overestimated, by 8-10 % with respect to the experimental one.

I have discussed in great detail the Kohn-Sham band structure within the LDA and GGA at the respective theoretical equilibrium lattice parameters, as well as at the experimental ones. I have also made a detailed comparison with previous theoretical and experimental studies. The overall band structure, and the subtleties near the Fermi level - electron and hole pockets - are well reproduced within the current *ab initio* DFT calculations including the spin-orbit coupling. It appears that the GGA at GGA equilibrium lattice parameters performs slightly better than the LDA at LDA-ELP, when compared to various experiments, like Shubnikov-de Haas, de Haas-van Alphen, and photoemission. A close agreement of the Kohn-Sham band structure with the photoemission data indicates

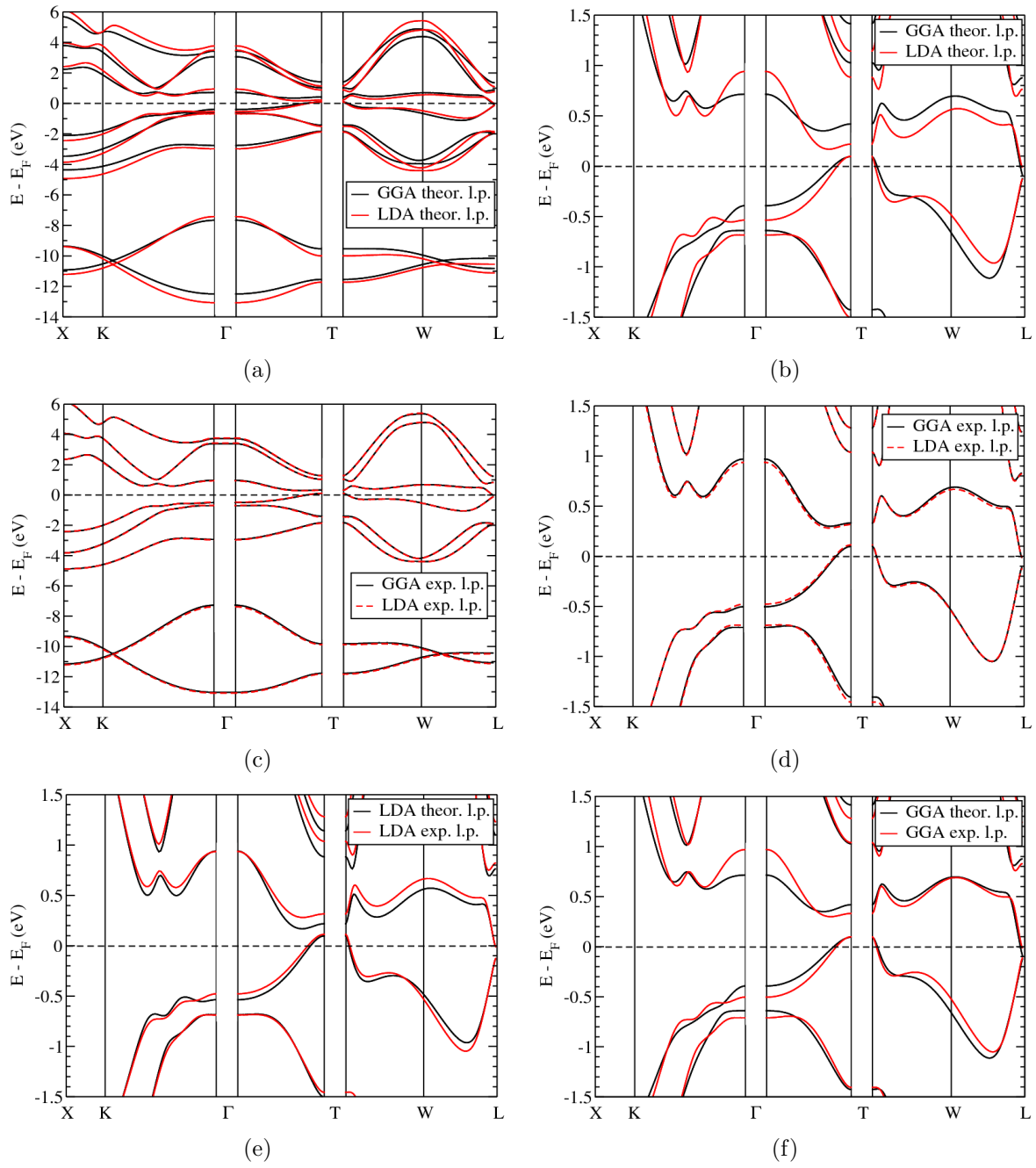

Figure 5.3: Comparison of the Kohn-Sham band structure of Bi including the spin-orbit coupling within the LDA and GGA. (a) The LDA at the LDA equilibrium lattice parameters (ELP), and the GGA at the GGA-ELP, (b) the same as (a) but zoomed on the region near the Fermi level. (c) The LDA and GGA at the experimental LP, (d) the same as (c) but zoomed on the region near the Fermi level. (e) The LDA at the LDA-ELP and experimental LP, (f) the GGA at the GGA-ELP and experimental LP. The Fermi level is taken to be equal to zero. (Unpublished)

that the quasiparticle corrections in bulk Bi, presumably, are not large. Though, *GW* calculations would be highly desirable in order to shed more light on this question.

In the following sections of this manuscript, most of the results will be presented by using both approximations, LDA and GGA.

5.2 Interpretation of time- and angle-resolved photoemission experiment

In this section I will present an *ab initio* DFT study of bulk bismuth in order to interpret the time-resolved and angle-resolved photoemission experiment on Bi(111) surface. As has been pointed out in Sec. 4.4, the high-density photoexcitation of bismuth leads to the generation of the A_{1g} coherent phonon mode with a large amplitude of oscillations. Such an atomic motion following the photoexcitation of Bi is nowadays well understood. Time-resolved X-ray diffraction experiments and DFT calculations could accurately describe the amplitude of oscillations and the frequency softening of the A_{1g} phonon mode (see Sec. 4.4). However, the temporal evolution of the electronic states after the photoexcitation has never been directly observed nor studied *ab initio*. This section aims at addressing this issue.

This section is organized as follows. In Secs. 5.2.1 and 5.2.2 I will present the experimental results, which have been obtained by our collaborators (E. Papalazarou, J. Faure, J. Mauchain, M. Marsi, A. Taleb-Ibrahimi, I. Reshetnyak, A. van Roekeghem, and L. Perfetti). Namely, I will show that the electronic structure of Bi displays a rich combination of bulk bands, surface states, and surface resonances, which upon the photoexcitation display a dynamics that depends on the wavevector and band index. In Sec. 5.2.3 I will present the details of my *ab initio* DFT calculations within the LDA and GGA, including the spin-orbit coupling. In Sec. 5.2.4 I will make a comparison of the Kohn-Sham band structure of *bulk* Bi with the photoelectron intensity map in order to reveal the origin of the electronic states which were measured. The symmetry arguments of the electronic states will also be used. In Secs. 5.2.5 and 5.2.6 I will demonstrate the generation mechanism of the A_{1g} phonon mode from the change of the electronic charge-density, and I will also evaluate *ab initio* the electron-phonon deformation potential within the frozen-phonon approximation. Finally, in Sec. 5.2.7 I will discuss the origin of the shift in the binding energy of electronic states immediately after the photoexcitation. At the end of the section, I will draw a conclusion.

In Appendix B.1 I give a brief introduction to the photoemission spectroscopy - technique, which has been used by our collaborators in the experiments on Bi(111) surface. The details of the experiment are also given in Appendix B.1.

The results, which will be presented in this section, have been published recently in Ref. [267].

5.2.1 Distinction between bulk states and surface resonances

Figure 5.4(a) shows the intensity map of the photoelectrons emitted along the $\overline{\Gamma} - \overline{\mathrm{M}}$ direction of the surface Brillouin zone (SBZ) [see Fig. 4.3(a)]. As has been pointed out in Sec. 4.3, the breakdown of translational symmetry in the [111] direction generates *surface states* that intersect the Fermi level and give rise to the Fermi surface [198]. These evanescent wavefunctions are localized at the topmost layers, thus conferring to the surface of bismuth good metallic properties. Although the band structure supports

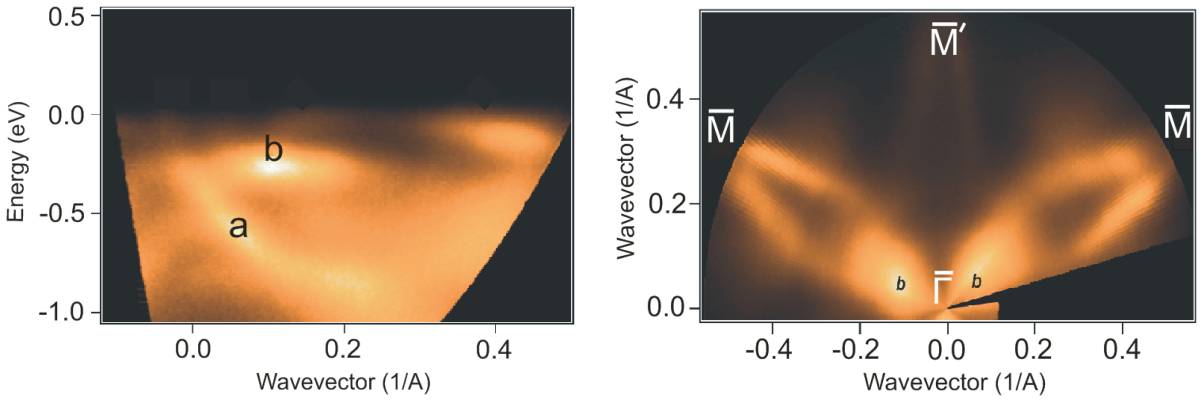

Figure 5.4: (a) Intensity map of photoelectrons emitted for parallel wave vector $k_{\|}$ along the $\overline{\Gamma} - \overline{\mathrm{M}}$ direction of the surface Brillouin zone [see Fig. 4.3(a)]. Band a is the surface resonance, and band b is the bulk state. (b) Intensity map of photoelectrons emitted at binding energy $\varepsilon_B = -0.26$ eV. An intense structure originating from band b is visible along the $\overline{\Gamma} - \overline{\mathrm{M}}$ directions, but not along $\overline{\Gamma} - \overline{\mathrm{M}}'$. From Ref. [267].

surface states only near the Fermi level, some *bulk states* and *surface resonances* are clearly visible at higher binding energy, in agreement with Ref. [262]. Two bands of a different nature are indicated in Fig. 5.4(a) by letters a and b. Due to the matrix elements of the photoemission process, band b is clearly visible only when the parallel component of the electronic wavevector is $k_{\|} < 0.25$ Å^{-1}. Band a has a larger value of the binding energy, it disperses more strongly, and intersects band b at the $\overline{\Gamma}$ point.

The overall agreement between current measurements and one-step photoemission calculations by Kimura *et al.* [204] is remarkable. Furthermore, the authors of Ref. [204] reported that band a is strongly spin-polarized, whereas band b has a negligible spin-polarization.[3] This finding suggests that band a is the surface resonance, and band b is the bulk band. Nevertheless, additional arguments confirming this hypothesis would be desirable. In Sec. 5.2.4 I will present two such additional arguments, which are based on the *ab initio* calculations and symmetry analysis.

More insights into the dispersion of band b can be obtained by mapping photoelectrons in the reciprocal space at a fixed kinetic energy. Figure 5.4(b) shows the intensity map of photoelectrons acquired at different wavevectors for the binding energy $\varepsilon_B = -0.26$ eV. As can be seen, the structure b is very intense along the $\overline{\Gamma} - \overline{\mathrm{M}}$ directions, whereas it vanishes in the $\overline{\Gamma} - \overline{\mathrm{M}}'$ directions. The experimental evidence that band b is invariant under the rotation of 120°, and not under the rotation of 60°, corroborates the bulk character of band b. In Sec. 5.2.4(c) I will make a comparison of Fig. 5.4(b) with *ab initio* results, and confirm this experimental finding.

[3] I recall, that the bulk electronic states of the centrosymmetric bismuth are *not* spin-polarized. In contrast, the breakdown of inversion symmetry at the surface induces a large spin-polarization of the surface states (see Sec. 4.3).

5.2.2 Oscillation of electronic bands after the photoexcitation

Large variations in the structure of the electronic states have been observed in the photoemission experiment. The oscillations are large for the bulk band b, whereas they fall below the detection limit for the surface resonance a and for all other surface states, as can be seen from the photoelectron intensity map in Fig. 5.5(a) and in Fig. 5.5(b). Indeed, on the upper panel of Fig. 5.5(b) it is clearly seen that the bulk band b displays periodic modulations. Moreover, the frequency of such periodic modulations is equal to the frequency of the A_{1g} phonon mode (see Sec. 4.4). This indicates the fact that there is a coupling between the electronic states and coherent phonons. The oscillations induced by the A_{1g} phonon mode have a frequency $\omega = 2.97 \pm 0.05$ THz, and a damping time 2.6 ± 0.2 ps. These values compare well with the ones obtained in the experiments on measuring the transient reflectivity [268]. On the other hand, the surface resonance does not display periodic modulations [see Fig. 5.5(b), lower panel]. This observation leads to two possible conclusions: either the amplitude of the A_{1g} phonon mode is smaller on the topmost bilayer, or the surface states have a weak coupling to this mode. Further experimental and theoretical investigations are required in order to clarify this point. In Sec. 5.2.6 I will present an *ab initio* study of the electron-phonon coupling in Bi, in order to confirm the origin of oscillations of bulk band b.

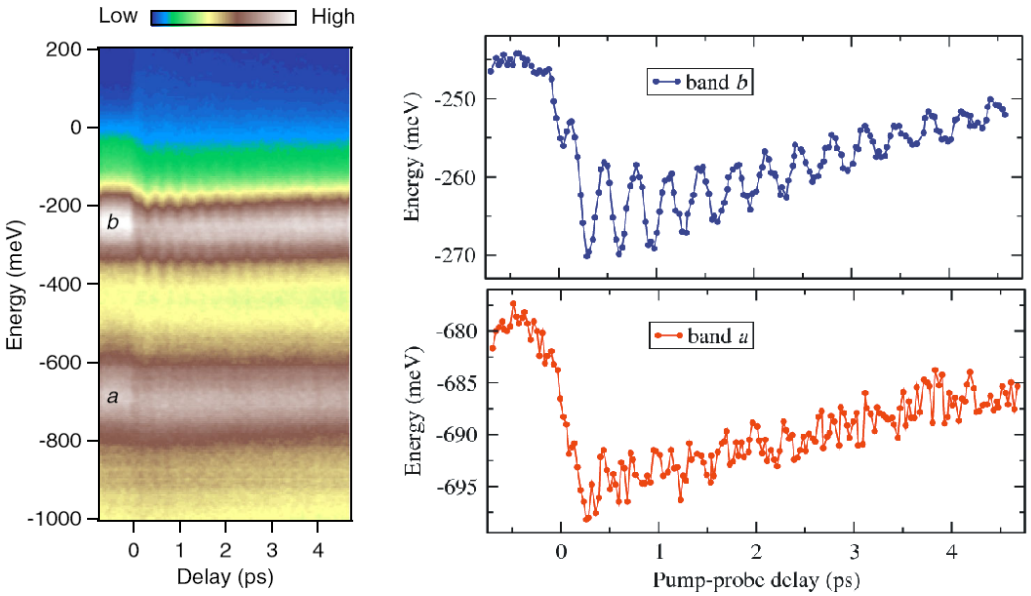

(a) (b)

Figure 5.5: (a) Intensity map of photoelectrons emitted at parallel wavevector $k_{\parallel} = 0.12$ Å^{-1} along the $\overline{\Gamma} - \overline{\mathrm{M}}$ direction as a function of the pump-probe delay. (b) Binding energy of the bulk band b (upper panel) and of the surface resonance a (lower panel) for parallel wavevector $k_{\parallel} = 0.12$ Å^{-1} along the $\overline{\Gamma} - \overline{\mathrm{M}}$ direction as a function of the pump-probe delay. From Ref. [267].

In addition, as can be seen in Fig. 5.5(b), the binding energy of both bulk band b and surface resonance a show a steep shift immediately after the photoexcitation. After such a shift the electronic bands show damping oscillations, which correspond to the fact that the electronic system cools down and goes towards the initial equilibrium state. I will address this issue in Sec. 5.2.7.

5.2.3 Computational method

I have performed *ab initio* DFT calculations within the LDA and GGA approximations at their respective theoretical equilibrium lattice parameters (see Sec. 5.1.2), including the spin-orbit coupling. I have used the norm-conserving pseudopotentials including the $5d$ semicore levels in the valence region (see Appendix A.1), and a kinetic-energy cutoff of 150 Ry.

After the photoexcitation of Bi sample, the electronic system is in the nonequilibrium state, and afterwards it is thermalized due to the electron-electron interaction, and can be described by the Fermi-Dirac distribution with the effective electronic temperature T [269]. In the photoemission experiment, the electronic temperature reached the maximum value of 2080 K (see Appendix B.1.5). Therefore, I have performed DFT calculations by using the Fermi-Dirac smearing function with a broadening parameter $\sigma = k_B T = 0.013$ Ry (k_B is the Boltzmann constant) in order to calculate integrals of different quantities over $\mathbf{k}$ points in the reciprocal space.

The $\mathbf{k}$ point sampling of the bulk Brillouin zone [see Fig. 4.3(a)] must be sufficiently dense in order to satisfy the condition, $|\varepsilon_{\mathbf{k}_i} - \varepsilon_{\mathbf{k}_j}| < \sigma$, where $\varepsilon_{\mathbf{k}_i}$ and $\varepsilon_{\mathbf{k}_j}$ are the Kohn-Sham energy values at the two nearest neighbouring points $\mathbf{k}_i$ and $\mathbf{k}_j$, respectively. Therefore, I have used a uniform $40 \times 40 \times 40$ $\mathbf{k}$ point mesh centered at the Γ point, yielding 5761 $\mathbf{k}$ points in the irreducible wedge of the Brillouin zone (IBZ).

5.2.4 Determination of bulk band

5.2.4 (a) Determination of $k_\perp$ from DFT

In Appendix B.1 it is pointed out that in the photoemission process the perpendicular component of the electronic wavevector $k_\perp$ is not conserved. Hence, it is not possible to determine from the experimental data to what $k_\perp$ the intensity maps in Figs. 5.4(a) and 5.4(b) correspond. However, *ab initio* calculations can help us to answer this question.

Let us consider the Kohn-Sham band structure of bulk Bi along the Γ-T direction in the bulk Brillouin zone [see Fig. 4.3(a)]. Figure 5.6 shows the highest valence band calculated within the LDA and GGA at their corresponding theoretical equilibrium lattice parameters (see Sec. 5.1.2). Since the lattice parameter a_0 is larger in the GGA than in the LDA (see Table 5.1), the distance between the Γ and T points in the reciprocal space is smaller in the GGA than in the LDA, as it is seen in Fig. 5.6. This means that at a given binding energy the wavevector component $k_\perp$ does not have the same value within the LDA and GGA. Therefore, in the following I will perform an analysis by using both approximations.

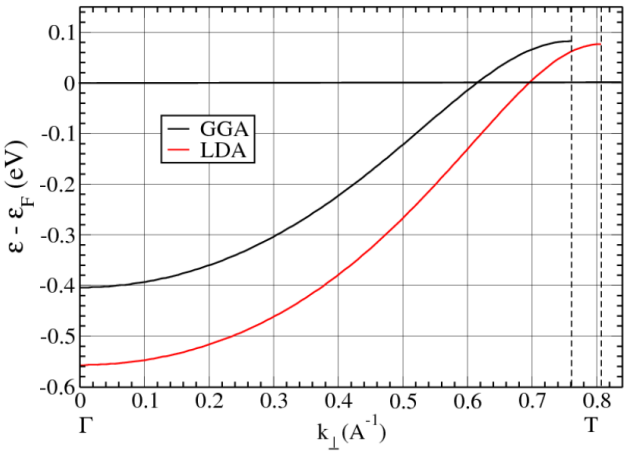

Figure 5.6: Kohn-Sham band structure within the LDA at the LDA-ELP (red curve) and within the GGA at the GGA-ELP (black curve) along the Γ-T direction in the bulk Brillouin zone [see Fig. 4.3(a)]. The Fermi level is at zero energy. (Unpublished)

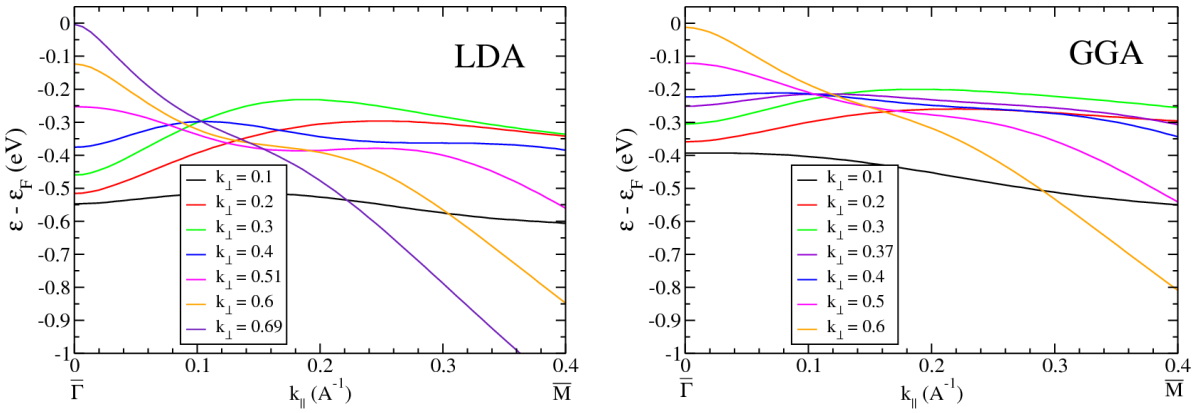

(a) (b)

Figure 5.7: Kohn-Sham band structure of bulk Bi calculated along the direction in the bulk Brillouin zone which is parallel to the $\overline{\Gamma}-\overline{\mathrm{M}}$ direction of the surface Brillouin zone, at various values of $k_\perp$. The unit of $k_\perp$ is $\mathrm{\AA}^{-1}$. (a) Calculation within the LDA at the LDA-ELP, (b) Calculation within the GGA at the GGA-ELP. (Unpublished)

Since the value of $k_\perp$ corresponding to the intensity map in Fig. 5.4(a) is not known, I have performed calculations at several values of $k_\perp$. By choosing a point between the Γ and T points in the bulk BZ, I have calculated the electronic band along the direction of the bulk BZ which is parallel to the $\overline{\Gamma} - \overline{\mathrm{M}}$ direction of the surface BZ [see Fig. 4.3(a)]. The results are shown in Figs. 5.7(a) and 5.7(b). It turns out, that the best agreement between the *ab initio* dispersion of the bulk electronic band and the experimental bulk band b [see Fig. 5.4(a)] is at $k_\perp = 0.45$ Å^{-1} within the LDA ($\varepsilon_B = -0.33$ eV at $\overline{\Gamma}$), and at $k_\perp = 0.37$ Å^{-1} within the GGA ($\varepsilon_B = -0.26$ eV at $\overline{\Gamma}$). In Sec. 5.2.4(b) I will present a detailed comparison with the experimental data.

5.2.4 (b) Determination of bulk band b from the dispersion of Kohn-Sham levels

Figures 5.8(a) and 5.8(b) show the bulk band b calculated *ab initio* on top of the experimental intensity maps of the photoelectrons emitted along the $\overline{\Gamma} - \overline{\mathrm{M}}$ and $\overline{\Gamma} - \overline{\mathrm{M}}'$ directions. The red and white lines are guides for the eye for the surface resonance a and for the surface states s, respectively. Notice, the energy dispersion of a and s are identical in the two intensity maps, whereas the dispersion of band b is much weaker along $\overline{\Gamma} - \overline{\mathrm{M}}$ than along $\overline{\Gamma} - \overline{\mathrm{M}}'$. The remarkable agreement between the calculated band b of bulk bismuth and the photoelectron intensity map reveals the bulk character of band b. On the other hand, the fact that no bulk electronic states match the dispersion of electronic states a and s indicates that they do not have the bulk character, but that they are related, rather, to the surface resonances and surface states, respectively.

5.2.4 (c) Determination of bulk band b using symmetry arguments

Symmetry arguments may also help us to assert the dominant character of the states a, b and s. As has been pointed out in Sec. 4.3, the surface states of Bi have six-fold symmetry with respect to the rotation around the [111] direction. On the other hand, the bulk states have only three-fold symmetry. Since the directions $\overline{\Gamma} - \overline{\mathrm{M}}$ and $\overline{\Gamma} - \overline{\mathrm{M}}'$ are connected by a rotation of 60°, from Figs. 5.8(a) and 5.8(b) one can see that states a and s have six-fold symmetry, because they are identical on the two intensity maps, whereas state b does not have six-fold symmetry, because its dispersion on different intensity maps is different. But how can one say that band b is three-fold symmetric? In order to answer this question, let us analyze Fig. 5.4(b), which illustrates the intensity map of photoelectrons acquired at different wave vectors for the binding energy $\varepsilon_B = -0.26$ eV.

I have performed *ab initio* calculation of the energy isosurface corresponding to the binding energy $\varepsilon_B = -0.26$ eV within the GGA at the GGA-ELP, and the result is shown in Fig. 5.9(a). Figure 5.9(b) represents the result of the cut of such an isosurface by a plane at $k_\perp = 0.37$ Å^{-1} within the GGA. As one can see from Fig. 5.9(b), there are prolongated structures along the $\overline{\Gamma} - \overline{\mathrm{M}}$ directions, but not along $\overline{\Gamma} - \overline{\mathrm{M}}'$. This is in remar-

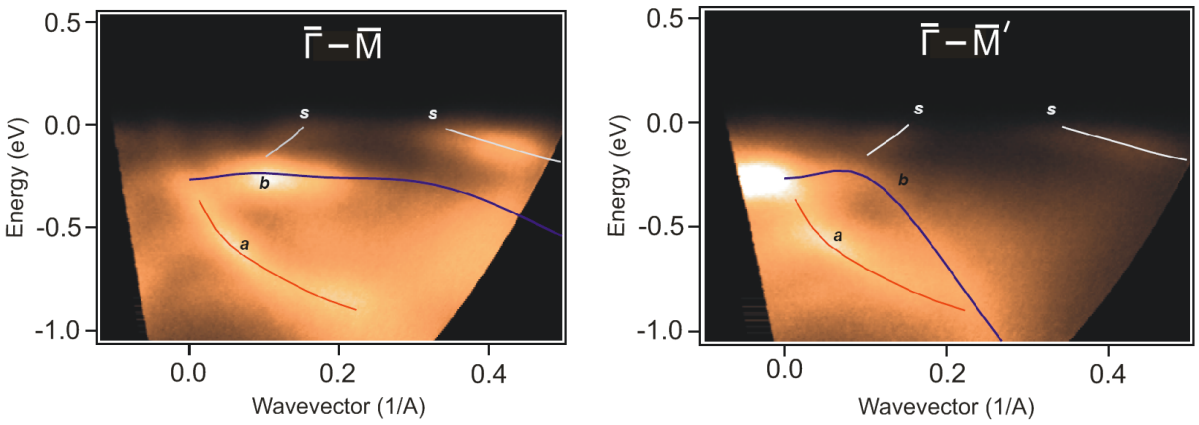

(a) (b)

Figure 5.8: Intensity map of photoelectrons emitted along the $\overline{\Gamma} - \overline{\mathrm{M}}$ direction (a) and along the $\overline{\Gamma} - \overline{\mathrm{M}}'$ direction (b). The bulk band b, calculated within DFT-LDA, is marked by a blue line. No bulk electronic states match the dispersion of band a and of the surface states s. The red and white lines are guides to the eye for the surface resonance a and for the surface states s, respectively. From Ref. [267].

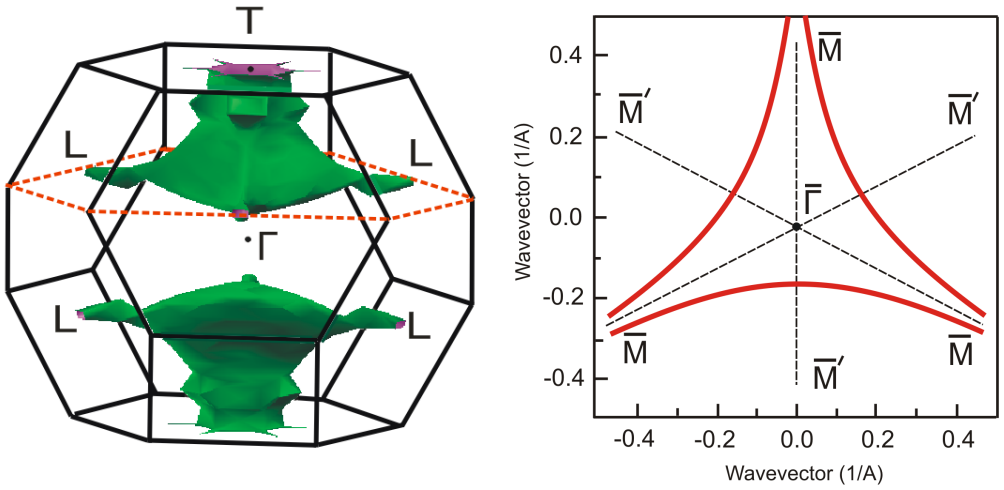

(a) (b)

Figure 5.9: (a) Energy isosurface corresponding to the binding energy $\varepsilon_B = -0.26$ eV in the bulk Brillouin zone, calculated from *ab initio* within the GGA at the GGA-ELP. Red dotted lines represent a plane which cuts the isosurface at $k_\perp = 0.37$ Å^{-1} within the GGA. The result of the cutting is shown in (b). Points Γ, T, and L are the high symmetry points in the bulk BZ, and $\overline{\Gamma}$, $\overline{\mathrm{M}}$, $\overline{\mathrm{M}}'$ are the high symmetry points in the surface BZ. (Unpublished)

kable agreement with the experimental finding presented in Fig. 5.4(b). These prolongated structures have a rotational symmetry of 120°, which was directly observed in the experiment. This is a feature of the bulk electronic bands, *i.e.* the three-fold symmetry. Eventually, the symmetry arguments give us yet another confirmation of the fact that band b has a bulk character, and that band a is the surface resonance and s is the surface state.

5.2.5 Analysis of electronic charge-density

Let us analyze the experimental results presented in Figs. 5.5(a) and 5.5(b). After the photoexcitation of Bi, the change in the electronic charge-density leads to the change in the distance between the two atoms in the unit cell along the [111] direction, which induces the A_{1g} phonon mode (see Sec. 4.4). In turn, the A_{1g} phonon mode induces oscillations of the bulk band b due to the electron-phonon coupling. *Ab initio* calculations can help us to illustrate this point.

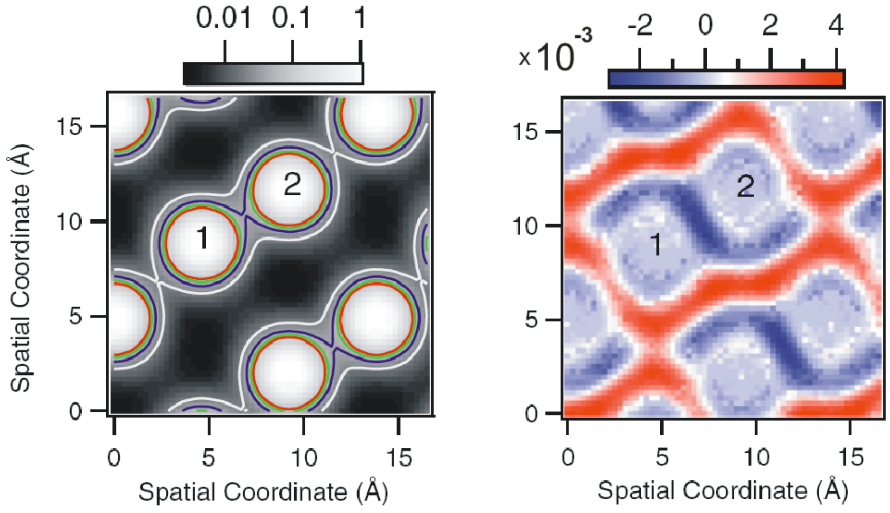

Figure 5.10: (a) Color scale plot of the charge-density at 130 K in the $(1\bar{1}0)$ plane. (b) Relative change of the charge-density for an increase of the electronic temperature from 130 K to 2080 K. From Ref. [267].

Figure 5.10(a) shows a color scale plot of the electronic charge-density $n(\mathbf{r}, T_i)$ at $T_i = 130$ K in the $(1\bar{1}0)$ plane. The sudden increase of the electronic temperature up to $T_f = 2080$ K (see Appendix B.1.5) after the photoexcitation changes the spatial distribution of the electronic charge-density. The relative change of the charge density, $[n(\mathbf{r}, T_f) - n(\mathbf{r}, T_i)]/n(\mathbf{r}, T_i)$, becomes negative in the region between the nearest neighbours (atoms 1 and 2), as illustrated in Fig. 5.10(b). Hence, the transfer of the electronic charge out of the bonding region increases the repulsion between the ionic cores. As a consequence, the atoms change their equilibrium position and oscillate around a new equilibrium position, until the energy dissipation into other phonon modes brings the system

back to the initial state. Such a change of the equilibrium position of the atoms induces the A_{1g} phonon mode, which in turn forces the oscillation of the bulk band b due to the electron-phonon interaction. This issue will be addressed in the next section.

5.2.6 Dispersion of the electron-phonon coupling

The lattice motion changes the binding energy of the Bloch state $|b, k_{\|}\rangle$ by $D_{b,k_{\|}} u$, where u is the A_{1g} phonon coordinate (see Sec. 4.4), and $D_{b,k_{\|}}$ is the deformation potential [270]. I have determined *ab initio* the value of the deformation potential within the LDA and GGA, within the frozen-phonon approximation [40]. To this end, I have calculated the Kohn-Sham band structure of bulk Bi along the $\overline{\Gamma} - \overline{\mathrm{M}}$ direction for several values of the displacement u, and keeping other lattice parameters (a_0 and α_0) equal to their theoretical equilibrium values (see Table 5.1). The results are shown in Figs. 5.11(a) and 5.11(b).

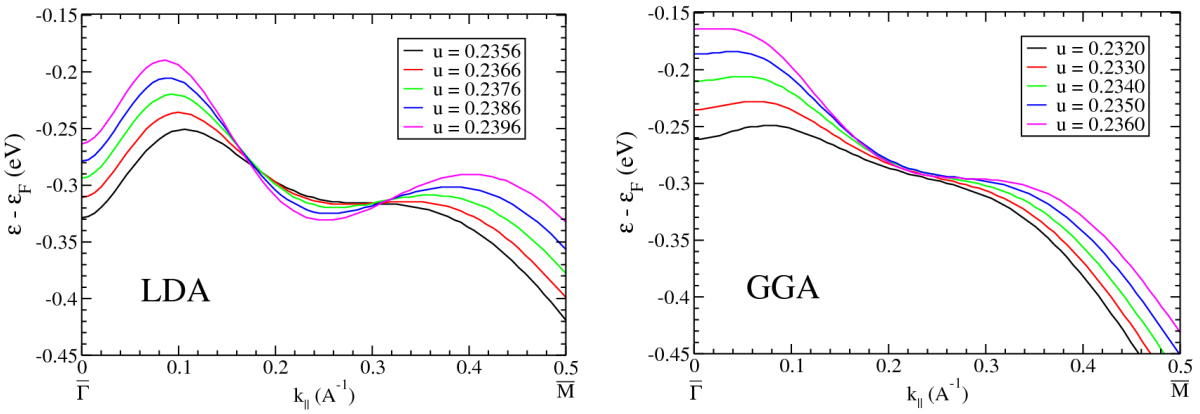

(a) (b)

Figure 5.11: Dispersion of bulk band b along the $\overline{\Gamma} - \overline{\mathrm{M}}$ direction for the several values of the displacement u. (a) LDA for $k_{\perp} = 0.45$ Å^{-1}, (b) GGA for $k_{\perp} = 0.37$ Å^{-1}. (Unpublished)

I would like to point out that in order to plot Figs. 5.11(a) and 5.11(b) I have used the advantage of the pseudopotential used in this thesis: the inclusion of the $5d$ semicore levels in the valence region [see Fig. 4.4(b)]. I have made an assumption that a relatively small change of the parameter u should not induce a shift of the deeply lying $5d$ semicore levels, whereas the highest valence bulk band b does move, because it is very sensitive to the change of u. Therefore, $5d$ levels have been used as a reference for the energy,[4] and they have been aligned when comparing the dispersion of the bulk band b for different values of the parameter u.[5]

[4]In *ab initio* DFT calculations there is no reference for the energy [271]. By changing u, the Fermi level also changes, therefore it cannot be considered as a reference. Instead, the $5d$ levels could be considered as a reference.

[5]The inclusion of the $5d$ semicore levels in the valence region is a necessary condition, in order to satisfy the transferability properties of the pseudopotential (see Appendix A.1). Moreover, as one can

The inclusion of the $5d$ semicore levels in the valence region means that the corresponding wavefunctions are orthogonal to the $6s$ and $6p$ wavefunctions, which are also in valence. The displacement of the atoms (change of u) changes the $6s$ and $6p$ wavefunctions, but the $5d$ wavefunctions are assumed to be unchanged. This is a reasonable approximation from the physical point of view, since the $5d$ levels are deeply lying and tightly bound levels which barely respond to small perturbations, like small change of atomic positions, in contrast to the $6s$ and $6p$ levels, which are very sensitive to perturbations. The $5d$ occupied levels are orthogonal also to the $6d$ unoccupied levels. If the excitation of electrons is such that the $6d$ levels are occupied, then due to the orthogonality of $5d$ and $6d$ wavefunctions, there will be a change of $5d$ wavefunctions. However, since the $6d$ levels are not populated after the photoexcitation, and they are not hybridized with the $6s$ and $6p$ levels, they do not contribute to the change of the self-consistent Kohn-Sham potential, and hence they do not change the $5d$ wavefunctions. Due to the orthogonality, the change of the $6s$ and $6p$ wavefunctions leads to the change of the $5d$ wavefunctions, but the later is negligible. Thus, the $5d$ levels can be assumed to be unchanged in the interpretation of the current photoemission experiment on photoexcited bismuth with a small perturbation of 1.5 eV. This assumption may be not valid in general case, *e.g.* when the perturbation is large or when $6d$ states are occupied.

The variation of the electronic bulk band b is somewhat different within the LDA and GGA. However, within both approximations the binding energy strongly varies near the $\overline{\Gamma}$ point, and it is less sensitive to the phonon coordinate u for $k_{\|} \approx 0.2$ Å^{-1}. This is in agreement with the measurements. Figure 5.12 shows the comparison of the experimental and theoretical oscillation amplitude of the binding energy of bulk band b as a function of the wavevector $k_{\|}$ along the $\overline{\Gamma} - \overline{\mathrm{M}}$ direction. The measured amplitude of the oscillation is 20 meV for $k_{\|} = 0.05$ Å^{-1}, and decreases down to 10 meV for $k_{\|} = 0.20$ Å^{-1}. At larger wave vectors, $k_{\|} > 0.20$ Å^{-1}, the photoelectron intensity of bulk band b is too low for a reliable extraction of the oscillation amplitude. The agreement between theory and experiment on the oscillation amplitude is achieved for $\Delta u \simeq 0.001$ (unitless) both within the LDA and GGA. Such a value of Δu corresponds to the atomic displacement of $\Delta u{\cdot}c = 1.17$ pm within the LDA, and of $\Delta u{\cdot}c = 1.24$ pm within the GGA.[6] The agreement between theory and experiment is remarkable in the range $0.05 < k_{\|} < 0.14$ Å^{-1}, and there is some discrepancy for $k_{\|} > 0.14$ Å^{-1} (see Fig. 5.12).

A displacement of the two atoms within the unit cell, Δu, which is induced by the excitation laser pulse, can be determined using the two-temperature model [16, 194]. Within such a model the electronic subsystem and the lattice are described by two distinct temperatures. Experimentally only the electronic temperature can be determined (see Appendix B.1.5), which has been found to be in remarkable agreement with the theoretical one [267]. On the basis of the two-temperature model, the atomic displacement Δu has been found to be also ≈ 0.001 [267].

The deformation potential is defined within the frozen-phonon approximation as $D_{b,k_{\|}} =$

see, the $5d$ levels serve also for other purposes - being the reference.

[6]Note, that $c = 11.684$ (Å) within the LDA, $c = 12.378$ (Å) within the GGA, and the experimental value is $c = 11.797$ (Å). For more details see Secs. 4.2.1 and 5.1.2.

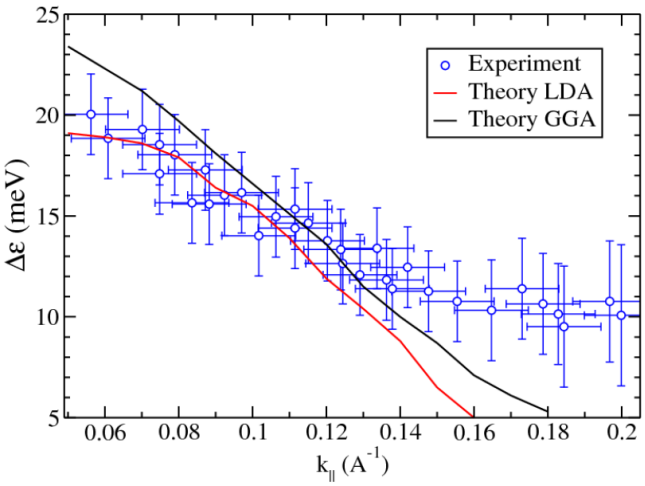

Figure 5.12: Oscillation amplitude of the binding energy of bulk band b, $\Delta\varepsilon$, as a function of the wave vector $k_\parallel$ along the $\overline{\Gamma}-\overline{\mathrm{M}}$ direction. The experimental data is marked by empty circles with error bars. The *ab initio* results are presented for the atomic displacements of $\Delta u \cdot c = 1.17$ pm within the LDA, and of $\Delta u \cdot c = 1.24$ pm within the GGA. (Unpublished)

$\Delta\varepsilon(k_\parallel)/(\Delta u\, c)$.[7] It can be directly computed from the data in Fig. 5.12. For example, for $k_\parallel = 0.12$ Å^{-1} the deformation potential is equal to $D_{b,k_\parallel} = 1.10$ eV/Å within the LDA, and $D_{b,k_\parallel} = 1.02$ eV/Å within the GGA. As a term of comparison, the optical phonons have the electron-phonon matrix element of 7.8 eV/Å in graphite [272], and 14 eV/Å in boron doped diamond [273]. The deformation potential in bismuth is very small compared to other materials.

The large $k_\parallel$-dependence of $D_{b,k_\parallel}$ has also been observed in $TbTe_3$ [274]. Due to the presence of a charge-density wave, the variation of the interaction strength as a function of the Bloch state in $TbTe_3$ has been explained by the good nesting properties of the Fermi surface. The $k_\parallel$-dependence of the electron-phonon coupling has been also known from calculations in semiconductors [275, 276, 277, 278, 279]. However, the current measurements on Bi suggest that the wavevector dependence of the electron-phonon coupling constitutes a *general* property of covalent crystals. This aspect of the coupling can be understood by a simple tight-binding model on a linear chain: if the atomic displacement modifies the overlap between the atomic orbitals, the binding energy of the Bloch states will change differently for different wave vectors.

5.2.7 Origin of the shift of binding energy

As has been pointed out in Sec. 5.2.2, the dynamics of the electronic states does not depend simply on the phonon coordinate u. As can be seen in Fig. 5.5(b) (upper panel), besides the oscillations of the binding energy of bulk band b with the frequency of the A_{1g} phonon mode, an additional effect shifts band b towards higher binding energy just after the photoexcitation. This photoinduced shift occurs also in the surface resonance a [see Fig. 5.5(b), lower panel], and in the surface states. The magnitude of such a shift depends on the electronic wavevector and band index. Under similar experimental conditions, the photoinduced increase of the binding energy has been also observed in the surface states

[7] Within the frozen-phonon approximation, a finite amplitude displacement $\Delta u\, c$ of atoms is "frozen" into the system, and the resulting deformation potential is calculated.

of Gd [280].

I have tried to reproduce such a shift from *ab initio* calculations on bulk Bi. I have performed two independent calculations of the Kohn-Sham band structure, corresponding to the electronic system at the equilibrium and in the photoexcited state. On one hand, as has been discussed in Sec. 5.2.3, I have performed a calculation of the Kohn-Sham band structure by using the Fermi-Dirac smearing function with the broadening parameter $\sigma = 0.013$ Ry, which mimics the electronic temperature of $T = 2080$ K, which was reached in the photoemission experiment (see Appendix B.1.5). On the other hand, I have performed a calculation of the Kohn-Sham band structure by using the tetrahedron method [197], in which there is no smearing σ, and which corresponds to zero temperature. In the latter case I have used a very dense $\mathbf{k}$ point sampling of the bulk Brillouin zone: a $50 \times 50 \times 50$ uniform $\mathbf{k}$ point mesh centered at the Γ point, yielding 11076 $\mathbf{k}$ points in the IBZ.

The $5d$ semicore levels of the two calculations have been aligned, and the relative shift of the topmost valence bulk band b has been evaluated, which corresponds to the increase of the electronic temperature from 0 to 2080 K. However, I have found that this shift is extremely small, ~ 2 meV, both within the LDA and GGA. Instead, in the experiment it was found that such a shift is equal to 20 meV for the bulk band b [see Fig. 5.5(b), upper panel]. It should be noted that the increase of the electronic temperature after the photoexcitation leads to the broadening of the Fermi-Dirac distribution around the top of the occupied valence bands. This fact has been taken into account in the experimental determination of the photoinduced shift of the electronic states (see Appendix B.1.5). It turns out that such a broadening of the Fermi-Dirac function has a minor effect on the band shift (6 meV).

The discrepancy between *ab initio* DFT calculations and experiment may be due to the fact that the former does not account for the charge redistribution nor the carrier transport on the surface of the sample. Alternatively, dynamical aspects of the electronic screening may require simulations that go beyond DFT, like the *GW* method [281]. Thus, the shift of 20 meV in the binding energy of the bulk band b is likely to be of a purely electronic nature. Additional theoretical investigations are required in order to reveal the origin of the shift.

5.2.8 Conclusions

In this section I have presented a theoretical interpretation of the time-resolved and angle-resolved photoemission experiment on Bi(111) surface, on the basis of the analysis of the Kohn-Sham band structure, which was obtained by performing *ab initio* DFT calculations on bulk Bi. I have performed the analysis within the LDA and GGA, and by including the spin-orbit coupling in the calculations, since it is crucial for the description of the band structure.

I have revealed a character of the electronic states in the experimental photoelectron intensity map, by making a comparison of the Kohn-Sham band structure of bulk Bi with the experimental electronic structure. With the help of symmetry arguments I have shown that one of the bands has a bulk character with a three-fold symmetry, in contrast

to surface states and surface resonances which have six-fold symmetry.

Furthermore, I have shown that a change of the electronic charge-density due to the increase of the electronic temperature after the photoexcitation of Bi, modulates the distance between two atoms in the unit cell, and thus is responsible for the generation of the A_{1g} phonon mode. The A_{1g} mode, in turn, provokes oscillations of the electronic bulk band b through the electron-phonon interaction.

In addition, I have found within the frozen-phonon approximation that the electron-phonon coupling in Bi strongly depends on the electronic wavevector, in remarkable agreement with experimental observations. Both approximations, LDA and GGA, give an amplitude of oscillation of bulk band b in very good agreement with the experimental one.

Finally, I have found that DFT calculations on bulk Bi neither within the LDA nor within the GGA can explain the shift of 20 meV in the binding energy of the bulk band b immediately after the photoexcitation. This may be due to the inability of the bulk model to account for the charge redistribution nor the carrier transport on the surface of the sample. Moreover, the dynamical aspects of the renormalization of the electronic screening, due to the increase of the electronic temperature, may be responsible for the shift of the electronic states. Further theoretical studies are required in order to reveal the origin of the shift.

Chapter 6

Free-carrier absorption in photoexcited Bi

In this chapter I will present a study of the low-energy Drude intraband response of electrons and holes in the photoexcited bismuth, by means of *ab initio* DFT calculations. I will perform methodological developments for the free-carrier absorption in order to interpret the time-resolved terahertz experiment on Bi, in which the Drude response has been observed. My analysis is based on a consideration of the intraband contribution to the dielectric function of Bi, and its change due to the photoexcitation.

In particular, I will investigate why the frequency of oscillation of the plasma in the photoexcited Bi does not show the usual behaviour, *i.e.* rapid decrease immediately after the photoexcitation of carriers [282, 283]. I will present a qualitative and quantitative explanation of such an observation, on the basis of the Kohn-Sham band structure of Bi near the Fermi level. The description of the latter is of major importance for the correct determination of the Fermi velocity of electrons and holes, effective masses in the local extrema of the band structure, optical masses of carriers near the Fermi level at the L and T points, and of the characteristic plasma frequency. All these ingredients are needed for the *ab initio* description of the free-carrier absorption in materials, and in particular in bismuth.

This chapter is divided on two parts. First, in Sec. 6.1 I will present methodological developments for the free-carrier absorption, and its application to Bi. Second, in Sec. 6.2 I will apply such methodological developments for the interpretation of the time-resolved terahertz experiment on Bi.

6.1 Methodological developments for free-carrier absorption

In Sec. 6.2 I will study a change of the intraband dielectric function of Bi after the low density photoexcitation. The intraband contribution to the dielectric function is found to be described by the Drude model [see Sec. 3.2.3(c)], and corresponds to the free-carrier absorption, well known in doped semiconductors [284]. This section aims at methodological developments for the free-carrier absorption, which will be needed for the theoretical description of the free-carrier response in the photoexcited Bi.

Free-carrier absorption (FCA) is the second-order process, which involves the absorption of photons by free carriers and scattering with phonons or impurities [285]. The scattering mechanism is necessary for the conservation of the momentum, because the absorbed photon has a negligible momentum. Quantum theory of the FCA was developed long ago [284, 285, 286], and nowadays the FCA can be described very accurately in complex materials (see, *e.g.*, Refs. [287, 288]).

Since in Bi the FCA corresponds to the Drude response, it is important to accurately determine properties of charge carriers such as their velocity, effective and optical masses, and the plasma frequency. In this section I will present how these quantities can be determined *ab initio*, and will be used in the semiclassical approximation to the FCA. In Sec. 6.1.2 I will present a derivation of the semiclassical expression for the plasma frequency. In Sec. 6.1.3 I will show how the carrier velocity can be calculated *ab initio*. In Sec. 6.1.4 I will determine effective masses of the true local extrema in the Kohn-Sham band structure of bulk Bi near the Fermi level. Finally, in Sec. 6.1.5 I will give a definition of the optical mass, and determine its values in Bi. At the end, I will draw a conclusion about the *ab initio* description of the free-carrier absorption.

6.1.1 Computational method

The results of Sec. 6.1 have been obtained by preforming *ab initio* DFT calculations within the generalized gradient approximation (GGA). As has been shown in Sec. 5.1.3, the GGA at the GGA equilibrium lattice parameters (see Table 5.1) gives somewhat better agreement of the Kohn-Sham energy levels with various experimental data than the LDA. Therefore, the GGA has been chosen for studies in this chapter. The details of the calculations are the same as described in Sec. 5.1.1. The spin-orbit coupling has been included in the calculations.

6.1.2 Plasma frequency

According to the Drude model, the plasma frequency ω_p is determined by the variation of the electron density [see Eq. (3.41)]. On the other hand, the plasma frequency can be defined as [114, 289, 290, 265]:

$$\omega_p^2 = \frac{8\pi e^2}{3V} \sum_{n,\mathbf{k}} \mathbf{v}_{n,\mathbf{k}}^2 \, \delta(\varepsilon_{n,\mathbf{k}} - \varepsilon_F) = \frac{4\pi e^2}{3} \sum_n \int \frac{d\mathbf{k}}{4\pi^3} \, \mathbf{v}_{n,\mathbf{k}}^2 \, \delta(\varepsilon_{n,\mathbf{k}} - \varepsilon_F), \tag{6.1}$$

where V is the volume of the primitive cell, $\mathbf{v}_{n,\mathbf{k}}$ is the carrier velocity at the n-th band with a wave vector $\mathbf{k}$, $\varepsilon_{n,\mathbf{k}}$ is the Kohn-Sham energy, and ε_F is the Fermi energy.[1] Equation (6.1) is valid only at zero temperature, $T = 0$ K. In the following I will show how Eq. (6.1) can be obtained and generalized to finite temperatures from the semiclassical theory of electrical conductivity [115].

In the semiclassical theory, the tensor of electrical conductivity reads [115]:

$$\hat{\sigma}(\omega, T) = e^2 \sum_n \int \frac{d\mathbf{k}}{4\pi^3} \frac{\mathbf{v}_{n,\mathbf{k}} \mathbf{v}_{n,\mathbf{k}}}{[1/\tau_n(\varepsilon_{n,\mathbf{k}})] - i\omega} \left[-\frac{\partial f(\varepsilon, T)}{\partial \varepsilon} \right]_{\varepsilon=\varepsilon_{n,\mathbf{k}}}, \tag{6.2}$$

where $\tau_n(\varepsilon_{n,\mathbf{k}})$ is the relaxation time which may differ from band to band, $f(\varepsilon)$ is the distribution function,[2] and T is the electronic temperature.[3] In metals, with a high level of accuracy, one may consider $\tau_n(\varepsilon)$ as $\tau_n(\varepsilon_F)$. Let us make the following approximations: (i) the relaxation time does not depend on the band number n nor the wave vector $\mathbf{k}$, *i.e.* τ is the constant, and (ii) the *isotropic model* for tensorial quantities. As a consequence, Eq. (6.2) will read:

$$\sigma(\omega, T) = \frac{e^2}{1/\tau - i\omega} \sum_n \int \frac{d\mathbf{k}}{4\pi^3} \frac{\mathbf{v}_{n,\mathbf{k}}^2}{3} \left[-\frac{\partial f(\varepsilon, T)}{\partial \varepsilon} \right]_{\varepsilon=\varepsilon_{n,\mathbf{k}}}. \tag{6.3}$$

If one substitutes Eq. (6.3) into the Drude expression for the dielectric function [74]:

$$\epsilon_{intra}(\omega) = 1 + \frac{4\pi i \sigma}{\omega}, \tag{6.4}$$

then one will immediately see that the plasma frequency can be defined as [see Eq. (3.39)]:

$$\omega_p^2(T) = \frac{4\pi e^2}{3} \sum_n \int \frac{d\mathbf{k}}{4\pi^3} \mathbf{v}_{n,\mathbf{k}}^2 \left[-\frac{\partial f(\varepsilon, T)}{\partial \varepsilon} \right]_{\varepsilon=\varepsilon_{n,\mathbf{k}}}. \tag{6.5}$$

If one considers a Fermi-Dirac distribution $f_{FD}(\varepsilon, T)$, then in the limit when temperature goes to zero, Eq. (6.5) will coincide with Eq. (6.1), because $\lim_{T\to 0}[-df_{FD}(\varepsilon, T)/d\varepsilon] = \delta(\varepsilon)$.

If contributions to the plasma frequency mainly come from the region around the Fermi level (like in semimetallic bismuth), then the sum over all bands n in Eq. (6.5) will be reduced to only those bands which cross the Fermi level. For this reason, among all the carriers with velocities $\mathbf{v}_{n,\mathbf{k}}$ we can consider only those which are near the Fermi level and which, thus, have the Fermi velocity $\mathbf{v}_F$. Hence, the Fermi velocity can be taken out from the integral. This is, so-called, *mid-point approximation*. Therefore, Eq. (6.5) reads:

$$\omega_p^2(T) = \frac{4\pi e^2}{3} \mathbf{v}_F^2 \sum_n \int \frac{d\mathbf{k}}{4\pi^3} \left[-\frac{\partial f(\varepsilon, T)}{\partial \varepsilon} \right]_{\varepsilon=\varepsilon_{n,\mathbf{k}}}. \tag{6.6}$$

[1] In Eq. (6.1) I have used the relation $(1/V)\sum_{\mathbf{k}} = \int d\mathbf{k}/(8\pi^3)$.

[2] The distribution function $f(\varepsilon)$ can be either the Fermi-Dirac function or any other distribution function, depending on the problem.

[3] The *electronic temperature* is defined as the temperature of a thermalized electronic distribution [291].

By introducing the density of states (DOS), $g(\varepsilon)$, Eq. (6.6) can be rewritten as:

$$\omega_p^2(T) = \frac{4\pi e^2}{3}\mathbf{v}_F^2 \int g(\varepsilon) \left[-\frac{\partial f(\varepsilon, T)}{\partial \varepsilon}\right] d\varepsilon, \tag{6.7}$$

where

$$g(\varepsilon) = \sum_n \int \frac{d\mathbf{k}}{4\pi^3}\, \delta(\varepsilon - \varepsilon_{n,\mathbf{k}}). \tag{6.8}$$

In order to calculate the plasma frequency, Eq. (6.7), one needs to know the following ingredients: the distribution function $f(\varepsilon, T)$, the density of states $g(\varepsilon)$, and the carrier velocity at the Fermi level $\mathbf{v}_F$. Let us comment on each of these ingredients.

The choice of the distribution function $f(\varepsilon, T)$ depends on the system under consideration. It can be the Fermi-Dirac distribution, $f_{FD}(\varepsilon, T) = \{1+\exp[(\varepsilon-\varepsilon_F)/(k_B T)]\}^{-1}$, or some specific model distribution, or it can be obtained by solving the kinetic Boltzmann equation [74].

The density of states can be computed *ab initio* by using a smearing technique to approximate the Dirac δ-function. Many kinds of smearing functions can be used: Fermi-Dirac broadening, Lorentzian, Gaussian [292], Gaussian combined with polynomials [244], or cold smearing functions [293], to recall only some of them. While the choice of a given smearing function is to some extent a matter of computational convenience, the specific choice of Fermi-Dirac broadening allows one to mimic the effects of a finite temperature ($T = \sigma/k_B$, where σ is a broadening parameter). Another approximation to the calculation of DOS is the tetrahedron method [197]. This method does not contain any smearing parameter, and it is more precise than the smearing technique. The choice between the tetrahedron method and the smearing technique depends on the precision which is needed for a specific problem.

The last but not least ingredient of the plasma frequency is the carrier velocity. A full section will be denoted to this question, since the accurate determination of the carrier velocity is challenging, and thus deserves special attention.

6.1.3 Carrier velocity

In this section, I will derive the expression for the carrier velocity, when the Hamiltonian contains or not the spin-orbit coupling.

6.1.3 (a) Hamiltonian without the spin-orbit coupling

Let us start from the Schrödinger equation:

$$\hat{H}\varphi_{n,\mathbf{k}} = \varepsilon_{n,\mathbf{k}}\, \varphi_{n,\mathbf{k}}, \tag{6.9}$$

where $\varphi_{n,\mathbf{k}}$ and $\varepsilon_{n,\mathbf{k}}$ are the Kohn-Sham (KS) wavefunctions and energy values, respectively, and the Hamiltonian $\hat{H}$ in the pseudopotential calculation reads:

$$\hat{H} = \hat{T} + \hat{V}_{loc} + \hat{V}_{NL}, \tag{6.10}$$

where $\hat{T} = \mathbf{p}^2/2m$ is the kinetic term, $\hat{V}_{loc} = \hat{V}(r)\delta(\mathbf{r} - \mathbf{r}')$ is the local potential, and $\hat{V}_{NL} = \sum_{Ilm} D_l^I |\beta_{lm}^I\rangle\langle\beta_{lm}^I|$ is the non-local potential in the Kleinman-Bylander form (see Sec. 2.3.2). The functions β_{lm}^I are defined as [see Eq. (2.69)]:

$$\beta_{lm}^I(\mathbf{r} - \boldsymbol{\tau}_I) = \delta\hat{V}_l^I(|\mathbf{r} - \boldsymbol{\tau}_I|)\,\chi_l(|\mathbf{r} - \boldsymbol{\tau}_I|)\,Y_{lm}(\theta, \varphi)\,, \tag{6.11}$$

where $\boldsymbol{\tau}_I$ is the position of the I-th ion, $\delta\hat{V}_l^I(|\mathbf{r} - \boldsymbol{\tau}_I|)$ is the potential corresponding to the I-th ion, $\chi_l(|\mathbf{r} - \boldsymbol{\tau}_I|)$ is the radial part of the wavefunction, and $Y_{lm}(\theta, \varphi)$ are the spherical harmonics.

The Hellmann - Feynman theorem [24] dictates that, given the relation $\varepsilon_{n,\mathbf{k}} = \langle\varphi_{n,\mathbf{k}}|\hat{H}|\varphi_{n,\mathbf{k}}\rangle$ [see Eq. (6.9)], there is a relationship for the derivatives:

$$\frac{\partial\varepsilon_{n,\mathbf{k}}}{\partial\mathbf{k}} = \left\langle\varphi_{n,\mathbf{k}}\right| \frac{\partial\hat{H}}{\partial\mathbf{k}} \left|\varphi_{n,\mathbf{k}}\right\rangle. \tag{6.12}$$

Now let us suppose for the moment that an electron moves only in the local potential ($\hat{V}_{NL} = 0$). It means that $(1/\hbar)(\partial\hat{H}/\partial\mathbf{k}) = \mathbf{p}/m = \mathbf{v}$, and, therefore, Eq. (6.12) gives the definition of the electron velocity. But when there is also a non-local potential ($\hat{V}_{NL} \neq 0$), then $(1/\hbar)(\partial\hat{H}/\partial\mathbf{k}) \neq \mathbf{p}/m$, and there will be a contribution from the non-local potential to the velocity [294]. Equation (6.12) is general, and, hence, the electron velocity can be defined as [115]:

$$\mathbf{v}_{n,\mathbf{k}} = \frac{1}{\hbar}\frac{\partial\varepsilon_{n,\mathbf{k}}}{\partial\mathbf{k}}, \tag{6.13}$$

or it can be calculated also as:

$$\mathbf{v}_{n,\mathbf{k}} = \frac{1}{\hbar}\left\langle\varphi_{n,\mathbf{k}}\right| \frac{\partial\hat{H}}{\partial\mathbf{k}} \left|\varphi_{n,\mathbf{k}}\right\rangle. \tag{6.14}$$

Thus, the carrier velocity can be computed either by evaluating the numerical derivative of the KS energy values $\varepsilon_{n,\mathbf{k}}$ with respect to $\mathbf{k}$ wavevector, Eq. (6.13), or it can be computed fully *ab initio* by evaluating the matrix element of the derivative of the Hamiltonian with respect to $\mathbf{k}$ wavevector, Eq. (6.14). In the following I will discuss the later case, *i.e. ab initio* calculation of the carrier velocity.

Three terms need to be calculated:

$$\mathbf{v}_{n,\mathbf{k}} = \frac{1}{\hbar}\left\langle\varphi_{n,\mathbf{k}}\right| \frac{\partial\hat{T}}{\partial\mathbf{k}} \left|\varphi_{n,\mathbf{k}}\right\rangle + \frac{1}{\hbar}\left\langle\varphi_{n,\mathbf{k}}\right| \frac{\partial\hat{V}_{loc}}{\partial\mathbf{k}} \left|\varphi_{n,\mathbf{k}}\right\rangle + \frac{1}{\hbar}\left\langle\varphi_{n,\mathbf{k}}\right| \frac{\partial\hat{V}_{NL}}{\partial\mathbf{k}} \left|\varphi_{n,\mathbf{k}}\right\rangle. \tag{6.15}$$

Let us consider the first term in Eq. (6.15). By using the expansion of the KS wavefunctions in plane waves [see Eq. (2.61)], and the fact that $\hat{T} = \mathbf{p}^2/(2m) = -(\hbar^2/2m)\nabla^2$, one will obtain:

$$\langle\varphi_{n,\mathbf{k}}|\hat{T}|\varphi_{n,\mathbf{k}}\rangle = \frac{\hbar^2}{2m}\sum_{\mathbf{G}} |\mathbf{k} + \mathbf{G}|^2\,|c_{n,\mathbf{k}+\mathbf{G}}|^2, \tag{6.16}$$

and, therefore,

$$\left\langle\varphi_{n,\mathbf{k}}\right| \frac{\partial\hat{T}}{\partial k_\alpha} \left|\varphi_{n,\mathbf{k}}\right\rangle = \frac{\hbar^2}{m}\sum_{\mathbf{G}} (\mathbf{k} + \mathbf{G})_\alpha\,|c_{n,\mathbf{k}+\mathbf{G}}|^2\,, \tag{6.17}$$

where the derivative is calculated along the cartesian components of the $\mathbf{k}$ wavevector, $\alpha = x, y, z$. Now let us consider the second term in Eq. (6.15), coming from the local potential:

$$\langle \varphi_{n,\mathbf{k}} | \hat{V}_{loc} | \varphi_{n,\mathbf{k}} \rangle = \sum_{\mathbf{G},\mathbf{G}'} c^*_{n,\mathbf{k}+\mathbf{G}}\, c_{n,\mathbf{k}+\mathbf{G}'} \int \hat{V}(r)\, e^{i(\mathbf{G}'-\mathbf{G})\cdot\mathbf{r}}\, d\mathbf{r}, \tag{6.18}$$

and, therefore,

$$\left\langle \varphi_{n,\mathbf{k}} \right| \frac{\partial \hat{V}_{loc}}{\partial \mathbf{k}} \left| \varphi_{n,\mathbf{k}} \right\rangle = 0. \tag{6.19}$$

And, finally, let us consider the third term in Eq. (6.15), coming from the non-local potential. Let us consider first the matrix element without the derivative:

$$\begin{aligned} \langle \varphi_{n,\mathbf{k}} | \hat{V}_{NL} | \varphi_{n,\mathbf{k}} \rangle &= \sum_{Ilm} D^I_l \langle \varphi_{n,\mathbf{k}} | \beta^I_{lm} \rangle \langle \beta^I_{lm} | \varphi_{n,\mathbf{k}} \rangle \\ &= \sum_{Ilm} \sum_{\mathbf{G},\mathbf{G}'} D^I_l\, c^*_{n,\mathbf{k}+\mathbf{G}}\, c_{n,\mathbf{k}+\mathbf{G}'}\, \tilde{\beta}^I_{lm}(\mathbf{k}+\mathbf{G})\, \tilde{\beta}^{I\,*}_{lm}(\mathbf{k}+\mathbf{G}'), \end{aligned} \tag{6.20}$$

where $\tilde{\beta}^I_{lm}(\mathbf{k}+\mathbf{G})$ is the Fourier transform of the function $\beta^I_{lm}(\mathbf{r}-\boldsymbol{\tau}_I)$, which reads:

$$\tilde{\beta}^I_{lm}(\mathbf{k}+\mathbf{G}) = \int \beta^I_{lm}(\mathbf{r}-\boldsymbol{\tau}_I)\, e^{-i(\mathbf{k}+\mathbf{G})\cdot\mathbf{r}}\, d\mathbf{r}. \tag{6.21}$$

By making a change of variables $\mathbf{r}-\boldsymbol{\tau}_I = \mathbf{r}'$, Eq. (6.21) will read:

$$\tilde{\beta}^I_{lm}(\mathbf{k}+\mathbf{G}) = e^{-i(\mathbf{k}+\mathbf{G})\cdot\boldsymbol{\tau}_I} \int \beta^I_{lm}(\mathbf{r}')\, e^{-i(\mathbf{k}+\mathbf{G})\cdot\mathbf{r}'}\, d\mathbf{r}'. \tag{6.22}$$

Further, let us use the explicit form of the functions $\beta^I_{lm}(\mathbf{r})$, Eq. (6.11), and the expansion of a plane wave in series:

$$e^{i\mathbf{k}\cdot\mathbf{r}} = 4\pi \sum_{lm} i^l\, j_l(|\mathbf{k}\cdot\mathbf{r}|)\, Y^*_{lm}(\theta_k, \varphi_k)\, Y_{lm}(\theta_r, \varphi_r), \tag{6.23}$$

where $j_l(|\mathbf{k}\cdot\mathbf{r}|)$ are the Bessel functions, and $Y_{lm}(\theta,\varphi)$ are the spherical harmonics. Hence, Eq. (6.22) will read:

$$\begin{aligned} \tilde{\beta}^I_{lm}(\mathbf{k}+\mathbf{G}) &= e^{-i(\mathbf{k}+\mathbf{G})\cdot\boldsymbol{\tau}_I} \int d\mathbf{r}\, \delta\hat{V}^I_l(r)\, \chi_l(r)\, Y_{lm}(\theta_r, \varphi_r) \\ &\quad \times 4\pi \sum_{l'm'} (-i)^{l'}\, j^*_{l'}(|\,(\mathbf{k}+\mathbf{G})\cdot\mathbf{r}|)\; Y_{l'm'}(\theta_{k+G}, \varphi_{k+G})\, Y^*_{l'm'}(\theta_r, \varphi_r). \end{aligned} \tag{6.24}$$

Let us use the orthogonality property of spherical harmonics:

$$\int Y^*_{lm}(\theta,\varphi)\, Y_{l'm'}(\theta,\varphi)\, d\Omega = \delta_{ll'}\, \delta_{mm'}, \tag{6.25}$$

and the fact that $\int d\mathbf{r} = \int dr\, r^2 \int d\Omega$. Thus, Eq. (6.24) will read:

$$\begin{aligned}\tilde{\beta}^I_{lm}(\mathbf{k}+\mathbf{G}) &= 4\pi\,(-i)^l\, e^{-i(\mathbf{k}+\mathbf{G})\cdot\boldsymbol{\tau}_I}\, Y_{lm}(\theta_{k+G},\varphi_{k+G}) \\ &\quad\times \int \delta\hat{V}^I_l(r)\,\chi_l(r)\, j^*_l(|\,(\mathbf{k}+\mathbf{G})\cdot\mathbf{r}|)\, r^2\, dr. \end{aligned} \tag{6.26}$$

Equation (6.26) is the final expression for the $\tilde{\beta}^I_{lm}(\mathbf{k}+\mathbf{G})$ functions. From Eq. (6.20) one can calculate the matrix element of the first derivative of the non-local potential. It reads:

$$\begin{aligned}\left\langle\varphi_{n,\mathbf{k}}\right| \frac{\partial\hat{V}_{NL}}{\partial k_\alpha} \left|\varphi_{n,\mathbf{k}}\right\rangle &= \sum_{Ilm}\sum_{\mathbf{G},\mathbf{G}'} D^I_l\, c^*_{n,\mathbf{k}+\mathbf{G}}\, c_{n,\mathbf{k}+\mathbf{G}'} \\ &\quad\times \left[\frac{\partial\tilde{\beta}^I_{lm}(\mathbf{k}+\mathbf{G})}{\partial k_\alpha}\,\tilde{\beta}^{I\,*}_{lm}(\mathbf{k}+\mathbf{G}') + \tilde{\beta}^I_{lm}(\mathbf{k}+\mathbf{G})\,\frac{\partial\tilde{\beta}^{I\,*}_{lm}(\mathbf{k}+\mathbf{G}')}{\partial k_\alpha}\right], \end{aligned} \tag{6.27}$$

where

$$\begin{aligned}\frac{\partial\tilde{\beta}^I_{lm}(\mathbf{k}+\mathbf{G})}{\partial k_\alpha} &= -i\,\tau_{I,\alpha}\,\tilde{\beta}^I_{lm}(\mathbf{k}+\mathbf{G}) \\ &+ 4\pi\,(-i)^l\, e^{-i(\mathbf{k}+\mathbf{G})\cdot\boldsymbol{\tau}_I}\,\frac{\partial Y_{lm}(\theta_{k+G},\varphi_{k+G})}{\partial k_\alpha} \\ &\qquad\times\int \delta\hat{V}^I_l(r)\,\chi_l(r)\, j^*_l(|\,(\mathbf{k}+\mathbf{G})\cdot\mathbf{r}|)\; r^2\, dr \\ &+ 4\pi\,(-i)^l\, e^{-i(\mathbf{k}+\mathbf{G})\cdot\boldsymbol{\tau}_I}\, Y_{lm}(\theta_{k+G},\varphi_{k+G}) \\ &\qquad\times\int \delta\hat{V}^I_l(r)\,\chi_l(r)\,\frac{\partial j^*_l(|\,(\mathbf{k}+\mathbf{G})\cdot\mathbf{r}|)}{\partial|\mathbf{k}+\mathbf{G}|}\,\frac{\partial|\mathbf{k}+\mathbf{G}|}{\partial k_\alpha}\, r^2\, dr\,, \end{aligned} \tag{6.28}$$

where $\alpha = x, y, z$ are the cartesian components, and $\tau_{I,\alpha}$ is the α component of the $\boldsymbol{\tau}_I$ vector.

In conclusion, the carrier velocity can be computed fully *ab initio* by using the definition Eq. (6.14) [or equivalently Eq. (6.15)] and Eqs. (6.17), (6.19) and (6.27). This approach has already been used by P. Gava *et al.* [295] for the calculation of the electron velocity in graphene.

In the next paragraph I will present an extension of the formalism explained above in the case when the spin-orbit coupling effect is included.

6.1.3 (b) Hamiltonian with the spin-orbit coupling

In the relativistic case, the carrier velocity reads:

$$\mathbf{v}_{n,\mathbf{k}} = \frac{1}{\hbar}\left\langle\psi_{n,\mathbf{k}}\right| \frac{\partial\hat{H}}{\partial\mathbf{k}} \left|\psi_{n,\mathbf{k}}\right\rangle, \tag{6.29}$$

where $\psi_{n,\mathbf{k}}(\mathbf{r}) = (\varphi^1_{n,\mathbf{k}}, \varphi^2_{n,\mathbf{k}})$ is the two-component spinor (see Sec. 2.2), and $\varphi^1_{n,\mathbf{k}}$, $\varphi^2_{n,\mathbf{k}}$ are the KS wavefunctions. The spinor components have a Bloch form [see Eq. (2.61)]:

$$\varphi^1_{n,\mathbf{k}}(\mathbf{r}) = \sum_{\mathbf{G}} c^1_{n,\mathbf{k}+\mathbf{G}}\, e^{i(\mathbf{k}+\mathbf{G})\cdot\mathbf{r}}, \qquad \varphi^2_{n,\mathbf{k}}(\mathbf{r}) = \sum_{\mathbf{G}} c^2_{n,\mathbf{k}+\mathbf{G}}\, e^{i(\mathbf{k}+\mathbf{G})\cdot\mathbf{r}}, \tag{6.30}$$

where $c^1_{n,\mathbf{k}+\mathbf{G}}$ and $c^2_{n,\mathbf{k}+\mathbf{G}}$ are the coefficients of the expansion. Since the kinetic operator $\hat{T}$ is local, Eq. (6.17) in the relativistic case reads:

$$\begin{aligned} \left\langle \psi_{n,\mathbf{k}} \right| \frac{\partial \hat{T}}{\partial \mathbf{k}} \left| \psi_{n,\mathbf{k}} \right\rangle &= \left\langle \varphi^1_{n,\mathbf{k}} \right| \frac{\partial \hat{T}}{\partial \mathbf{k}} \left| \varphi^1_{n,\mathbf{k}} \right\rangle + \left\langle \varphi^2_{n,\mathbf{k}} \right| \frac{\partial \hat{T}}{\partial \mathbf{k}} \left| \varphi^2_{n,\mathbf{k}} \right\rangle \\ &= \frac{\hbar^2}{m} \sum_{\mathbf{G}} (\mathbf{k}+\mathbf{G})_\alpha \Big(\left| c^1_{n,\mathbf{k}+\mathbf{G}} \right|^2 + \left| c^2_{n,\mathbf{k}+\mathbf{G}} \right|^2 \Big). \end{aligned} \tag{6.31}$$

The contribution to the carrier velocity from the derivative of the local potential is also zero, like in the non-relativistic case, Eq. (6.19).

Let us consider the last contribution coming from the derivative of the non-local potential. In the relativistic case, Eq. (6.20) reads:

$$\begin{aligned} \langle \psi_{n,\mathbf{k}} | \hat{V}_{NL} | \psi_{n,\mathbf{k}} \rangle &= \sum_{Ilm} D^I_{l,11} \langle \varphi^1_{n,\mathbf{k}} | \beta^I_{lm} \rangle \langle \beta^I_{lm} | \varphi^1_{n,\mathbf{k}} \rangle + \sum_{Ilm} D^I_{l,12} \langle \varphi^1_{n,\mathbf{k}} | \beta^I_{lm} \rangle \langle \beta^I_{lm} | \varphi^2_{n,\mathbf{k}} \rangle \\ &+ \sum_{Ilm} D^I_{l,21} \langle \varphi^2_{n,\mathbf{k}} | \beta^I_{lm} \rangle \langle \beta^I_{lm} | \varphi^1_{n,\mathbf{k}} \rangle + \sum_{Ilm} D^I_{l,22} \langle \varphi^2_{n,\mathbf{k}} | \beta^I_{lm} \rangle \langle \beta^I_{lm} | \varphi^2_{n,\mathbf{k}} \rangle, \end{aligned} \tag{6.32}$$

where we are now dealing with the matrix of $D^I_{l,i}$ coefficients, containing the information about the spin-orbit coupling [see Eq. (2.73)]:

$$\hat{D}^I_l = \begin{pmatrix} D^I_{l,11} & D^I_{l,12} \\ D^I_{l,21} & D^I_{l,22} \end{pmatrix}. \tag{6.33}$$

It can be shown, that Eq. (6.27) in the relativistic case will read:

$$\begin{aligned} \left\langle \varphi_{n,\mathbf{k}} \right| \frac{\partial \hat{V}_{NL}}{\partial k_\alpha} \left| \varphi_{n,\mathbf{k}} \right\rangle &= \sum_{Ilm} \sum_{\mathbf{G},\mathbf{G}'} \Big(D^I_{l,11}\, c^{1\,*}_{n,\mathbf{k}+\mathbf{G}}\, c^1_{n,\mathbf{k}+\mathbf{G}'} + D^I_{l,12}\, c^{1\,*}_{n,\mathbf{k}+\mathbf{G}}\, c^2_{n,\mathbf{k}+\mathbf{G}'} \\ &\qquad + D^I_{l,21}\, c^2_{n,\mathbf{k}+\mathbf{G}}\, c^{1\,*}_{n,\mathbf{k}+\mathbf{G}'} + D^I_{l,22}\, c^{2\,*}_{n,\mathbf{k}+\mathbf{G}}\, c^2_{n,\mathbf{k}+\mathbf{G}'} \Big) \\ &\times \left[\frac{\partial \tilde{\beta}^I_{lm}(\mathbf{k}+\mathbf{G})}{\partial k_\alpha}\, \tilde{\beta}^{I\,*}_{lm}(\mathbf{k}+\mathbf{G}') + \tilde{\beta}^I_{lm}(\mathbf{k}+\mathbf{G})\, \frac{\partial \tilde{\beta}^{I\,*}_{lm}(\mathbf{k}+\mathbf{G}')}{\partial k_\alpha} \right]. \end{aligned} \tag{6.34}$$

Thus, in order to calculate the carrier velocity *ab initio*, one has to use the definition Eq. (6.29), and Eqs. (6.31) and (6.34).

6.1.3 (c) Application to Bi

Let us apply the methodology of an *ab initio* calculation of the carrier velocity to bismuth. In order to calculate the plasma frequency in Eq. (6.7), one needs to know the Fermi velocity $\mathbf{v}_F$ of electrons in the vicinity of the three equivalent L points, and the Fermi velocity of holes in the vicinity of the T point [see Fig. 4.3(b)]. Both the electron pocket at L and the hole pocket at T can be approximated by ellipsoids. Each point on the ellipsoid corresponds to different velocities, hence, let us calculate the average velocity of the carriers.

Let us consider an electron pocket, *i.e.* an ellipsoid centered at the L point. Such an ellipsoid is the isosurface of constant energy which corresponds to the Fermi energy. Let us consider three $\mathbf{k}$ points from this ellipsoid, namely along L - Γ, L -W, and L - U [see Fig. 4.3(a)]. For each of these three $\mathbf{k}$ points, let us determine its three velocity components in the cartesian axes (v_x, v_y, v_z), and the modulus of the velocity, $\mathrm{v}_F = \sqrt{\mathrm{v}_x^2 + \mathrm{v}_y^2 + \mathrm{v}_z^2}$. The results are presented in Table 6.1. In order to obtain the average Fermi velocity of electrons, $\langle \mathrm{v}_F \rangle_{el}$, let us take the average of the three velocities listed in Table 6.1. The average Fermi velocity of electrons has been found to be $\langle \mathrm{v}_F \rangle_{\mathrm{e}} \approx 655$ (km/s).

Now let us consider a hole pocket, *i.e.* an ellipsoid centered at the T point, and consider three $\mathbf{k}$ points on this ellipsoid, namely, along T - Γ, T -W, and T - U [see Fig. 4.3(a). The results are presented in Table 6.1. The average Fermi velocity of holes has been found to be $\langle \mathrm{v}_F \rangle_{\mathrm{h}} \approx 363$ (km/s).

	v_x	v_y	v_z	v_F	$\langle \mathrm{v}_F \rangle$
			electrons		
L - Γ	5	3	451	451	
L - W	439	760	0	878	655
L - U	65	37	632	636	
			holes		
T - Γ	0	0	148	148	
T - W	235	407	0	469	363
T - U	410	237	5	473	

Table 6.1: Velocity of electrons on the Fermi surface at the L point, calculated at three $\mathbf{k}$ points lying along high symmetry directions: L - Γ, L - W, and L - U; and the velocity of holes on the Fermi surface at the T point, calculated at three $\mathbf{k}$ points lying along high symmetry directions: T - Γ, T - W, and T - U. Unit of velocity is km/s. (Unpublished)

Thus, it turns out that the average Fermi velocity of electrons is about two times larger than the average Fermi velocity of holes. Since the velocity is the gradient of the band energy, Eq. (6.13), thus the steeper the band the larger the velocity [see Fig. 5.1(b)].

The results of Table 6.1 are in good agreement with the calculations of the carrier velocity as a gradient of the band energy, *i.e.* the evaluation of the numerical derivative [see Eq. (6.13)]. Both calculations agree within $< 1\%$.

	$\mathrm{v}_{F,1}$	$\mathrm{v}_{F,2}$	$\mathrm{v}_{F,3}$	$\langle \mathrm{v}_F \rangle$
		electrons		
Refs. [296, 297]	89	1000	750	613
Ref. [121]	71	1080	669	607
		holes		
Refs. [296, 297]	252	838	838	643

Table 6.2: Experimental values of the modulus of the Fermi velocity, v_F, along three mutually orthogonal directions in the Brillouin zone, and the average value of the Fermi velocity, $\langle \mathrm{v}_F \rangle$. Unit of velocity is km/s. From Refs. [121, 296, 297].

Table 6.2 shows the experimental values of the Fermi velocity of electrons and holes. As can be seen, the theoretical value of the average Fermi velocity of electrons is in quite good agreement with the experimental values, and differs by $\sim 7\%$. Such a difference is due to the limited accuracy of *ab initio* calculations in reproducing tiny electron pockets at the L points (see Sec. 5.1.3). In contrast, there is a factor of ~ 2 between the theoretical and experimental values of the average Fermi velocity of holes. Such a disagreement is due to the fact that the energy at the top of the valence band at the T point, i.e. $T_{45}^{-}(1)$ level, is quite largely overestimated within the DFT-LDA and DFT-GGA with respect to the experimental value (see Fig. 5.1(b) and Table 5.2). This means that the slope of the band crossing the Fermi level near the T point is different, which shows up in the value of the Fermi velocity.

In this thesis, I will use the theoretical values of the average Fermi velocity of electrons and holes, listed in Table 6.1.

6.1.4 Effective mass

The effective mass tensor (EMT) of carriers, corresponding to the energy band n at point $\mathbf{k}$, is defined as [115]:

$$\left[m^{*-1}(\mathbf{k})\right]_{ij} = \pm \frac{1}{\hbar^2} \frac{\partial^2 \varepsilon_{n,\mathbf{k}}}{\partial k_i \partial k_j} = \pm \frac{1}{\hbar} \frac{\partial \mathrm{v}^i_{n,\mathbf{k}}}{\partial k_j}, \tag{6.35}$$

where $i, j = \overline{1,3}$, $\varepsilon_{n,\mathbf{k}}$ is the Kohn-Sham energy, $\mathrm{v}^i_{n,\mathbf{k}}$ is the i-th component of the carrier velocity, and the sign "+" or "-" is chosen according to whether $\mathbf{k}$ is near a band minimum (electrons) or maximum (holes), respectively. In this thesis, the EMT will be calculated from *ab initio* in two steps: (1) *ab initio* calculation of the carrier velocity $\mathbf{v}_{n,\mathbf{k}}$ by means of Eq. (6.29), and (2) numerical differentiation of $\mathbf{v}_{n,\mathbf{k}}$ with respect to $\mathbf{k}$, Eq. (6.35).

6.1.4 (a) The search of true local extrema

In order to investigate the carrier relaxation in Bi after a photoexcitation of 1.6 eV (as will be discussed in Sec. 6.2), let us inspect the Kohn-Sham band structure of Bi

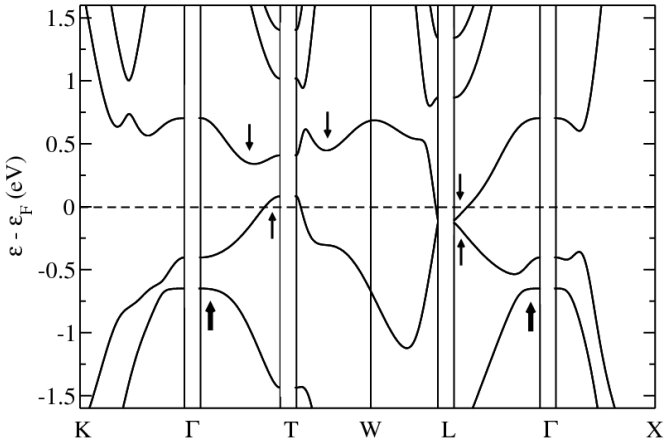

Figure 6.1: Local extrema in the valence and conduction bands near the Fermi level. Black arrows indicate the true local extrema found in the high symmetry directions. From Ref. [245].

near the Fermi level, in the energy range from -1.6 eV to 1.6 eV (see Fig. 6.1). Let us check whether there are true local minima in the lowest conduction bands and true local maxima in the highest valence bands. For the analysis of the band structure, I will use the calculations within the GGA at the GGA theoretical equilibrium lattice parameters, since the GGA gives the closest agreement with the experimental data (see Sec. 5.1.3).

Let us define a true local (TL) maximum (minimum) as the top (bottom) of a valley where the energy band is at an extremum along three principal axes.[4] I have investigated the full Brillouin zone of Bi [see Fig. 4.3(a)] with the precision of $\Delta k = 0.026\,(2\pi/a_0) = 0.033\,(\mathring{A}^{-1})$, and found six TL extrema. Three of them are maxima, at the Γ, T, and L points. The energy value of the maximum at T lies above the Fermi level, while maxima at Γ and L lie below the Fermi level. Two minima lie above the Fermi level, in the lowest conduction band along high symmetry directions, close to the T point.[5] The remaining minimum lies at the L point, below the Fermi level. These six extrema are indicated in Fig. 6.1 by black arrows. Let us compute the tensor of effective mass of these true local extrema.

6.1.4 (b) Effective mass approximation

I have applied the *effective mass approximation* (EMA), Eq. (6.35), to all of the TL extrema. It is worth noting that the bands at the L point in the vicinity of the Fermi level are strongly non-parabolic [4]. Thus, the EMA, strictly speaking, is not applicable. Instead, one usually applies the *Lax two-band model* [298, 12], which is also called the

[4] In the principal axes, the tensorial quantities have a diagonal form, *i.e.* the off-diagonal matrix elements are zero.

[5] The minimum along the Γ-T direction is located 0.25 $\mathring{A}^{-1}$ from the T point ($\varepsilon - \varepsilon_F = 0.34$ eV), and the minimum along the T-W direction is located 0.29 $\mathring{A}^{-1}$ from the T point ($\varepsilon - \varepsilon_F = 0.45$ eV).

ellipsoidal non-parabolic model, or the *non-ellipsoidal non-parabolic model* developed by Cohen [188]. These models are used in the analysis of the magnetoreflection experiments where the magnetic field is applied. Nevertheless, in this thesis I will use the EMA in order to compare the effective mass with the optical mass (see Sec. 6.1.5). The EMA is found to give remarkable results for the effective mass tensor at the L point. Such a good agreement is attributed to the fact that the calculation is *ab initio*.

The EMT of the true local extrema has been calculated in the following way. First, the inverse EMT in the basis of the cartesian framework, $\hat{M}^{-1}_{\mathrm{XYZ}}$, was computed. Each component of the inverse EMT was calculated by means of Eq. (6.35). Second, the inverse EMT was transformed to the basis of the trigonal, binary and bisectrix axes [see Fig. 4.3(a)], $\hat{M}^{-1}_{\mathrm{TBB}}$. Third, the tensor $\hat{M}^{-1}_{\mathrm{TBB}}$ was inverted in order to obtain $\hat{M}_{\mathrm{TBB}}$. And, finally, the tensor $\hat{M}_{\mathrm{TBB}}$ was diagonalized, *i.e.* expressed in the basis of the principal axes, $\hat{M}_{diag}$. In order to make a transformation of the inverse EMT from the cartesian framework (XYZ framework) to the trigonal-binary-bisectrix framework (TBB framework), one has to use the transformation relation:

$$\hat{M}^{-1}_{\mathrm{TBB}} = \hat{A}^T \hat{M}^{-1}_{\mathrm{XYZ}} \hat{A}, \tag{6.36}$$

where $\hat{A}$ is the transformation matrix which reads:

$$\hat{A} = \begin{pmatrix} \cos\alpha & \sin\alpha & 0 \\ \sin\alpha & \cos\alpha & 0 \\ 0 & 0 & 1 \end{pmatrix}, \tag{6.37}$$

where α is the angle between the (X, Y) axes and (binary, bisectrix) axes. Note that the Z axis coincides with the trigonal axis. In the TBB framework, the EMT has the form:

$$\hat{M}_{\mathrm{TBB}} = \begin{pmatrix} m^*_{11} & 0 & 0 \\ 0 & m^*_{22} & m^*_{23} \\ 0 & m^*_{23} & m^*_{33} \end{pmatrix}, \tag{6.38}$$

where 1, 2, and 3 refer to the binary, bisectrix, and trigonal axes, respectively. Indeed, the EMT of the true local extrema at the L point in the TBB framework has the form of Eq. (6.38) [299, 253].

6.1.4 (c) Results

Table 6.3 reports the components of the EMT in the trigonal-binary-bisectrix framework of all six true local extrema in the Kohn-Sham band structure of Bi, as well as the EMT in the framework of the principal axes. The average effective mass was calculated as [300]:

$$\frac{1}{\langle m^* \rangle} = \frac{1}{3}\left(\frac{1}{m^*_1} + \frac{1}{m^*_2} + \frac{1}{m^*_3}\right), \tag{6.39}$$

where the indices 1, 2, and 3 refer to the principal axes. The principal axes are different for the six true local extrema, however, for some of the extrema the principal axes are the

	m^*_{11}	m^*_{22}	m^*_{33}	m^*_{23}	m^*_1	m^*_2	m^*_3	$\langle m^* \rangle$
	Maxima				Maxima			
Γ	48.1	48.1	8.1	0.0	48.1	48.1	8.1	18.1
T	0.06	0.06	0.85	0.0	0.056	0.056	0.850	0.081
L	0.003	0.268	0.010	0.035	0.003	0.27	0.005	0.006
	Maxima				Maxima			
T - Γ	0.14	0.14	1.50	0.0	0.14	0.14	1.50	0.20
T - W	0.94	0.31	2.17	0.76	0.94	0.04	2.44	0.11
L	0.003	0.289	0.010	0.038	0.003	0.29	0.005	0.006

Table 6.3: Effective mass tensor expressed in: (1) the trigonal-binary-bisectrix framework (m^*_{11}, m^*_{22}, m^*_{33}, m^*_{23}), where the indices 1, 2, and 3 refer to the binary, bisectrix, and trigonal axes, respectively; (2) the principal axes (m^*_1, m^*_2, m^*_3), where the indices 1, 2, and 3 refer to the principal axes, which are not the same for all six extrema. $\langle m^* \rangle$ is the average effective mass. Unit is the free electron mass m_0. Extension of the table from Ref. [245].

same. Namely, the maxima at Γ and T, and the minimum along T - Γ have the trigonal, binary and bisectrix axes as their principal axes.

A detailed comparison of the EMT at the T and L points in the framework of the principal axes with other theoretical and experimental works is given in Table 6.4. As can be seen, the agreement is remarkable both for the hole pocket at the T point and for the electron pocket at the L point.

		m_1^*	m_2^*	m_3^*	$\langle m^* \rangle$
		T point			
This work					
Theory	Maximum	0.056	0.056	0.850	0.081
Previous works	Maximum				
Theory[a]		0.0675	0.0675	0.612	0.096
Expt.[b]		0.0644	0.0644	0.696	0.092
Expt.[c]		0.064	0.064	0.69	0.092
Expt.[d]		0.0678	0.0678	0.721	0.097
Expt.[e]		0.063	0.063	0.654	0.090
		L point			
This work					
Theory	Minimum	0.00302	0.294	0.00523	0.006
Theory	Maximum	0.00305	0.273	0.00524	0.006
Previous works	Minimum				
Theory[a]		0.00147	0.198	0.00215	0.003
Expt.[b]		0.00139	0.295	0.00263	0.003
Expt.[c]		0.00113	0.261	0.00295	0.002
Expt.[d]		0.00124	0.260	0.00283	0.003
Previous works	Maximum				
Expt.[b]		0.00651	1.382	0.00993	0.012
Expt.[f]		0.005	1.290	0.01142	0.010
Previous works	at E_F				
Expt.[c]		0.00521	1.207	0.01357	0.011
Expt.[e]		0.00705	1.567	0.00958	0.012

[a] Tight-binding method, Liu *et al.* Ref. [9].

[b] Alfvén-Wave propagation, Isaacson *et al.* Ref. [252].

[c] Shubnikov-de Haas oscillations, Smith *et al.* Ref. [253].

[d] Nernst experiment, Zhu *et al.* Ref. [301].

[e] Far-infrared magnetospectroscopy, Verdun *et al.* Ref. [256].

[f] Alfvén-Wave propagation, Isaacson *et al.* Ref. [299].

Table 6.4: Comparison of the effective mass tensor of the true local minimum at T and true local minimum and maximum at L, expressed in the framework of the principal axes, with other theoretical and experimental works. The indices 1, 2, and 3 refer to the principal axes. $\langle m^* \rangle$ is the average effective mass. Unit is the free electron mass m_0. (Unpublished)

6.1.4 (d) Discussion

As reported in Table 6.3, the average effective mass of the maximum at the Γ point is strikingly large, $\langle m^* \rangle = 18.1\ m_0$, and is approximatively two orders of magnitude larger than the average effective masses at other extrema. The existence of the maximum at Γ turns out to be robust: for instance, when evaluated at a hydrostatic pressure of 10 kbar, the extremum is still located at the Γ point, and the value of the average effective mass becomes even larger, $\langle m^* \rangle = 64\ m_0$ (see Fig. 6.2). Moreover, it has been verified experimentally that there is a true local maximum at the Γ point and that the band is very flat, which essentially indicates the large effective mass [302, 240]. This is the main result of this section, which will be used in Sec. 6.2.

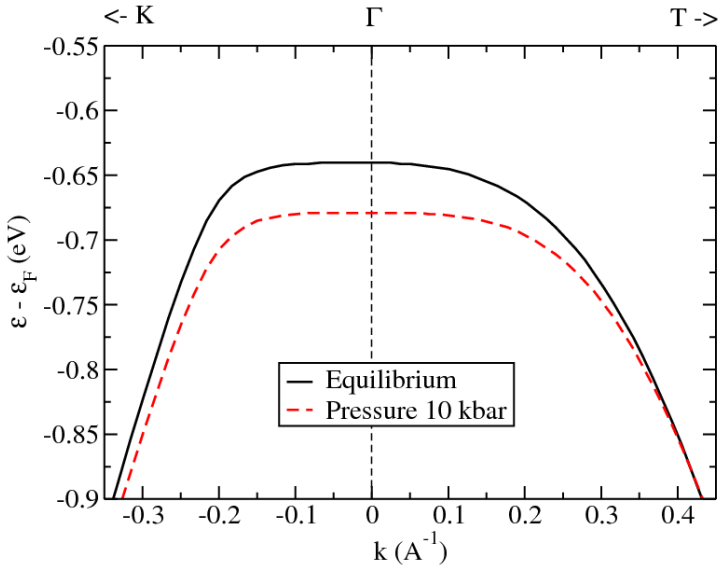

Figure 6.2: Kohn-Sham band structure of Bi including spin-orbit coupling, obtained within the DFT-GGA at the GGA theoretical equilibrium lattice parameters (see Table 5.1) and at the non-equilibrium lattice parameters ($a = 9.203$ a.u., $\alpha = 56.36°$, $u = 0.23197$) which induce a hydrostatic pressure of 10 kbar. Fermi level is at zero energy. (Unpublished)

Finally, I would like to point out that it was noted in Ref. [252] that the true local minimum in the lowest conduction band is exactly at the T point, and has the EMT components in the principal axes 0.059, 0.059, and 0.634 m_0. However, from my DFT calculations, and in agreement with the DFT calculations of Gonze *et al.* [5], I have found that this minimum is slightly displaced along the T - Γ direction (see Fig. 6.1), and has the EMT components in the principal axes 0.14, 0.14, and 1.50 m_0 (see Table 6.3).

6.1.5 Optical mass

6.1.5 (a) Definition

The *optical mass* (also called *optical effective mass*) has been first defined by Cohen [303]:

$$\frac{1}{m^{op}} \equiv \frac{1}{4\pi^3\hbar^2 n} \int \frac{1}{3} \frac{\partial^2 \varepsilon_{n,\mathbf{k}}}{\partial \mathbf{k}^2}\, d\mathbf{k}, \tag{6.40}$$

where m^{op} is the optical mass, n is the density of carriers (electrons and/or holes), and $\varepsilon_{n,\mathbf{k}}$ is the energy. Authors of Refs. [117, 304, 305] used the definition (6.40) for the determination of the optical mass in various experiments with the free-carrier-like response.

In order to interpret the terahertz experiment on photoexcited Bi (see Sec. 6.2), I will use a slightly different definition of the optical mass. The starting point is the application of the Drude law [see Eq. (3.41)], under the assumption that the mass does not change after the photoexcitation, to express a change of the carrier density, Δn, after the photoexcitation, and to obtain the corresponding change of the squared plasma frequency, $\Delta\omega_p^2$, at various temperatures T. Thus, I define the optical mass as:

$$\frac{1}{m^{op}} \equiv \frac{\Delta\omega_p^2(T)}{4\pi e^2 \Delta n(T)}, \tag{6.41}$$

where the change of the carrier density $\Delta n(T)$ reads:

$$\Delta n(T) = \int_{-\infty}^{+\infty} \tilde{g}(\varepsilon) \left| f_{\mathrm{FD}}(\varepsilon, T) - f_{\mathrm{FD}}(\varepsilon, T_0) \right| d\varepsilon, \tag{6.42}$$

and the change of the squared plasma frequency $\Delta\omega_p^2(T)$ reads [see Eq. (6.7)]:

$$\Delta\omega_p^2(T) = \frac{4\pi e^2}{3} \mathbf{v}_F^2 \int_{-\infty}^{\infty} \tilde{g}(\varepsilon) \left[\left(-\frac{\partial f_{FD}(\varepsilon, T)}{\partial \varepsilon} \right) - \left(-\frac{\partial f_{FD}(\varepsilon, T_0)}{\partial \varepsilon} \right) \right] d\varepsilon. \tag{6.43}$$

Here, T is the electronic temperature after the photoexcitation of the carriers, T_0=300 K is the temperature at the equilibrium, $\mathbf{v}_F$ is the Fermi velocity of carriers (see Sec. 6.1.3), $f_{FD}(\varepsilon, T) = \{1+\exp[(\varepsilon-\varepsilon_F)/(k_B T)]\}^{-1}$ is the Fermi-Dirac distribution function, and $\tilde{g}(\varepsilon)$ is the *restricted* density of states to the region in the reciprocal space around $\mathbf{k}$ point at which the optical mass is being calculated. Notice that $\Delta n(T)$ and $\Delta\omega_p^2(T)$ are calculated *independently* at various temperatures, and afterwards m^{op} is determined from Eq. (6.41).

Figure 6.3(a) shows the function $|f_{\mathrm{FD}}(\varepsilon, T) - f_{\mathrm{FD}}(\varepsilon, T_0)|$ at several temperatures T, which is used in the calculation of the change of the carrier density $\Delta n(T)$, Eq. (6.42). Note that one has to take a *modulus* of the difference because there are contributions both from electrons and holes. Without the modulus, the contribution from holes would come with the minus sign, which would reduce $\Delta n(T)$. Figure 6.3(b) shows the function $(-\partial f_{FD}(\varepsilon, T)/\partial\varepsilon) - (-\partial f_{FD}(\varepsilon, T_0)/\partial\varepsilon)$ at several temperatures T, which is used in the calculation of the change of the squared plasma frequency $\Delta\omega_p^2(T)$, Eq. (6.43).

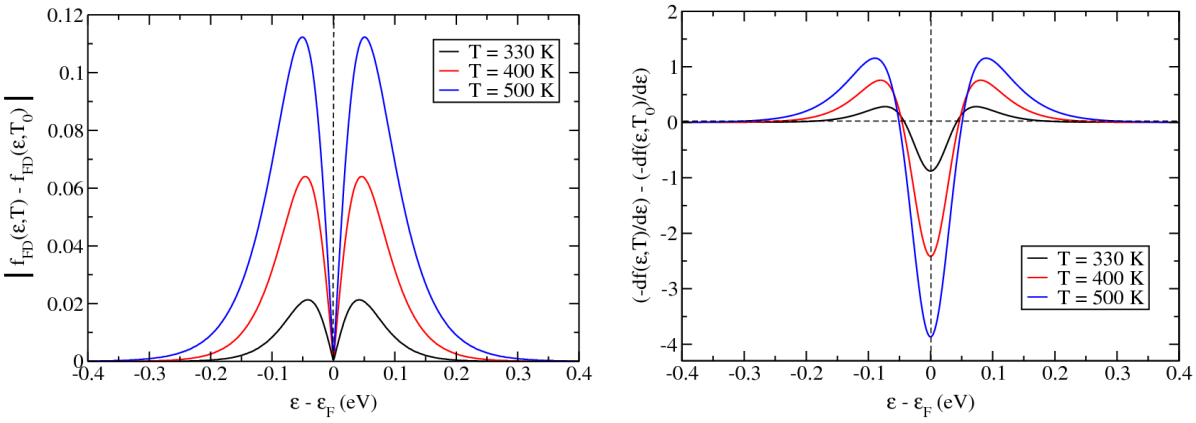

(a) (b)

Figure 6.3: Functions which are used in the calculation of $\Delta n(T)$ and $\Delta\omega_p^2(T)$. (a) Plot of the modulus of the difference between the Fermi-Dirac functions at temperatures T and T_0, (b) Plot of the difference between the derivatives of the Fermi-Dirac functions at temperatures T and T_0. The reference temperature is T_0=300 K. (Unpublished)

The restricted DOS, $\tilde{g}(\varepsilon)$, and the Fermi velocity of carriers, $\mathbf{v}_F$, are specific for each material. The detailed discussion about the calculation of the Fermi velocity was given in Sec. 6.1.3, and the explanation of how to calculate the restricted DOS is given in the Appendix A.3. Both quantities are calculated *ab initio*, and, thus, the optical mass is also determined fully *ab initio*.

6.1.5 (b) Application to Bi

Figure 6.4 shows the plot of the change of the squared plasma frequency, $\Delta\omega_p^2(T)$, and of the change of the carrier density (electrons and holes), $\Delta n(T)$, at several temperatures in the range $330 < T < 500$ K, near the T and L points. This data has been fitted by Eq. (6.41) in order to obtain the values of the optical mass at the T and L points. As a result, I have obtained the following values: $m_{\rm T}^{op} \simeq 0.20\ m_0$ is the optical mass at T, and $m_{\rm L}^{op} \simeq 0.05\ m_0$ is the optical mass at L. Thus, it turns out that the optical mass at the T point is four times larger than optical mass at the L point, $m_{\rm T}^{op}/m_{\rm L}^{op} \simeq 4$.

The optical masses at T and L are larger than corresponding average effective masses (see Table 6.3): $m_{\rm T}^{op}/\langle m^*\rangle_{\rm T} \simeq 2.5$, and $m_{\rm L}^{op}/\langle m^*\rangle_{\rm L} \simeq 8.3$.

Finally, it turns out that the optical masses at T and L are (much) smaller than some of the average effective masses of the true local extrema in the valence and conduction bands away from the Fermi level [see Fig. (6.1)]. In particular, the optical masses at T and L are smaller by two orders of magnitude with respect to the average effective mass of the true local maximum of the valence band at the Γ point, $\langle m^*\rangle_\Gamma = 18.1\, m_0$ (see Sec. 6.1.4). This finding is the main result of this section. This argument will be used in Sec. 6.2 for the interpretation of the time-resolved terahertz experiment on photoexcited Bi.

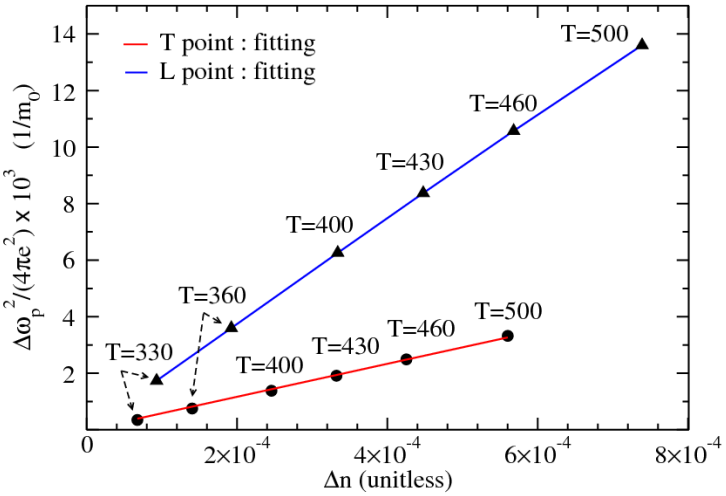

Figure 6.4: Plot of the change of the squared plasma frequency, $\Delta\omega_p^2(T)$, and of the change of the carrier density, $\Delta n(T)$, at several temperatures in the range $330 < T < 500$ K, near the T and L points. Theis data is indicated by circles (for holes) and triangles (for electrons), and are fitted by Eq. (6.41) (solid lines). As a result of the fitting, the following values of the optical mass are obtained: $m_{\mathrm{T}}^{op} \simeq 0.20\ m_0$ at the T point, and $m_{\mathrm{L}}^{op} \simeq 0.05\ m_0$ at the L point. (Unpublished)

6.1.6 Conclusions

In this section I have performed methodological developments for the free-carrier absorption, which will be needed in the next section for a theoretical interpretation of the free-carrier response in the photoexcited bismuth.

According to the classical Drude model, the intraband contribution to the dielectric function is determined by the Drude plasma frequency, which is defined simply by a variation of the charge-density of electrons and holes. However, in this section I have derived a semiclassical expression for the plasma frequency at finite temperatures, $\omega_p(T)$, which accounts for the electronic structure of the material. Namely, the semiclassical $\omega_p(T)$ requires a knowledge of such properties of electrons and holes as their Fermi velocity and the (restricted) density of states. These quantities are directly determined by the Kohn-Sham band structure of Bi. In addition, a knowledge of the effective and optical masses of carriers is essential for the description of the free-carrier response. Furthermore, the spin-orbit coupling appears to be of the biggest and crucial importance for the description of the free-carrier response in Bi.

I have shown that the Fermi velocity of carriers can be calculated *ab initio* by making use of the Hellmann-Feynman theorem: It can be computed as a matrix element of the derivative of the Hamiltonian with respect to the wavevector. Within the plane-wave pseudopotential description of solids, the main difficulty in the calculation of the carrier velocity arises from the non-local part of the pseudopotential. I have generalized this approach to the relativistic case, when the spin-orbit coupling is essential. I have applied the current approach to Bi and have found that *ab initio* Fermi velocity is very close

to the one calculated as a numerical derivative of the energy bands with respect to the wavevector, though the former is more precise. It turns out that the Fermi velocity of electrons is in a good agreement with the experimental one, whereas the Fermi velocity of holes is two times smaller than the experimental one due to the overestimation of the $T_{45}^{-}(1)$ level within the LDA and GGA.

I have analyzed the Kohn-Sham band structure of Bi close to the Fermi level in the range from -1.6 to 1.6 eV, and have found six true local extrema. There are two true local minima in the lowest conduction band close to the T point, one minimum at the L point, one maximum in the second highest valence band at the Γ point, and two maxima in the highest valence band at the T and L points. I have calculated the tensor of effective mass and the average effective mass of these extrema by applying the effective mass approximation. I have found that the maximum at Γ has an extremely large average effective mass, $\langle m^* \rangle_\Gamma = 18.1\, m_0$, which is two orders of magnitude larger than all other masses. Moreover, I have shown that this maximum is robust with respect to a hydrostatic pressure of 10 kbar.

Finally, I have determined optical masses of electrons and holes near the Fermi level at the L and T points, respectively. It appears that the optical mass of electrons is $m_{\mathrm{L}}^{op} \simeq 0.05\, m_0$, and the optical mass of holes is $m_{\mathrm{T}}^{op} \simeq 0.20\, m_0$. These masses are smaller than average effective masses of carriers in the true local extrema of the valence and conduction bands away from the Fermi level, in particular the true local maximum at Γ.

In the next section I will show that the methodological developments for the free-carrier absorption of this section can help to interpret the time-resolved terahertz experiment on bismuth, which shows the free-carrier response.

6.2 Interpretation of time-resolved terahertz experiment

As has been pointed out in Sec. 4.1, bismuth is a reference material for the investigation of lattice and carrier dynamics in out-of-equilibrium conditions. In this section, I will present a study of the carrier dynamics in photoexcited Bi by means of *ab initio* DFT calculations and time-resolved terahertz experiment. Due to the low center frequency of the terahertz pulses, it is possible to probe the Drude-like response of the electron-hole system, which arises from intraband transitions. I will show that *ab initio* calculations and the methodological developments for the free-carrier absorption presented in Sec. 6.1 can explain the Drude-like response in Bi at equilibrium and in the photoexcited state.

This section is organized as follows. In Secs. 6.2.1 and 6.2.2 I will present the experimental results, which have been obtained by our collaborators (T. Kampfrath, J. Faure, C. R. Ast, C. Frischkorn, M. Wolf, and L. Perfetti). Namely, I will show that Bi at equilibrium and in the photoexcited state shows the Drude-like response, which has been determined from the intraband contribution to the dielectric function. In Sec. 6.2.3 I will show that the *ab initio* methodological developments for the free-carrier absorption of Sec. 6.1 allow us to explain the two regimes observed experimentally in temporal evolution of the plasma frequency in photoexcited Bi. In Sec. 6.2.4 I will present a simple model based on the rate equations, which allows us to obtain the relaxation times of photoexcited carriers in Bi from the fit of the experimental data. At the end of the section, I will draw a conclusion.

In Appendix B.2 I give a brief introduction to the terahertz spectroscopy - technique, which has been used by our collaborators in the experiments on Bi. The details of the experiment are also presented in Appendix B.2.

The results, which will be presented in this section, and part of the results of Sec. 6.1, have been published recently in Ref. [245].

6.2.1 Intraband contribution to dielectric function of Bi at equilibrium

Figure 6.5 shows the equilibrium intraband dielectric function $\epsilon_{intra}(\omega)$ [see Eq. (3.42)], where $\mathrm{Re}\,\epsilon_{intra}(\omega)$ was shifted up by an offset ϵ_∞. A fit of the experimental data in Fig. 6.5 with the Drude model [see Eq. (3.43)] gives the following values: the plasma frequency $\hbar\omega_p = 560$ meV, the scattering rate $\hbar\gamma = 37$ meV, and $\varepsilon_\infty = 100$. The reasonably good fit achieved with the Drude model confirms that free carriers dominate $\epsilon_{intra}(\omega)$ in the mid-infrared spectral region.

The Drude response originates from intraband optical transitions. The absorption of a photon is accompanied by the scattering of a charge carrier (electron or hole) with impurities, phonons, or other charge carriers [286]. In principle, two effects may cause deviations from the classical Drude model:

(i) The interband optical transitions. In metals, the onset of interband absorption is associated with transitions from the Fermi level to the next higher empty band, or

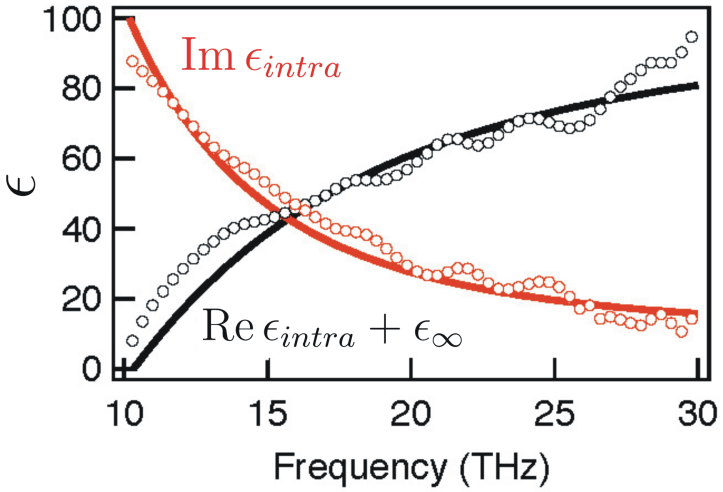

Figure 6.5: The equilibrium intraband dielectric function, $\epsilon_{intra}(\omega)$, measured as a function of frequency (circles), and the result of a fit with the Drude model (solid lines), Eq. (3.43). The real part of the intraband dielectric function, $\mathrm{Re}\,\epsilon_{intra}(\omega)$, was shifted up by an offset $\epsilon_\infty = 100$. Note, 1 THz = 4.14 meV. From Ref. [245].

with transitions from a lower lying occupied band to the Fermi level [113]. In bismuth, it is associated with a vertical transition at the L point from the highest valence band to the Fermi level,[6] and is equal to 67 meV (16 THz) [123]. It should induce additional absorption in the mid-infrared window. However, optical measurements on an extended energy range suggest that the contribution from this term is negligible [123].

(*ii*) The coupling of single particles to plasmons, results in a temperature-dependent plasmaronic absorption [123]. Within the extended Drude model [116], this many-body correction induces a strong dependence of the effective scattering rate on the probing frequency, $\gamma_{eff}(\omega)$. In Bi films, which were used by our collaborators in the experiments, this relative variation of the scattering rate is reduced by the presence of strong extrinsic scattering (due to impurities). As a consequence, the real and imaginary parts of the intraband dielectric function, $\epsilon_{intra}(\omega)$, have been accurately fitted with a constant scattering rate, $\gamma = const$. On the other hand, a nonresonant contribution to the real part of intraband dielectric function, $\mathrm{Re}\,\epsilon_{intra}(\omega)$, results in a frequency-independent offset ϵ_∞ [see Eq. (3.43)].

The plasma frequency, ω_p, and the scattering rate, γ, obtained from the Drude model are larger than the values measured for single crystals of bismuth. According to Armitage *et al.* [121], the plasma frequency and the scattering rate of crystalline bismuth are 400 meV and 5 meV, respectively. Such a discrepancy is due to the granular structure of the polycrystalline Bi film used in the experiments by our collaborators. The high concentration of scattering centers reduces the mean free path of the charge carriers down to

[6]The transition at the L point is not from the *top* of the highest valence band to the Fermi level, but from the point which is lower than the top of the highest valence band, because there is an electron-hole symmetry.

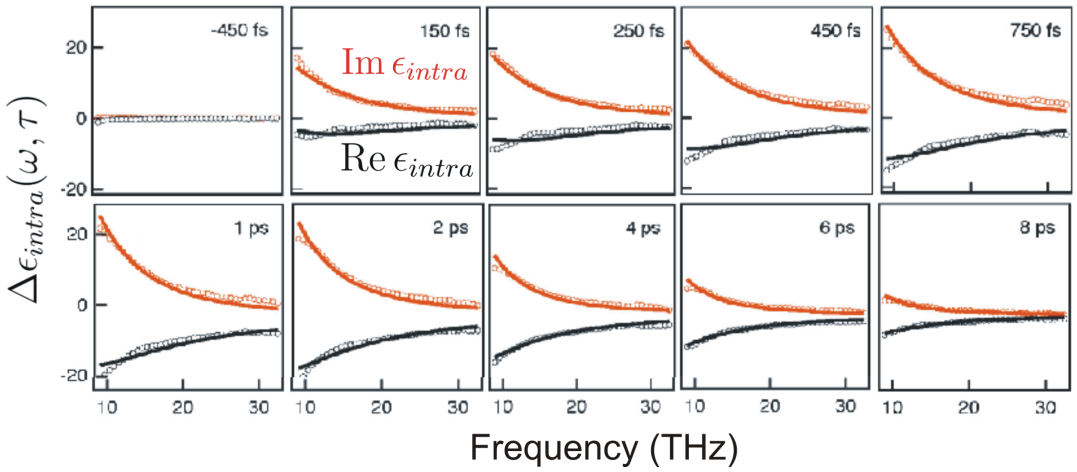

Figure 6.6: Pump-induced change of the intraband dielectric function $\Delta\epsilon_{intra}(\omega,\tau)$ at several pump-probe delays (circles). In each panel, the upper (lower) curve is the imaginary (real) part of the variation of the intraband dielectric function. Fits obtained with the Drude model (solid lines) are superimposed onto the experimental data. From Ref. [245].

100 nm. Despite this fact, all findings on the charge carrier dynamics are expected to be qualitatively valid also for the Bi single crystals.

6.2.2 Intraband contribution to dielectric function of photoexcited Bi

The pump-induced change of the intraband dielectric function at several delays is shown in Fig. 6.6. As can be seen, the Drude model accurately fits the experimental data. This means that the non-equilibrium distribution function of charge carriers also displays a free-carrier response, as in the equilibrium case. The amplitude of the photoinduced signal is very large. This is due to the fact that, since the density of states near the Fermi level is very low [see Fig. 4.5(b)], the photoinduced redistribution of the occupation numbers leads to a large increase in the number of conducting carriers. In Fig. 6.6 the measured $\Delta\epsilon_{intra}(\omega,\tau)$ first increases up to around $\tau = 1$ ps, and afterwards decreases for larger pump-probe delays. Such a non-monotonous dynamics has not been observed in other semimetals like graphite, which instead display a continuous decrease of the photoinduced signal [282].

Our collaborators have verified in their experiment, that the temporal evolution of the THz signal does not show any sign of periodic oscillations due to the coherent A_{1g} phonon mode (see Sec. 4.4). Usually, such a coherent phonon mode affects the optical spectral region by modulating the joint density of states, and consequently can be observed in optical reflectivity experiments [14, 306]. In the current experiment, the lack of oscillations in the temporal evolution of the THz signal indicates that the transient change of

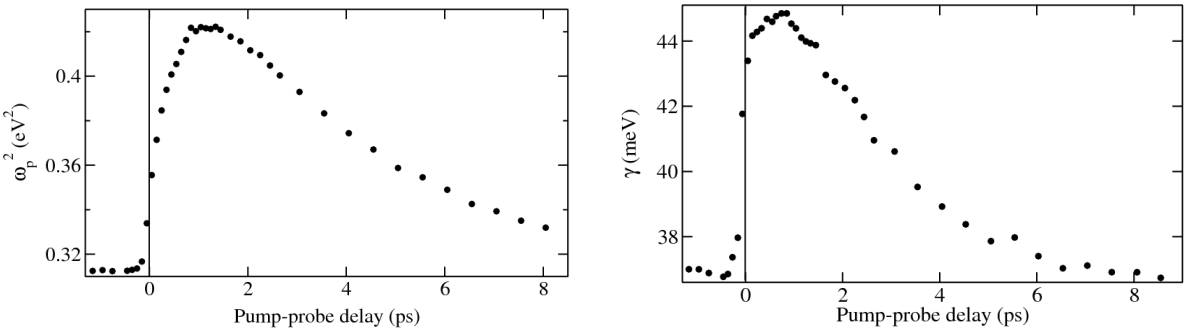

(a) (b)

Figure 6.7: (a) Squared plasma frequency as a function of the pump-probe delay. (b) Scattering rate as a function of the pump-probe delay. From Ref. [245].

the nuclear positions has a negligible effect on the photoinduced plasma frequency $\Delta\omega_p$. Simple considerations on the magnitude of the lattice motion induced by the laser field support this conclusion. According to time-resolved X-ray experiments, a laser pulse of 3 mJ/cm^2 shifts the A_{1g} coordinate u [see Fig. 4.1(a)] by 6 picometers [15]. Scaling this value with respect to the pump fluence of the current experiment (10 μJ/cm^2), I estimate a photoinduced displacement of 0.02 pm. Since the isothermal compressibility of bismuth is 0.0317 GPa^{-1} [4], an applied pressure of 40 bar would induce a displacement of comparable amplitude. The direct comparison to the data of Armitage *et al.* [121] suggests that such a pressure should change the plasma frequency by ~ 1 meV. This indicates that the photoinduced activation of the A_{1g} mode has minor effects on the plasma frequency. Instead, the THz response is strongly dominated by the non-equilibrium distribution of the photoexcited electrons and holes, which leads to the larger increase of the plasma frequency (two orders of magnitude larger that the change due to the coherent phonons).

Figures 6.7(a) and 6.7(b) show the evolution of the squared plasma frequency ω_p^2, and of the Drude scattering rate γ as a function of the pump-probe delay τ. They were extracted from the complex intraband dielectric function by means of Eq. (3.43). Figure 6.7(a) shows that the value of the squared plasma frequency ω_p^2 at equilibrium is 0.31 eV^2, and it increases up to 0.37 eV^2 just after the photoexcitation. It reaches the maximum value of 0.42 eV^2 for a pump-probe delay of 1 ps, and afterwards decays exponentially at larger delays. Thus, there are two regimes in the behaviour of ω_p^2: an initial increase and a subsequent decay. In the next section I will explain why there are two such regimes in the evolution of ω_p^2.

Figure 6.7(b) shows that the value of the scattering rate γ at equilibrium is 37 meV, and it increases up to 44 meV just after the photoexcitation. It reaches the maximum value of 45 meV for a pump-probe delay of 1 ps, and afterwards decays exponentially at larger delays. The exponential decay is faster than that of the squared plasma frequency. The sudden increase of γ in the photoexcited state is due to the larger phase space that becomes available for scattering events. The carrier scattering is dominated by the large defect concentration in the polycrystalline Bi film. Further experiments on high-quality

single crystals of Bi would be necessary in order to observe the behavior of the intrinsic scattering channels.

6.2.3 Theoretical interpretation of two regimes in plasma frequency

In this section I will give a qualitative explanation of the non-monotonic behaviour of the plasma frequency in photoexcited Bi, which has no analogy in other semimetals, *e.g.* graphite [282]. To this end, I will use the results of Sec. 6.1.

As shown in Fig. 6.8(a), direct optical transitions generated by the pump beam of 1.6 eV promote electrons to highly excited states, and create holes in the valence bands. Afterwards, the photoexcited carriers (electrons and holes) "stick" in the local extrema of the band structure, which act as charge reservoirs: electrons reside in the local minima of the lowest conduction bands, and holes reside in the local maxima of the valence bands. I have verified the existence of *true* local extrema in the valence and conduction bands of bismuth in Sec. 6.1.4, and found that there are two true local minima in the lowest conduction band near the T point, and one true local maximum in the second highest valence band at the Γ point (they are indicated by arrows in Fig. 6.8(a)). While residing in these extrema, the trapped carriers barely respond to the THz field.

After the photoexcitation, the carriers are described by a nonequilibrium distribution, which is basically unknown.[7] Afterwards, owing to the carrier-carrier and carrier-phonon scattering,[8] the excited electrons and holes redistribute their internal energy, *i.e.* a thermalization of carriers occurs, after which the charge distribution can be described by the Fermi-Dirac function [269].

How occurs the relaxation of carriers which were trapped in the true local extrema? These carriers start to decay to the Fermi level, namely: excited electrons decay from the two true local minima around the T point to the Fermi level near the L point, due to the intervalley electron-phonon interaction; and excited holes decay from the true local maximum at the Γ point to the Fermi level near the T point, due to the intervalley hole-phonon interaction [see Fig. 6.8(b)]. In turn, the energy states at the Fermi level in the vicinity of the T and L points, strongly respond to the THz field and contribute to the Drude conductivity.

This explanation of the dynamics of the photoexcited electrons and holes would hold only if the average effective masses of the true local extrema are (much) larger than the optical masses near the Fermi level in the vicinity of the T and L points. Indeed, this is the case. In Sec. 6.1.4 and 6.1.5 I have determined these masses, and it turns out that:

- The average effective masses, $\langle m^* \rangle$, of the true local minima of the lowest conduction band along T - Γ and T - W are 0.20 m_0 and 0.11 m_0, respectively (see Table 6.3).

[7] In order to determine the nonequilibrium distribution function, one can either solve the kinetic Boltzmann equation (see, *e.g.* Ref. [307]), or use some models.

[8] By carrier-carrier scattering I mean electron-electron and hole-hole interaction, and by carrier-phonon scattering I mean electron-phonon and hole-phonon interaction. Interaction of electrons and holes results in Auger recombination, and this is not what is meant here; it will be discussed in Sec. 6.2.4.

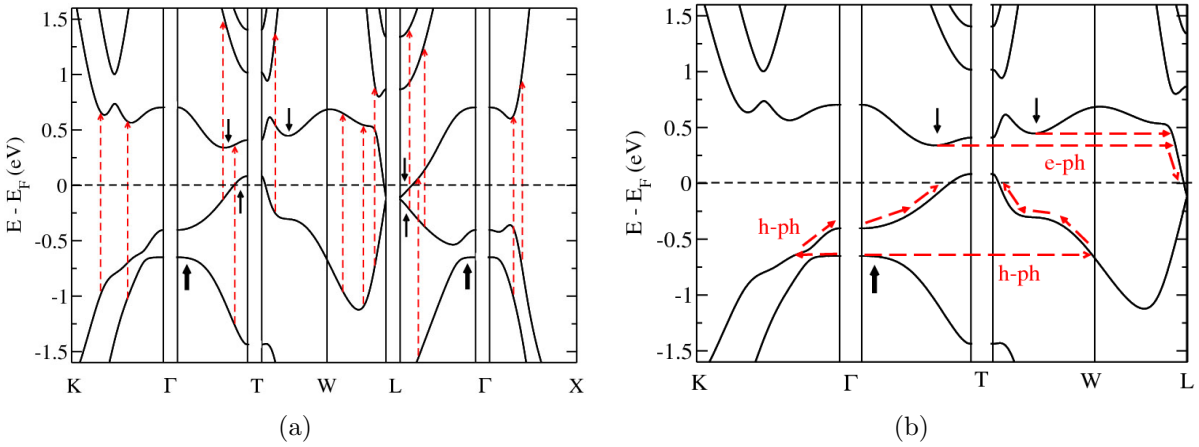

Figure 6.8: (a) Schematic illustration of the direct optical transitions generated by the pump beam of 1.6 eV, which promote electrons to highly excited states, and create holes in the valence bands (red dashed arrows). True local extrema in the valence and conduction bands near the Fermi level are indicated (black arrows). (b) Schematic illustration of decay of electrons and holes from the true local extrema to the Fermi level, due to the electron-phonon (e-ph) and hole-phonon (h-ph) scattering. From Ref. [245].

They are larger than the optical mass near the Fermi level around the L point, which is equal to 0.05 m_0 (see Sec. 6.1.5).

- The average effective mass, $\langle m^* \rangle$, of the true local maximum of the second highest valence band at the Γ point is 18.1 m_0 (see Table 6.3). This mass is larger by two orders of magnitude than the optical mass near the Fermi level around the T point, which is equal to 0.20 m_0 (see Sec. 6.1.5). The decay of holes out of the maximum at Γ is likely dominating the initial rise of the plasma frequency.

One may wonder, how such a dynamics of carriers shows up in the non-monotonous behaviour of the plasma frequency? In the experiments, which have been carried out by our collaborators, the signal is coming from the Fermi level near the T and L points. Immediately after the photoexcitation, the carriers stick in the reservoirs. When they start to decay to the Fermi level [see Fig. 6.8(b)], there is an increase of the conductivity σ, and thus the plasma frequency also increases (see Sec. 6.1.2). Afterwards, when all carriers have decayed to the Fermi level, there is no further increase of ω_p, it reached its maximum value of 0.65 eV [see Fig. 6.7(a)]. Subsequently, the plasma frequency decays due to the electron-hole recombination.

In fact, there are two contributions to the plasma frequency: one coming from the Fermi level near the L point, $\Delta\omega^2_{p,\mathrm{L}}$, and the second one coming from the Fermi level near the T point, $\Delta\omega^2_{p,\mathrm{T}}$. This means that there are two plasmas: the plasma of electrons and the plasma of holes, which coexist simultaneously and interact [111]. Thus, the intraband dielectric function must be described by Eq. (3.42). However, the following approximation is reasonable in the current study: to assume that both types of carriers, electrons and

holes, have the same effective relaxation time τ.[9] Therefore, the problem is reduced to the equation:

$$\Delta\epsilon_{intra}(\omega) = 1 - \frac{\Delta\omega_p^2}{\omega\,(\omega + i/\tau)}, \tag{6.44}$$

where $\Delta\omega_p^2 = \Delta\omega_{p,\mathrm{L}}^2 + \Delta\omega_{p,\mathrm{T}}^2$ is the total change of the squared plasma frequency.

Let us determine the relaxation timescales in bismuth, by considering a simple model based on the rate equations (see, *e.g.*, Ref. [308]).

6.2.4 A model for the temporal evolution of the plasma frequency

Let us assume that there are two characteristic timescales, which determine the temporal evolution of the photoexcited carriers: (*i*) electrons and holes residing in the local extrema decay to the Fermi level with a rate $1/\tau_h$, and (*ii*) the electron-hole plasma recombination at the Fermi level with a rate $1/\tau_l$ (h stands for *heavy carriers*, and l stands for *light carriers*). The simplest model accounting for such a dynamics is described by the following system of rate equations:

$$\frac{\partial n_h}{\partial t} = -\frac{n_h}{\tau_h}, \tag{6.45}$$

$$\frac{\partial \Delta n_l}{\partial t} = -\frac{\Delta n_l}{\tau_l} + \frac{\lambda n_h}{\tau_h}, \tag{6.46}$$

where $n_h(t)$ is the number of heavy carriers in the true local extrema, $\Delta n_l(t)$ is the change of the number of light carriers at the Fermi level near the T and L points, and λ is the carrier multiplication factor accounting for secondary electron-hole pairs generated by impact ionization [309, 310]. Equation (6.45) describes the decay of carriers from the true local extrema where they were stuck. In Eq. (6.46) the first term on the right hand side describes the recombination of the electron-hole plasma at the Fermi level near the T and L points, and the second term describes the augmentation of the number of carriers at the Fermi level due to the fact that carriers decay from the true local extrema by means of the carrier-phonon scattering. In the experiment which was carried out by our collaborators, only Δn_l was probed by the THz field, which is proportional to the pump-induced change in the squared plasma frequency $\Delta\omega_p^2$, due to the Drude law [see Eq. (3.41)]. The initial increase in $\Delta\omega_p^2$ for the pump-probe delays up to 1 ps, can be explained by the fact that the term $\lambda n_h/\tau_h$ is larger than the term $-\Delta n_l/\tau_l$ in Eq. (6.46) [see Fig. 6.7(a)]. Instead, for pump-probe delays larger than 1 ps, the first term dominates the second term, and, thus, there is a decrease of $\Delta\omega_p^2$.

The solutions of Eqs. (6.45) - (6.46) read:

$$n_h(t) = n_h^0\, e^{-t/\tau_h}, \tag{6.47}$$

[9]Both electrons and holes are assumed to have the same scattering rate $\gamma = 1/\tau$, due to the strong extrinsic scattering with impurities in Bi film. Hence, the scattering rage γ (or, equivalently, the relation time τ) is likely very similar for electrons near the L point and for holes near the T point.

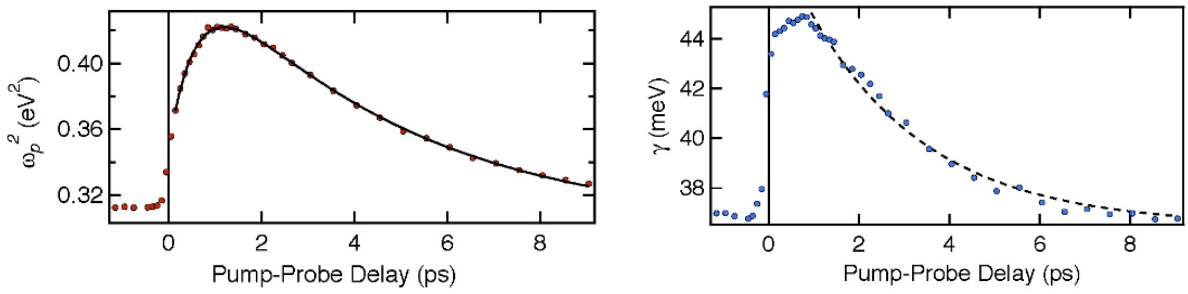

(a) (b)

Figure 6.9: (a) Fit by rate equations of the squared plasma frequency as a function of the pump-probe delay (solid line). (b) Fit by an exponential of the scattering rate as a function of the pump-probe delay (dashed line). From Ref. [245].

$$\Delta n_l(t) = \left(\Delta n_l^0 - \frac{\lambda n_h^0}{\tau_h/\tau_l - 1}\right) e^{-t/\tau_l} + \frac{\lambda n_h^0}{\tau_h/\tau_l - 1}\, e^{-t/\tau_h}, \tag{6.48}$$

where n_h^0 and Δn_l^0 are the values of $n_h(t)$ and $\Delta n_l(t)$ just after the photoexcitation (at $t = 0$), respectively. Figure 6.9(a) shows the curve obtained with the best fitting parameters $\tau_h = 0.6 \pm 0.1$ ps, $\tau_l = 4.0 \pm 0.5$ ps, and $\lambda n_h^0/\Delta n_l^0 = 2.24 \pm 0.5$. The value of λ depends on the relative weights of impact ionization, Auger recombination and carrier-phonon scattering.[10] If the photoexcited carriers could decay solely by phonon emission, the number of carriers would be conserved. On the other hand, the carrier multiplication factor should be larger than one when the carrier-carrier interaction dominates the thermalization process. Simulations on photoexcited graphene [309] and experiments on PbSe [310], suggest that $1 < \lambda < 2$ for an excitation with a photon energy of 1.5 eV. According to this estimation, a consistent fraction of the electrons and holes created during the photoexcitation of bismuth populates the local extrema soon after the photoexcitation.

The timescale of $\tau_h = 0.6$ ps is comparable to the electron-phonon intervalley scattering time observed in semiconductors [311, 312, 279, 119]. In fact, it has been observed that in some semiconductors the electron-phonon intervalley scattering can be a much faster process - as fast as the electron-electron scattering [313]. In bismuth, electron thermalization is a particularly slow process leading to time scales of the order of 0.23 ps for the fluence 20 μJ/cm^2 [314]. Therefore, our time scale of $\tau_h = 0.6$ ps should be attributed both to electron-electron and electron-phonon scattering. Additional *ab initio* calculations are called for in order to disentangle these two time scales [315].

On the other hand, the recombination of the electron-hole plasma at the T and L points is a slower process, τ_l=4 ps. A similar timescale has also been observed in the

[10] *Auger recombination* is the process, in which an electron is scattered from the conduction band to the valence band, while at the same time, the energy is transferred to another electron, which is excited to an energetically higher state within the conduction band. *Impact ionization* is the opposite process (inverse Auger recombination): an electron relaxes to an energetically lower state inducing the excitation of an electron from the valence band to the conduction band. The result of the impact ionization is an increase of the carrier density (carrier multiplication). Both processes also occur for holes in an analogous way. See, *e.g.*, Ref. [309], for more details.

recovery time of transient conductivity [306]. Such an inefficient cooling of the plasma is due to the very low density of states near the Fermi level (see Sec. 4.2.3), which reduces the number of final states available for the electron-phonon and hole-phonon scattering.

Figure 6.9(b) shows the result of the fit by exponential of the Drude scattering rate, γ, as a function of the pump-probe delay. Note that γ slightly increases during the first picosecond, and decreases exponentially at longer delays with a time constant of 2.6 ps. The scattering rate decreases almost twice as fast as the carrier density. As I have already pointed out in Sec. 6.2.2, the carrier scattering is dominated by the large defect concentration in Bi polycrystalline films used by our collaborators. The value of 37 meV corresponds to such a carrier-defect scattering. The sudden increase of γ in the photoexcited state is due to the larger phase space that becomes available for scattering events. Further experiments on high quality single crystals would be necessary to observe the behaviour of the intrinsic scattering channels.

6.2.5 Conclusions

In this section I have studied by means of *ab initio* DFT calculations the free-carrier response in the photoexcited bismuth, which was measured in the time-resolved terahertz experiment. The photoexcitation of Bi leads to an exceptionally large change of the intraband dielectric function, which is found to be accurately described by the Drude model, as has been observed experimentally. The free-carrier dynamics of the photoexcited Bi shows a Drude response that evolves in time, and which yields to a non-monotonic behaviour of the plasma frequency, which has not been observed in other materials.

Methodological developments for the free-carrier absorption of Sec. 6.1 have allowed me to explain two regimes in the temporal evolution of the plasma frequency in the photoexcited Bi. I have found that the reason for the initial increase (for the pump-probe delays ≤ 1 ps) and subsequent decrease of the plasma frequency is the presence of local extrema in the valence and conduction bands, where the photoexcited electrons and holes spend several hundreds of femtoseconds before thermalizing to the Fermi level due to the electron-phonon and hole-phonon interaction. I have shown that the average effective masses of carriers in these true local extrema are significantly larger than the optical masses of carriers around the Fermi level near the L and T points, which explains the fact that photoexcited carriers do not decay immediately to the Fermi level.

The main effect yielding the non-monotonic behaviour of the plasma frequency arises from the accumulation of holes in the true local maximum at Γ in the valence band. As has been shown in Sec. 6.1, the average effective mass of holes in the maximum at Γ is $\langle m^* \rangle_\Gamma = 18.1 m_0$, and it is two orders of magnitude larger the the optical mass of holes near the T point, $m_{\mathrm{T}}^{op} \simeq 0.20 m_0$. The decay of heavy holes out of this maximum, and the decay of less heavy electrons out of the minima in the conduction band near the T point, to the Fermi level at T and L takes place with an inverse rate of 0.6 ps. Such a decay mechanism is similar to the intervalley electron-phonon scattering observed in many semiconductors. The subsequent electron-hole recombination has been found to be a slower process, with a time constant of 4 ps.

Chapter 7

A new method to EELS & application to Bi

In this chapter I will present a new *ab initio* approach to the electron energy-loss spectroscopy (EELS) within the time-dependent density functional perturbation theory (TDDFPT). This approach is an extension of the Liouville-Lanczos approach of Sec. 3.4 from the case of optical absorption ($\mathbf{q} = 0$) to the case of EELS ($\mathbf{q} \neq 0$), and from finite systems (like molecules) to periodic solids. The new approach is based on the iterative solution of the TDDFPT equations within the linear-response theory, by means of the Lanczos recursion method (see Sec. 3.4.2). Techniques based on the density functional perturbation theory (DFPT) [40] are used to avoid the explicit computation of single-particle unoccupied states and inversion of dielectric matrices. This allows for accurate and efficient calculations of the electron energy-loss (EEL) spectra with a computational workload comparable to ground-state DFT calculations. Such an approach has been successfully applied to the calculation of the optical absorption spectra of finite systems (see Sec. 3.4), and, more recently, it has been extended to the calculation of the optical absorption spectra of extended systems by solving the Bethe-Salpeter equation [151].

This chapter is organized as follows. In Sec. 7.1 I will present an extension of the Liouville-Lanczos approach to EELS. The derivation of the theory is coherent with Sec. 3.4 and DFPT theory [40]. In Sec. 7.2 I will demonstrate how the method works on prototypical examples of bulk silicon and bulk aluminum. I will show what are the convergence properties of the new method, and the way by which they can be improved. Finally, in Sec. 7.3 I will apply the new method to bulk bismuth. I will present a detailed analysis of the EEL spectra of bismuth, and discuss the plasmon dispersion, the effect of the spin-orbit coupling, anisotropy, effects of exchange-correlation and crystal local field effects. At the end of the chapter I will draw a conclusion.

The results which will be presented in this chapter, have been obtained in collaboration with Prof. Stefano Baroni and Dr. Ralph Gebauer. These results have not been published yet.

7.1 Methodological developments

In this section I will present an extension of the Liouville-Lanczos approach of Sec. 3.4 to EELS of extended systems. The derivation of the theory is made within the linear-response regime. I will not repeat here the details of the theory of Sec. 3.4, but make a generalization of basic equations to the case of general **k** points for periodic solids (not only the Γ point, as for molecules) and to the non-zero momentum transfer, $\mathbf{q} \neq 0$.

The derivation made in this section is one of the main achievements of my PhD work.

7.1.1 TDDFPT linear-response equations

7.1.1 (a) Monochromatic perturbation

Let us start from the time-dependent Kohn-Sham equations of linear-response TDDFPT, Eqs. (3.74) - (3.88). The time-dependent weak external perturbation is given by a beam of electrons freely propagating in space and time from the source towards the target, which can be described by plane waves $e^{i(\mathbf{q}\cdot\mathbf{r}-\omega t)}$. Let us write the external perturbing potential as:

$$V'_{ext}(\mathbf{r},t) = \int_{-\infty}^{\infty} \tilde{V}'_{ext}(\mathbf{r},\omega)\, e^{-i\omega t}\, d\omega = \int_{0}^{\infty} \left[\tilde{V}'_{ext}(\mathbf{r},\omega)\, e^{-i\omega t} + c.c.\right] d\omega, \tag{7.1}$$

where $\tilde{V}'_{ext}(\mathbf{r},\omega)$ can be further decomposed into Fourier monochromatic **q** components:[1]

$$\tilde{V}'_{ext}(\mathbf{r},\omega) = \sum_{\mathbf{q}}^{1\text{BZ}} e^{i\mathbf{q}\cdot\mathbf{r}}\, \tilde{v}_{ext,\mathbf{q}}(\mathbf{r},\omega), \qquad \tilde{v}_{ext,\mathbf{q}}(\mathbf{r}+\mathbf{R},\omega) = \tilde{v}_{ext,\mathbf{q}}(\mathbf{r},\omega), \tag{7.2}$$

where $\tilde{v}_{ext,\mathbf{q}}(\mathbf{r},\omega)$ is the lattice-periodic function, and **R** is the radius-vector of the primitive unit cell. In the case of EELS, $\tilde{v}_{ext,\mathbf{q}}(\mathbf{r},\omega) = e^{i\mathbf{G}\cdot\mathbf{r}}$, since the transferred momentum is presented as $\mathbf{Q} = \mathbf{q} + \mathbf{G}$, where $\mathbf{q} \in$ 1BZ, and **G** is the reciprocal lattice vector. If **Q** is small enough and it is in 1BZ, then $\mathbf{Q} = \mathbf{q}$, $\mathbf{G} = \mathbf{0}$, and therefore $\tilde{v}_{ext,\mathbf{q}}(\mathbf{r},\omega) = 1$. Note, the time-dependent external potential is *real*, *i.e.* $V'^{*}_{ext}(\mathbf{r},t) = V'_{ext}(\mathbf{r},t)$. Therefore, in Eq. (7.1) we used the fact that $\tilde{V}'^{*}_{ext}(\mathbf{r},\omega) = \tilde{V}'_{ext}(\mathbf{r},-\omega)$.

The external perturbation $\tilde{V}'_{ext}$ induces the response of the charge-density of the system $\tilde{n}'$ through the response orbitals [see Eq. (3.94)]. In turn, the response charge-density induces the change of the Hartree-plus-XC potential $\tilde{V}'_{H\text{xc}}$ [see Eq. (3.96)]. Thereby, since the external perturbation can be decoupled into the monochromatic **q** components, so can be done with the response charge-density $\tilde{n}'$ [as will be discussed in Sec. 7.1.2(a)], and therefore the Hartree-plus-XC potential also can be split into the monochromatic **q** components:

$$\tilde{V}'_{H\text{xc}}(\mathbf{r},\omega) = \sum_{\mathbf{q}}^{\text{BZ}} e^{i\mathbf{q}\cdot\mathbf{r}}\, \tilde{v}_{H\text{xc},\mathbf{q}}(\mathbf{r},\omega), \qquad \tilde{v}_{H\text{xc},\mathbf{q}}(\mathbf{r}+\text{R},\omega) = \tilde{v}_{H\text{xc},\mathbf{q}}(\mathbf{r},\omega), \tag{7.3}$$

[1] In the electronic beam different electrons have different values of **q**, thus a decomposition of Eq. (7.2) is relevant.

where $\tilde{v}_{H\mathrm{xc},\mathbf{q}}(\mathbf{r},\omega)$ is the lattice-periodic function. Therefore, the potential $\tilde{V}'$ of Eq. (3.80), reads:

$$\tilde{V}'(\mathbf{r},\omega) = \sum_{\mathbf{q}}^{\mathrm{BZ}} e^{i\mathbf{q}\cdot\mathbf{r}}\,\tilde{v}_{\mathbf{q}}(\mathbf{r},\omega), \qquad \tilde{v}_{\mathbf{q}}(\mathbf{r},\omega) = \tilde{v}_{ext,\mathbf{q}}(\mathbf{r},\omega) + \tilde{v}_{H\mathrm{xc},\mathbf{q}}(\mathbf{r},\omega). \tag{7.4}$$

7.1.1 (b) TDDFPT equation for periodic systems

Let us consider the Fourier transform of the linearized time-dependent Kohn-Sham equation (3.87), which reads:

$$(\hat{H}^0 - \varepsilon_v - \hbar\omega)\,\tilde{\varphi}'_v(\mathbf{r},\omega) = -\hat{P}_c\,\tilde{V}'(\mathbf{r},\omega)\,\varphi^0_v(\mathbf{r}), \tag{7.5}$$

where $\hat{H}^0$ is the Hamiltonian of the unperturbed system, ε_v and $\varphi^0_v(\mathbf{r})$ are the Kohn-Sham energy values and wavefunctions, respectively, $\tilde{V}' = \tilde{V}'_{ext} + \tilde{V}'_{H\mathrm{xc}}$, and $\hat{P}_c = \sum_c |\varphi^0_c\rangle\langle\varphi^0_c|$ is the projector on empty states.

In periodic systems, the index v splits into two indices, $\{v\} \equiv \{n,\mathbf{k}\}$, where n indicates the set of valence bands, and $\mathbf{k}$ is a wavevector belonging to the first Brillouin zone. Hence, according to the Bloch theorem [74], the ground-state Kohn-Sham wavefunctions $\varphi^0_{n,\mathbf{k}}(\mathbf{r})$ of Eq. (7.5) read [see Eq. (2.59)]:

$$\varphi^0_{n,\mathbf{k}}(\mathbf{r}) = e^{i\mathbf{k}\cdot\mathbf{r}}\,u^0_{n,\mathbf{k}}(\mathbf{r}), \qquad u^0_{n,\mathbf{k}}(\mathbf{r}+\mathbf{R}) = u^0_{n,\mathbf{k}}(\mathbf{r}), \tag{7.6}$$

where $u^0_{n,\mathbf{k}}(\mathbf{r})$ is the lattice-periodic function. By making use of Eqs. (7.4) and (7.6), one can rewrite Eq. (7.5) as:

$$(\hat{H}^0 - \varepsilon_{n,\mathbf{k}} - \hbar\omega)\,\tilde{\varphi}'_{n,\mathbf{k}}(\mathbf{r},\omega) = -\hat{P}_c \sum_{\mathbf{q}} e^{i(\mathbf{k}+\mathbf{q})\cdot\mathbf{r}}\,\tilde{v}'_{\mathbf{q}}(\mathbf{r},\omega)\,u^0_{n,\mathbf{k}}(\mathbf{r}). \tag{7.7}$$

Let us consider the projector on empty states $\hat{P}_c$, by using the notations of Refs. [40, 316]. In the coordinate representation it reads:

$$\begin{aligned} P_c(\mathbf{r},\mathbf{r}') &= \sum_{n',\mathbf{k}'}^{unocc} \varphi^0_{n',\mathbf{k}'}(\mathbf{r})\,\varphi^{0*}_{n',\mathbf{k}'}(\mathbf{r}') \\ &= \sum_{n',\mathbf{k}'}^{unocc} e^{i\mathbf{k}'\cdot\mathbf{r}}\,u^0_{n',\mathbf{k}'}(\mathbf{r})\,u^{0*}_{n',\mathbf{k}'}(\mathbf{r}')\,e^{-i\mathbf{k}'\cdot\mathbf{r}'} \\ &= \sum_{\mathbf{k}'} e^{i\mathbf{k}'\cdot\mathbf{r}}\,P^{\mathbf{k}'}_c(\mathbf{r},\mathbf{r}')\,e^{-i\mathbf{k}'\cdot\mathbf{r}'}, \end{aligned} \tag{7.8}$$

where the summation is over unoccupied states n', and $P^{\mathbf{k}'}_c(\mathbf{r},\mathbf{r}')$ is the coordinate representation of the projector on empty states at point $\mathbf{k}'$ which reads:

$$\begin{aligned} P^{\mathbf{k}'}_c(\mathbf{r},\mathbf{r}') &= \sum_{n'}^{unocc} u^0_{n',\mathbf{k}'}(\mathbf{r})\,u^{0*}_{n',\mathbf{k}'}(\mathbf{r}') \\ &= \delta(\mathbf{r}-\mathbf{r}') - \sum_{n'}^{occ} u^0_{n',\mathbf{k}'}(\mathbf{r})\,u^{0*}_{n',\mathbf{k}'}(\mathbf{r}'). \end{aligned} \tag{7.9}$$

Thereby, when the projector $\hat{P}_c$ in the form of Eq. (7.8) is applied on the right-hand side of Eq. (7.7), only the term $\mathbf{k}' = \mathbf{k} + \mathbf{q}$ gives a non-zero contribution. Thus, one obtains:

$$(\hat{H}^0 - \varepsilon_{n,\mathbf{k}} - \hbar\omega)\,\tilde{\varphi}'_{n,\mathbf{k}}(\mathbf{r},\omega) = -\sum_{\mathbf{q}} e^{i(\mathbf{k}+\mathbf{q})\cdot\mathbf{r}}\,\hat{P}_c^{\mathbf{k}+\mathbf{q}}\,\tilde{v}'_{\mathbf{q}}(\mathbf{r},\omega)\,u^0_{n,\mathbf{k}}(\mathbf{r}). \tag{7.10}$$

Inspection of the right-hand side of Eq. (7.10) suggests that the response wavefunction $\tilde{\varphi}'_{n,\mathbf{k}}(\mathbf{r},\omega)$ on the left-hand side can be decomposed into the monochromatic $\mathbf{q}$ components as:

$$\tilde{\varphi}'_{n,\mathbf{k}}(\mathbf{r},\omega) = \sum_{\mathbf{q}} \tilde{\varphi}'_{n,\mathbf{k}+\mathbf{q}}(\mathbf{r},\omega) = \sum_{\mathbf{q}} e^{i(\mathbf{k}+\mathbf{q})\cdot\mathbf{r}}\,\tilde{u}'_{n,\mathbf{k}+\mathbf{q}}(\mathbf{r},\omega), \tag{7.11}$$

where $\tilde{u}'_{n,\mathbf{k}+\mathbf{q}}(\mathbf{r},\omega)$ is the lattice-periodic function. Hence, Eq. (7.10) takes the form:

$$(\hat{H}^0 - \varepsilon_{n,\mathbf{k}} - \hbar\omega)\sum_{\mathbf{q}} e^{i(\mathbf{k}+\mathbf{q})\cdot\mathbf{r}}\,\tilde{u}'_{n,\mathbf{k}+\mathbf{q}}(\mathbf{r},\omega) = -\sum_{\mathbf{q}} e^{i(\mathbf{k}+\mathbf{q})\cdot\mathbf{r}}\,\hat{P}_c^{\mathbf{k}+\mathbf{q}}\,\tilde{v}'_{\mathbf{q}}(\mathbf{r},\omega)\,u^0_{n,\mathbf{k}}(\mathbf{r}). \tag{7.12}$$

From Eq. (7.12) it is easy to see that the perturbations of different periodicity, *i.e.* different monochromatic $\mathbf{q}$ components, can be treated independently of each other. Therefore, for a given monochromatic component $\mathbf{q}$ one can solve the equation:

$$(\hat{H}^0_{\mathbf{k}+\mathbf{q}} - \varepsilon_{n,\mathbf{k}} - \hbar\omega)\,\tilde{u}'_{n,\mathbf{k}+\mathbf{q}}(\mathbf{r},\omega) = -\hat{P}_c^{\mathbf{k}+\mathbf{q}}\,\tilde{v}'_{\mathbf{q}}(\mathbf{r},\omega)\,u^0_{n,\mathbf{k}}(\mathbf{r}), \tag{7.13}$$

where $\hat{H}^0_{\mathbf{k}+\mathbf{q}}$ reads [40, 316]:

$$\hat{H}^0_{\mathbf{k}+\mathbf{q}} = e^{-i(\mathbf{k}+\mathbf{q})\cdot\mathbf{r}}\,\hat{H}^0\,e^{i(\mathbf{k}+\mathbf{q})\cdot\mathbf{r}}. \tag{7.14}$$

Equation (7.13) is the direct generalization of static linear-response equation of the density functional perturbation theory to the frequency domain (see Eq. (33) in Ref. [40]).

7.1.1 (c) Complex-conjugate TDDFPT equation for periodic systems

Let us obtain the second linear-response equation, as Eq. (3.88) in the optical case. To this end, let us complex-conjugate Eq. (7.13), and change the signs of $\mathbf{k}$, $\mathbf{q}$ and ω. By making use of the time-reversal symmetry of the unperturbed wavefunctions, $u^{0\,*}_{n,-\mathbf{k}}(\mathbf{r}) = u^0_{n,\mathbf{k}}(\mathbf{r})$, and of the potential, $\tilde{v}'^{\,*}_{-\mathbf{q}}(\mathbf{r},-\omega) = \tilde{v}'_{\mathbf{q}}(\mathbf{r},\omega)$, one obtains:

$$(\hat{H}^0_{\mathbf{k}+\mathbf{q}} - \varepsilon_{n,\mathbf{k}} + \hbar\omega)\,\tilde{u}'^{\,*}_{n,-\mathbf{k}-\mathbf{q}}(\mathbf{r},-\omega) = -\hat{P}_c^{\mathbf{k}+\mathbf{q}}\,\tilde{v}'_{\mathbf{q}}(\mathbf{r},\omega)\,u^0_{n,\mathbf{k}}(\mathbf{r}). \tag{7.15}$$

The response wavefunctions $\tilde{u}'_{n,\mathbf{k}+\mathbf{q}}(\mathbf{r},\omega)$ and $\tilde{u}'^{\,*}_{n,-\mathbf{k}-\mathbf{q}}(\mathbf{r},-\omega)$ satisfy the same equation but for the sign of ω on the left-hand side [cf. Eqs. (7.13) and (7.15)]. Therefore, the system of two coupled linear-response TDDFPT equations reads:

$$(\hat{H}^0_{\mathbf{k}+\mathbf{q}} - \varepsilon_{n,\mathbf{k}} - \hbar\omega)\,\tilde{u}'_{n,\mathbf{k}+\mathbf{q}}(\mathbf{r},\omega) + \hat{P}_c^{\mathbf{k}+\mathbf{q}}\,\tilde{v}'_{H\mathrm{xc},\mathbf{q}}(\mathbf{r},\omega)\,u^0_{n,\mathbf{k}}(\mathbf{r}) = -\hat{P}_c^{\mathbf{k}+\mathbf{q}}\,\tilde{v}'_{ext,\mathbf{q}}(\mathbf{r},\omega)\,u^0_{n,\mathbf{k}}(\mathbf{r}), \tag{7.16}$$

$$(\hat{H}^0_{\mathbf{k}+\mathbf{q}} - \varepsilon_{n,\mathbf{k}} + \hbar\omega)\,\tilde{u}'^{\,*}_{n,-\mathbf{k}-\mathbf{q}}(\mathbf{r},-\omega) + \hat{P}_c^{\mathbf{k}+\mathbf{q}}\,\tilde{v}'_{H\mathrm{xc},\mathbf{q}}(\mathbf{r},\omega)\,u^0_{n,\mathbf{k}}(\mathbf{r}) = -\hat{P}_c^{\mathbf{k}+\mathbf{q}}\,\tilde{v}'_{ext,\mathbf{q}}(\mathbf{r},\omega)\,u^0_{n,\mathbf{k}}(\mathbf{r}). \tag{7.17}$$

Equations (7.16) and (7.17) are generalizations of the optical equations (3.87) and (3.88) to $\mathbf{q} \neq 0$. In general EELS case, when $\tilde{v}'_{ext,\mathbf{q}}(\mathbf{r},\omega) = e^{i\mathbf{G}\cdot\mathbf{r}}$, the right-hand side of the above equations reads, $-\hat{P}_c^{\mathbf{k}+\mathbf{q}}\, e^{i\mathbf{G}\cdot\mathbf{r}}\, u^0_{n,\mathbf{k}}(\mathbf{r})$.[2]

7.1.2 Expression of the electronic response

7.1.2 (a) Response charge-density

To first order in the perturbation, the charge-density reads:

$$n(\mathbf{r},t) = 2\sum_{n,\mathbf{k}} |\varphi_{n,\mathbf{k}}(\mathbf{r},t)|^2 \simeq n^0(\mathbf{r}) + n'(\mathbf{r},t), \tag{7.18}$$

where $\varphi_{n,\mathbf{k}}(\mathbf{r},t)$ is the wavefunction given by Eq. (3.82), $n^0(\mathbf{r})$ is the charge-density of the unperturbed system:

$$n^0(\mathbf{r}) = 2\sum_{n,\mathbf{k}} |\varphi^0_{n,\mathbf{k}}(\mathbf{r})|^2, \tag{7.19}$$

and $n'(\mathbf{r},t)$ is the first-order response charge-density which reads:

$$n'(\mathbf{r},t) = 2\sum_{n,\mathbf{k}} \left[\varphi'_{n,\mathbf{k}}(\mathbf{r},t)\,\varphi^{0*}_{n,\mathbf{k}}(\mathbf{r}) + \varphi'^{*}_{n,\mathbf{k}}(\mathbf{r},t)\,\varphi^0_{n,\mathbf{k}}(\mathbf{r})\right]. \tag{7.20}$$

Notice, since the external time-dependent perturbation is real, the response of the charge-density to such a perturbation is also real, *i.e.* $n'^*(\mathbf{r},t) = n'(\mathbf{r},t)$. By Fourier transforming Eq. (7.20) [see Eqs. (3.85) and (3.86)], one will obtain:

$$\tilde{n}'(\mathbf{r},\omega) = 2\sum_{n,\mathbf{k}} \left[\tilde{\varphi}'_{n,\mathbf{k}}(\mathbf{r},\omega)\,\varphi^{0*}_{n,\mathbf{k}}(\mathbf{r}) + \tilde{\varphi}'^{*}_{n,\mathbf{k}}(\mathbf{r},-\omega)\,\varphi^0_{n,\mathbf{k}}(\mathbf{r})\right]. \tag{7.21}$$

Since the response wavefunctions $\tilde{\varphi}'$ can be decoupled into the monochromatic $\mathbf{q}$ components, Eq. (7.11), so can be done also with the response charge-density $\tilde{n}'$. Therefore, Eq. (7.21) reads:

$$\tilde{n}'(\mathbf{r},\omega) = 2\sum_{n,\mathbf{k},\mathbf{q}} \left[\tilde{\varphi}'_{n,\mathbf{k}+\mathbf{q}}(\mathbf{r},\omega)\,\varphi^{0*}_{n,\mathbf{k}}(\mathbf{r}) + \tilde{\varphi}'^{*}_{n,\mathbf{k}+\mathbf{q}}(\mathbf{r},-\omega)\,\varphi^0_{n,\mathbf{k}}(\mathbf{r})\right]. \tag{7.22}$$

Simple inspection of Eq. (7.22) allows one to identify the first term in parenthesis within the sum as the $+\mathbf{q}$ component of the response charge-density, whereas the second term is the $-\mathbf{q}$ component. This comes from the fact that $\tilde{\varphi}'$ and φ^0 are the Bloch functions

[2] The term $-\hat{P}_c^{\mathbf{k}+\mathbf{q}}\, e^{i\mathbf{G}\cdot\mathbf{r}}\, u^0_{n,\mathbf{k}}(\mathbf{r})$ can be alternatively written as $-\hat{P}_c^{\mathbf{k}+\mathbf{Q}}\, u^0_{n,\mathbf{k}}(\mathbf{r})$, where $\mathbf{Q} = \mathbf{q} + \mathbf{G}$, and on the left-hand side of Eqs. (7.16), (7.17) there will be $\hat{H}^0_{\mathbf{k}+\mathbf{Q}}$, $\hat{P}_c^{\mathbf{k}+\mathbf{Q}}$, $\tilde{v}'_{Hxc,\mathbf{Q}}(\mathbf{r},\omega)$, $\tilde{u}'_{n,\mathbf{k}+\mathbf{Q}}(\mathbf{r},\omega)$, and $\tilde{u}'^{*}_{n,-\mathbf{k}-\mathbf{Q}}(\mathbf{r},-\omega)$.

of wavevectors $\mathbf{k}+\mathbf{q}$ and $\mathbf{k}$, respectively. Indeed, by using Eqs. (7.6) and (7.11), one obtains:

$$\tilde{n}'(\mathbf{r},\omega) = 2\sum_{n,\mathbf{k},\mathbf{q}} \left[e^{i\mathbf{q}\cdot\mathbf{r}}\, \tilde{u}'_{n,\mathbf{k}+\mathbf{q}}(\mathbf{r},\omega)\, u^{0*}_{n,\mathbf{k}}(\mathbf{r}) + e^{-i\mathbf{q}\cdot\mathbf{r}}\, \tilde{u}'^{*}_{n,\mathbf{k}+\mathbf{q}}(\mathbf{r},-\omega)\, u^{0}_{n,\mathbf{k}}(\mathbf{r}) \right]. \tag{7.23}$$

In order to have the two terms in Eq. (7.22) or (7.23) to display the same wavevector, let us change the sign of both $\mathbf{q}$ and $\mathbf{k}$ in the second term.[3] Thus, the response charge-density will read:

$$\tilde{n}'(\mathbf{r},\omega) = \sum_{\mathbf{q}} \tilde{n}'_{\mathbf{q}}(\mathbf{r},\omega) = \sum_{\mathbf{q}} e^{i\mathbf{q}\cdot\mathbf{r}}\, \overline{n}'_{\mathbf{q}}(\mathbf{r},\omega), \tag{7.24}$$

where $\tilde{n}'_{\mathbf{q}}(\mathbf{r},\omega)$ is the monochromatic $\mathbf{q}$ component which reads:

$$\tilde{n}'_{\mathbf{q}}(\mathbf{r},\omega) = 2\sum_{n,\mathbf{k}} \varphi^{0*}_{n,\mathbf{k}}(\mathbf{r}) \left[\tilde{\varphi}'_{n,\mathbf{k}+\mathbf{q}}(\mathbf{r},\omega) + \tilde{\varphi}'^{*}_{n,-\mathbf{k}-\mathbf{q}}(\mathbf{r},-\omega) \right], \tag{7.25}$$

and $\overline{n}'_{\mathbf{q}}(\mathbf{r},\omega)$ is its lattice-periodic part which reads:

$$\overline{n}'_{\mathbf{q}}(\mathbf{r},\omega) = 2\sum_{n,\mathbf{k}} u^{0*}_{n,\mathbf{k}}(\mathbf{r}) \left[\tilde{u}'_{n,\mathbf{k}+\mathbf{q}}(\mathbf{r},\omega) + \tilde{u}'^{*}_{n,-\mathbf{k}-\mathbf{q}}(\mathbf{r},-\omega) \right]. \tag{7.26}$$

Notice, there is a property:

$$\overline{n}'^{*}_{\mathbf{q}}(\mathbf{r},\omega) = \overline{n}'_{-\mathbf{q}}(\mathbf{r},-\omega). \tag{7.27}$$

It is worth noting that none of the monochromatic $\mathbf{q}$ components $\tilde{n}'_{\mathbf{q}}(\mathbf{r},\omega)$ is real. Therefore, they cannot be associated to any physical response charge-density. They are the mathematical tools which allow us to split the problem for each $\mathbf{q}$ and be solved independently.

7.1.2 (b) Response Hartree potential

From the knowledge of $\tilde{n}'(\mathbf{r},\omega)$, one can determine the Hartree and exchange-correlation potentials, Eq. (3.96). Let us consider the Hartree potential. By making a Fourier transformation with respect to the spatial coordinate $\mathbf{r}$, it is easy to show that the lattice-periodic monochromatic $\mathbf{q}$ component of the Hartree potential reads:

$$\tilde{v}'_{H,\mathbf{q}}(\mathbf{r},\omega) = \sum_{\mathbf{G}} e^{i\mathbf{G}\cdot\mathbf{r}}\, \tilde{v}'_{H,\mathbf{q}}(\mathbf{G},\omega) = \sum_{\mathbf{G}} e^{i\mathbf{G}\cdot\mathbf{r}}\, \frac{4\pi e^2}{|\mathbf{q}+\mathbf{G}|^2}\, \overline{n}'_{\mathbf{q}}(\mathbf{G},\omega), \tag{7.28}$$

where $\overline{n}'_{\mathbf{q}}$ is given by Eq. (7.26). If we keep only the $\mathbf{G}=0$ term in the sum of Eq. (7.28) and neglect all the other contributions $\mathbf{G}\neq 0$, it would mean that we have neglected the crystal local-field effects [see Sec. 3.2.3(d)].[4]

[3] In fact, changing the sign of $\mathbf{k}$ is not strictly necessary, but it appears to be convenient for further notational purposes.

[4] The $\mathbf{G}=0$ term in Eq. (7.28), which is the long-rang Coulomb term, makes the difference between EELS and optics (see Secs. 3.3.1 and 3.3.3). Therefore, by neglecting this term, one can calculate the dielectric function for a given $\mathbf{q}$, and describe optical properties in the limit $\mathbf{q}\to 0$.

7.1.3 Quantum Liouville equation

The quantum Liouville equation of Eq. (3.89) can be generalized to $\mathbf{q} \neq 0$, and split into different monochromatic $\mathbf{q}$ components. According to above considerations, the response density-matrix $\tilde{\rho}'$ can be decoupled with respect to $\mathbf{q}$, and its kernel reads:

$$\tilde{\rho}'(\mathbf{r},\mathbf{r}';\omega) = \sum_{\mathbf{q}} \tilde{\rho}'_{\mathbf{q}}(\mathbf{r},\mathbf{r}';\omega) = \sum_{\mathbf{q}} e^{i\mathbf{q}\cdot\mathbf{r}}\, \overline{\rho}'_{\mathbf{q}}(\mathbf{r},\mathbf{r}';\omega), \tag{7.29}$$

where $\tilde{\rho}'_{\mathbf{q}}(\mathbf{r},\mathbf{r}';\omega)$ is the monochromatic $\mathbf{q}$ component which reads [cf. with Eq. (3.93)]:

$$\tilde{\rho}'_{\mathbf{q}}(\mathbf{r},\mathbf{r}';\omega) = 2\sum_{n,\mathbf{k}} \left[\tilde{\varphi}'_{n,\mathbf{k}+\mathbf{q}}(\mathbf{r},\omega)\, \varphi^{0\,*}_{n,\mathbf{k}}(\mathbf{r}') + \tilde{\varphi}'^{\,*}_{n,-\mathbf{k}-\mathbf{q}}(\mathbf{r}',-\omega)\, \varphi^{0\,*}_{n,\mathbf{k}}(\mathbf{r})\right], \tag{7.30}$$

and $\overline{\rho}'_{\mathbf{q}}(\mathbf{r},\mathbf{r}';\omega)$ is its lattice-periodic part which reads:

$$\overline{\rho}'_{\mathbf{q}}(\mathbf{r},\mathbf{r}';\omega) = 2\sum_{n,\mathbf{k}} \left[\tilde{u}'_{n,\mathbf{k}+\mathbf{q}}(\mathbf{r},\omega)\, u^{0\,*}_{n,\mathbf{k}}(\mathbf{r}') + \tilde{u}'^{\,*}_{n,-\mathbf{k}-\mathbf{q}}(\mathbf{r}',-\omega)\, u^{0\,*}_{n,\mathbf{k}}(\mathbf{r})\right]. \tag{7.31}$$

Therefore, the Fourier transform of the linearized quantum Liouville equation will read [see Eq. (3.100)]:

$$(\hbar\omega - \hat{\mathcal{L}}) \cdot \hat{\overline{\rho}}'_{\mathbf{q}}(\mathbf{r},\omega) = [\tilde{v}'_{ext,\mathbf{q}}(\mathbf{r},\omega), \hat{\rho}^0(\mathbf{r})], \tag{7.32}$$

where $\hat{\overline{\rho}}'_{\mathbf{q}}(\mathbf{r},\omega)$ is the lattice-periodic part of the monochromatic $\mathbf{q}$ component of the density-matrix operator, $\tilde{v}'_{ext,\mathbf{q}}(\mathbf{r},\omega)$ is the lattice-periodic part of the monochromatic $\mathbf{q}$ component of the external potential, $\hat{\rho}^0(\mathbf{r})$ is the density-matrix operator of the unperturbed system, and $\hat{\mathcal{L}}$ is the Liouvillian super-operator whose action on $\hat{\overline{\rho}}'_{\mathbf{q}}$ reads:

$$\hat{\mathcal{L}} \cdot \hat{\overline{\rho}}'_{\mathbf{q}} = [\,\hat{H}^0, \hat{\overline{\rho}}'_{\mathbf{q}}\,] + [\,\tilde{v}'_{H\mathrm{xc},\mathbf{q}}\,[\,\hat{\overline{\rho}}'_{\mathbf{q}}\,], \hat{\rho}^0\,]. \tag{7.33}$$

7.1.4 Electronic susceptibility

Our final goal is to determine the susceptibility $\chi(\mathbf{q},\omega)$, which would give access to the loss function, $-\mathrm{Im}[1/\epsilon_{\mathrm{M}}(\mathbf{q},\omega)]$, and thus to the double-differential cross section measured in the EELS experiments [see Eq. (3.69)]. How to determine $\chi(\mathbf{q},\omega)$ within the current formalism? In Sec. 3.4.1(c) I have pointed out that the expectation value of any one-electron operator can be expressed as the trace of its product with the one-electron density-matrix. Therefore, one can define the susceptibility $\chi(\mathbf{q},\omega)$ as [cf. with Eq. (3.102)]:

$$\chi(\mathbf{q},\omega) \equiv \mathrm{Tr}\,[\,\tilde{v}'_{ext,\mathbf{q}}(\mathbf{r},\omega)\,\hat{\overline{\rho}}'_{\mathbf{q}}(\mathbf{r},\omega)\,], \tag{7.34}$$

and it can be rewritten as the scalar product, using Eq. (7.32):

$$\chi(\mathbf{q},\omega) = \left\langle \tilde{v}'_{ext,\mathbf{q}}(\mathbf{r},\omega) \middle| (\hbar\omega - \hat{\mathcal{L}})^{-1} \cdot [\tilde{v}'_{ext,\mathbf{q}}(\mathbf{r},\omega), \hat{\rho}^0(\mathbf{r})] \right\rangle. \tag{7.35}$$

As in the optical case [see Eq. (3.106)], this is the off-diagonal matrix element of the resolvent of the Liouvillian superoperator. It can be efficiently calculated using the Lanczos recursion method, as will be shown in Sec. 7.1.10.

7.1.5 Batch representation

7.1.5 (a) Batch representation of the response charge-density

Similarly to the optical case, one can see that the two sets of response wavefunctions uniquely determine the response charge-density $\overline{n}'_{\mathbf{q}}$, Eq. (7.26), and the coupled equations (7.16) and (7.17), namely:

$$\mathbf{x} = \{x_{n,\mathbf{k}+\mathbf{q}}(\mathbf{r})\} = \{\tilde{u}'_{n,\mathbf{k}+\mathbf{q}}(\mathbf{r},\omega)\}, \tag{7.36}$$

$$\mathbf{y} = \{y_{n,\mathbf{k}+\mathbf{q}}(\mathbf{r})\} = \{\tilde{u}'^{*}_{n,-\mathbf{k}-\mathbf{q}}(\mathbf{r},-\omega)\}, \tag{7.37}$$

which are called *batches*. It is convenient to go to the *standard batch representation* (SBR), by performing a 45° rotation in the space of batches, and define $\mathbf{q} = \{q_{n,\mathbf{k}+\mathbf{q}}(\mathbf{r})\}$ and $\mathbf{p} = \{p_{n,\mathbf{k}+\mathbf{q}}(\mathbf{r})\}$, where

$$q_{n,\mathbf{k}+\mathbf{q}}(\mathbf{r}) = \frac{1}{2}\left[\tilde{u}'_{n,\mathbf{k}+\mathbf{q}}(\mathbf{r},\omega) + \tilde{u}'^{*}_{n,-\mathbf{k}-\mathbf{q}}(\mathbf{r},-\omega)\right], \tag{7.38}$$

$$p_{n,\mathbf{k}+\mathbf{q}}(\mathbf{r}) = \frac{1}{2}\left[\tilde{u}'_{n,\mathbf{k}+\mathbf{q}}(\mathbf{r},\omega) - \tilde{u}'^{*}_{n,-\mathbf{k}-\mathbf{q}}(\mathbf{r},-\omega)\right]. \tag{7.39}$$

In the SBR, the lattice-periodic monochromatic $\mathbf{q}$ component of the response charge-density reads [see Eq. (7.26)]:

$$\overline{n}'_{\mathbf{q}}(\mathbf{r},\omega) = 4\sum_{n,\mathbf{k}} u^{0\,*}_{n,\mathbf{k}}(\mathbf{r})\, q_{n,\mathbf{k}+\mathbf{q}}(\mathbf{r}). \tag{7.40}$$

7.1.5 (b) Quantum Liouville equation in the batch representation

In the SBR, the quantum Liouville equation (7.32), or equivalently the coupled equations (7.16) and (7.17), can be written in the matrix form:

$$\begin{pmatrix} \hbar\omega & -\hat{\mathcal{D}} \\ -\hat{\mathcal{D}} - 2\hat{\mathcal{K}} & \hbar\omega \end{pmatrix} \begin{pmatrix} \mathbf{q} \\ \mathbf{p} \end{pmatrix} = \begin{pmatrix} 0 \\ \{\hat{P}_c^{\mathbf{k}+\mathbf{q}}\, \tilde{v}'_{ext,\mathbf{q}}(\mathbf{r},\omega)\, u^0_{n,\mathbf{k}}(\mathbf{r})\} \end{pmatrix}, \tag{7.41}$$

where the action of the $\hat{\mathcal{D}}$ and $\hat{\mathcal{K}}$ superoperators on the batches of orbitals is defined as:

$$\hat{\mathcal{D}} \cdot q_{n,\mathbf{k}+\mathbf{q}}(\mathbf{r}) = (\hat{H}^0_{\mathbf{k}+\mathbf{q}} - \varepsilon_{n,\mathbf{k}})\, q_{n,\mathbf{k}+\mathbf{q}}(\mathbf{r}), \tag{7.42}$$

and

$$\hat{\mathcal{K}} \cdot q_{n,\mathbf{k}+\mathbf{q}}(\mathbf{r}) = 2\hat{P}_c^{\mathbf{k}+\mathbf{q}} \sum_{n',\mathbf{k}'} \int K_{n\mathbf{k};n'\mathbf{k}'}(\mathbf{r},\mathbf{r}')\, q_{n',\mathbf{k}'+\mathbf{q}}(\mathbf{r}')\, d\mathbf{r}', \tag{7.43}$$

where the kernel $K_{n\mathbf{k};n'\mathbf{k}'}(\mathbf{r},\mathbf{r}')$ reads:

$$K_{n\mathbf{k};n'\mathbf{k}'}(\mathbf{r},\mathbf{r}') = \kappa(\mathbf{r},\mathbf{r}')\, u^0_{n,\mathbf{k}}(\mathbf{r})\, u^{0\,*}_{n',\mathbf{k}'}(\mathbf{r}'), \tag{7.44}$$

where $\kappa(\mathbf{r},\mathbf{r}')$ is the Hartree-plus-XC kernel defined in Eq. (3.97).

7.1.5 (c) Batch representation of the electronic susceptibility

Let us present the susceptibility $\chi(\mathbf{q},\omega)$ in the SBR [see Eq. (7.35)]. The components of the matrix element in Eq. (7.35) in the SBR read:

$$\tilde{v}'_{ext,\mathbf{q}}(\mathbf{r},\omega) \xrightarrow{\text{SBR}} \begin{pmatrix} \{\hat{P}_c^{\mathbf{k}+\mathbf{q}}\,\tilde{v}'_{ext,\mathbf{q}}(\mathbf{r},\omega)\,u^0_{n,\mathbf{k}}(\mathbf{r})\} \\ 0 \end{pmatrix}, \tag{7.45}$$

and

$$[\,\tilde{v}'_{ext,\mathbf{q}}(\mathbf{r},\omega),\hat{\rho}^0(\mathbf{r})\,] \xrightarrow{\text{SBR}} \begin{pmatrix} 0 \\ \{\hat{P}_c^{\mathbf{k}+\mathbf{q}}\,\tilde{v}'_{ext,\mathbf{q}}(\mathbf{r},\omega)\,u^0_{n,\mathbf{k}}(\mathbf{r})\} \end{pmatrix}. \tag{7.46}$$

Hence, the susceptibility $\chi(\mathbf{q},\omega)$ reads:

$$\chi(\mathbf{q},\omega) = \left\langle (\{\hat{P}_c^{\mathbf{k}+\mathbf{q}}\,\tilde{v}'_{ext,\mathbf{q}}\,u^0_{n,\mathbf{k}}\},0) \middle| (\hbar\omega\hat{I}-\hat{\mathcal{L}})^{-1}\cdot(0,\{\hat{P}_c^{\mathbf{k}+\mathbf{q}}\,\tilde{v}'_{ext,\mathbf{q}}\,u^0_{n,\mathbf{k}}\}) \right\rangle, \tag{7.47}$$

where

$$\hat{\mathcal{L}} = \begin{pmatrix} 0 & \hat{\mathcal{D}} \\ \hat{\mathcal{D}}+2\hat{\mathcal{K}} & 0 \end{pmatrix}, \tag{7.48}$$

or, equivalently [see Eq. (7.41)],

$$\chi(\mathbf{q},\omega) = \left\langle (\{\hat{P}_c^{\mathbf{k}+\mathbf{q}}\,\tilde{v}'_{ext,\mathbf{q}}\,u^0_{n,\mathbf{k}}\},0) \middle| \begin{pmatrix} \hbar\omega & -\hat{\mathcal{D}} \\ -\hat{\mathcal{D}}-2\hat{\mathcal{K}} & \hbar\omega \end{pmatrix}^{-1} \begin{pmatrix} 0 \\ \{\hat{P}_c^{\mathbf{k}+\mathbf{q}}\,\tilde{v}'_{ext,\mathbf{q}}\,u^0_{n,\mathbf{k}}\} \end{pmatrix} \right\rangle. \tag{7.49}$$

Such a matrix element can be efficiently calculated using the Lanczos recursion method.

7.1.6 Use of symmetry

One may exploit the symmetry of the system in order to reduce the computational time and the memory requirements of the calculations. In addition to lattice translations, the space group of a crystal contains symmetry operations $\hat{S}$, combining rotations and translations that leave the crystal unchanged: $\hat{S} \equiv \{R|\mathbf{f}\}$, where R is a 3×3 orthogonal matrix, and $\mathbf{f}$ is the fractional translation vector. The rotational part of these operations, R, defines the crystal point group. As a consequence of symmetry, the unperturbed roto-translated orbitals are the orbitals with the rotated Bloch vector [68]:

$$\hat{S}\varphi^0_{n,\mathbf{k}}(\mathbf{r}) = \varphi^0_{n,\mathbf{k}}(R^{-1}\mathbf{r}-\mathbf{f}) = \varphi^0_{n,R\mathbf{k}}(\mathbf{r}). \tag{7.50}$$

The ground-state calculation and the TDDFPT linear-response calculation involve the evaluation of integrals over a grid of $\mathbf{k}$ points in the first Brillouin zone (BZ). By exploiting the symmetry, instead of using all the $\mathbf{k}$ points in the BZ, one can use only those

which belong to the irreducible wedge of the BZ (IBZ). This leads to the appearance in the sum over irreducible $\mathbf{k}$ points of the geometrical factors $w_{\mathbf{k}}$, which are called *weights* [68]. The weights $w_{\mathbf{k}}$ are proportional to the number of vectors in the star, *i.e.* inequivalent $\mathbf{k}$ vectors among all the $\{R\mathbf{k}\}$ vectors generated by the point-group rotations, and are normalized to 1: $\sum_{\mathbf{k}\in\mathrm{IBZ}} w_{\mathbf{k}} = 1$.

7.1.6 (a) Symmetrization of the unperturbed charge-density

The non-symmetrized ground-state charge-density, Eq. (7.19), calculated on the IBZ, reads:

$$n^0(\mathbf{r}) = 2\sum_n \sum_{\mathbf{k}\in\mathrm{IBZ}} w_{\mathbf{k}} \left|\varphi^0_{n,\mathbf{k}}(\mathbf{r})\right|^2. \tag{7.51}$$

The ground-state charge-density is then symmetrized as:

$$n^{0,(s)}(\mathbf{r}) = \frac{1}{N_s}\sum_{\hat{S}} \hat{S} n^0(\mathbf{r}) = \frac{1}{N_s}\sum_{\hat{S}} n^0(R^{-1}\mathbf{r} - \mathbf{f}), \tag{7.52}$$

where the sum runs over all N_s symmetry operations.

7.1.6 (b) Symmetrization of the response charge-density

The symmetrization technique must be applied to all quantities that are expressed as sums over $\mathbf{k}$ points in the BZ. Therefore, one has to symmetrize the lattice-periodic part of the monochromatic $\mathbf{q}$ component of the response charge-density $\overline{n}'_{\mathbf{q}}$, Eq. (7.26). Since the monochromatic $\mathbf{q}$ component of the external perturbation reduces the symmetry of the system to the *small group of* $\mathbf{q}$, $\hat{S}_{\mathbf{q}}$, which leaves the $\mathbf{q}$ vector invariant up to a reciprocal lattice vector $\mathbf{G}$:

$$\hat{S}_{\mathbf{q}}\,\mathbf{q} = \mathbf{q} + \mathbf{G}, \tag{7.53}$$

the unsymmetrized $\overline{n}'_{\mathbf{q}}$ then reads:

$$\overline{n}'_{\mathbf{q}}(\mathbf{r},\omega) = 2\sum_n \sum_{\mathbf{k}\in\mathrm{IBZ}(\mathbf{q})} w_{\mathbf{k}}\, u^{0*}_{n,\mathbf{k}}(\mathbf{r}) \left[\tilde{u}'_{n,\mathbf{k}+\mathbf{q}}(\mathbf{r},\omega) + \tilde{u}'^{*}_{n,-\mathbf{k}-\mathbf{q}}(\mathbf{r},-\omega)\right], \tag{7.54}$$

where the notation IBZ($\mathbf{q}$) indicates the IBZ calculated assuming the small group of $\mathbf{q}$ as a symmetry group, and the weights $w_{\mathbf{k}}$ are calculated accordingly, *i.e.* $\sum_{\mathbf{k}\in\mathrm{IBZ}(\mathbf{q})} w_{\mathbf{k}} = 1$. By using the relation:

$$\hat{S}\left[\tilde{n}'_{\mathbf{q}}(\mathbf{r},\omega)\right] = \tilde{n}'_{\hat{S}\mathbf{q}}(\mathbf{r},\omega) = \tilde{n}'_{\mathbf{q}}(R^{-1}\mathbf{r} - \mathbf{f},\omega), \tag{7.55}$$

where $\tilde{n}'_{\mathbf{q}}(\mathbf{r},\omega)$ is the Bloch function containing the phase and the periodic part, $\tilde{n}'_{\mathbf{q}}(\mathbf{r},\omega) = e^{i\mathbf{q}\cdot\mathbf{r}}\,\overline{n}'_{\mathbf{q}}(\mathbf{r},\omega)$ [see Eq. (7.24)], the symmetrized lattice-periodic monochromatic $\mathbf{q}$ component of the response charge-density reads:

$$\overline{n}'^{(s)}_{\mathbf{q}}(\mathbf{r},\omega) = \frac{1}{N_s(\mathbf{q})}\sum_{\hat{S}_{\mathbf{q}}} e^{i\mathbf{G}\cdot\mathbf{r}}\,\overline{n}'_{\mathbf{q}}(R^{-1}\mathbf{r} - \mathbf{f},\omega). \tag{7.56}$$

where the sum runs over all $N_s(\mathbf{q})$ symmetry operations.

7.1.7 Extension of the formalism to metals

So far I have been assuming that the target is a semiconductor or an insulator, *i.e.* there is an energy band gap between the highest valence band and the lowest conduction band. The current formalist can be straightforwardly extended to the case of a metallic target, *i.e.* when the valence and conduction bands intersect. In the following, I will closely follow the formulation of the static density functional perturbation theory for metals by de Gironcoli [317, 40], which is based on the smearing technique for dealing with Fermi-surface effects.

7.1.7 (a) Unperturbed charge-density

In the smearing approach, each Kohn-Sham energy level is broadened by a smearing function $(1/\sigma)\,\tilde{\delta}(\varepsilon/\sigma)$, which is an approximation to the Dirac δ-function in the limit of vanishing smearing width σ. Many kinds of smearing functions can be used: Fermi-Dirac broadening, Lorentzian, Gaussian [292], Gaussian combined with polynomials [244], or cold smearing functions [293], to recall only some of them. The local density of states resulting from the broadened energy levels will be the original density of states convoluted with the smearing function [see Eq. (7.19)]:

$$n^0(\mathbf{r},\varepsilon) = 2\sum_{n,\mathbf{k}} \frac{1}{\sigma}\,\tilde{\delta}\left(\frac{\varepsilon-\varepsilon_{n,\mathbf{k}}}{\sigma}\right)|\varphi^0_{n,\mathbf{k}}(\mathbf{r})|^2. \tag{7.57}$$

From this basic quantity the electron charge-density follows [317]:

$$n^0(\mathbf{r}) = \int_{-\infty}^{\varepsilon_F} n^0(\mathbf{r},\varepsilon)\,d\varepsilon = 2\sum_{n,\mathbf{k}} \tilde{\theta}\left(\frac{\varepsilon_F-\varepsilon_{n,\mathbf{k}}}{\sigma}\right)|\varphi^0_{n,\mathbf{k}}(\mathbf{r})|^2, \tag{7.58}$$

where $\tilde{\theta}(x) = \int_{-\infty}^{x}\tilde{\delta}(y)dy$ is a smooth approximation to the step function, and ε_F is the Fermi energy which is determined by the normalization to the total number of electrons:

$$N = \int_{-\infty}^{\varepsilon_F} n^0(\varepsilon)\,d\varepsilon = \sum_{n,\mathbf{k}} \tilde{\theta}\left(\frac{\varepsilon_F-\varepsilon_{n,\mathbf{k}}}{\sigma}\right). \tag{7.59}$$

The advantage of this procedure is that after the convolution the (modified) local density of states can be computed accurately on a discrete grid of $\mathbf{k}$ points in the Brillouin zone, provided that the average separation between neighboring eigenvalues is small with respect to the broadening width σ.

7.1.7 (b) Response charge-density

In the metallic case, the lattice-periodic monochromatic $\mathbf{q}$ component of the response charge-density reads [see Eq. (7.26)]:

$$\overline{n}'_{\mathbf{q}}(\mathbf{r},\omega) = 2\sum_{n,\mathbf{k}} \tilde{\theta}_{F;n,\mathbf{k}}\, u^{0\,*}_{n,\mathbf{k}}(\mathbf{r})\left[\tilde{u}'_{n,\mathbf{k}+\mathbf{q}}(\mathbf{r},\omega) + \tilde{u}'^{\,*}_{n,-\mathbf{k}-\mathbf{q}}(\mathbf{r},-\omega)\right], \tag{7.60}$$

where I have used a notation $\tilde{\theta}_{F;n,\mathbf{k}} \equiv \tilde{\theta}[(\varepsilon_F - \varepsilon_{n,\mathbf{k}})/\sigma]$. Let us substitute in Eq. (7.60) the definitions of the linear-response wavefunctions $\tilde{u}'_{n,\mathbf{k}+\mathbf{q}}(\mathbf{r},\omega)$ and $\tilde{u}'^{\,*}_{n,-\mathbf{k}-\mathbf{q}}(\mathbf{r},-\omega)$, Eqs. (7.16) and (7.17), which can be rewritten as:

$$\tilde{u}'_{n,\mathbf{k}+\mathbf{q}}(\mathbf{r},\omega) = \sum_{m\neq n}^{\infty} u^0_{m,\mathbf{k}+\mathbf{q}}(\mathbf{r})\,\frac{\langle u^0_{m,\mathbf{k}+\mathbf{q}}|\tilde{v}'_{\mathbf{q}}(\mathbf{r},\omega)|u^0_{n,\mathbf{k}}\rangle}{\varepsilon_{n,\mathbf{k}} - \varepsilon_{m,\mathbf{k}+\mathbf{q}} + \hbar\omega}, \tag{7.61}$$

and

$$\tilde{u}'^{\,*}_{n,-\mathbf{k}-\mathbf{q}}(\mathbf{r},-\omega) = \sum_{m\neq n}^{\infty} u^0_{m,\mathbf{k}+\mathbf{q}}(\mathbf{r})\,\frac{\langle u^0_{m,\mathbf{k}+\mathbf{q}}|\tilde{v}'_{\mathbf{q}}(\mathbf{r},\omega)|u^0_{n,\mathbf{k}}\rangle}{\varepsilon_{n,\mathbf{k}} - \varepsilon_{m,\mathbf{k}+\mathbf{q}} - \hbar\omega}, \tag{7.62}$$

where $\tilde{v}'_{\mathbf{q}}(\mathbf{r},\omega)$ contains the external and Hartree-plus-XC potentials [see Eq. (7.4)]. Note, the difference between Eqs. (7.61) and (7.62) is the sign of $\hbar\omega$ in the denominator. By exploiting the symmetry between the two contributions in square brackets in Eq. (7.60), it is easy to show that it will read:

$$\overline{n}'_{\mathbf{q}}(\mathbf{r},\omega) = 2\sum_{n,m,\mathbf{k}} \frac{\tilde{\theta}_{F;n,\mathbf{k}} - \tilde{\theta}_{F;m,\mathbf{k}+\mathbf{q}}}{\varepsilon_{n,\mathbf{k}} - \varepsilon_{m,\mathbf{k}+\mathbf{q}} + \hbar\omega}\, u^{0\,*}_{n,\mathbf{k}}(\mathbf{r})\, u^0_{m,\mathbf{k}+\mathbf{q}}(\mathbf{r})\,\langle u^0_{m,\mathbf{k}+\mathbf{q}}|\tilde{v}'_{\mathbf{q}}(\mathbf{r},\omega)|u^0_{n,\mathbf{k}}\rangle, \tag{7.63}$$

Note, $\overline{n}'_{\mathbf{q}}(\mathbf{r},\omega)$ in the form of Eq. (7.63) satisfies the relation Eq. (7.27). In order to avoid the double sum over occupied and empty states in Eq. (7.63), let us use the relation $\tilde{\theta}(x) + \tilde{\theta}(-x) = 1$. It is easy to show that Eq. (7.63) will read:

$$\begin{aligned}\overline{n}'_{\mathbf{q}}(\mathbf{r},\omega) \;=\; & 2\sum_{n,m,\mathbf{k}} (\tilde{\theta}_{F;n,\mathbf{k}} - \tilde{\theta}_{F;m,\mathbf{k}+\mathbf{q}})\,\tilde{\theta}_{m,\mathbf{k}+\mathbf{q};n,\mathbf{k}}\, u^{0\,*}_{n,\mathbf{k}}(\mathbf{r})\, u^0_{m,\mathbf{k}+\mathbf{q}}(\mathbf{r})\,\langle u^0_{m,\mathbf{k}+\mathbf{q}}|\tilde{v}'_{\mathbf{q}}(\mathbf{r},\omega)|u^0_{n,\mathbf{k}}\rangle \\ & \times\left(\frac{1}{\varepsilon_{n,\mathbf{k}} - \varepsilon_{m,\mathbf{k}+\mathbf{q}} + \hbar\omega} + \frac{1}{\varepsilon_{n,\mathbf{k}} - \varepsilon_{m,\mathbf{k}+\mathbf{q}} - \hbar\omega}\right),\end{aligned} \tag{7.64}$$

where the index n runs over the *partially occupied states*, and the index m runs over the *partially unoccupied states*, and $\tilde{\theta}_{m,\mathbf{k}+\mathbf{q};n,\mathbf{k}} \equiv \tilde{\theta}[(\varepsilon_{m,\mathbf{k}+\mathbf{q}} - \varepsilon_{n,\mathbf{k}})/\sigma]$. Equation (7.64) can be further simplified, avoiding the sum over the unoccupied states, by writing

$$\overline{n}'_{\mathbf{q}}(\mathbf{r},\omega) = 2\sum_{n,\mathbf{k}} u^{0\,*}_{n,\mathbf{k}}(\mathbf{r})\left[\overline{u}'_{n,\mathbf{k}+\mathbf{q}}(\mathbf{r},\omega) + \overline{u}'^{\,*}_{n,-\mathbf{k}-\mathbf{q}}(\mathbf{r},-\omega)\right], \tag{7.65}$$

where I have defined new response wavefunctions, $\overline{u}'_{n,\mathbf{k}+\mathbf{q}}(\mathbf{r},\omega)$ and $\overline{u}'^{\,*}_{n,-\mathbf{k}-\mathbf{q}}(\mathbf{r},-\omega)$, which satisfy the following equations, respectively [cf. with Eqs. (7.16) and (7.17)]:

$$(\hat{H}^0_{\mathbf{k}+\mathbf{q}} - \varepsilon_{n,\mathbf{k}} - \hbar\omega)\,\overline{u}'_{n,\mathbf{k}+\mathbf{q}}(\mathbf{r},\omega) = -[\,\tilde{\theta}_{F;n,\mathbf{k}} - \hat{P}^{\mathbf{k}+\mathbf{q}}_{n,\mathbf{k}}\,]\,\tilde{v}'_{\mathbf{q}}(\mathbf{r},\omega)\,u^0_{n,\mathbf{k}}(\mathbf{r}), \tag{7.66}$$

$$(\hat{H}^0_{\mathbf{k+q}} - \varepsilon_{n,\mathbf{k}} + \hbar\omega)\, \overline{u}'^{*}_{n,-\mathbf{k}-\mathbf{q}}(\mathbf{r}, -\omega) = -[\,\tilde{\theta}_{F;n,\mathbf{k}} - \hat{P}^{\mathbf{k+q}}_{n,\mathbf{k}}\,]\, \tilde{v}'_{\mathbf{q}}(\mathbf{r}, \omega)\, u^0_{n,\mathbf{k}}(\mathbf{r}), \tag{7.67}$$

where

$$\hat{P}^{\mathbf{k+q}}_{n,\mathbf{k}} = \sum_{m}^{occ} \beta_{n,\mathbf{k};m,\mathbf{k+q}}\, |u^0_{m,\mathbf{k+q}}\rangle\langle u^0_{m,\mathbf{k+q}}|, \tag{7.68}$$

and

$$\beta_{n,\mathbf{k};m,\mathbf{k+q}} = \tilde{\theta}_{F;n,\mathbf{k}}\, \tilde{\theta}_{n,\mathbf{k};m,\mathbf{k+q}} + \tilde{\theta}_{F;m,\mathbf{k+q}}\, \tilde{\theta}_{m,\mathbf{k+q};n,\mathbf{k}}. \tag{7.69}$$

It can be easily verified that the coefficients $\beta_{n,\mathbf{k};m,\mathbf{k+q}}$ vanish when any of its indices refers to an unoccupied state. Therefore, the operator $\hat{P}^{\mathbf{k+q}}_{n,\mathbf{k}}$ involves only the small number of partially filled bands, and the first-order variation of the wavefunctions and of the charge-density can be computed avoiding any explicit reference to unoccupied states, much in the same way as for insulating materials.

7.1.8 Relativistic case: inclusion of the spin-orbit coupling

In the relativistic case, instead of simple Kohn-Sham wavefunctions there are two-component spinors (see Sec. 2.2). The ground-state and response spinors read, respectively:

$$\psi^0_{n,\mathbf{k}}(\mathbf{r}) = \begin{pmatrix} \varphi^0_{n,\mathbf{k},1}(\mathbf{r}) \\ \varphi^0_{n,\mathbf{k},2}(\mathbf{r}) \end{pmatrix}, \quad \tilde{\psi}'_{n,\mathbf{k}}(\mathbf{r}, \omega) = \begin{pmatrix} \tilde{\varphi}'_{n,\mathbf{k},1}(\mathbf{r}, \omega) \\ \tilde{\varphi}'_{n,\mathbf{k},2}(\mathbf{r}, \omega) \end{pmatrix}, \tag{7.70}$$

where the ground-state wavefunctions $\varphi^0_{n,\mathbf{k},1}$, $\varphi^0_{n,\mathbf{k},2}$ are defined by Eq. (7.6), and the response wavefunctions $\tilde{\varphi}'_{n,\mathbf{k},1}$, $\tilde{\varphi}'_{n,\mathbf{k},2}$ are defined by Eq. (7.11). Thereby, the lattice-periodic part of the monochromatic $\mathbf{q}$ component of the response charge-density reads [see Eqs. (7.26), (7.38) and (7.40)]:

$$\overline{n}'_{\mathbf{q}}(\mathbf{r}, \omega) = 2 \sum_{n,\mathbf{k}} \left[u^{0\,*}_{n,\mathbf{k},1}(\mathbf{r})\, q^1_{n,\mathbf{k+q}}(\mathbf{r}) + u^{0\,*}_{n,\mathbf{k},2}(\mathbf{r})\, q^2_{n,\mathbf{k+q}}(\mathbf{r}) \right], \tag{7.71}$$

where $q^1_{n,\mathbf{k+q}}$ and $q^2_{n,\mathbf{k+q}}$ are defined by Eq. (7.38).

In the relativistic case, the Hamiltonian $\hat{H}^0_{\mathbf{k+q}}$, which figures out in Eq. (7.42), has a potential part given by Eq. (2.73), which contains the spin-orbit contribution.

7.1.9 Calculation of the dielectric function

The Liouville-Lanczos approach to EELS can be applied for the calculation of the real and imaginary part of the dielectric function at any finite value of $\mathbf{q}$. To this end, one has to apply exactly the same approach as described above for EELS, but for one single change: in the Fourier transform of the Hartree potential, Eq. (7.28), one has to drop the long-range Coulomb term which corresponds to $\mathbf{G} = 0$.

The long-range Coulomb term makes the difference between the loss function and the imaginary part of the dielectric function, as has been explained in Secs. 3.3.1 and

3.3.3. Thus, on one hand, when the $\mathbf{G} = 0$ is included, one obtains the susceptibility χ [see Eq. (3.72)], and afterwards one can calculate the inverse dielectric function [see Eqs. (3.32) and (3.71)]. On the other hand, when the $\mathbf{G} = 0$ is neglected in Eq. (7.28), one obtains the susceptibility $\overline{\chi}$ [see Eq. (3.49)], and afterwards one can calculate the dielectric function [see Eq. (3.48)].

Such an approach allows accurate determination of the dielectric function without relying on the Kramers-Kronig relations. I will demonstrate how such an approach works on the example of Bi in Sec. 7.3.5.

7.1.10 Use of Lanczos recursion method

Let us turn back to the question of the evaluation of the susceptibility $\chi(\mathbf{q}, \omega)$ given by Eq. (7.47), which is the off-diagonal matrix element of the resolvent of the Liouvillian superoperator. Such a matrix element can be efficiently calculated using the Lanczos recursion method, much in the same way as in the optical case for the calculation of the dynamical polarizability $\alpha_{ij}(\omega)$ (see Sec. 3.4.2). The application of the Lanczos algorithm is exactly the same as in the optical case. The extension of the Lanczos method to $\mathbf{q} \neq 0$ and $\mathbf{k} \neq 0$ presents no particular difficulty. Thus, I will not repeat here all the details of the method, but give a few remarks.

The starting point is the definition of two two-component Lanczos vectors:

$$\mathbf{V}_i = \begin{pmatrix} q^i_{n,\mathbf{k}+\mathbf{q}} \\ p^i_{n,\mathbf{k}+\mathbf{q}} \end{pmatrix}, \quad \text{and} \quad \mathbf{U}_i = \begin{pmatrix} \tilde{q}^i_{n,\mathbf{k}+\mathbf{q}} \\ \tilde{p}^i_{n,\mathbf{k}+\mathbf{q}} \end{pmatrix}, \tag{7.72}$$

where the index i denotes the number of the Lanczos iteration, n is the energy band index, and $\mathbf{k} + \mathbf{q}$ is the point in the Brillouin zone. Here $q^i_{n,\mathbf{k}+\mathbf{q}}$ and $\tilde{q}^i_{n,\mathbf{k}+\mathbf{q}}$ are the *upper* (or q-like) components of the SBR, and $p^i_{n,\mathbf{k}+\mathbf{q}}$ and $\tilde{p}^i_{n,\mathbf{k}+\mathbf{q}}$ are the *lower* (or p-like) components of the SBR. I define the starting Lanczos vectors $\mathbf{V}_1$ and $\mathbf{U}_1$ according to the right-hand side of Eq. (7.41):

$$\mathbf{V}_1 = \mathbf{U}_1 = \begin{pmatrix} 0 \\ \hat{P}_c^{\mathbf{k}+\mathbf{q}}\, \hat{v}'_{ext,\mathbf{q}}(\mathbf{r}, \omega)\, u^0_{n,\mathbf{k}}(\mathbf{r}) \end{pmatrix}. \tag{7.73}$$

Subsequently, the starting vectors are normalized to unity. Afterwards, one applies the equations (3.131) - (3.136), similarly to the optical case.

Within the Lanczos recursion method, the susceptibility $\chi(\mathbf{q}, \omega)$ reads:

$$\chi(\mathbf{q}, \omega) \simeq \langle \boldsymbol{\zeta}^N_{\mathbf{q}} | (\hbar\omega \hat{I} - \hat{T}^N)^{-1} \cdot \mathbf{e}^N_1 \rangle, \tag{7.74}$$

where N is the maximal number of Lanczos iterations, $\hat{I}$ is the $N \times N$ identity matrix, $\hat{T}^N$ is the tridiagonal matrix defined in Eq. (3.136), $\mathbf{e}^N_1 = (1, 0, \ldots, 0)$ is the unit vector in N-dimensional space, and $\boldsymbol{\zeta}^N_{\mathbf{q}} = (\zeta_{1,\mathbf{q}}, \zeta_{2,\mathbf{q}}, \ldots, \zeta_{N,\mathbf{q}})$ is the vector composed of the coefficients $\zeta_{i,\mathbf{q}}$ which are defined as:

$$\zeta_{i,\mathbf{q}} = \langle (\hat{P}_c^{\mathbf{k}+\mathbf{q}}\, \hat{v}'_{ext,\mathbf{q}}(\mathbf{r}, \omega)\, u^0_{n,\mathbf{k}}(\mathbf{r}), 0) | \mathbf{V}_i \rangle, \tag{7.75}$$

where the index i denotes the number of the Lanczos iteration. All the discussions of Sec. 3.4.2 hold also for the current case,[5] including the extrapolation technique.

7.1.11 Conclusions

I have presented a generalization of the TDDFPT formalism from the optical case ($\mathbf{q} = 0$) to the case of EELS ($\mathbf{q} \neq 0$). I have shown that the electronic susceptibility $\chi(\mathbf{q}, \omega)$ can be rationally calculated with the Lanczos recursion method, without the need to calculate numerous unoccupied states and inversion of large matrices, as is the case in the conventional TDDFT approach (see Sec. 3.3.3). In the next section I will demonstrate how the current approach works on the prototypical examples, silicon and aluminum.

I have implemented the Liouville-Lanczos approach to EELS in the `QUANTUM ESSPRESSO` package [68]. A short summary of the program is given in Appendix C.

[5] An important difference of EELS with respect to the optical case, is that the Tamm-Dancoff approximation fails to describe plasmons in solids [318]. An example of such a failure is the description of EEL spectrum of bulk silicon, where both electron-hole pairs and antipairs need to be taken into account [139].

7.2 Test cases

In this section I proceed to a numerical benchmark of the new methodology of EELS against the test cases of silicon and aluminum, systems for which several TDDFT studies already exist, and whose electron energy-loss (EEL) spectra are known to be accurately described within the adiabatic approximation. My purpose is not to analyze the features of the EEL spectra of silicon and aluminum, which are already rather well understood (see, *e.g.*, Refs. [138, 140, 319] regarding Si, and Refs. [320, 321, 322] regarding Al), nor to dwell on the comparison between theory and experiment, but rather to understand the factors that determine the convergence properties of the new method, and how they can be improved.

7.2.1 Semiconductors: bulk Si

7.2.1 (a) Computational method

Calculations have been performed by using norm-conserving pseudopotential with the Perdew-Zunger (LDA) [34] parameterization of the exchange-correlation functional. The $3s$ and $3p$ electrons were treated as valence electrons. I have used an experimental lattice parameter $a_{exp} = 10.263$ a.u. [323], and the kinetic-energy cutoff $E_{cut} = 16$ Ry. The geometry was specified using the primitive *fcc* unit cell, with two atoms of Si positioned at (0,0,0) and (1/4,1/4,1/4) in cartesian coordinates, in units of the lattice parameter a_{exp}. The first Brillouin zone (BZ) was sampled with a Monkhorst-Pack (MP) $\mathbf{k}$ point mesh [324] (see the discussion below). To plot the EEL spectra I have used a Lorentzian smearing with a broadening parameter σ (see the discussion below).

7.2.1 (b) Convergence of the EEL spectrum

The EEL spectrum must be checked for a convergence with respect to the number of Lanczos iterations and number of $\mathbf{k}$ points in the Brillouin zone. Let us define the convergence criterion: a maximal relative change of the intensity, due to the increase of the convergence parameter (number of Lanczos iterations or number of $\mathbf{k}$ points), constitutes the accuracy with which the EEL spectrum is converged.

Figure 7.1(a) shows the convergence of the EEL spectrum of Si for a momentum transfer $\mathbf{q} = 0.53$ a.u. along the [100] direction, as a function of the number of Lanczos iterations. As can be seen, after 500 iterations the spectrum shows large spurious unphysical wiggles. By increasing the number of Lanczos iterations up to 1500, the wiggles disappear.[6] The maximal relative change of the intensity between the EEL spectra obtained after 500 and 1500 iterations is 21 % at 19.6 eV, which is too large, indicating that 500 iterations is not sufficient for the convergence. The comparison of the maximal

[6]There is a dependence between the number of Lanczos iterations needed to obtain the converged spectrum on one hand, and the kinetic-energy cutoff E_{cut} on the other hand. The larger the cutoff, the more iterations is needed for the convergence [18].

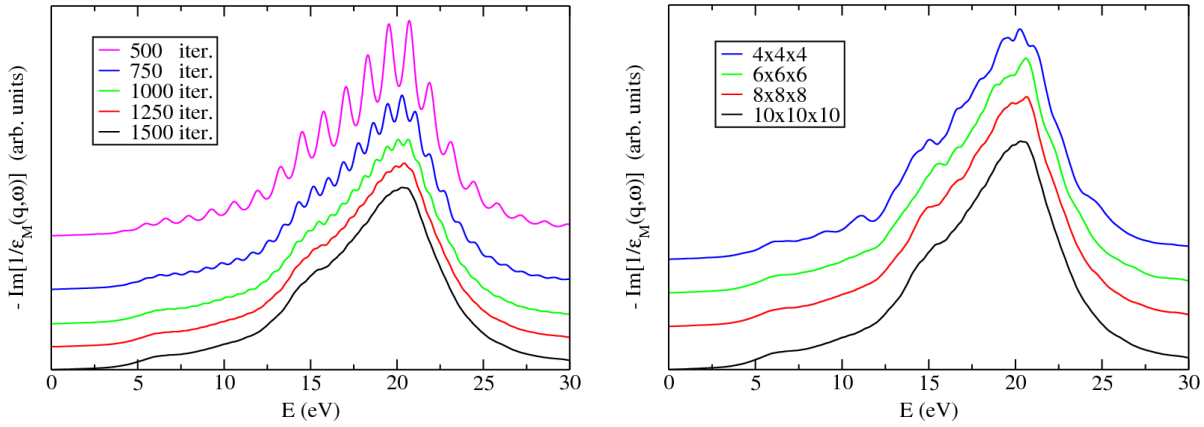

(a) (b)

Figure 7.1: EEL spectrum of bulk silicon, $\mathbf{q} = 0.53\,\text{a.u.}||\,[100]$. (a) Convergence of the EEL spectrum with respect to the number of Lanczos iterations, using a $10 \times 10 \times 10$ Monkhorst-Pack $\mathbf{k}$ point mesh. (b) Convergence of the EEL spectrum with respect to the size of the $\mathbf{k}$ point mesh, for 1500 Lanczos iterations. Both figures have been obtained with a Lorentzian broadening $\sigma = 0.035$ Ry. Curves have been shifted vertically for clarity.

relative change of the intensity between the EEL spectra obtained after 1500 and 2000 iterations gives 0.3 % at 19.8 eV, which is extremely satisfactory. Therefore, in the following I will consider the EEL spectrum obtained after 1500 iterations, which constitutes the accuracy of 0.3 %.

Figure 7.1(b) shows the convergence of the EEL spectrum with respect to the $\mathbf{k}$ point sampling of the Brillouin zone. The $4 \times 4 \times 4$ MP $\mathbf{k}$ point mesh is not dense enough to obtain the converged spectrum, because the maximal relative change of the intensity with respect to the calculation with a $10 \times 10 \times 10$ MP $\mathbf{k}$ point mesh is 5.5 % at 21.4 eV. The maximal relative difference in the intensity between the EEL spectra calculated with $10 \times 10 \times 10$ and $12 \times 12 \times 12$ MP $\mathbf{k}$ point meshes is 1.5 % at 17.6 eV, which is sufficient. Therefore, in the following I will consider the $10 \times 10 \times 10$ MP $\mathbf{k}$ point mesh converged with the accuracy of 1.5 %. Such a mesh corresponds to 110 $\mathbf{k}$ points in the IBZ for the ground-state calculation, and 550 $\mathbf{k}$ points in the IBZ($\mathbf{q}$) for the linear-response calculation (see Sec. 7.1.6).[7]

Figures 7.1(a) and 7.1(b) have been obtained with a Lorentzian broadening parameter $\sigma = 0.035$ Ry. There is a link between the broadening σ and the $\mathbf{k}$ point sampling of the BZ: the smaller the broadening, the larger the number of $\mathbf{k}$ points needed for the convergence.

[7] In the linear-response calculation the number of $\mathbf{k}$ points is doubled, since one has $\mathbf{k}$ and $\mathbf{k}+\mathbf{q}$. Thus, in total there are 1100 points $\mathbf{k}$ and $\mathbf{k}+\mathbf{q}$.

7.2.1 (c) Use of the extrapolation technique

As has been pointed out in Sec. 3.4.2(b), a speed of the convergence of the EEL spectrum with respect to the number of Lanczos iterations can be drastically increased using an extrapolation technique. Figures 7.2(a) and 7.2(b) show a numerical behaviour of the β and ζ coefficients of the Larczos recursion method [see Eqs. (3.133) and (3.138)]. It is seen that the β coefficients tend to a constant,[8] whereas the ζ coefficients rapidly tend towards zero. The fast decrease of ζ coefficients implies that the quality of the calculated spectrum depends only on the first hundred iterations in the present test. However, a relatively large number of iterations is necessary to generate a tridiagonal matrix consisting of β and γ coefficients [see Eq. (3.136)].

Closer inspection of Fig. 7.2(a) shows that the values of the β coefficients are scattered around two close, but distinct, values for odd and even iteration numbers. The average value for odd β's is 8.08 Ry, and the average value for even β's is 8.03 Ry. The average values of β's are approximately equal to half of the kinetic-energy cutoff, which is in this case $E_{cut}/2 = 8$ Ry.

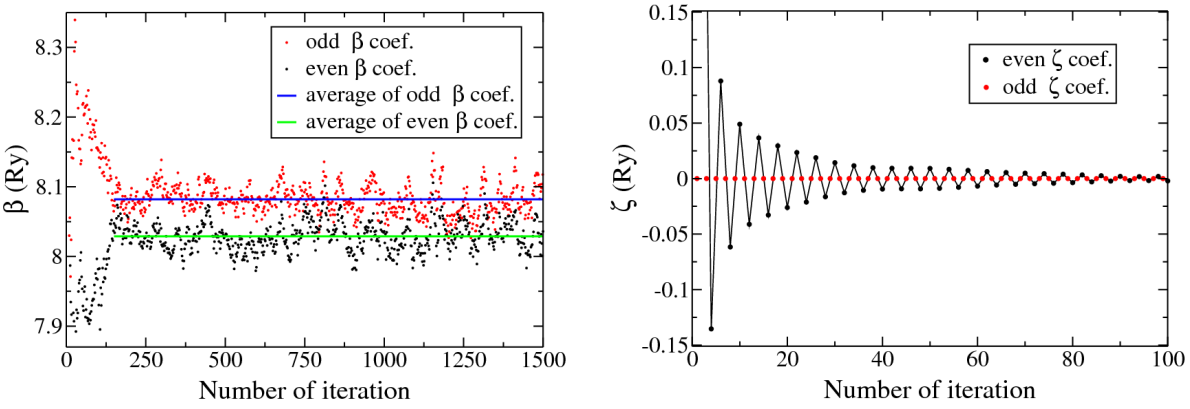

(a) (b)

Figure 7.2: Coefficients of the Lanczos recursion method for bulk Si, $\mathbf{q} = 0.53$ a.u.|| [100]. (a) Numerical behaviour of odd and even β coefficients as functions of the Lanczos iteration number. The horizontal lines are the averages of odd and even β coefficients. (b) Numerical behaviour of odd and even ζ coefficients as functions of the Lanczos iteration number. Solid lines are guides for the eye.

The extrapolation technique consists in the fact that instead of making 1500 iterations in order to obtain the converged EEL spectrum [see Fig. 7.1(a)], one might explicitly make only 400 iterations, and then extrapolate the β coefficients up to, say, 5 000 iterations.[9]

[8] I recall that $\gamma_i = \pm|\beta_i|$. It very rarely occurs that γ_i and β_i have a different sign. Thus, extrapolating them to the same positive value does not affect the accuracy of the extrapolation [see Sec. 3.4.2(b)].

[9] The value of 5 000 has been chosen rather arbitrarily because both the numerical workload and the resulting accuracy depend very little on it, as long as it is large enough. Such a value can be chosen

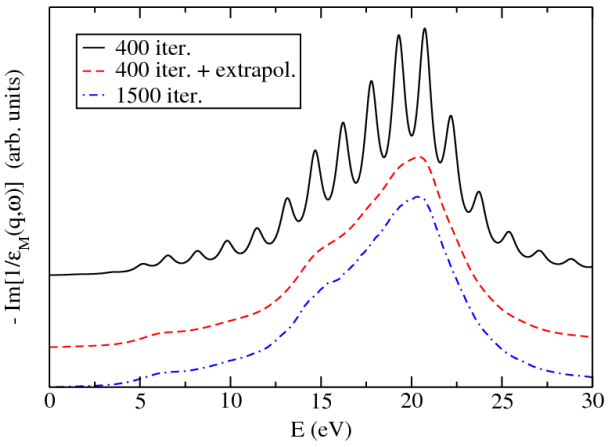

Figure 7.3: Effect of the extrapolation technique on the convergence of the EEL spectrum of bulk Si for $\mathbf{q} = 0.53$ a.u.$||$[100]. Curves have been shifted vertically for clarity.

Thus, the dimension of the tridiagonal matrix $\hat{T}^N$ [see Eq. (3.136)], which is needed for the calculation of the susceptibility $\chi(\mathbf{q},\omega)$ [see Eq. (7.74)], is $5\,000 \times 5\,000$, instead of 400×400. There are two ways to make the extrapolation of the β coefficients from 400 to 5 000, namely, *constant* and *bi-constant* extrapolation. In the constant extrapolation one has to take one average value for both even and odd β coefficients, which is 8.055 Ry, whereas in the bi-constant extrapolation one has to use different average values for even and odd β coefficients, 8.03 Ry and 8.08 Ry, respectively [see Fig. 7.2(a)]. These two extrapolation schemes give almost identical EEL spectra in the current case. In the following, I will use the bi-constant extrapolation.

Figure 7.2(b) shows the numerical behaviour of the odd and even ζ coefficients. The odd coefficients equal to zero, whereas the even coefficients show an exponential decay as the number of Lanczos iterations grows. The fact that even ζ's are non-zero and odd ζ's are zero, is due to the definition (7.75).

Figure 7.3 shows that the EEL spectrum calculated with 400 iterations without the extrapolation has large oscillations when compared to the converged spectrum with 1500 iterations. However, if after 400 iterations the Lanczos coefficients β, γ and ζ are extrapolated to a sufficiently large number (*e.g.*, 5 000 in this case), the calculated spectrum becomes indistinguishable from the converged spectrum. This example shows that the extrapolation technique can significantly reduce the computational effort needed to obtained the converged spectrum.

7.2.1 (d) Comparison with experiment and conventional TDDFT calculations

Let us make a comparison between the EEL spectrum of Si calculated with the Liouville-Lanczos approach, the experimental spectrum, and the theoretical EEL spectrum obtained with the conventional TDDFT method (see Sec. 3.3.3). Figure 7.4(a) shows the comparison of the theoretical EEL spectrum for $\mathbf{q} = 0.53$ a.u. along the [100] direction with the experimental EEL spectrum. As can be seen, the agreement is remarkable. The theoretical EEL spectrum reproduces the main plasmon peak around 20

arbitrarily large at an extremely small computational cost [18].

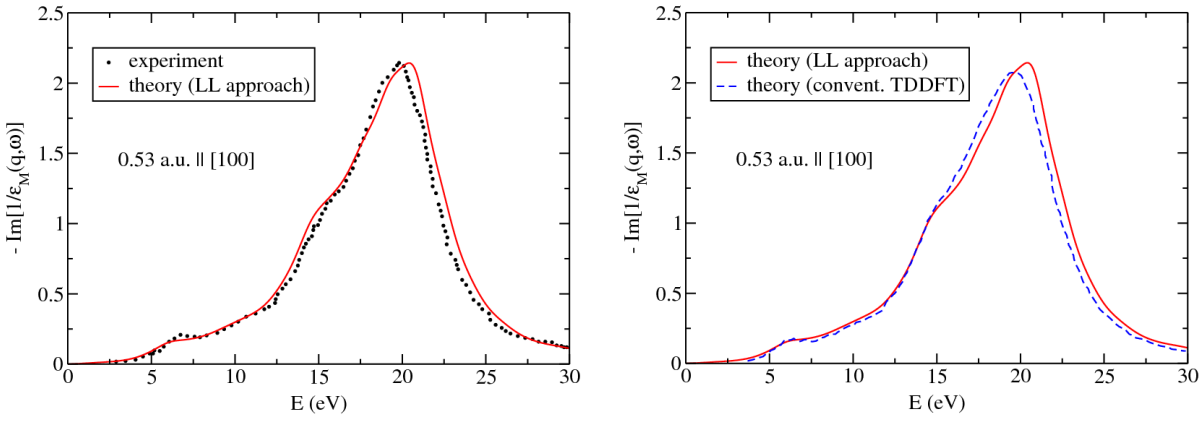

(a) (b)

Figure 7.4: Comparison between the EEL spectrum of Si for $\mathbf{q} = 0.53$ a.u.$||$ [100] calculated with the Liouville-Lanczos (LL) approach, using a $10 \times 10 \times 10$ MP $\mathbf{k}$ point mesh, a Lorentzian broadening $\sigma = 0.035$ Ry, 400 Lanczos iterations, and the extrapolation scheme, with (a) the experimental spectrum [140], and (b) the theoretical EEL spectrum obtained within the conventional TDDFT approach [140] (see Sec. 3.3.3).

eV, a shoulder around 15 eV, and a weak peak around 6.5 eV. Figure 7.4(b) shows the comparison of two theoretical EEL spectra, one obtained with the Liouville-Lanczos approach and the other one with the conventional TDDFT approach. I attribute a slight difference between the two EEL spectra to the fact that they have not been calculated with the same parameters.[10] In particular, the authors of Ref. [140] have used a lifetime broadening.

Figures 7.5(a) and 7.5(b) show the comparisons between the calculated and the experimental EEL spectra, for $\mathbf{q} = 0.80$ a.u. and $\mathbf{q} = 1.45$ a.u. along the [111] direction, respectively. As can be seen, the agreement is also remarkable. Though, there are some small discrepancies between theory and experiment; I attribute them to the lifetime effects [140], which have been approximated in my calculations by a *constant* broadening. The theoretical EEL spectra reproduce all features of the experimental spectra. In order to reach a better agreement of the theoretical spectra with the experimental ones, I had to increase the Lorentzian broadening up to $\sigma = 0.060$ Ry for $\mathbf{q} = 0.80$ a.u., and $\sigma = 0.080$ Ry for $\mathbf{q} = 1.45$ a.u. As a consequence, I could reduce the size of the $\mathbf{k}$ point mesh down to $8 \times 8 \times 8$ for $\mathbf{q} = 0.80$ a.u., and $6 \times 6 \times 6$ for $\mathbf{q} = 1.45$ a.u., without a loss of accuracy.

7.2.1 (e) Test of the f-sum rule

I have checked the f-sum rule of the EEL spectra of Si calculated with the Liouville-

[10] The authors of Ref. [140] have used a Hamann pseudopotential [325], the kinetic-energy cutoff of 32 Ry, 2048 off-symmetry $\mathbf{k}$ points, and a Gaussian broadening of 0.015 Ry plus a lifetime broadening.

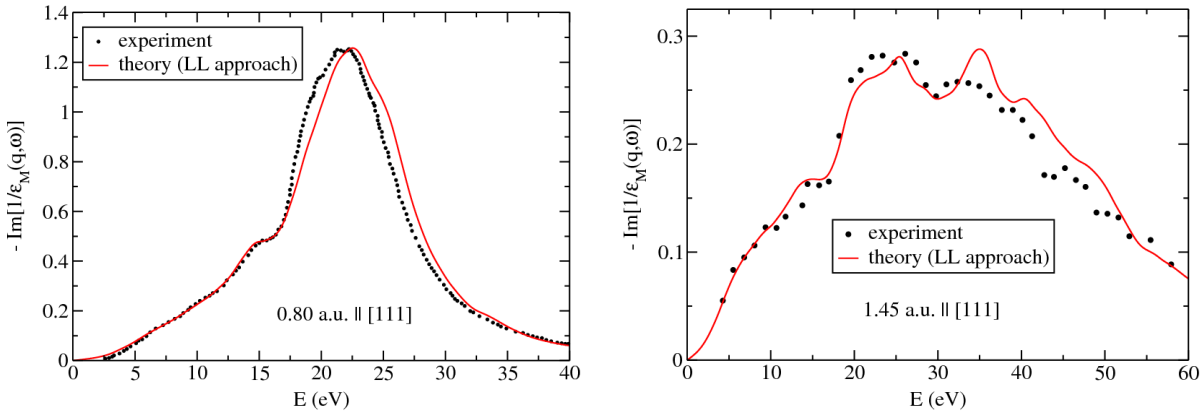

(a) (b)

Figure 7.5: (a) Comparison of the EEL spectra of Si for $\mathbf{q} = 0.80$ a.u.$||$ [111] between experiment [140] and theory, using a $8 \times 8 \times 8$ MP $\mathbf{k}$ point mesh, and a Lorentzian broadening $\sigma = 0.060$ Ry. (b) Comparison of the EEL spectra of Si for $\mathbf{q} = 1.45$ a.u.$||$ [111] between experiment [319] and theory, using a $6 \times 6 \times 6$ MP $\mathbf{k}$ point mesh, and a Lorentzian broadening $\sigma = 0.080$ Ry. The convergence has been achieved after 400 Lanczos iterations using the extrapolation technique.

Lanczos approach, by using Eq. (3.73). I have found that there is a violation of the f-sum rule by 5.3 % in Fig. 7.4(a), by 5.6 % in Fig. 7.5(a), and by 5.8 % in Fig. 7.5(b). I recall that the violation of the f-sum rule is due to the use of non-local pseudopotentials [see Sec. 3.4.2(c)]. The f-sum rule does not depend on the number of Lanczos iterations, as has been proven rigorously mathematically in Ref. [169]. Instead, it is sensitive to the $\mathbf{k}$ point sampling of the Brillouin zone.

7.2.2 Metals: bulk Al

In this section I will demonstrate the applicability the Liouville-Lanczos approach to metals, by using an extension of the formalism of Sec. 7.1.7.

7.2.2 (a) Computational method

Calculations have been performed by using norm-conserving pseudopotential with the Perdew-Zunger (LDA) [34] parameterization of the exchange-correlation functional. The $3s$ and $3p$ electrons were treated as valence electrons. I used an experimental lattice parameter $a_{exp} = 7.60$ a.u. [326], and the kinetic-energy cutoff $E_{cut} = 16$ Ry. The geometry was specified using the primitive *fcc* unit cell, with one atom of Al positioned at (0,0,0). The first Brillouin zone (BZ) was sampled with a Monkhorst-Pack (MP) $\mathbf{k}$ point mesh [324] (see the discussion below). For the ground-state calculation I have used a Methfessel-Paxton smearing [244] with a broadening parameter of 0.02 Ry. To plot

the EEL spectra I have used a Lorentzian smearing with a broadening parameter σ (see the discussion below), which is different from the one used in the ground-state calculation.

7.2.2 (b) Convergence of the EEL spectrum

Figure 7.6(a) shows the convergence of the EEL spectrum of Al for a momentum transfer $\mathbf{q} = 0.513$ a.u. along the [100] direction, as a function of the number of Lanczos iterations. As can be seen, after 200 iterations there are spurious wiggles in the spectrum, whereas when increasing the number of Lanczos iterations up to 600 the wiggles disappear.

Let us apply the convergence criterion defined in Sec. 7.2.1(b). The maximal relative change of the intensity between the EEL spectra obtained after 200 and 600 iterations is 17 % at 17.5 eV, which is too big. However, the maximal relative change of the intensity between the EEL spectra obtained after 600 and 1 000 iterations is 0.6 % at 18.0 eV, which constitutes an extremely good level of convergence. Note, the convergence of the EEL spectrum of Al is reached after a much smaller number of iterations than in the case of Si [see Fig. 7.1(a)].

Let us investigate the convergence of the EEL spectrum of Al with respect to the size of the **k** point mesh. Figure 7.6(b) shows that the convergence of the EEL spectrum is achieved when using a $10 \times 10 \times 10$ mesh, and a broadening parameter $\sigma = 0.056$ Ry. The maximal relative change of the intensity between the EEL spectra calculated with $10 \times 10 \times 10$ and $12 \times 12 \times 12$ **k** point meshes is 2.8 %. If the broadening parameter is decreased, then a larger **k** point mesh is required to converge the spectrum.

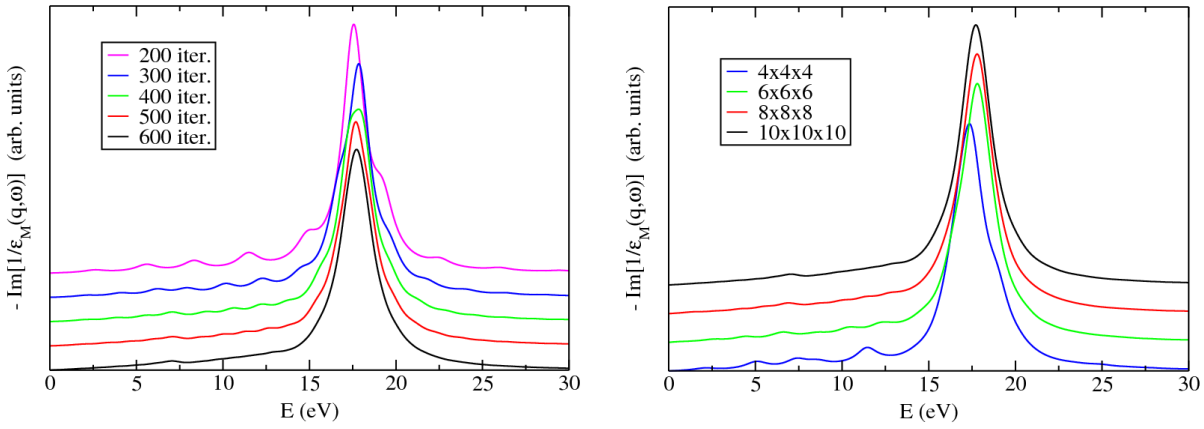

(a) (b)

Figure 7.6: EEL spectrum of bulk Al, $\mathbf{q} = 0.513$ a.u.$||$ [100]. (a) Convergence of the EEL spectrum with respect to the number of Lanczos iterations, using a $10 \times 10 \times 10$ MP **k** point mesh. (b) Convergence of the EEL spectrum with respect to the size of the **k** point mesh, with 600 Lanczos iterations. Both figures have been obtained with a Lorentzian broadening $\sigma = 0.056$ Ry. Curves have been shifted vertically for clarity.

7.2.2 (c) Use of the extrapolation technique

Let us see how to speed up the convergence of the EEL spectrum of Al by using the extrapolation technique. Figures 7.7(a) and 7.7(b) show the numerical behaviour of the β and ζ coefficients of the Lanczos recursion method. In contrast to silicon [see Fig. 7.2(a)], in aluminum the odd and even β coefficients do not oscillate around two different average values, instead they oscillate around the same average value of 7.9 Ry. This average value is approximatively equal to half of the kinetic-energy cutoff.

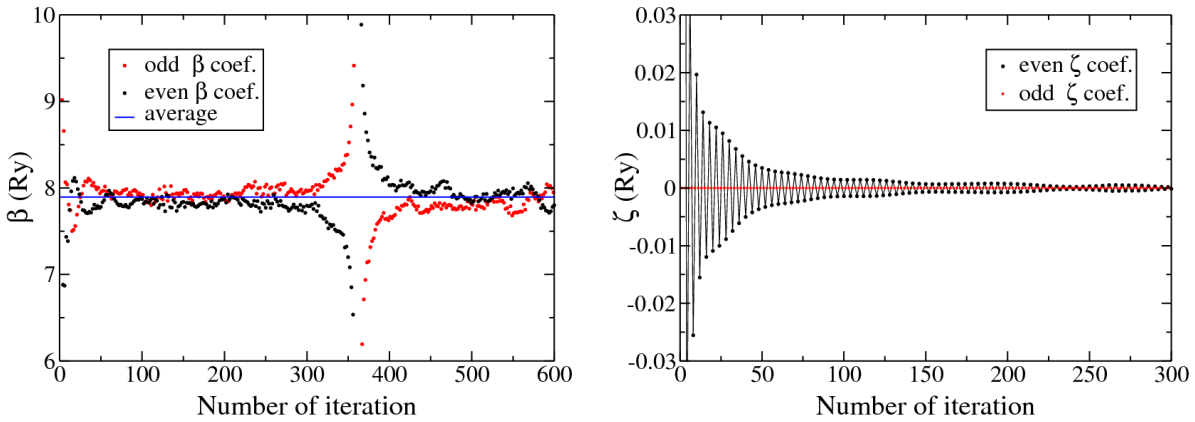

(a) (b)

Figure 7.7: Coefficients of the Lanczos recursion method for bulk Al, $\mathbf{q} = 0.513\,\text{a.u.}||\,[100]$. (a) Numerical behaviour of odd and even β coefficients as functions of the Lanczos iteration number. The horizontal line is the average of β coefficients. (b) Numerical behaviour of odd and even ζ coefficients as functions of the Lanczos iteration number. Solid lines are guides for the eye.

As can be seen in Fig. 7.7(a), there is a jump of the β coefficients around the iteration number 365. This corresponds to an instability of the Lanczos algorithm [18], which occurs when the inner products in Eqs. (3.133) and (3.134) tend to small values. However, the final spectrum is robust with respect to such instabilities. This issue has been discussed in detail in Ref. [18].

The even ζ coefficients tend to zero as the number of Lanczos iterations increases, whereas the odd ζ coefficients are zero, as illustrated in Fig. 7.7(b). The decay of even ζ's is much slower than for Si [see Fig. 7.2(b)].

The extrapolation technique consists in performing explicitly some number of Lanczos iterations, which provide β, γ, and ζ coefficients, and then extrapolating these coefficients. The EEL spectrum has to be checked for a convergence with respect to the number of Lanczos iterations, which are performed explicitly.

The effect of the use of the extrapolation technique is shown in Fig. 7.8. The EEL spectrum calculated with only 300 iterations without the extrapolation contains spurious oscillations when compared to the converged spectrum with 600 iterations. However, if

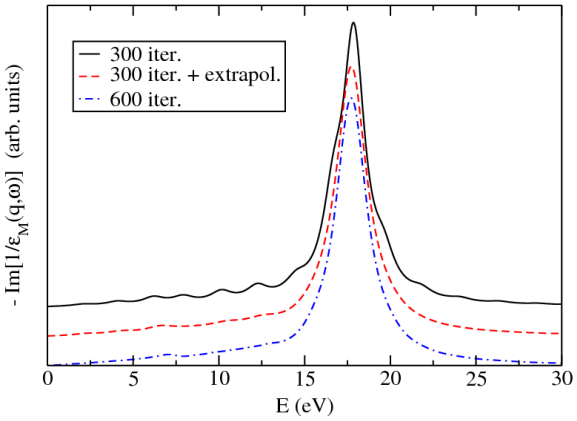

Figure 7.8: Effect of the extrapolation technique on the convergence of the EEL spectrum of bulk Al for $\mathbf{q} = 0.513\,\text{a.u.}||\,[100]$. Curves have been shifted vertically for clarity.

after 300 iterations the Lanczos coefficients β, γ and ζ are extrapolated to a sufficiently large iteration number (*e.g.*, 5 000 in this case), the calculated spectrum becomes indistinguishable from the converged spectrum. In fact, in the current case, the extrapolation technique allows us to gain only a factor of 2 in the number of Lanczos iterations. However, in more complex systems, this factor can be larger. Hence, the use of the extrapolation technique may significantly reduce the computational effort needed to obtain the converged EEL spectrum.

7.2.1 (d) Comparison with experiment and conventional TDDFT calculations

Let us make a comparison between the EEL spectrum of Al calculated with the Liouville-Lanczos approach, the experimental spectrum, and the theoretical EEL spectrum obtained with the conventional TDDFT method (see Sec. 3.3.3). Figure 7.9(a) shows a comparison of the EEL spectrum for $\mathbf{q} = 0.616$ a.u. along the [100] direction obtained with the Liouville-Lanczos approach and the experimental one. As can be seen, the agreement is remarkable, but for the slight misalignment of the plasmon peak. Figure 7.9(b) shows a comparison of the EEL spectrum obtained with the Liouville-Lanczos approach and with the conventional TDDFT method [320]. As can be seen, both theoretical approaches give very similar spectra. The small difference between the two EEL spectra can be attributed to the fact that the two calculations have not been performed with the same parameters.[11]

[11] The authors of Ref. [320] have used the kinetic-energy cutoff of 32 Ry, a $16 \times 16 \times 16$ MP $\mathbf{k}$ point mesh, a Fermi-Dirac broadening of 0.002 Ry for the ground-state calculation, and a Gaussian broadening of 0.073 Ry plus a lifetime broadening to plot the EEL spectra.

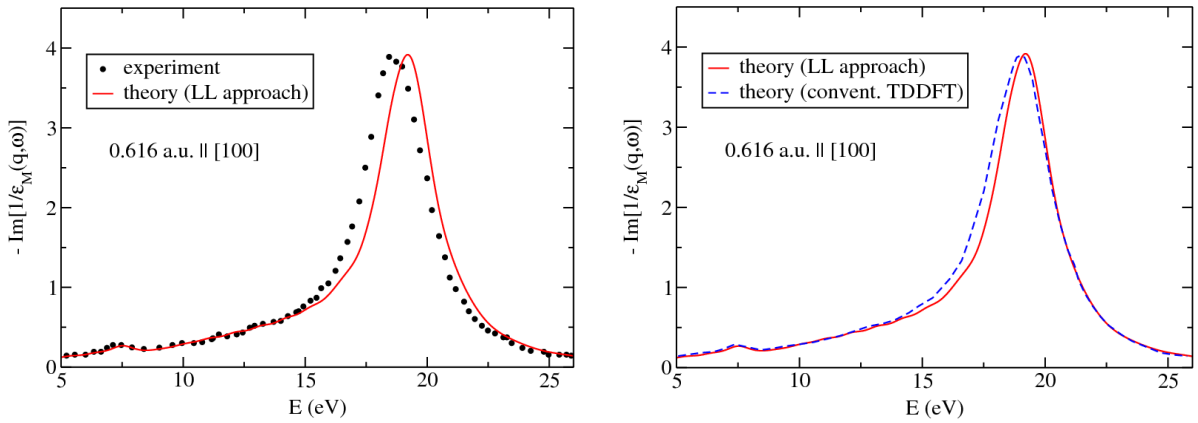

(a) (b)

Figure 7.9: Comparison between the EEL spectrum of Al for $\mathbf{q} = 0.616$ a.u.|| [100] calculated with the Liouville-Lanczos (LL) approach, using a $10 \times 10 \times 10$ MP $\mathbf{k}$ point mesh, a Lorentzian broadening $\sigma = 0.051$ Ry, 400 Lanczos iterations, and the extrapolation scheme, with (a) the experimental spectrum [320], and (b) the theoretical EEL spectrum obtained within the conventional TDDFT approach [320] (see Sec. 3.3.3).

Figures 7.9(a) and 7.10(b) show the comparisons between the calculated and the experimental EEL spectra, for $\mathbf{q} = 0.513$ a.u. and $\mathbf{q} = 0.821$ a.u. along the [100] direction, respectively. As can be seen, the agreement is also good. I attribute the remaining discrepancies to the lifetime effects [320], which have been approximated in my calculations by a *constant* broadening. In order to have the same intensity of the plasmon peaks as in the experiment, I have used $\sigma = 0.056$ Ry for $\mathbf{q} = 0.513$ a.u., and $\sigma = 0.068$ Ry for $\mathbf{q} = 0.821$ a.u. In the case of $\mathbf{q} = 0.821$ a.u., I had to use a MP $\mathbf{k}$ point mesh as dense as $14 \times 14 \times 14$ in order to converge the spectrum, which corresponds to 280 $\mathbf{k}$ points in the IBZ, and 1470 $\mathbf{k}$ points in the IBZ($\mathbf{q}$). By using the extrapolation technique, I had to make 300 Lanczos iterations for $\mathbf{q} = 0.513$ a.u. and 450 Lanczos iterations for $\mathbf{q} = 0.821$ a.u., in order to converge the EEL spectra.

7.2.2 (e) Test of the f-sum rule

I have checked the f-sum rule of the EEL spectra of Al calculated with the Liouville-Lanczos approach, by using Eq. (3.73). The violation of the f-sum rule is about 6.7 % in all cases considered above, *i.e.* in Figs. 7.9(a), 7.10(a), and 7.10(b).

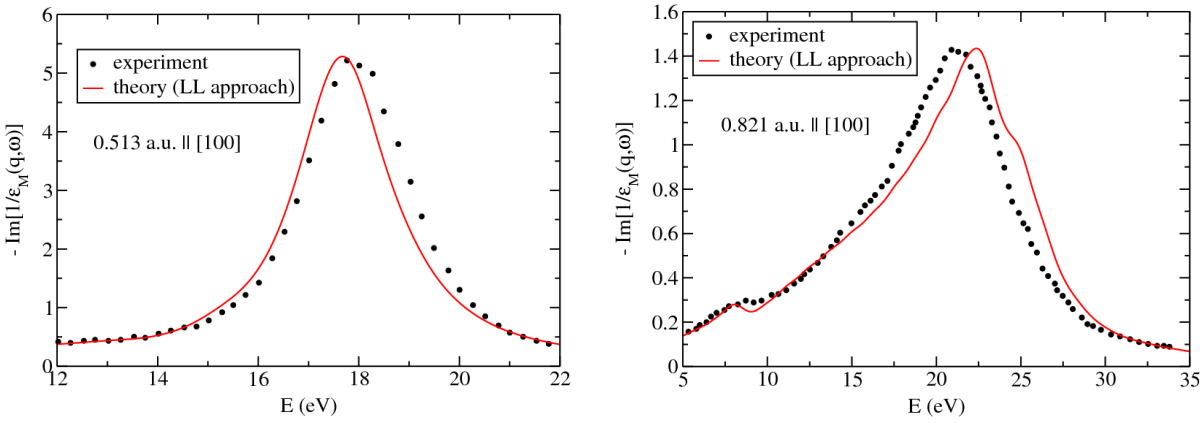

(a) (b)

Figure 7.10: (a) Comparison of the EEL spectra of Al for $\mathbf{q} = 0.513$ a.u.|| [100] between experiment [320] and theory, using a $10 \times 10 \times 10$ MP $\mathbf{k}$ point mesh, a Lorentzian broadening $\sigma = 0.056$ Ry, 300 Lanczos iterations, and the extrapolation technique. (b) Comparison of the EEL spectra of Al for $\mathbf{q} = 0.821$ a.u.|| [100] between experiment [320] and theory, using a $14 \times 14 \times 14$ MP $\mathbf{k}$ point mesh, a Lorentzian broadening $\sigma = 0.068$ Ry, 450 Lanczos iterations, and the extrapolation technique.

7.3 Application to Bi

In this section I will present the first *ab initio* study of the EEL spectra of bulk bismuth by applying the Liouville-Lanczos approach developed in Sec. 7.1. In particular, I will demonstrate the effect of the spin-orbit coupling on the EEL spectra of Bi, by using the extension of the Liouville-Lanczos formalism to the relativistic case (see Sec. 7.1.8).

This section is organized as follows. In Sec. 7.3.1 I will present the computational details of my calculations. In Sec. 7.3.2 I will present the investigation of the convergence of the EEL spectrum. In Sec. 7.3.3 I will make a comparison of the EEL spectra within the LDA and GGA with the experimental one (see Sec. 4.5). In Sec. 7.3.4 I will present the first study of the effect of the spin-orbit coupling on the EEL spectra of Bi. In Sec. 7.3.5 I will demonstrate the application of the Liouville-Lanczos approach to the calculation of the real and imaginary part of the dielectric function of Bi. In Sec. 7.3.6 I will demonstrate the plasmon dispersion in Bi within the LDA and GGA, with and without spin-orbit coupling. In Sec. 7.3.7 I will present an investigation of various effects in the EEL spectrum of Bi: exchange-correlation effects, crystal local field effects, and the anisotropy. Finally, in Sec. 7.3.8 I will show a comparison between the loss function and the imaginary part of the dielectric function at various finite values of the momentum transfer $\mathbf{q}$.

7.3.1 Computational method

Calculations have been performed by using fully-relativistic norm-conserving pseudopotentials described in Appendix A.1. I have considered two approximations for the exchange-correlation functional, LDA and GGA. Within each of them I have used the corresponding theoretical equilibrium lattice parameters (see Table 5.1) optimized when the spin-orbit coupling (SOC) was included. I have used the kinetic-energy cutoff $E_{cut} = 60$ Ry, which was sufficient to obtain converged EEL spectra, with respect to a cutoff of 80 Ry. The geometry is described in detail in Sec. 4.2.1. The first Brillouin zone (BZ) was sampled with a uniform $\mathbf{k}$ point mesh centered at the Γ point. For the ground-state calculation I have used a Methfessel-Paxton smearing [244] with a broadening parameter of 0.02 Ry. To plot the EEL spectra I have used a Lorentzian smearing with a broadening parameter σ. The details about the $\mathbf{k}$ point mesh and the broadening parameter σ will be given in the following.

7.3.2 Convergence of the EEL spectrum

Let us examine the convergence of the EEL spectrum of Bi with respect to the number of Lanczos iterations and number $\mathbf{k}$ points in the BZ. To this end, let us consider the LDA without the spin-orbit coupling. The convergence properties are similar when the spin-orbit coupling is included in the calculations, and within the GGA.

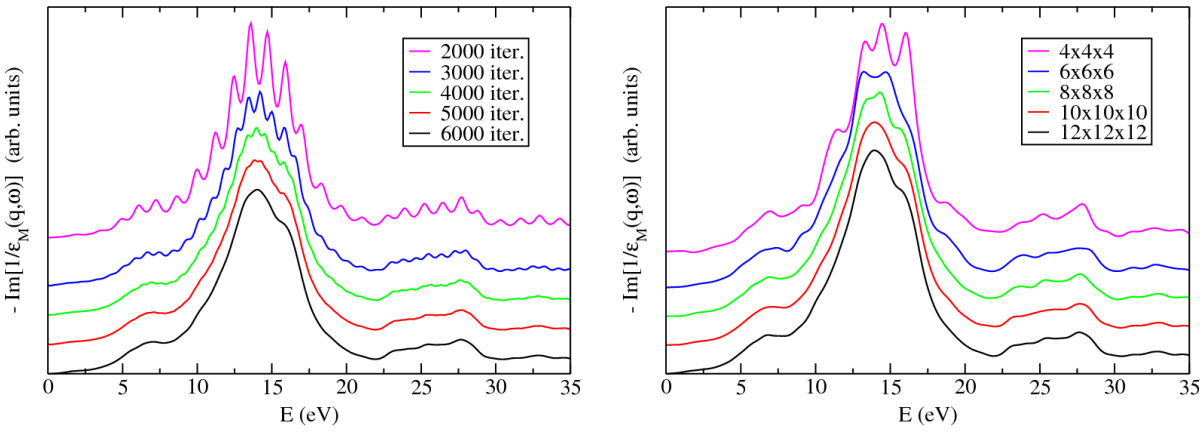

Figure 7.11: EEL spectrum of bulk Bi, calculated within the LDA without the spin-orbit coupling for $\mathbf{q} = 0.2$ Å^{-1} $||$ [111]. (a) Convergence of the EEL spectrum with respect to the number of Lanczos iterations, using a $12 \times 12 \times 12$ uniform $\mathbf{k}$ point mesh centered at the Γ point. (b) Convergence of the EEL spectrum with respect to the size of the $\mathbf{k}$ point mesh, for 6000 Lanczos iterations. Both figures have been obtained with a Lorentzian broadening $\sigma = 0.035$ Ry. Curves have been shifted vertically for clarity.

Figure 7.11(a) shows the convergence of the EEL spectrum of Bi for a momentum

transfer $\mathbf{q} = 0.2$ Å^{-1} along the [111] direction [see Fig. 4.3(a)], as a function of the number of Lanczos iterations. As can be seen, the convergence is achieved after as much as 6000 iterations. The maximal relative change of the intensity when comparing the EEL spectra after 6000 and 8000 iterations is 0.4 % at 14.3 eV, which is extremely satisfactory. This number of iterations (6 000) is much larger than in the case of silicon (1500 iterations) and aluminum (600 iterations). This is due to the fact that the kinetic-energy cutoff in Bi is much larger than the one I used for Si and Al (60 Ry compared to 16 Ry), and thus a larger number of Lanczos iterations is necessary to achieve the convergence.

Figure 7.11(b) shows the convergence of the EEL spectrum with respect to the $\mathbf{k}$ point sampling of the BZ. As can be seen, the convergence is reached by using a $12 \times 12 \times 12$ uniform $\mathbf{k}$ point mesh. The maximal relative change of the intensity when comparing the EEL spectra obtained with $12 \times 12 \times 12$ and $14 \times 14 \times 14$ $\mathbf{k}$ point meshes is 0.9 % at 12.3 eV. The $12 \times 12 \times 12$ mesh corresponds to 189 $\mathbf{k}$ points in the IBZ for the ground-state calculation, and 364 $\mathbf{k}$ points in the IBZ($\mathbf{q}$) for the linear-response calculation.

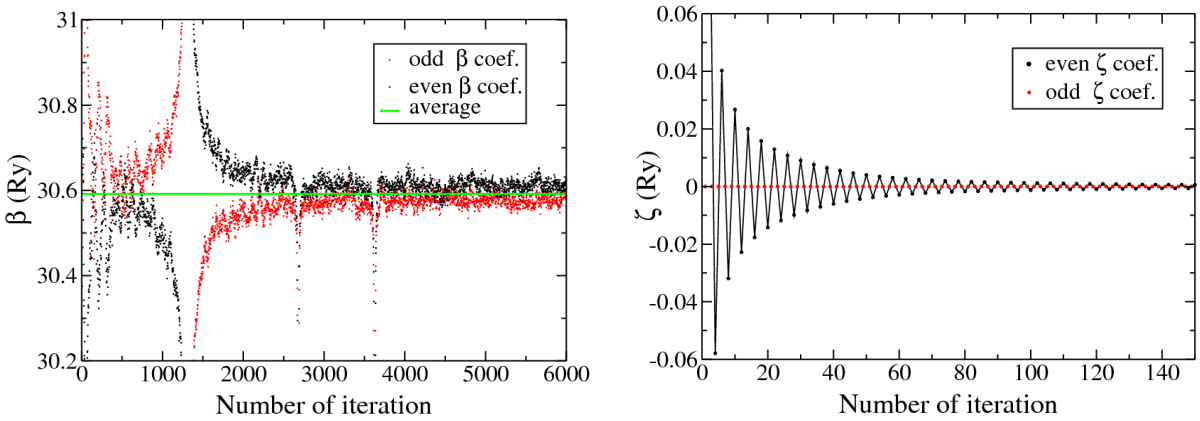

(a) (b)

Figure 7.12: Coefficients of the Lanczos recursion method for bulk Bi, $\mathbf{q} = 0.2$ Å^{-1} || [111]. (a) Numerical behaviour of odd and even β coefficients as functions of the Lanczos iteration number. The horizontal line is the average of β coefficients. (b) Numerical behaviour of odd and even ζ coefficients as functions of the Lanczos iteration number. Solid lines are guides for the eye.

The computational effort needed to obtain the converged spectrum can be greatly reduced by using the extrapolation technique. Figures 7.12(a) and 7.12(b) show the numerical behaviour of β and ζ coefficients of the Lanczos recursion method. In contrast to silicon, and similarly to aluminum, in semimetallic bismuth the odd and even β coefficients do not oscillate around two different average values, instead they oscillate around the same average value of 30.59 Ry. This average value is approximatively equal to the half of the kinetic-energy cutoff.

There is an instability in the chain of β coefficients, which occurs around the iteration number 1250, and there are some deviations of β's from the average value around the

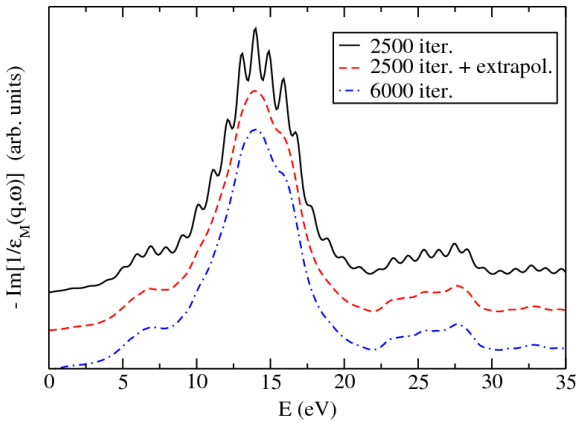

Figure 7.13: Effect of the extrapolation technique on the convergence of the EEL spectrum of bulk Bi for $\mathbf{q} = 0.2$ Å^{-1} $||$ [111]. Curves have been shifted vertically for clarity.

iteration numbers 2750 and 3600. However, the final EEL spectrum is stable with respect to such instabilities. Figure 7.12(b) shows that even ζ coefficients oscillate around zero and decay exponentially almost as fast as in silicon [see Fig. 7.2(b)], whereas odd ζ's are zero by definition, Eq. (3.138).

It turns out that the extrapolation technique can be applied after 2500 Lanczos iterations, as illustrated in Fig. 7.13. Indeed, by making explicitly 2500 iterations, and then using the average value of 30.59 Ry for β's and zero for ζ's up to, say, 20 000, one can readily obtained the converged EEL spectrum. Thus, I gain a factor of $6000/2500 = 2.4$ in the number of iterations, which is very significant. In Bi each Lanczos iteration is much more computationally expensive than in Si or Al, and therefore it is important to spare computer resources.

7.3.3 Comparison between LDA, GGA and experiment

Figures 7.14(a) and 7.14(b) show the comparison of the experimental EEL spectrum of bulk Bi for $\mathbf{q} \to 0$ [227] with the theoretical one for $\mathbf{q} = 0.1$ Å^{-1} $||$ [111], calculated within the LDA and GGA, including the spin-orbit coupling (SOC). It turns out that the finite[12] value of the momentum transfer $\mathbf{q} = 0.1$ Å^{-1} is sufficient for the comparison with the experiment.[13]

As can be seen, despite the big difference of the volume of the unit cell within the LDA and GGA (see Table 5.1), both approximations give very similar EEL spectra. Though, there are some small differences. The intensity of the main plasmon peak is slightly smaller within the GGA, but the peak position is the same within both approximations.

[12]If one chooses $\mathbf{q} = 0$, then the starting Lanczos vectors in Eq. (7.73) will be exactly zero, because $\hat{P}_c^{\mathbf{k}} u^0_{n,\mathbf{k}}(\mathbf{r}) = 0$, and thus the solution of linear-response equations will be also zero. Therefore, in practice one should choose some small but finite value of $\mathbf{q}$.

[13]The distance between the Γ and T points in the bulk Brillouin zone is ≈ 0.8 Å^{-1} [see Fig. 4.3(a)]. Therefore, the momentum transfer $\mathbf{q} = 0.1$ Å^{-1} $||$ [111] can be considered to be small enough. Moreover, I have tested that a further decrease of $\mathbf{q}$ does not lead to significant changes in the EEL spectra in Figs. 7.14(a) and 7.14(b). In addition, the fact that I have chosen $\mathbf{q}$ along the specific direction is justified by the fact that the anisotropic effects are small for small $\mathbf{q}$, as will be shown in Sec. 7.3.7.

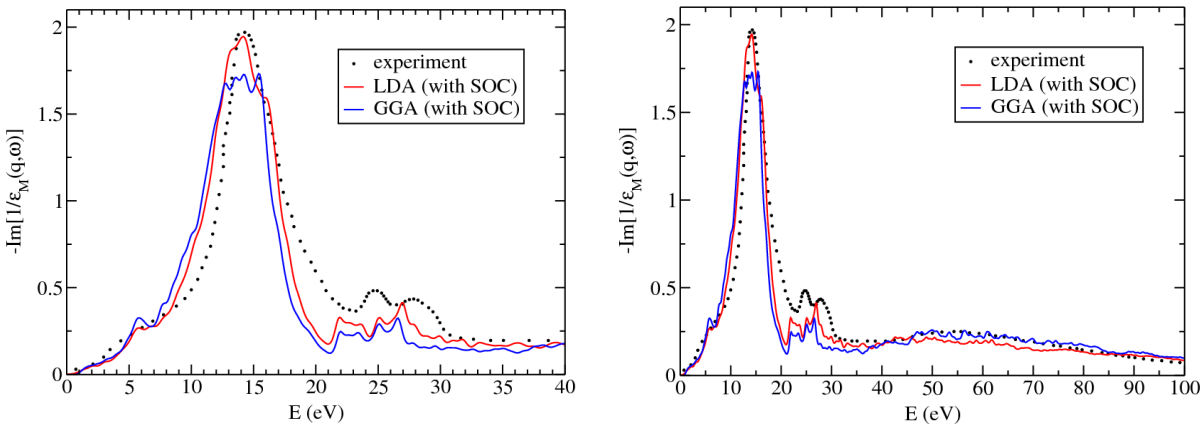

Figure 7.14: (a) Comparison of the EEL spectrum of bulk Bi within the LDA and GGA with the spin-orbit coupling (SOC) for $\mathbf{q} = 0.1$ Å^{-1} $||$ [111], and experimental spectrum for $\mathbf{q} \to 0$ [227]. (b) The same as (a) but in the larger energy range. Calculations have been performed by using a $14 \times 14 \times 14$ uniform $\mathbf{k}$ point mesh centered at the Γ point, and a Lorentzian broadening $\sigma = 0.015$ Ry.

Peaks due to the interband transitions from the $5d$ levels, in the energy range from 20 to 30 eV, also look very similar within the LDA and GGA.

Both approximations give EEL spectra in good agreement with the experimental one of Ref. [227]. The position of the plasmon peak around 14 eV coincides between theory and experiment. In my calculations I have also found a peak at about 6 eV, which corresponds to the shoulder in the experimental spectrum of Ref. [227]. As can be seen in Fig. 7.14(a), positions of the peaks due to transitions from the $5d$ levels are red-shifted by about 2 eV with respect to the experimental ones. Such a shift comes from the delocalization of the $5d$ semicore levels in the LDA and GGA (see Fig. 4.2.2). As a consequence, they appear at higher binding energy in the theory than in the experiment, which red-shifts the peak positions in the EEL spectrum.

Figure 7.14(b) shows that the theory remarkably reproduces the broad structure extending between 40 and 100 eV. The GGA reproduces this structure better than LDA. It is worth noting that it is extremely difficult to reproduce this broad structure with the conventional TDDFT approach (see Sec. 3.3.3), as one would require a huge number of empty states in order to converge the EEL spectrum in such a wide energy range. However, within the Liouville-Lanczos approach, no empty states are calculated, and thus one can easily consider large energy range. The excellent description of this broad structure in Bi is a good example showing one of the power points of the new approach.

A detailed comparison of the peak positions in the theoretical EEL spectrum with various experimental data is given in Table 7.1. In Fig. 7.14(a) I do not find a surface plasmon peak at about 10 eV, because I have performed calculations on *bulk* Bi. Moreover, I do not find in the theoretical EEL spectrum a peak at about 29 eV, which was observed in some experiments (see Table 7.1). Presumably, such a peak was measured

peak	This work	Ref.[a]	Ref.[b]	Ref.[c]	Ref.[d]	Ref.[e]
1	5.8 ± 0.1	5	5	5.3 ± 0.2	5.3	5.6
2			10	9.9 ± 0.2	9.5 ± 0.2	
3	14.0 ± 0.2	13.95 ± 0.15	14	14.7 ± 0.2	14.4 ± 0.2	14.1 ± 0.3
4	22.6 ± 0.1	24.45 ± 0.2	24	24.8 ± 0.2	24.6	
5	25.9 ± 0.2	27.3 ± 0.2	27		27.8	28
6			29	29 ± 0.2	29.7	
7	51 ± 1	52	52			

[a] Wehenkel and Gauthe, Ref. [227].
[b] Gauthe and Wehenkel, Ref. [226].
[c] Powell, Refs. [221, 222].
[d] Zacharias, Ref. [225].
[e] Sueoka, Ref. [224].

Table 7.1: Comparison of the peak positions in the EEL spectrum of bulk Bi as obtained in this work and various experiments. The error bar in my calculations has been determined as a difference between the LDA and GGA.

due to some experimental conditions. Namely, as has been pointed out by Wehenkel and Gauthe [227], Bi_2O_3 has a peak at 29 eV. Therefore, the origin of such a peak is probably due to the oxidation of Bi films in the experiments.

7.3.4 Effect of the spin-orbit coupling on EEL spectrum

The effect of the SOC is rather strong both within the LDA and GGA, as can be seen in Figs. 7.15(a) and 7.15(b). The position of the plasmon peak at about 14 eV does not change, however its intensity changes significantly: it increases by $\sim 26\%$ when the SOC is "switched off", both within the LDA and GGA. The change in the intensity of the plasmon peak in Bi due to SOC is more pronounced than in Pb [56], for which the SOC is also large. In Figs. 7.15(a) and 7.15(b) the Lorentzian broadening, $\sigma = 0.015$ Ry, has been chosen in such a way that the intensity of the plasmon peak within the LDA with the SOC is equal to the experimental one.

When the SOC is "switched off" the peak at ~ 6 eV and the peaks between 20 and 30 eV blue-shift, and their intensity changes only slightly. Positions of the peaks due to transitions from the $5d$ levels are fortuitously in better agreement with experiment when the SOC is neglected. This can be understood from Fig. 4.4(b), which shows that when the SOC is included the $5d$ levels split, and some of them appear at higher binding energy values than the $5d$ levels without SOC.

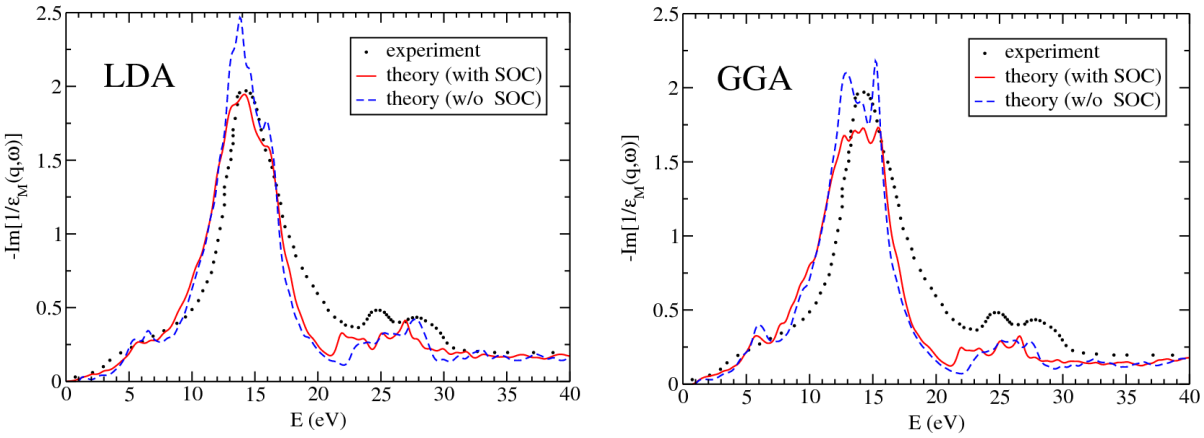

(a) (b)

Figure 7.15: Comparison of the experimental EEL spectrum of bulk Bi for $\mathbf{q} \to 0$ [227] with the theoretical ones for $\mathbf{q} = 0.1$ Å^{-1} || [111], calculated with and without spin-orbit coupling (SOC) within (a) the LDA, and (b) the GGA. Calculations have been performed by using a $14 \times 14 \times 14$ uniform $\mathbf{k}$ point mesh centered at the Γ point, and a Lorentzian broadening $\sigma = 0.015$ Ry.

7.3.5 Real and imaginary part of the dielectric function

Although the origin of all peaks in the EEL spectrum of Bi was revealed a long time ago from the experimental works, I give here a first *ab initio* confirmation. To this end, let us consider the real and imaginary parts of the dielectric function, Re[$\epsilon_{\rm M}$] and Im[$\epsilon_{\rm M}$]. They can be obtained by using the loss function and by applying the Kramers-Kronig transformation [131]. However, I have used another method: I performed a direct *ab initio* calculation of Re[$\epsilon_{\rm M}$] and Im[$\epsilon_{\rm M}$], by means of the Liouville-Lanczos approach, as described in Sec. 7.1.9.

The result of the application of such an approach is illustrated in Figs. 7.16(a) and 7.16(b). In Fig. 7.16(a) it is seen that the agreement between the TDLDA calculation of Re[$\epsilon_{\rm M}$] and Im[$\epsilon_{\rm M}$] on the one hand, and the data of Ref. [225], which was obtained by applying the Kramers-Kronig relation to the loss function, on the other hand, is remarkable. In particular, the peak at about 6 eV, which is due to interband transitions, is well reproduced. Also, in my calculations I reproduce the peaks between 20 and 30 eV, which are indeed due to the interband transitions from the $5d$ levels. In Fig. 7.16(b) it can be seen that these peaks coincide with the peaks in the loss function. Also, one can see that the plasmon peak at 14 eV occurs when the Re[$\epsilon_{\rm M}$] changes its sign with a positive slope, which confirms that this is indeed a plasmon.

In fact, a more stringent test of the Liouville-Lanczos approach can be a comparison of Re[$\epsilon_{\rm M}$] and Im[$\epsilon_{\rm M}$] with those obtained by applying the Kramers-Kronig relation to the reflectivity spectrum of Bi, which was measured with high accuracy [238], and where 6 peaks were found between 0 - 10 eV. From a computational point of view of the Liouville-Lanczos approach, such a comparison may require a decrease of the Lorentzian

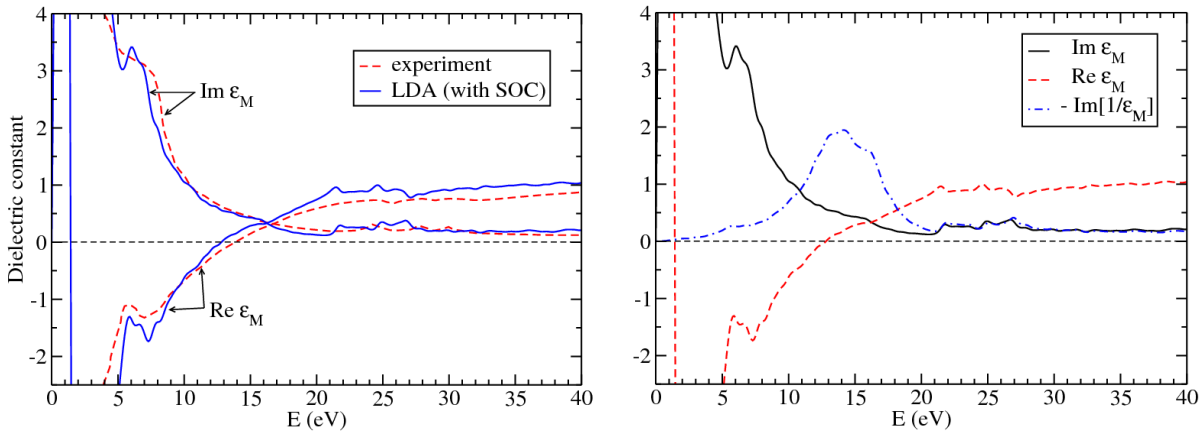

(a) (b)

Figure 7.16: (a) Comparison of $\mathrm{Re}[\epsilon_{\mathrm{M}}(\mathbf{q})]$ and $\mathrm{Im}[\epsilon_{\mathrm{M}}(\mathbf{q})]$ at $\mathbf{q} = 0.1$ Å^{-1}, calculated within the LDA with the spin-orbit coupling (SOC) included, with the data of Ref. [225] which were obtained from the measured loss function by applying the Kramers-Kronig transformation. (b) Comparison of the calculated $\mathrm{Re}[\epsilon_{\mathrm{M}}(\mathbf{q})]$, $\mathrm{Im}[\epsilon_{\mathrm{M}}(\mathbf{q})]$, and $-\mathrm{Im}[1/\epsilon_{\mathrm{M}}(\mathbf{q})]$. Calculations have been performed by using a $14 \times 14 \times 14$ uniform $\mathbf{k}$ point mesh centered at the Γ point, and a Lorentzian broadening $\sigma = 0.015$ Ry.

broadening and increase of the $\mathbf{k}$ point sampling of the Brillouin zone (with respect to those parameters given in the caption of Fig. 7.16), in order to resolve fine features in $\mathrm{Re}[\epsilon_{\mathrm{M}}]$ and $\mathrm{Im}[\epsilon_{\mathrm{M}}]$.

7.3.6 Plasmon dispersion

In this thesis I report for the first time the plasmon dispersion in bulk Bi, *i.e.* how the plasmon peak position changes when the transferred momentum $\mathbf{q}$ changes. Figures 7.17(a) and 7.17(b) show the comparison between the LDA and GGA, both with and without the spin-orbit coupling. As can be seen, despite the large variation of the equilibrium volume of the unit cell (see Table 5.1), both the LDA and GGA give very similar EEL spectra, but for some quite small differences.[14] The plasmon dispersion within the LDA and GGA shows the same behaviour when the transferred momentum $\mathbf{q}$ is increased. The plasmon peak is blue-shifted, but the peaks due to transitions from the $5d$ levels do not move, which confirms that they are not plasmons and due to interband transitions. In contrast, the peak below the plasmon peak, which was attributed to the interband transition, does move (blue-shifts) when $\mathbf{q}$ increases.

When $\mathbf{q}$ is increased, the plasmon peak merges with the $5d$ interband transitions. Namely, the spectrum becomes very broad, and it has a much smaller intensity, so that

[14] If LDA and GGA are used with the same (*e.g.* experimental) lattice parameters, the EEL spectra are the same, because the corresponding Kohn-Sham band structures are identical [see Figs. 5.3(c) and 5.3(d)].

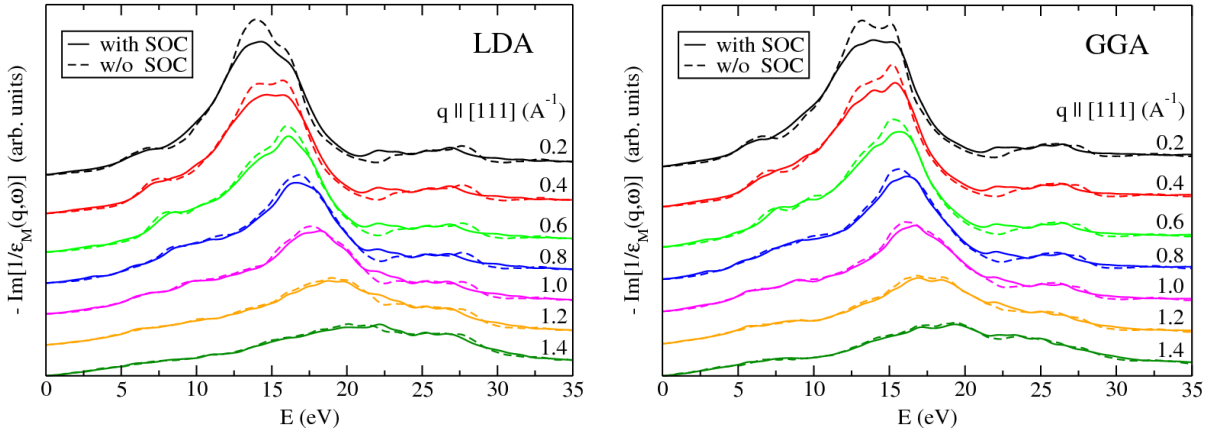

Figure 7.17: EEL spectra of bulk Bi at various values of the transferred momentum $\mathbf{q}$ along the [111] direction, in units of Å^{-1}. (a) Calculations within the LDA with and without spin-orbit coupling (SOC), (b) Calculations within the GGA with and without SOC. Curves have been shifted vertically for clarity. Calculations have been performed by using a $12 \times 12 \times 12$ uniform $\mathbf{k}$ point mesh centered at the Γ point, and a Lorentzian broadening $\sigma = 0.035$ Ry.

the f-sum rule is satisfied at any transferred momentum $\mathbf{q}$. Such a broadening of the EEL spectrum occurs due to the electron-hole continuum [130].

The effect of the spin-orbit coupling on the EEL spectrum is more pronounced for small $\mathbf{q}$, and becomes less important for large $\mathbf{q}$. This feature is present both for the LDA and GGA.

7.3.7 Exchange-correlation, crystal local field and anisotropy effects

It is important to understand the effects of the exchange and correlation (XC), the crystal local field effects (CLFE) and the anisotropy in the EEL spectrum of Bi. Let us consider the LDA without the spin-orbit coupling effect. In Fig. 7.18(a) it can be seen that XC effects are not significant for small $\mathbf{q}$, and they become more important for larger $\mathbf{q}$. Thus, the random phase approximation (RPA) including CLFE already gives accurate description of the EEL spectrum.

Crystal local field effects are more important than XC effects. When CLFE are neglected, *i.e.* when one uses RPA without CLFE, one can see in Fig. 7.18(a) quite significant changes in the EEL spectrum. For example, for $\mathbf{q} = 0.2$ Å^{-1} the plasmon peak is blue-shifted by ~ 2 eV, and its intensity is reduced. The peaks due to interband transitions from the $5d$ levels do not move but increase their intensity. By increasing $\mathbf{q}$, CLFE become more pronounced.

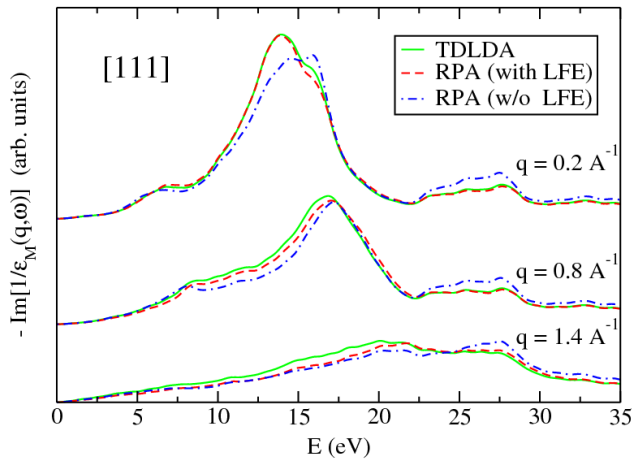

(a)

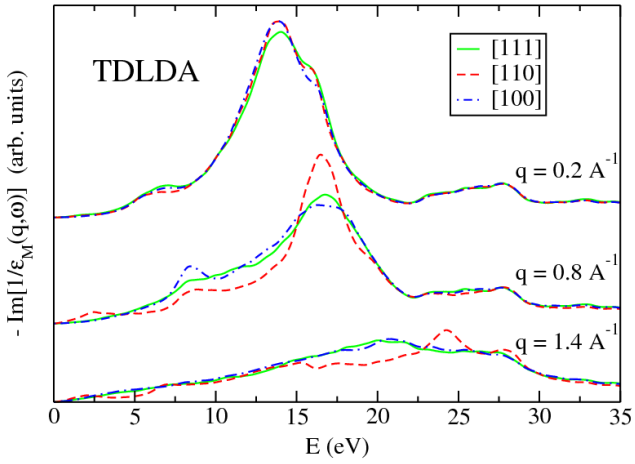

(b)

Figure 7.18: EEL spectra of bulk Bi, calculated within the LDA without the spin-orbit coupling, by using a $12 \times 12 \times 12$ uniform $\mathbf{k}$ point mesh centered at the Γ point, and a Lorentzian broadening $\sigma = 0.035$ Ry. (a) Comparison between TDLDA, RPA with and without crystal local field effects (CLFE) for several values of $\mathbf{q}$ along the [111] direction. (b) Effect of the anisotropy for several values of $\mathbf{q}$ along the [111], [110], and [100] directions, within the TDLDA. Curves have been shifted vertically for clarity.

I have found that the EEL spectrum of bulk Bi is anisotropic[15] for large transferred momenta, as can be seen in Fig. 7.18(b). However, for small transferred momenta, *e.g.* $\mathbf{q} = 0.2$ Å^{-1}, the anisotropy is very small. When $\mathbf{q}$ is increased up to, *e.g.* 0.8 Å^{-1} or larger, the anisotropy becomes very significant. When $\mathbf{q} = 0.2$ Å^{-1} and $\mathbf{q} = 0.8$ Å^{-1} the peaks due to the interband transitions from the $5d$ levels are isotropic, in contrast to the plasmon peak and the peak at ~ 6 eV.

[15]The anisotropy is determined by the electronic bandstructure [140].

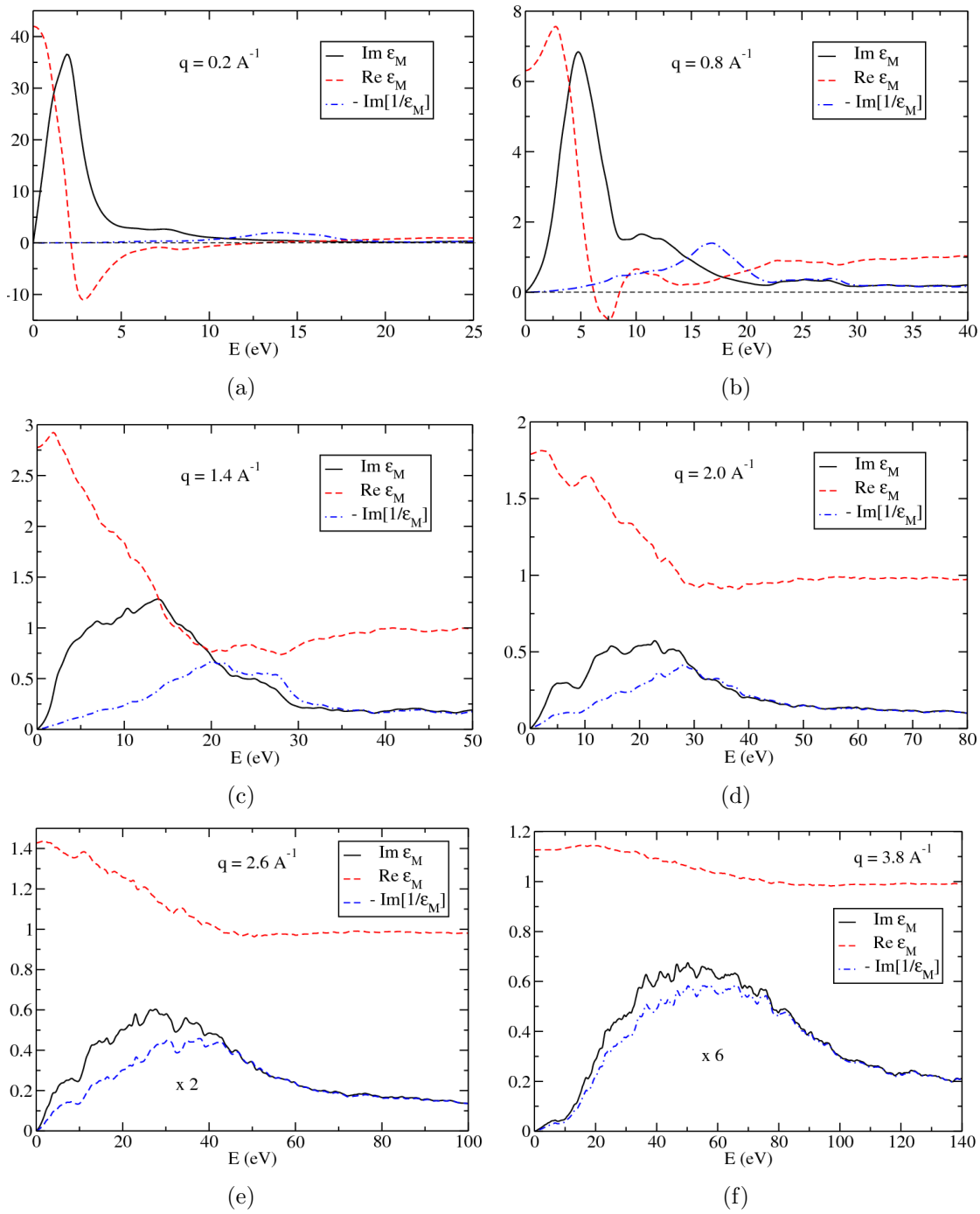

Figure 7.19: (a)-(f) Comparison of $\mathrm{Re}[\epsilon_{\mathrm{M}}]$, $\mathrm{Im}[\epsilon_{\mathrm{M}}]$, and $-\mathrm{Im}\,[1/\epsilon_{\mathrm{M}}(\mathbf{q})]$ at various values of $\mathbf{q}$ along the [111] direction. Calculations have been performed within the LDA without the spin-orbit coupling, by using a $12 \times 12 \times 12$ uniform $\mathbf{k}$ point mesh centered at the Γ point, and a Lorentzian broadening $\sigma = 0.035$ Ry. In panels (e) and (f), $\mathrm{Im}[\epsilon_{\mathrm{M}}]$ and $-\mathrm{Im}\,[1/\epsilon_{\mathrm{M}}(\mathbf{q})]$ have been multiplied by a factor for better visibility.

7.3.8 Comparison between $-\mathrm{Im}\,[1/\epsilon_{\mathrm{M}}(\mathbf{q})]$ & $\mathrm{Im}\,[\epsilon_{\mathrm{M}}(\mathbf{q})]$

Figure 7.19 shows the comparison of the loss function, $-\mathrm{Im}\,[1/\epsilon_{\mathrm{M}}(\mathbf{q})]$, and the imaginary part of the dielectric function, $\mathrm{Im}\,[\epsilon_{\mathrm{M}}(\mathbf{q})]$, at various values of the transferred momenta $\mathbf{q}$. It is seen that for small $\mathbf{q}$ these two spectra are very different, but for large $\mathbf{q}$ they become almost identical. As has been pointed out in Sec. 3.3.3(d), this is due to the fact that for small $\mathbf{q}$, the long-range component is important, whereas for large $\mathbf{q}$ the short-range effects dominate. The same trend has been confirmed by Weissker *et al.* on the example of silicon (see Fig. 20 in Ref. [140]).

7.3.9 Effect of the $5d$ semicore levels

Figure 7.20 shows the comparison of the EEL spectrum of bismuth with $5d$ semicore levels in the valence region and without $5d$ semicore levels.[16] As can be seen, without $5d$ levels the broad structure between 30 - 100 eV is not present in the spectrum, which means that this structure is due to the interband transitions from the $5d$ levels to higher conduction bands (see Sec. 4.5). It is worth noting that it would be computationally very expensive to describe such a broad structure in the EEL spectrum using the conventional TDDFT approach, because one would need to include very large number of empty states in the calculations [see Sec. 3.2.1 (b)], whereas in the Liouville-Lanczos approach there are no empty states.

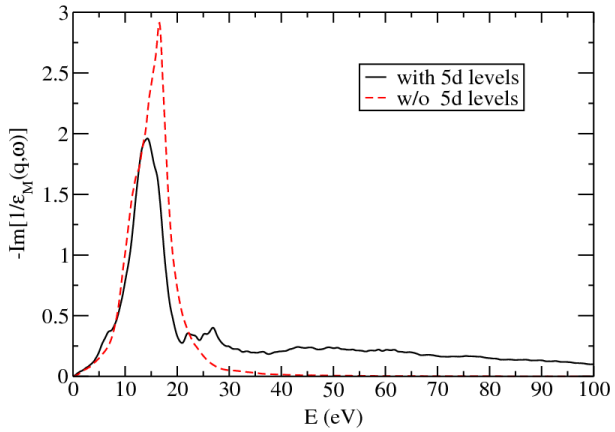

Figure 7.20: Comparison of the EEL spectrum of bulk Bi within the LDA with the spin-orbit coupling for $\mathbf{q} = 0.1$ Å^{-1} $\parallel$ [111] with $5d$ semicore levels (solid black line) and without $5d$ semicore levels (red dashed line). The calculations have been performed using a $12 \times 12 \times 12$ uniform $\mathbf{k}$ point mesh centered at the Γ point, a Lorentzian broadening $\sigma = 0.035$ Ry, and 2500 Lanczos iterations using the extrapolation technique.

Moreover, when the $5d$ levels are not included in the valence region there are no peaks between 20 - 30 eV, which are due to the interband transitions from the $5d$ levels to the

[16] Without $5d$ semicore levels in the valence region the transferability of the pseudopotential is worse than when the $5d$ levels are included in the valence region (see Appendix A.1).

lowest conduction bands. In addition, there is a blue-shift of the plasmon peak by 2.5 eV, and increase in its intensity.

A more precise comparison of the spectrum in the 0 - 10 eV range is beyond the scope of this study. The pseudopotential without $5d$ semicore states has not been optimized, and thus the corresponding band structure shows deviations from the one obtained when $5d$ levels are included in the valence region.

7.4 Conclusions

In this chapter I have presented a new *ab initio* method to the electron energy-loss spectroscopy. It is an extension of the Liouville-Lanczos approach from the optical case ($\mathbf{q} = 0$) to EELS ($\mathbf{q} \neq 0$). The theory, which has been developed in this chapter, unites the theory of TDDFPT for optics (see Sec. 3.4) and the theory of the static density functional perturbation theory for $\mathbf{q} \neq 0$ [40]. The new method consists in solving the linearized TDDFPT equations in the frequency domain. The electronic susceptibility $\chi(\mathbf{q}, \omega)$ is expressed as an off-diagonal matrix element of the resolvent of the Liouvilian superoperator, which can be efficiently calculated by means of the Lanczos recursion method, much like in the optical case.

The Liouville-Lanczos approach to EELS has several advantages over the conventional TDDFT approach to EELS, based on the solution of the Dyson-like equation. Firstly, no empty states are calculated, which allows for an extension of the calculations of the EEL spectra from the low-loss to the 50-100 eV region. Secondly, the new approach scales computationally only a few times larger than the ground-state DFT calculations, which allows us to consider systems containing hundreds of atoms. However, currently the new method is limited by the adiabatic approximation to the exact exchange-correlation kernel.

I have tested the Liouville-Lanczos approach to EELS on prototypical examples of silicon and aluminum. The agreement between theory and experiment is remarkable. I have paid special attention to a study of the convergence properties of the new method. It turns out, that the use of the extrapolation technique can greatly reduce the computational effort needed to obtain the converged EEL spectra, as in the optical case.

I have applied the new method to a study of the EEL spectrum of bismuth. The agreement between theory and experiment is extremely good. In particular, I have found that the effect of the spin-orbit coupling on the EEL spectrum of Bi is large. The SOC influences the intensities as well as the positions of the peaks due to interband transitions, whereas the plasmon peak position is not sensitive to the SOC, and its intensity is increased by 26 % when the SOC is not included. Moreover, with the new method I could easily reproduce the broad structure in the 40-100 eV range in the EEL spectrum of Bi. I have calculated the plasmon dispersion, and have found that by increasing $\mathbf{q}$ the plasmon peak merges with the peaks due to the interband transitions from the $5d$ levels, due to the electron-hole continuum. I have also shown that the description of the EEL spectrum of Bi within the RPA with crystal local field effects is very close to TDLDA, whereas a neglect of the CLFE leads to significant changes in the EEL spectrum. In addition, I have shown that the anisotropy in the EEL spectrum of Bi becomes pronounced with

increasing the transferred momentum $\mathbf{q}$.

The Liouville-Lanczos approach to EELS is very promising in the field of plasmonics [327]. In particular, it is expected to be very efficiently applied for calculations of surface plasmons [328], which implies an inclusion in the simulations of large number of atoms - a challenging task for conventional state-of-the-art methods.

Chapter 8

General conclusions and perspectives

In this thesis, I have interpreted the time-resolved and angle-resolved photoemission experiment on the Bi(111) surface, on the basis of the Kohn-Sham band structure within the LDA and GGA. I have revealed the character of the electronic states - bulk states or surface resonances - in the experimental intensity map. By using the symmetry arguments I have shown that one of the electronic bands has a bulk character with a three-fold symmetry, and the other bands correspond to the surface states and surface resonances having a six-fold symmetry. Moreover, by using the frozen-phonon approximation I have computed the electron-phonon coupling in Bi, and have shown that it strongly depends on the electronic wavevector, confirming the experimental finding. The amplitude of the oscillation of the electronic bulk band, which is induced by the A_{1g} coherent phonon mode through the electron-phonon interaction, has been accurately reproduced within both the LDA and GGA. I have also shown that the DFT calculations on bulk Bi cannot explain a very steep shift of 20 meV in the binding energy of the highest valence bulk band immediately after the photoexcitation of the sample, and that further theoretical studies that go beyond DFT are required.

I have performed a detailed study of the low-energy and high-energy plasmonic excitations in Bi. To this end, theoretical developments and implementation of a new method for the electron energy-loss spectroscopy (EELS) have been performed.

I have studied the low-energy carrier-response in the photoexcited Bi in the range from tens to hundreds of meV, which is determined by the intraband contribution to the dielectric function of the material. I have developed a new methodology to describe the free-carrier absorption *from-first-principles*, which allowed us to interpret the free-carrier Drude response in Bi at equilibrium and in the photoexcited state in the time-resolved terahertz experiment. The new methodology is based on the semiclassical description of the frequency of the electron-and-hole plasma oscillations, which in Bi displays a non-monotonic behaviour as initial increase and subsequent decay. By determining various carriers properties as the Fermi velocity, effective and optical masses, restricted density of states near the Fermi level, I could explain the peculiar behaviour of the plasma frequency. I have shown that such a behaviour is induced by an accumulation of electrons and holes in the true local extrema of the electronic band structure near the Fermi level, where the photoexcited carriers spend several hundreds of femtoseconds before thermalizing

to the Fermi level due to the electron-phonon and hole-phonon interaction, where the recombination of the electron-hole plasma subsequently takes place. In particular, I have shown that the maximum in the valence band at the Γ point serves as a charge-reservoir for extremely heavy holes, having the average effective mass of $\sim 18m_0$, and slows down the hole thermalization process, which is likely to be dominant and responsible for the non-monotonic evolution of the plasma frequency.

I have also studied the high-energy carrier-response in Bi in the energy range up to 100 eV, which is determined by the single-particle interband excitations and collective excitations of carriers at various momenta $\mathbf{q}$, the information about which is incorporated in the inverse dielectric function of the material. To this end, I have developed an new *ab initio* method to EELS, the so-called Liouville-Lanczos (LL) approach. Such a method is based on the evaluation of the carrier susceptibility as an off-diagonal matrix element of the resolvent of the Liouvillian superoperator, which can be readily computed by using the Lanczos recursion method. The LL approach is superior with respect to the traditional TDDFT approach based on the solution of the Dyson-like equation for the susceptibility. Namely, the new method avoids the computation of numerous empty states, which allows us to extend the calculations of the electron energy-loss (EEL) spectra to the 50-100 eV range, and which scales computationally only a few times larger than the ground-state DFT calculations, which allows us to treat hundreds of atoms. However, currently the LL approach is limited by the adiabatic approximation to the exact exchange-correlation kernel. After a successful test of the new method on silicon and aluminum, I have performed a detailed analysis of the EEL spectra of Bi. I have found the following features of the EEL spectra of Bi: (*i*) the spin-orbit coupling is essential for a description of the plasmon peak and the peaks due to interband transitions, (*ii*) the increase of the transferred momentum $\mathbf{q}$ leads to a merging of the plasmon peak with the peaks coming from the interband transitions, which is due to the electron-hole continuum, (*iii*) the crystal local field effects become important when $\mathbf{q}$ increases, and (*iv*) the anisotropy of the EEL spectrum of Bi becomes pronounced when $\mathbf{q}$ increases.

The perspectives of this PhD work are numerous.

- *Surfaces of Bi and of Bi compounds.*

  In the past years, a new field has emerged in solid state physics when it was realized that the spin-orbit coupling leads to topological insulating phases that cannot be adiabatically connected to conventional insulators and semiconductors [179]. Many of these topological insulators are based on Bi compounds, *e.g.*, Bi_2Te_3 and Bi_2Se_3. My understanding of both the spin-orbit coupling and the modelling of Bi can be used to attack this field of research.

- *Thermoelectricity in Bi.*

  In this thesis I have discussed little the thermoelectric properties of Bi. However, thanks to my *ab initio* modelling of Bi, the thermal transport is going to be computed including the phonon-phonon interaction, in collaboration with J. Sjakste (LSI, École Polytechnique), F. Mauri, M. Lazzeri, and L. Paulatto (IMPMC, Université

Paris VI, France), and N. Mingo (CEA-LITEN, Grenoble, France). Next step then will be an understanding of the thermoelectric properties of Bi, where the electron-phonon interaction plays a big role known as the *phonon drag effect* [329, 330].

- *Ab initio calculation of the relaxation times.*

  In the interpretation of the time-resolved terahertz experiment of Chapter 6, the rates of recombination τ_h and τ_l have been obtained as fitting parameters. In the future, they could be obtained *ab initio* by calculating the electron-hole plasma recombination carried by the carrier-phonon interaction.

- *Charge density waves.*

  Another topic which my PhD leaves open for the future is the *ab initio* calculation of the electron-phonon coupling in materials sustaining a charge density wave (CDW). Indeed, phase coexistence due to the coupling between various degrees of freedom (spin, charge, lattice) are a characteristic of emerging materials which are "hot topics" because of their important physical properties, such as materials with a CDW, or materials showing superconductivity at high temperatures, or with large magnetoresistivity [331]. Charge density wave is a structural transition in which the electronic subsystem is strongly coupled to the atomic one [332]. The structural transition can be dominated by the electronic subsystem (Mott instability) or by phonons, *i.e.* the collective atomic motion (Peierls instability). The electronic correlations, which are present in the Mott instability, are difficult to take into account in the calculation. In contrast, it has been shown that Peierls instabilities can be calculated in the framework of DFT [333]. The formation of a CDW is expected in a system showing a large anisotropy. In order to understand the formation of a CDW, the electron-phonon coupling is an essential ingredient, and more specifically, the dispersion of the electron-phonon coupling in the Brillouin zone is crucial [332]. In my PhD, I have shown that this dispersion of the electron-phonon coupling is in extremely satisfactory agreement with experiments in bismuth, which opens the way to the study of other materials where a Peierls-driven CDW occurs, like in $CeTe_3$.

- *Liouville-Lanczos approach to EELS.*

  Finally, one of the main achievements of my PhD is the new method to EELS. I believe that the Liouville-Lanczos approach is the next-generation method, which can be readily applied for various challenging problems in the field of plasmonics [327], *e.g.*, for a calculation of surface plasmons [328] in complex materials containing hundreds of atoms in the unit cell.

Appendix A

Bismuth

A.1 Pseudopotential

I have generated a fully-relativistic norm-conserving pseudopotential (PP) of Bi in a separable form [77, 80] (see Sec. 2.3.2). For the PP generation I used the `ATOMIC` code which is a part of the `QUANTUM ESPRESSO` package [68]. The work has been done in collaboration with Prof. Andrea Dal Corso.

The electronic configuration of a neutral Bi atom is [Xe]$4f^{14}5d^{10}6s^26p^3$. At the first step of the PP generation, all of these electronic levels have to be separated into the valence region and the core region [see Sec. 2.3.2(a)]. I have included the $5d^{10}6s^26p^3$ levels in the valence region, and the rest - into the core. As pointed out in Sec. 4.2.2, the $5d$ semicore levels can be included either in the core region or in the valence region. I have found that it is necessary to include the $5d$ levels in the valence region in order to greatly improve the transferability of the PP. However, this makes the NC-PP extremely hard, which shows up in the necessity to use a very high kinetic-energy cutoff.[1] Thus, it is usually recommended to switch from NC-PP to Ultrasoft-PP, which are much softer and require smaller kinetic-energy cutoff. Nonetheless, I have decided to generate a NC-PP. The results obtained with such a NC-PP are used as a reference for the development of Ultrasoft-PPs.

At the next step of the PP generation, I solved the relativistic Dirac equation for a single Bi atom by performing all-electron (AE) calculation. The AE-wavefunctions serve as a reference for the construction of the PP. Since I am interested in the generation of the norm-conserving PP, certain conditions must be satisfied (see Sec. 2.3.2). One of these conditions is that the pseudo-wavefunctions must coincide with the AE-wavefunctions outside of the sphere with a cutoff radius r_c. To this end, I have set up the $5d$, $6s$, and $6p$ wavefunctions with the cutoff radii r_c of 1.88, 1.79, and 2.30 (a.u.), respectively. In the generation process, I have also included the unoccupied $5f$ levels with $r_c = 2.41$ (a.u.). For a pseudization of the wavefunctions I have used the Troullier-Martins method [334]. The nonlinear core correction was not used [76]. As a local part of the PP I have taken the s channel, which insured the absence of ghost states [81]. I have checked that if one of the channels p, d or f is taken as a local part of the PP, then the ghost states appear.

[1] For the ground-state calculation of Bi I had to use a kinetic-energy cutoff as large as 150 Ry.

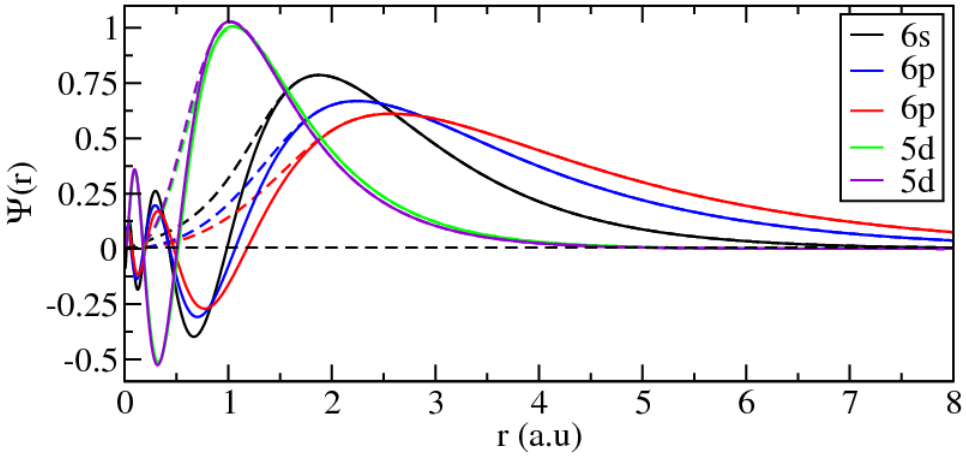

Figure A.1: Comparison of the all-electron wavefunctions (solid lines) with the pseudo-wavefunctions (dashed lines) of a single Bi atom. When r approaches zero, the all-electron wavefunctions become frequently oscillating functions, while the pseudo-wavefunctions remain smooth nodeless functions. (Unpublished)

Figure A.1 shows the comparison of the AE-wavefunctions with the pseudo-wavefunctions of a single Bi atom. As can be seen, the AE-wavefunctions become rapidly oscillating functions when the radius r approaches zero ($r = 0$ corresponds to the center of the nucleus), while the pseudo-wavefunctions remain smooth and nodeless. Due to the spin-orbit coupling effect, there are two different $6p$ wavefunctions, two different $5d$ wavefunctions, and only one $6s$ wavefunction (there is no splitting of the $6s$ level, because the orbital momentum is zero). Thus, all electronic levels, except the s levels, are split on $j + 1/2$ and $j - 1/2$ levels, where j is the total angular momentum (see Sec. 2.2.1).

During the PP generation, the approximation for the exchange-correlation energy has to be specified. I have generated two pseudopotentials: one within the LDA by using Perdew-Zunger parametrization of the Ceperley-Alder functional [34], and another one within the GGA by using Perdew-Burke-Ernzerhof parametrization [36].

The transferability of the LDA and GGA PPs has been tested. By considering different electronic configurations apart from the neutral one, I have compared the total energy of the all-electron and pseudopotential calculations. The energy differences are within 0.001-0.01 (Ry), which confirms good transferability properties of my PPs. I have also compared logarithmic derivatives of the pseudo-wavefunctions with the ones of AE-wavefunctions. It turns out, that the logarithmic derivatives of the two are close, and no ghost states are present. All of these tests confirm good properties of the new PPs.

A.2 Phase diagram

As illustrated in Fig. A.2, bismuth has a very complex phase diagram, with as many as 10 different phases. The phase diagram of Bi is much more intricate in comparison with other group-V elements (*e.g.*, As, Sb). The literature on the Bi phase diagram is confused by controversy over the existence of certain phases and by changes in phase numbering due to conflicting observations [335]. In Fig. A.2 I use the numbering according to Homan [336].

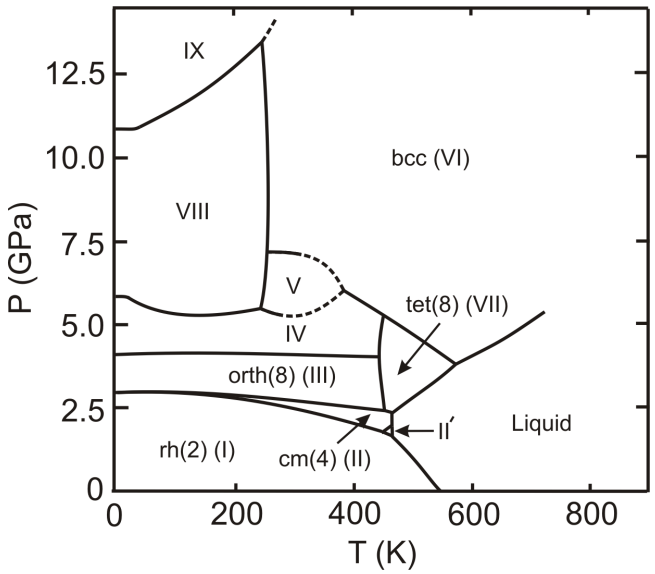

Figure A.2: Phase diagram of bismuth according to Ref. [335]. Numbering of phases according to Ref. [336].

At ambient pressure and room temperature, bismuth crystallizes in the $A7$ rhombohedral structure (see Sec. 4.2.1). I will label this phase by $rh(2)$, where 2 in the brackets indicates the number of atoms in the primitive unit cell. The compression at room temperature to 40 GPa produces the structure sequence I $\rightarrow$ II $\rightarrow$ III $\rightarrow$ IV $\rightarrow$ V $\rightarrow$ VI. Phase II has been identified as base-centered monoclinic with 4 atoms per unit cell - $cm(4)$, and phase III has been tentatively identified as orthorombic with 8 atoms per unit cell - $orth(8)$ [335]. The high-pressure phase VI is body-centered cubic - *bcc* [335]. No further transitions were found up to 40 GPa.

At temperatures below 300 K, the I - II transition disappears in a triple point, and two new phases, VIII and IX, appear. At temperatures above 300 K, two additional phases, VII and II′, with a very small stability field, were found [335]. Phase VII has been identified as tetragonal with 8 atoms per unit cell - $tet(8)$, very similar to phase III [335].

The melting curve of bismuth has been measured up to 7.0 GPa. Interestingly, the $rh(2)$ melting curve has a large negative slope, unlike the other group-V elements, and like silicon [337]. This is a signature of covalent bonding in the material.

The structural phase transitions of Bi as a function of pressure, and the associated large changes in the electrical resistivity, have been of great importance in high pressure physics where Bi has been used as a pressure calibrant [338]. The interest is in the fact that Bi becomes a superconductor under pressure [338]. The pressure is one of the mechanisms which can induce a superconductivity in solids, which are not superconducting at ambient pressure, *e.g.* Bi in the $rh(2)$ phase. Bismuth is not superconducting in the $rh(2)$ phase because the density of states at the Fermi level is extremely small [see Fig. 4.5(b)]. However, Bi in the *bcc* phase at pressure of 9 GPa is superconducting, with the critical temperature of superconductivity of $T_c = 8.6$ K [338]. This is due to the fact that the density of states at the Fermi level is high, and thus the (theoretical) electron-phonon coupling constant is also large, $\lambda \sim 0.8$ [338].

A.3 Restricted density of states

The purpose of this appendix is to calculate the restricted density of states of bismuth near the T and L points (see Figs. 4.3(a) and 4.3(b)), which is needed for the calculation of the change of the number of carriers, Δn, and the change of the squared plasma frequency, $\Delta\omega_p^2$, due to the photoexcitation [see Eqs. (6.42) and (6.43)].

Let us define the *restricted density of states* (RDOS) as the number of states per eV in a restricted region of the Brillouin zone (BZ).

For the calculation of the RDOS, I have modified the tetrahedron method of Blochl *et al.* [197]. In the tetrahedron method, the Brillouin zone is divided into tetrahedra. There are four vertices in each tetrahedron, and these vertices coincide with the **k** points with which the BZ is sampled. It is worth noting that the **k** point sampling of the BZ must be *uniform*, thus one can use a Monkhorst-Pack scheme [324].

In bismuth, as a restricted region for the RDOS I have used a sphere of radius $R = 0.3\,(2\pi/a_0)$, where a_0 is the equilibrium lattice parameter.[2] Once the full BZ is sampled with the tetrahedra, one has to select only those tetrahedra which are inside of the sphere. There are some tetrahedra which are exactly on the border of the sphere: if at least one vertex of the tetrahedron is outside of the sphere, this tetrahedron is not included in the calculation of the RDOS. This is an approximation which leads to some small error in the RDOS. However, this error can be reduced by sampling the BZ by a larger number of smaller tetrahedra, *i.e.* by sampling the BZ with very dense **k** point mesh. In the case of Bi, I have sampled the BZ with a $58 \times 58 \times 58$ uniform **k** point mesh centered at the Γ point, which resulted in 5221 **k** points in the sphere. It is worth noting that the RDOS has to be normalized on the volume of the sphere, $V = (4/3)\pi R^3$, whereas the total DOS is normalized on the volume of the full BZ.

In the case of Bi, I am interested in the RDOS in the energy range from -0.3 to 0.3 eV with respect to the Fermi level. The reason why this energy range is considered is the following. The aim is to calculate the optical mass with Eqs. (6.41) - (6.43). In these equations, the RDOS, $\tilde{g}(\varepsilon)$, is multiplied by the modulus of the difference of the Fermi-Dirac functions, $|f_{\rm FD}(\varepsilon, T) - f_{\rm FD}(\varepsilon, T_0)|$, and by the difference of its derivatives,

[2] Note that the distance between Γ and T (or between Γ and L) is equal to $\approx 0.6\,(2\pi/a_0)$.

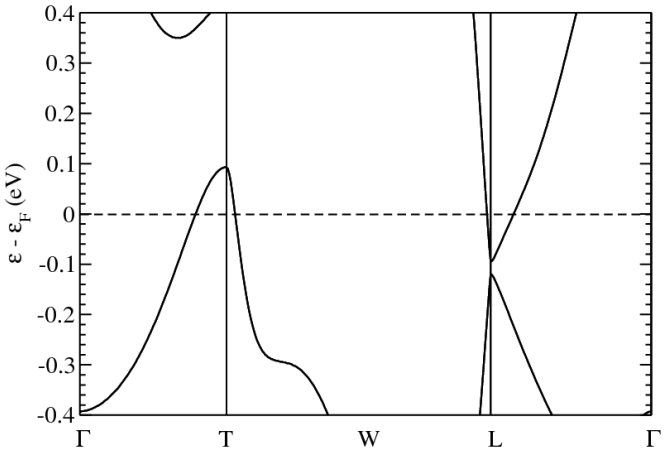

Figure A.3: Kohn-Sham band structure of Bi near the Fermi level, calculated within the GGA at the GGA theoretical equilibrium lattice parameters (see Table 5.1), including the spin-orbit coupling. The Fermi level is at zero energy. See Sec. 5.1.1 for computational details. (Unpublished)

$(-\partial f_{FD}(\varepsilon,T)/\partial\varepsilon) - (-\partial f_{FD}(\varepsilon,T_0)/\partial\varepsilon)$. From Figs. 6.3(a) and 6.3(b) it can be seen that these functions vanish for energy values $\varepsilon < -0.3$ eV and $\varepsilon > 0.3$ eV, if one considers the temperatures $300 < T < 500$ K. Therefore, it is sufficient to determine the RDOS for the energy range $-0.3 < \varepsilon < 0.3$ eV (see Fig. A.3).

Figures A.4(a) and A.4(b) show the comparison of the RDOS near the T and L points with the total DOS. In the energy range $0.09 < \varepsilon < 0.3$ eV the RDOS with a sphere centered at the L point fully coincides with the total DOS. This is due to the fact that the contribution to the RDOS near L comes only from the lowest conduction band (see Fig. A.3.1). For instance, in Fig. A.5(a) the isosurface of constant energy $\varepsilon - \varepsilon_F = 0.20$ eV is shown. It can be seen that the whole isosurface is contained inside the sphere centered at the L point. Note, the energy $\varepsilon = 0.09$ eV corresponds to the top of the highest valence band at the T point (see Table 5.2, GGA at the GGA theoretical equilibrium lattice parameters). Hence, for energy values $\varepsilon < 0.09$ eV the highest valence band comes into play, and its states make a contribution to the DOS (see Fig. A.3.1).

At the L point, there is a "gap" between the top and the bottom of the bands (see Fig. A.3), which covers the energy range $-0.120 < \varepsilon < -0.096$ eV (see Table 5.2, GGA at the GGA theoretical equilibrium lattice parameters). These bands at the L point are extremely sharp, which means that the density of states is exceedingly small. Indeed, in Fig. A.4(b) it can be seen that the RDOS near the L point is non-distinguishable from zero in the energy range $-0.18 < \varepsilon < -0.06$ eV. For this reason, the RDOS near the T point fully coincides with the total DOS in this energy range. Figure A.5(b) confirms this feature: the isosurface of constant energy $\varepsilon - \varepsilon_F = -0.11$ eV consists only of the part coming from the highest valence band near the T point, and it is fully contained in the sphere centered at the T point.

Finally, in the energy range $-0.30 < \varepsilon < -0.18$ eV, both the RDOS near the T point

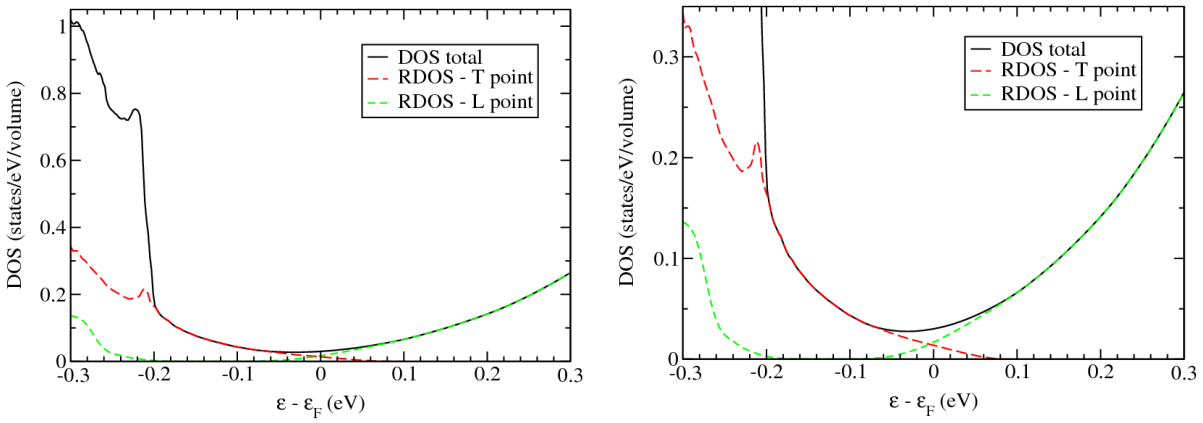

Figure A.4: (a) Comparison of the restricted density of states (RDOS) near the T and L points with the total DOS. (b) The same as (a) but zoomed. The (R)DOS is in units of states per eV and per volume [in the case of the total DOS, the volume of the full Brillouin zone, and in the case of the RDOS, the volume of the sphere centered at T or L]. (Unpublished)

and the RDOS near the L point differ considerably from the total DOS [see Fig. A.4(a)]. This can be understood from Figs. A.5(c) and A.5(d): a large portion of the isosurfaces $\varepsilon - \varepsilon_F = -0.21$ eV and $\varepsilon - \varepsilon_F = -0.26$ eV is contained outside of the spheres centered at the T and L points. There is a very steep rise of the total DOS in this energy range. This is so because the highest valence band in the vicinity of the T point becomes very flat (see Fig. A.3), which enhances the DOS appreciably.

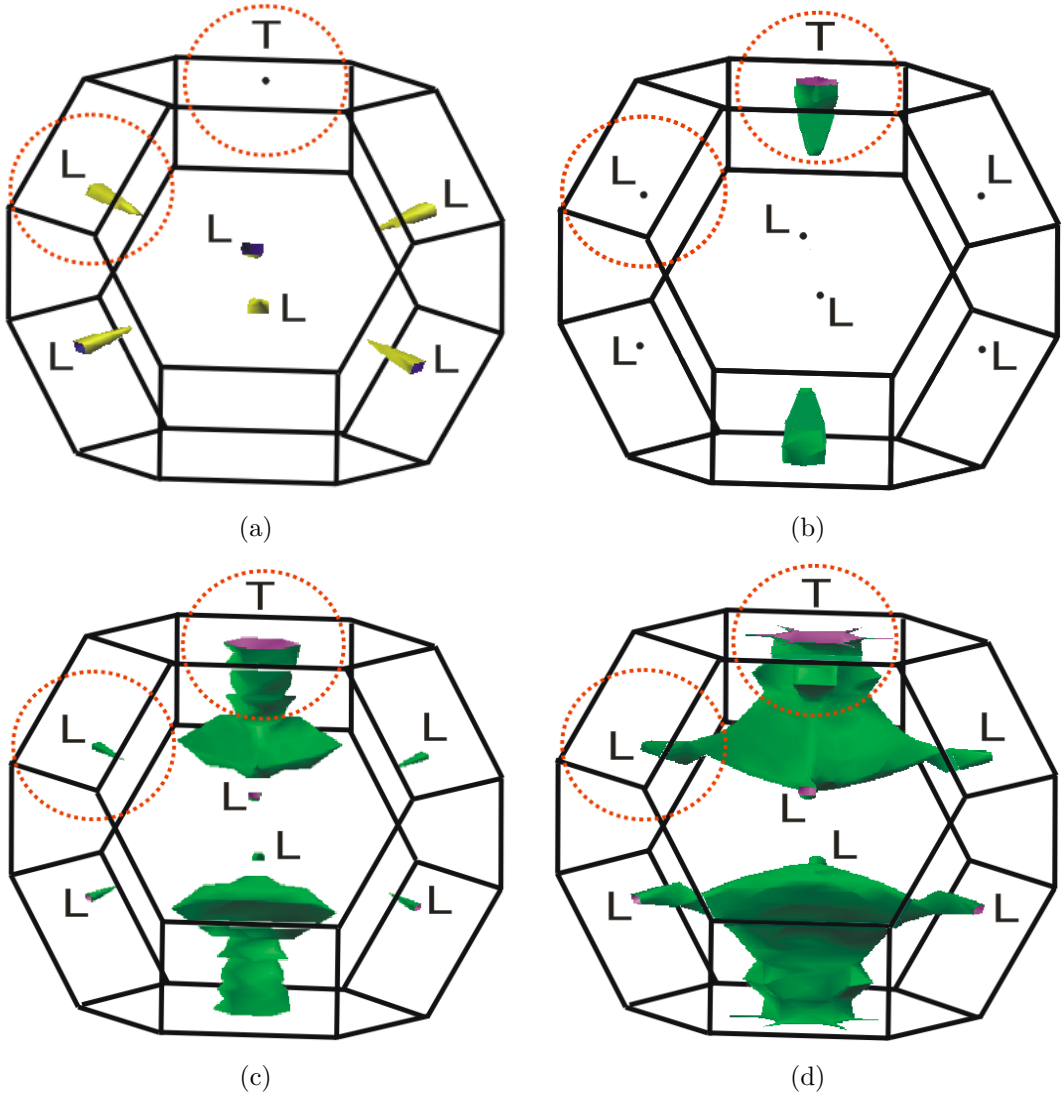

Figure A.5: Energy isosurfaces in the Brillouin zone of the rhombohedral lattice. The yellow color corresponds to the contribution from the lowest conduction band, and the green color - from the highest valence band. (a) Energy isosurface $\varepsilon - \varepsilon_F = 0.20$ eV, (b) Energy isosurface $\varepsilon - \varepsilon_F = -0.11$ eV, (c) Energy isosurface $\varepsilon - \varepsilon_F = -0.21$ eV, (d) Energy isosurface $\varepsilon - \varepsilon_F = -0.26$ eV. Circles denote spheres with the radius $R = 0.3\,(2\pi/a_0)$, which restrict regions in the reciprocal space around the high symmetry points T and L. (Unpublished)

Appendix B

Spectroscopy

B.1 Photoemission spectroscopy

Photoemission spectroscopy (PES), also known as *photoelectron spectroscopy*, is a general term which refers to all techniques based on the *photoelectric effect* [339, 340, 341]. In the photoelectric effect, electrons are emitted from matter as a consequence of the absorption of photons, and they are called *photoelectrons*. PES is one of the most sensitive and accurate techniques for measuring the energy of electronic states [340].

B.1.1 Mechanism of photoemission

A beam of monochromatic radiation, provided either by a gas-discharge lamp, or laser, or synchrotron beamline, is incident on a sample. If an electron in the sample absorbs the energy of one photon and it is larger than the work function of the sample,[1] then this electron is ejected from the sample. A part of the photon energy is used to liberate the electron from the atomic binding, and the rest contributes to the kinetic energy of the free electron. Instead, if the photon energy is too low, the electron is unable to escape from the material.

B.1.2 Angle-resolved photoemission spectroscopy

Angle-resolved photoemission spectroscopy (ARPES) is one of the most direct methods of studying the electronic structure of solids [341]. By measuring the kinetic energy and angular distribution of the photoelectrons, one can gain information on both the energy and momentum of the electrons propagating inside a material. Nowadays, ARPES experiments can reach the energy resolution of ~ 2 meV and angular resolution of $\sim 0.2^\circ$ [341].

Since photoelectrons have different momenta, they escape in different directions. By collecting these photoelectrons with an electron energy analyzer, one measures their kinetic energy ε_{kin} for a given emission angle [340]. Thus, the wavevector $\mathbf{k}$ of the photo-

[1] The *work function* is the measure of the potential barrier at the surface of the material that prevents the valence electrons from escaping [339].

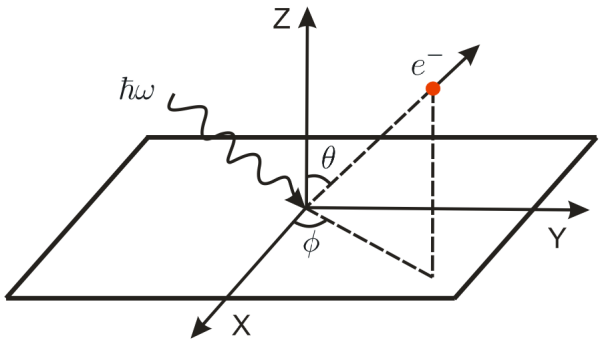

Figure B.1: Geometry of the ARPES experiment. The emission direction of the photoelectron is specified by the polar emission angle θ and azimuthal emission angle ϕ. According to Ref. [341].

electron can be determined: its modulus is given by $|\mathbf{k}| = \sqrt{2m_0\varepsilon_{kin}}/\hbar$, and its parallel component $\mathbf{k}_\parallel$ and perpendicular component $\mathbf{k}_\perp$ to the sample surface are obtained from the polar emission angle θ and azimuthal emission angle ϕ (see Fig. B.1). The goal is then to deduce the electronic band dispersion of the solid $\varepsilon_n(\mathbf{k})$ (where n is the band index), *i.e.* the relation between the binding energy ε_B and momentum $\mathbf{k}$ for the electrons propagating *inside the solid*, starting from ε_{kin} and $\mathbf{k}$ measured for the photoelectrons *in vacuum*. In order to do that, one has to use the conservation laws of the total energy and momentum.[2]

Within the non-interacting electron picture, one can relate the kinetic energy and momentum of the photoelectron to the binding energy ε_B and crystal momentum $\mathbf{k}$ inside the solid as [340]:

$$\varepsilon_{kin} = \hbar\omega - W - |\varepsilon_B|, \tag{B.1}$$

$$\mathbf{k}_\parallel = \frac{1}{\hbar}\sqrt{2m_0\varepsilon_{kin}}\,\sin\theta, \tag{B.2}$$

where W is the work function of the material, m_0 is the free-electron mass, and $\mathbf{k}_\parallel$ is the component of the momentum parallel to the surface of the crystal.

In order to map the electronic dispersion $\varepsilon_n(\mathbf{k})$, one needs to know the full crystal wave vector $\mathbf{k}$, *i.e.* its parallel and perpendicular components. However, the perpendicular component $\mathbf{k}_\perp$ is not conserved across the sample surface due to the lack of translational symmetry along the surface normal [340]. This implies that, in general, even experiments performed for all $\mathbf{k}_\parallel$, *i.e.* by collecting photoelectrons at all possible angles, will not allow for a complete determination of the total crystal wavevector $\mathbf{k}$ [340]. However, there are two possible solutions to this problem, experimental and theoretical. On one hand, several specific experimental methods for absolute three-dimensional band mapping have been developed (see, *e.g.* Ref. [339]). On the other hand, $\mathbf{k}_\perp$ can be determined from *ab initio* DFT calculations [see Sec. 5.2.4(a)]. A particular case in which the uncertainty

[2]The photon momentum can be neglected at the low photon energy typically used in ARPES experiments [341].

in $\mathbf{k}_\perp$ is less relevant is that of the low-dimensional systems characterized by a negligible dispersion along the z axis, *i.e.* the surface normal [340].

B.1.3 Time-resolved ARPES

The femtosecond ARPES can be used for the investigation of the time-resolved electron dynamics by the pump-probe experiment [339]. By pumping an electron to a higher-level excited state with the first photon, the subsequent evolution and interaction of electronic states as a function of time can be studied by the second probing photon. The pump-probe ARPES can be used to study complicated electronic systems with a sub-picosecond resolution [339].

B.1.4 Experimental set-up

In this section I present the details of the time-resolved and angle-resolved photoemission experiment, which has been carried out by our collaborators.

The FemtoARPES setup has been employed, using a Ti:Sapphire laser that generated 35 fs pulses centered at 810 nm, corresponding to the energy $\hbar\omega = 1.5$ eV, with a repetition rate of 250 kHz. Part of the beam was employed to generate the fourth harmonic by frequency doubling in BBO crystals (β-BaB_2O_4).[3] The 50 fs probe pulse, corresponding to the energy $\hbar\omega = 6$ eV, was centered at 205 nm. The 205 nm probe and the 810 nm pump were focused on the sample with spot diameters of 100 μm and 200 μm, respectively. Their cross-correlation in a BBO crystal had a full width at half maximum (FWHM) of 80 fs. An electrostatic spectrometer with an energy resolution better than 10 meV and an angular resolution better than 0.5° was used to analyze the emitted photoelectrons. The overall energy resolution was, nonetheless, limited to 50 meV by the bandwidth of the 205 nm beam. The (111) surface of bismuth was obtained by sputtering and annealing cycles of a single crystal. All measurements were carried out at the base temperature of 130 K and at the base pressure of 7×10^{-11} mbar. The out-of-equilibrium spectra were collected with the incident pump fluence of 0.6 mJ/cm^2.

B.1.5 Electronic temperature after the photoexcitation of Bi

Photoexcitation by an intense and ultrafast laser pulse generates sizable effects on the photoelectron current. Figure B.2(a) shows the spectrum acquired at $k_\parallel = 0.12$ Å^{-1} along the $\overline{\Gamma} - \overline{\mathrm{M}}$ direction for two different pump-probe delays [see Fig. 5.4(a)]. There is a large shift of band b and a somewhat smaller shift of band a towards higher binding energy. Moreover, there is a large reduction of the spectral weight, taking place 300 fs after the arrival of the pump beam, due to the electron depopulation. This depopulation has been used for the extraction of the electronic temperature as described in the following.

Let us denote by $S(\varepsilon, \tau_-)$ the spectrum taken at the pump-probe delay τ_- before the photoexcitation corresponding to the equilibrium temperature T_-, and $S(\varepsilon, \tau_+)$ is the spectrum taken at the pump-probe delay τ_+ after the photoexcitation corresponding to

[3]Note that BBO crystals absorb light at 200 nm.

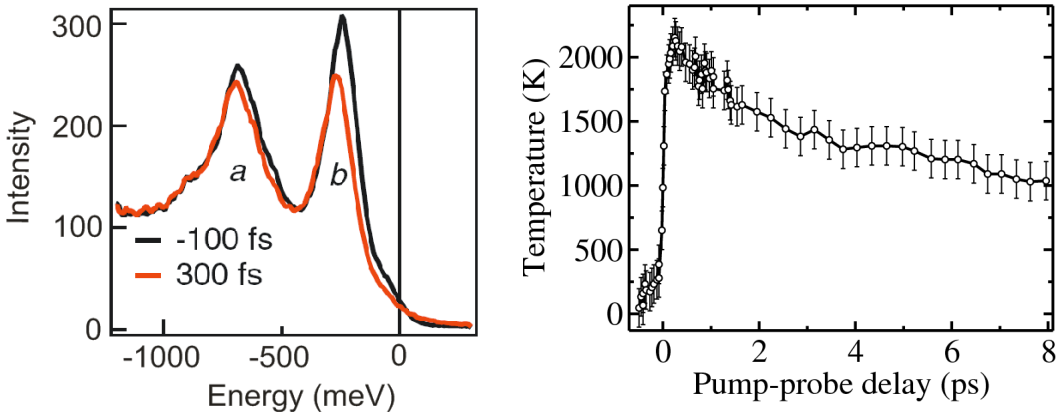

(a) (b)

Figure B.2: (a) Photoelectron spectra acquired 100 fs before and 300 fs after the arrival of the pump beam along the $\overline{\Gamma}-\overline{\mathrm{M}}$ direction at $k_{\|} = 0.12$ Å^{-1}. (b) The effective temperature T_+ of the photoexcited electrons as a function of the pump-probe delay. From Ref. [267].

the temperature T_+. It is worth noting that at high electronic temperature T_+ the spectral weight of bands a and b is modified also due to the Fermi-Dirac distribution. Thus, the weighting factor has to be corrected by multiplying the spectrum of the photoexcited state $S(\varepsilon, \tau_+)$ by $f_{FD}(\varepsilon, T_-)/f_{FD}(\varepsilon, T_+)$. Therefore, in order to determine the electronic temperature T_+, let us define the functional:

$$F(T_+) = \int_{\varepsilon_1}^{\varepsilon_2} \left[S(\varepsilon, \tau_+) \frac{f_{FD}(\varepsilon, T_-)}{f_{FD}(\varepsilon, T_+)} - S(\varepsilon, \tau_-) \right]^2 d\varepsilon, \tag{B.3}$$

where $f_{FD}(\varepsilon, T_{\mp})$ is the Fermi-Dirac distribution function, $\tau_- = -130$ fs and $\tau_+ = 300$ fs are the pump-probe delays before and after the photoexcitation, respectively, $\varepsilon_1 = -400$ meV and $\varepsilon_1 = -150$ meV are the energy limits of the interval in which the integral is calculated, $T_- = 130$ K is the temperature of electrons at equilibrium, and T_+ is the temperature of electrons in the photoexcited state, which is unknown. The temperature T_+ can be determined by minimizing the functional in Eq. (B.3), $dF(T_+)/dT_+ = 0$. As a result, the following value of the maximum electronic temperature has been obtained: $T_+ = 2080$ K. The temporal evolution of $T_+(\tau)$ is shown in Fig. B.2(b). By using a fitting by an exponential, it has been determined that T_+ decays as a function of the pump-probe delay τ with a time constant of 6 ps.

It turns out that the correction of the weighting factor in Eq. (B.3) due to the Fermi-Dirac distribution has a minor effect on the photoinduced shift of the electronic states: the position of band b changes only by 6 meV, which corresponds to 23% of the total shift. Moreover, the temporal evolution of this correction follows the monotonic and slow decay of the electronic temperature T_+. Therefore, its contribution completely cancels out when evaluating the amplitude of the fast oscillations induced by the A_{1g} phonon mode.

B.2 Terahertz spectroscopy

What is terahertz (THz) spectroscopy? As a working definition, THz spectroscopy covers the spectral range from 3 cm^{-1} to 600 cm^{-1}, also known as the far-infrared region of the spectrum [342, 343, 344]. This implies frequencies between 0.1 and 20 THz.[4] Though, any work in the frequency range from 0.1 to 100 THz can be regarded as THz spectroscopy [342]. However, in view of developments over the last 23 years, the connotation of this terminology is that it implies generation and detection of THz pulses in a synchronous, coherent manner using visible or near-IR laser pulses [342].

Terahertz radiation can probe physical phenomena such as low-energy excitations and carrier dynamics in electronic materials, and collective vibrational modes in condensed-phase media [344]. However, until 1988, when THz spectroscopy was developed, it has been very challenging to access this region of the electromagnetic spectrum, leading to the "terahertz gap". The THz spectral region bridges microwave and infrared domains (see Fig. B.3). However, developments in THz sources and detectors over the last 20 years have allowed for the coverage of this spectral region [344].

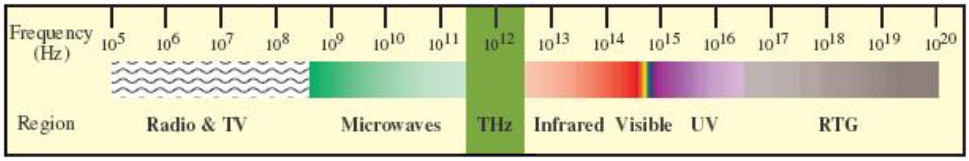

Figure B.3: Spectrum of electromagnetic radiation. The terahertz region is marked by a green rectangle. According to Ref. [344].

The THz pulses are created and detected using short-pulsed visible lasers with pulse widths ranging from 100 fs down to 10 fs [342]. This allows for the possibility to carry out time-resolved far-IR studies with sub-picosecond temporal resolution, which is not possible with conventional far-IR studies [342]. An additional advantage of the THz spectroscopy is that the transient electric field is measured itself, not simply its intensity. This determines the amplitude and the phase of each of the spectral components that make the pulse. The amplitude and the phase are directly related to the absorption coefficient and index of refraction of the sample, and thus the complex permittivity of the sample can be obtained without relying on the Kramers-Kronig analysis [343].

B.2.1 Time-resolved THz spectroscopy

There are different forms of THz spectroscopy [344]: THz time-domain spectroscopy, time-resolved THz spectroscopy, THz emission spectroscopy, and THz imaging. Let us focus on the time-resolved THz spectroscopy, which probes the dynamical properties of the material as a function of the pump-probe delay.

[4]Notice that 1 THz = 10^{12} Hz $\approx$ 1 ps $\approx$ 0.3 mm $\approx$ 33.33 cm^{-1} $\approx$ 4.14 meV $\approx$ 48 K.

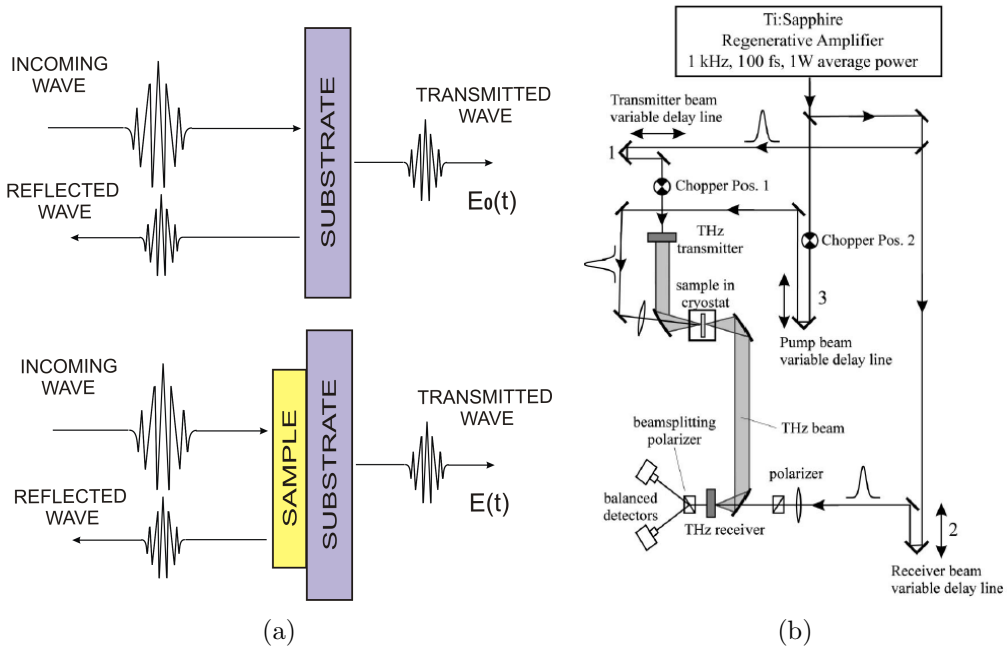

Figure B.4: (a) Schematic illustration of the transmittance and reflection of the incoming THz pulse. Upper panel: the incoming THz pulse passes through the substrate only, lower panel: the incoming THz pulse passes through the sample and substrate. (b) Experimental apparatus used to collect time-resolved THz spectra, from Ref. [342].

In the time-resolved THz spectroscopy (also called, optical pump - terahertz probe spectroscopy), the sample is photoexcited with an ultrafast laser pump pulse with energy ranging from ultraviolet to mid-infrared (and even THz), and is probed by the THz pulse after delay times ranging from less than 100 fs to several nanoseconds [343]. In this way, the THz frequency-dependent complex dielectric function can be determined as a function of the pump-probe delay τ. Owing to the low energy of the THz photons, time-resolved THz spectroscopy constitutes an excellent non-destructive non-contact electrical probe of various transport processes [342].

In the limit of small film thickness, the dielectric function $\epsilon(\omega)$ reads:

$$\epsilon(\omega) = \left[\frac{E_0(\omega)}{E(\omega)} - 1\right] \frac{c}{i\omega d}(n+1), \tag{B.4}$$

and the pump-induced change of the dielectric function at a given pump-probe delay τ, $\Delta\epsilon(\omega,\tau)$, reads:

$$\Delta\epsilon(\omega,\tau) = \frac{\Delta E(\omega,\tau)}{E(\omega)} \frac{c}{i\omega d}\left[n+1+\frac{\omega d}{ic}\epsilon(\omega)\right], \tag{B.5}$$

where n is the refractive index of the substrate, c is the light velocity, d is the film thickness, $E_0(\omega)$ is the Fourier transform of the electric field transmitted only through the substrate, $E(\omega)$ is the Fourier transform of the electric field transmitted through the unexcited sample and substrate, and $\Delta\epsilon(\omega,\tau)$ is its pump-induced change at given pump-probe delay τ [see Fig. B.4(a)].

The experimental apparatus used to collect time-resolved THz spectra is shown in Fig. B.4(b). A reference scan is collected with the chopper in position 1, and a photoexcited difference scan is collected with the chopper in position 2. The THz amplitude is monitored by changing the relative delay of table 1 or table 2 depending on the type of experiment being performed. Delay table 3 is used to change the relative delay of the pump beam.

B.2.2 Experimental set-up

In this section I present the details of the time-resolved THz experiment, which has been carried out by our collaborators.

In the experiment, the THz spectrometer is driven by a Ti:sapphire laser oscillator, delivering 10 fs pulses at a 780 nm center wavelength, and energy 1.6 eV. Part of the laser output is used to excite the sample with an incident fluence of about $10\mu\text{J/cm}^2$. The THz pulses are obtained from the residual 10% of the laser output by difference-frequency generation in a 90 μm GaSe crystal. The THz pulses have a duration of 100 fs (covering a spectral range from 10 to 30 THz) (see Fig. B.5), and energy 0.1 eV. The time-dependent THz electric field is detected by electro-optic sampling using the 12 fs pulses of the seed laser and a 300 μm thick ZnTe crystal. The sample is a polycrystalline Bi film that was evaporated onto a diamond substrate. The purity of Bi film was not high, and the presence of defects was detected. Current measurements have been carried out in the regime of low excitation densities, $\sim 10^{-4}$ electrons per unit cell.

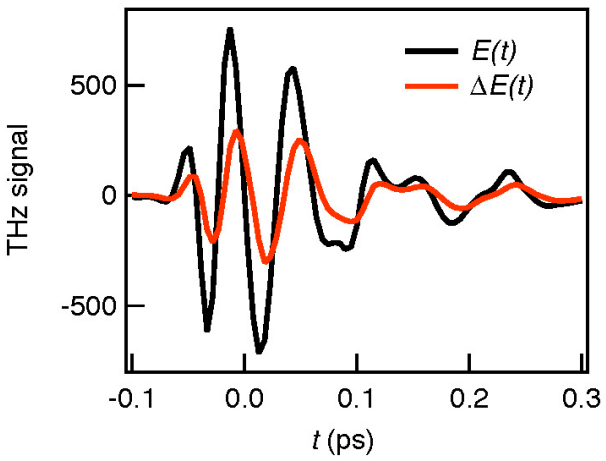

Figure B.5: The electric field transmitted through the unexcited bismuth film and diamond substrate $E(t)$ (dark line), and the pump-induced change $\Delta E(t, \tau)$ at τ= 100 fs (red line). From Ref. [245].

Appendix C

Implementation of the new method to EELS

This thesis will be presented to the C3I committee associated to CPU,[1] GENCI,[2] and "Maison de la Simulation"[3] for the evaluation to obtain the C3I label of skills *"Certificat de Compétences en Calcul Intensif"*. To this end, as well as for the sake of highlighting its main features, in this appendix I present a summary of the implementation of the Liouville-Lanczos approach to the electron energy-loss spectroscopy (EELS), which I have developed during my thesis, and which is described in detail in Chapter 7.

C.1 Program summary

Program title: `EELS` code

Authors: I. Timrov, N. Vast, R. Gebauer, and S. Baroni.

Nature of the problem: Calculation of the electron energy-loss spectra.

Solution method: The susceptibility of a system is calculated within the time-dependent density functional perturbation theory. It is expressed in terms of the resolvent of the Liouvillian superoperator, and calculated using the Lanczos recursion method.

Programming language: Fortran 95

Computer: Any computer architecture

Operating system: Linux, Mac OS X, and other UNIX-like OS's

External routines: The program is tightly integrated component of the `QUANTUM ESPRESSO` distribution [68], which is an integrated suite of computer codes for electronic-structure calculations and materials modelling. The `EELS` code resides in a self-contained directory under the root directory of the `QUANTUM ESPRESSO` tree.

Libraries: The program uses standard mathematical libraries: BLAS, LAPACK [345], and FFTW [346], for which highly optimized implementations exist on many platforms.

Performance: High, both in serial and in parallel execution.

[1] Conférence des Présidents d'Universités, www.cpu.fr

[2] Grand Equipement National de Calcul Intensif, www.genci.fr

[3] www.maisondelasimulation.fr

Current implementation: The program supports norm-conserving (NC) and ultrasoft (US) pseudopotentials; local density approximation (LDA) and generalized gradient approximation (GGA); it works for insulators and metals; non-polarized and noncollinear spin-polarized calculations are possible; spin-orbit coupling can be included; use of symmetry is supported.

Current restrictions: Linear-response regime; adiabatic exchange-correlation kernels only; no hybrid functionals; no projected-augmented wave method; no collinear spin-polarized calculations (LSDA).

Unusual features: Empty states neither used nor even calculated. The new approach scales computationally a few times larger than ground-state calculations. A single Lanczos recursion gives access to the whole electron energy-loss spectrum, *i.e.* there is no need to perform Lanczos recursions for each value of a frequency separately. The new approach is readily applicable to systems containing hundreds of atoms.

Running time: From a few minutes for small systems with few atoms in the unit cell on serial machines, up to many hours on multiple processors for complex systems with hundreds of atoms.

Additional comments: 1. The `EELS` code requires a preliminary ground-state DFT calculation by `PWscf` code, which is also a component of the `QUANTUM ESPRESSO` package. The `PWscf` code yields the Kohn-Sham wavefunctions and energy values for all occupied states, and then this information is further used as an input for the `EELS` code. 2. The `EELS` code contains a *restart* option, which is very useful for: (*i*) testing a convergence of the spectrum with respect to the number of Lanczos iterations, (*ii*) calculations for large systems on massively parallel architectures, which can have a time limit (*e.g.* 24 hours) for one single run.

C.2 Parallelization

As with other components of the `QUANTUM ESPRESSO` package, the `EELS` code is optimized to run on a variety of different platforms, from laptops to massively parallel architectures. The parallelization of the `EELS` code is achieved by using *message-passing paradigm* and calls to standard MPI (message-passing interface) libraries [347]. High performance on massively parallel architectures is achieved by distributing both data and computations in a hierarchical way across processors. The `EELS` code supports a plane-wave parallelization, which is implemented by distributing real- and reciprocal-space grids across the processors. The FFT's (Fast Fourier Transforms), which are used for transformations from real space to reciprocal space and vice versa, are also efficiently parallelized among processors.

The size of a specific application sets limits to the maximum number of processors up to which the performance of the `EELS` code is expected to scale. This is demonstrated in Fig. C.1, where the CPU time as a function of the number of cores is shown, on the example of bismuth. As can be seen, the optimal number of cores is 24, which corresponds to 1 h 11 min. If the number of cores is increased further, *e.g.* up to 32, the calculation will *not* be faster, even contrarily - it takes 1 h 14 min. This is due to the fact that the number of cores is too large for this specific case, and the communication between the cores takes too much time, which slows down the calculation. Therefore, before launching

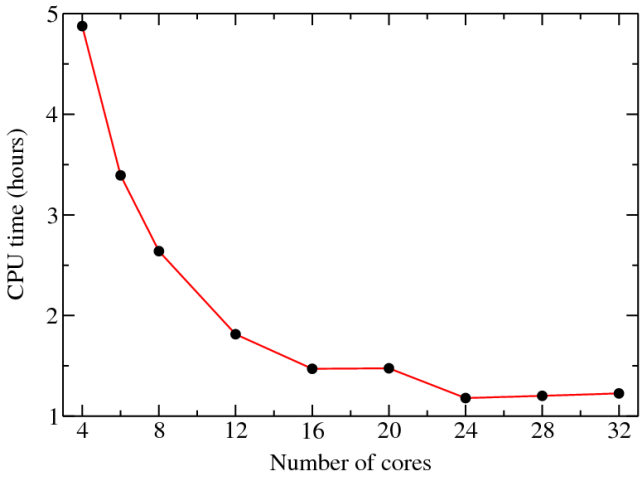

Figure C.1: Scalability of the EELS code: CPU time as a function of the number of cores. The system is bulk bismuth, calculated within the LDA without the spin-orbit coupling, with the following parameters: kinetic-energy cutoff was 60 Ry, a $12 \times 12 \times 12$ uniform $\mathbf{k}$ point mesh centered at the Γ point, norm-conserving pseudopotential, 500 Lanczos iterations.

large calculations one has to determine the optimal number of cores for the system under study.

The performance of the EELS code is optimized also for simulations of intermediate size (on systems containing several tens of atoms or so), which can be performed on medium-size clusters readily available to many groups.

During my thesis, I have performed calculations with the EELS code for Si, Al, and Bi, and the results are presented in Chapter 7. Calculations have been performed on massively parallel supercomputers JADE (CINES) and TITANE (TGCC).

Appendix D

Curriculum Vitae

D.1 Personal information

Family name: Timrov
First name: Iurii
Date of birth: 14.08.1987
Nationality: Ukrainian
E-mail: iurii.timrov@polytechnique.edu

Education

2009 - 2013:

PhD student at the Laboratoire des Solides Irradiés of the École Polytechnique (Palaiseau, France), in the group *Théorie: Science des matériaux* headed by Dr. Nathalie Vast.

2008 - 2009:

MSc student at the Department of Theoretical Physics of the National Taras Shevchenko University of Kyiv (Kyiv, Ukraine). Obtained *Master's degree with honours*, qualification: theoretician.

2004 - 2008:

BSc student at the Department of Theoretical Physics of the National Taras Shevchenko University of Kyiv. Obtained *Bachelor's degree with honours*, qualification: theoretician.

1994 - 2004:

Studied at the school *Collegium 11* with an emphasis on mathematics (Chernigov, Ukraine). Obtained *Honours degree* with a *Golden medal*.

Languages

Native: Ukrainian, Russian.
Other: Excellent knowledge of written and spoken English; good knowledge of French.

Professional skills

I handle a lot of methods of theoretical physics, have strong knowledge and experience in computational physics, and have a high level of knowledge in mathematics.

Membership

Member of American Physical Society since 2011.

Participation in international conferences and workshops

1. "TD-DFT conference", Nantes, France (23.04.2013 - 26.04.2013)

   Oral talk "A new *ab initio* approach for electron energy-loss and inelastic X-ray scattering spectroscopies from linear-response TD-DFT"

2. "XVI International Workshop on Computational Physics and Materials Science: Total Energy and Force Methods", ICTP, Trieste, Italy (10.01.2013 - 12.01.2013)

   Presented a poster "A new *ab initio* approach to Electron Energy Loss Spectroscopy based on Lanczos recursion chains within Time-Dependent Density Functional Perturbation Theory"

3. Conference "JEELS", Aix les Bains, France, (23.10.2012 - 25.10.2012)

   Oral talk "A new *ab initio* approach to EELS based on Lanczos recursion chains within TDDFPT"

4. Conference "APS March Meeting", Boston, USA (27.02.2012 - 02.03.2012)

   Oral talk "Thermalization of photoexcited carriers in bismuth investigated by time-resolved THz spectroscopy and *ab initio* calculations"

5. Conference "Le XXIeme Congres General de la Societe Francaise de Physique", Bordeux, France (04.07.2011 - 08.07.2011)

   Oral talk "Time-Resolved Terahertz Spectroscopy of Bismuth Films: Experiment and Theory"

6. Conference "Co-DFT", Obernai, France (27.06.2011 - 30.06.2011)

   Presented a poster "Time-Resolved Terahertz Spectroscopy of Bismuth Films: Experiment and Theory"

7. "XV International Workshop on Computational Physics and Materials Science: Total Energy and Force Methods", ICTP, Trieste, Italy (13.01.2011 - 15.01.2011)

   Presented a poster "*Ab initio* study of electronic properties of bismuth"

8. Workshop "Electron-phonon interaction in metals, superconductors and semiconducting nanostructures", Paris, France (29.11.2010 - 30.11.2010)

   Presented a poster "*Ab initio* study of electronic properties of bismuth"

9. MORE 2010 ("Meeting on Optical Response in Extended Systems"), Vienna, Austria (03.11.2010 - 05.11.2010)

10. 18th Annual Student Conference "Week of Doctoral Students 2009", Prague, Czech Republic (02.06.2009 - 05.06.2009)

Participation in international tutorials and schools

1. CECAM Tutorial "Computational spectroscopy using `QUANTUM ESPRESSO` and related codes", SISSA, Trieste, Italy (26.07.2010 - 30.07.2010)

2. CECAM "Summer school on atomistic simulation techniques for material science, nanotechnology and biophysics", SISSA, Trieste, Italy (05.07.2010 - 23.07.2010)

3. CECAM "Spring College on Computational Nanoscience", ICTP, Trieste, Italy (17.05.2010 - 28.05.2010)

4. CECAM Tutorial "Calculation of Solid-State NMR parameters Using the GIPAW Method", Zurich, Switzerland (21.09.2009 - 25.09.2009)

D.2 List of publications

1. I. Timrov, T. Kampfrath, J. Faure, N. Vast, C. R. Ast, C. Frischkorn, M. Wolf, P. Gava, and L. Perfetti, *"Thermalization of photoexcited carriers in bismuth investigated by time-resolved THz spectroscopy and ab initio calculations"*, Phys. Rev. B **85**, 155139 (2012).

2. E. Papalazarou, J. Faure, J. Mauchain, M. Marsi, A. Taleb-Ibrahimi, I. Reshetnyak, A. van Roekeghem, I. Timrov, N. Vast, B. Arnaud, and L. Perfetti, *"Coherent Phonon Coupling to Individual Bloch States in Photoexcited Bismuth"*, Phys. Rev. Lett. **108**, 256808 (2012).

3. J. Sjakste, I. Timrov, P. Gava, N. Mingo, and N. Vast, *"First-principles calculations of electron-phonon scattering"*, Annual Reviews of Heat Transfer, book chapter, accepted (2013).

4. I. Timrov, N. Vast, R. Gebauer, and S. Baroni, *"Electron energy-loss and inelastic X-ray scattering cross sections from time-dependent density-functional perturbation theory"*, in preparation.

5. J. Faure, J. Mauchain, E. Papalazarou, M. Marsi, D. Boschetto, I. Timrov, N. Vast, Y. Ohtsubo, B. Arnaud, and L. Perfetti, *"Direct observation of electron thermalization and electron-phonon coupling in photoexcited bismuth"*, in preparation.

6. I. Timrov, N. Vast, C. Guedj, R. Gebauer, and S. Baroni, *"Electron Energy-Loss Spectroscopy of bulk bismuth for finite momentum transfer: Ab initio calculations and experiments"*, in preparation.

7. I. Timrov, P. Gava, N. Vast, J. Faure, and L. Perfetti, *"Ab initio calculation of carrier mass in bismuth"*, in preparation.

D.3 High performance computing and programming

- Programming in Fortran
- Knowledge of LaTeX and Maple.
- High Performance Computing (HPC)

During my thesis, I have performed the following numerical developments:

1. *Program for calculation of the electron energy-loss spectra* (see Appendix C)

   I have extended the Liouville-Lanczos approach to the electron energy-loss spectroscopy for non-zero momentum transfer ($\mathbf{q} \neq 0$), with the help of N. Vast, S. Baroni, and R. Gebauer. I have performed an implementation of this approach on top of the `turboTDDFT` code, which is the implementation of Liouville-Lanczos approach to optical case, with zero momentum transfer ($\mathbf{q} = 0$). To this end, I have used some routines of the `PHonon` code, which can be used for calculation of phonons with non-zero momentum transfer ($\mathbf{q} \neq 0$). The `turboTDDFT` and `PHonon` codes are components of the `QUANTUM ESPRESSO` package, as well as newly developed `EELS` code (see Appendix C), which is merged with the `turboTDDFT` code.

2. *Program for calculation of the carrier velocity* (see Sec. 6.1.3)

   I have extended the `LIGHT` code, which is used for the calculation of carrier velocity, to the relativistic case, by including the spin-orbit coupling (see Sec. 6.1.3), with the help of P. Gava. The `LIGHT` code was originally written by P. Gava on the basis of the `PHonon` code. The `LIGHT` code is a component of the `QUANTUM ESPRESSO` package.

3. *Program for calculation of the restricted density of states* (see Appendix A.3)

   I have extended the `DOS` code, which is used for the calculation of the density of states, to the calculation of the *restricted* density of states (see Appendix A.3), with the help of N. Vast. To this end, slight modifications of the `PWscf` code were also necessary. The `PWscf` and `DOS` codes are components of the `QUANTUM ESPRESSO` package.

For each of these developments, the standards for implementation of the HPC environments have been followed. In particular, the parallelization has been implemented, and calculations have been performed using the French HPC facilities of GENCI (Grand Equipement National de Calcul Intensif) at CINES (Centre Informatique National de l'Enseignement Supérieur) and TGCC (Très Grand Centre de calcul du CEA).

Bibliography

[1] P. Hohenberg and W. Kohn. Inhomogeneous electron gas. *Phys. Rev.*, 136:B864, 1964.

[2] W. Kohn and L.J. Sham. Self-consistent equations including exchange and correlation effects. *Phys. Rev.*, 140:A1133, 1965.

[3] E. Runge and E.K.U. Gross. Density-functional theory for time-dependent systems. *Phys. Rev. Lett.*, 52:997, 1984.

[4] J.-P. Issi. Low temperature transport properties of the group V semimetals. *Aus. J. Phys.*, 32:585, 1979.

[5] X. Gonze, J.-P. Michenaud, and J.-P. Vigneron. First-principles study of As, Sb, and Bi electronic properties. *Phys. Rev. B*, 41:11827, 1990.

[6] L. E. Diaz-Sanchez, A. H. Romero, and X. Gonze. Phonon band structure and interatomic force constants for bismuth: Crucial role of spin-orbit interaction. *Phys. Rev. B*, 76:104302, 2007.

[7] Ph. Hofmann. The surfaces of bismuth: Structural and electronic properties. *Progr. Surf. Sci.*, 81:191, 2006.

[8] A.B. Shick, J.B. Ketterson, D.L. Novikov, and A.J. Freeman. Electronic structure, phase stability, and semimetal-semiconductor transitions in Bi. *Phys. Rev. B*, 60:15484, 1999.

[9] Y. Liu and R.E. Allen. Electronic structure of the semimetals Bi and Sb. *Phys. Rev. B*, 52:1566, 1995.

[10] S. Golin. Band structure of bismuth: Pseudopotential approach. *Phy. Rev.*, 166:643, 1968.

[11] P.W. Chao, H.T. Chu, and Y.H. Kao. Nonlinear band-parameter variations in dilute bismuth-antimony alloys. *Phys. Rev. B*, 9:4030, 1974.

[12] M. Maltz and M.S. Dresselhaus. Magnetoreflection studies in bismuth. *Phys. Rev. B*, 2:2877, 1970.

[13] G. Jezequel, J. Thomas, and I. Pollini. Experimental band structure of semimetal bismuth. *Phys. Rev. B*, 56:6620, 1997.

[14] M. Hase, M. Kitajima, S. Nakashima, and K. Mizoguchi. Dynamics of coherent anharmonic phonons in bismuth using high density photoexcitation. *Phys. Rev. Lett.*, 88:067401, 2002.

[15] D.M. Fritz, D.A. Reis, B. Adams, R.A. Akre, J. Arthur, C. Blome, P.H. Bucksbaum, A.L. Cavalieri, S. Engemann, S. Fahy, R.W. Falcone, P.H. Fuoss, K.J. Gaffney, M.J. George, J. Hajdu, M.P. Hertlein, P.B. Hillyard, M. Horn von Hoegen, M. Kammler, J. Kaspar, R. Kienberger, P. Krejcik, S.H. Lee, A.M. Lindenberg, B. McFarland, D. Meyer, T. Montagne, É.D. Murray, A.J. Nelson, M. Nicoul, R. Pahl, J. Rudati, H. Schlarb, D.P. Siddons, K. Sokolowski-Tinten, , Th. Tschentscher, D. von der Linde, and J.B. Hastings. Ultrafast bond softening in bismuth: Mapping a solid's interatomic potential with X-rays. *Science*, 315:633, 2007.

[16] Y. Giret, A. Gellé, and B. Arnaud. Entropy driven atomic motion in laser-excited bismuth. *Phys. Rev. Lett.*, 106:155503, 2011.

[17] G. Onida, L. Reining, and A. Rubio. Electronic excitations: Density functional versus many body Green's functions approaches. *Rev. Mod. Phys.*, 74:601, 2002.

[18] D. Rocca, R. Gebauer, Y. Saas, and S. Baroni. Turbo charging time-dependent density-functional theory with Lanczos chains. *J. Chem. Phys.*, 128:154105, 2008.

[19] F. Jensen, *Introduction to Computational Chemistry*. Wiley, Chichester, 1999.

[20] W.M.C. Foulkes, L. Mitas, R.J. Needs, and G. Rajagopal. Quantum Monte Carlo simulations of solids. *Rev. Mod. Phys.*, 73:33, 2001.

[21] A. Georges, G. Kotliar, W. Krauth, and M. J. Rozenberg. Dynamical mean-field theory of strongly correlated fermion systems and the limit of infinite dimensions. *Rev. Mod. Phys.*, 68:13, 1996.

[22] A. L. Fetter and J. D. Walecka, *Quantum Theory of Many-Particle Systems*. Dover, New York, 2003.

[23] W. Kohn. Nobel lecture: Electronic structure of matter - wave functions and density functionals. *Rev. Mod. Phys.*, 71:1253, 1999.

[24] R. M. Martin, *Electronic Structure: Basic Theory and Practical Methods*. Cambridge University Press, Cambridge, 2004.

[25] D. S. Sholl and J. A. Steckel. *Density Functional Theory: A Practical Introduction*. Wiley, New Jersey, 2009.

[26] R. G. Parr and W. Yang. *Density-Functional Theory of Atoms and Molecules*. Oxford University Press, Oxford, 1989.

[27] L. L. Landau and E. M. Lifschitz. *Quantum Mechanics: non-relativistic theory.* Permagon Press, Oxford, 1977.

[28] A. Messiah, *Quantum Mechanics.* North-Holland, Amsterdam, 1962.

[29] M. Born and R. Oppenheimer. Zur quantentheorie der molekeln. *Ann. Phys. (Leipzig)*, 84:457, 1927.

[30] M. Born and K. Huang, *Dynamical Theory of Crystal Lattices.* Oxford University Press, New York, 1988.

[31] C.-O. Almbladh and U. von Barth. Exact results for the charge and spin densities, exchange-correlation potentials, and density-functional eigenvalues. *Phys. Rev. B*, 31:3231, 1985.

[32] J.P. Perdew, A. Ruzsinszky, J.M. Tao, V.N. Staroverov, G.E. Scuseria, and G.I. Csonka. Prescription for the design and selection of density functional approximations: More constraint satisfaction with fewer fits. *J. Chem. Phys.*, 123:062201, 2005.

[33] D.M. Ceperley and B.J. Alder. Ground state of the electron gas by a stochastic method. *Phys. Rev. Lett.*, 45:566, 1980.

[34] J.P. Perdew and A. Zunger. Self-interaction correction to density-functional approximations for many-electron systems. *Phys. Rev. B*, 23:5048, 1981.

[35] J.P. Perdew and Y. Wang. Accurate and simple analytic representation of the electron-gas correlation energy. *Phys. Rev. B*, 45:13244, 1992.

[36] J. P. Perdew, K. Burke, and M. Ernzerhof. Generalized gradient approximation made simple. *Phys. Rev. Lett.*, 77:3865, 1996.

[37] N. D. Mermin. Thermal properties of the inhomogeneous electron gas. *Phys. Rev.*, 137:A1441, 1965.

[38] S. Baroni, P. Giannozzi, and A. Testa. Green's-function approach to linear response in solids. *Phys. Rev. Lett.*, 58:1861, 1987.

[39] X. Gonze. Adiabatic density-functional perturbation theory. *Phys. Rev. A*, 52:1096, 1995.

[40] S. Baroni, S. de Gironcoli, A. Dal Corso, and P. Giannozzi. Phonons and related crystal properties from density-functional perturbation theory. *Rev. Mod. Phys.*, 73:515, 2001.

[41] F. Furche. On the density matrix based approach to time-dependent density functional response theory. *J. Chem. Phys.*, 114:5982, 2001.

[42] A. Messiah, *Quantum Mechanics, Vol.II.* Wiley, New York, 1964.

[43] J.D. Bjorken and S.D. Drell, *Relativistic Quantum Mechanics*. McGraw-Hill, New York, 1964.

[44] L. Kleinman. Relativistic norm-conserving pseudopotentials. *Phys. Rev. B*, 21:2630, 1980.

[45] J. Kübler and V. Eyert. *Electronic structure calculations in: Electronic and Magnetic Properties of Metals and Ceramics*. K. H. J. Buschow (VCH Verlagsgesellschaft), Weinheim, 1991-1996, 1992.

[46] A.H. MacDonald, W.E. Pickett, and D. Koelling. A linearised relativistic augmented-plane-wave method utilising approximate pure spin basis functions. *J. Phys. C: Solid State Phys.*, 13:2675, 1980.

[47] A.H. MacDonald and S.H. Vosko. A relativistic density functional formalism. *J. Phys. C: Solid State Phys.*, 12:2977, 1979.

[48] A.K. Rajagopal and J. Callaway. Inhomogeneous electron gas. *Phys. Rev. B*, 7:1912, 1973.

[49] E. Engel and R.M. Dreizler. *Density Functional Theory II*. Topics in Current Chemistry Vol. 181. Springer, Berlin, 1996.

[50] E. Engel, R.M. Dreizler, S. Varga, and B. Fricke, *Relativistic Effects in Heavy-Element Chemistry and Physics*. Wiley, New York, 2001.

[51] E. Engel, *Relativistic Electronic Structure Theory, Part I: Fundamentals*. Elsevier, Amsterdam, 2002.

[52] J. Anton, B. Fricke, and E. Engel. Noncollinear and collinear relativistic density-functional program for electric and magnetic properties of molecules. *Phys. Rev. A*, 69:012505, 2004.

[53] W. Klopper, J. H. van Lenthe, and A. C. Hennum. An improved *ab initio* relativistic zeroth-order regular approximation correct to order $1/c^2$. *J. Chem. Phys.*, 113:9957, 2000.

[54] A. Dal Corso. Projector augmented-wave method: Application to relativistic spin-density functional theory. *Phys. Rev. B*, 82:075116, 2010.

[55] A. Dal Corso. Spin-orbit coupling with ultrasoft pseudopotentials: Application to Au and Pt. *Phys. Rev. B*, 71:115106, 2005.

[56] X. Z. Iriarte. *First-principles study of the electronic structure and dynamical electronic excitations of strong spin-orbit metal Pb: bulk, surface and nanosized films*. PhD thesis, Universidad del Pais Vasco, Spain, 2012.

[57] L.A. Hemstreet, C.Y. Fong, and J.S. Nelson. First-principles calculations of spin-orbit splittings in solids using nonlocal separable pseudopotentials. *Phys. Rev. B*, 47:4238, 1993.

[58] M.P. Surh, M.-F. Li, and S.G. Louie. Spin-orbit splitting of GaAs and InSb bands near Γ. *Phys. Rev. B*, 43:4286, 1991.

[59] M.S. Hybertsen and S.G. Louie. Spin-orbit splitting in semiconductors and insulators from the *ab initio* pseudopotential. *Phy. Rev. B*, 34:2920, 1986.

[60] D.M. Bylander and L. Kleinman. Self-consistent relativistic calculation of the energy bands and cohesive energy of W. *Phys. Rev. B*, 29:1534, 1984.

[61] K.M. Rabe and J.D. Joannopoulos. *Ab initio* relativistic pseudopotential study of the zero-temperature structural properties of SnTe and PbTe. *Phys. Rev. B*, 32:2302, 1985.

[62] G. Theurich and N.A. Hill. Self-consistent treatement of spin-orbit coupling in solids using relativistic fully separable *ab initio* pseudopotentials. *Phys. Rev. B*, 64:073106, 2001.

[63] A.K. Rajagopal. Inhomogeneous relativistic electron gas. *J. Phys. C*, 11:L943, 1978.

[64] E. Engel, S. Keller, and R.M. Dreizler. Generalized gradient approximation for the relativistic exchange-only energy functional. *Phys. Rev. A*, 53:1367, 1996.

[65] E. Engel, T. Auth, and R.M. Dreizler. Relativistic spin-density-functional theory: Robust solution of single-particle equations for open-subshell atoms. *Phys. Rev. B*, 64:235126, 2001.

[66] V. Theileis and H. Bross. Relativistic modified augmented plane wave method and its application to the electronic structure of gold and platinum. *Phys. Rev. B*, 62:13338, 2000.

[67] M.C. Payne, M.P. Teter, D.C. Allan, T.A. Arias, and J.D. Joannopoulos. Iterative minimization techniques for *ab initio* total-energy calculations: molecular dynamics and conjugate gradients. *Rev. Mod. Phys.*, 64:1045, 1992.

[68] P. Giannozzi, S. Baroni, N. Bonini, M. Calandra, R. Car, C. Cavazzoni, D. Ceresoli, G.L. Chiarotti, M. Cococcioni, I. Dabo, A. Dal Corso, S. De Gironcoli, S. Fabris, G. Fratesi, R. Gebauer, U. Gerstmann, C. Gougoussis, A. Kokalj, M. Lazzeri, L. Martin-Samos, N. Marzari, F. Mauri, R. Mazzarello, S. Paolini, A. Pasquarello, L. Paulatto, C. Sbraccia, S. Scandolo, G. Sclauzero, A.P. Seitsonen, A. Smogunov, P. Umari, and R.M. Wentzcovitch. QUANTUM ESPRESSO: A modular and open-source software project for quantum simulations of materials. *J. Phys.: Condens. Matter*, 21(39):395502, 2009.

[69] B. N. Harmon, W. Weber, and D. R. Hamann. Total-energy calculations for Si with a first-principles linear-combination-of-atomic-orbitals method. *Phys. Rev. B*, 25:1109, 1982.

[70] I. Cacelli, R. Moccia, and A. Rizzo. Gaussian-type-orbital basis sets for the calculation of continuum properties in molecules: The differential photoionization cross section of molecular nitrogen. *Phys. Rev. A*, 57:1895, 1998.

[71] S. Y. Savrasov. Linear-response theory and lattice dynamics: A muffin-tin-orbital approach. *Phys. Rev. B*, 54:16470, 1996.

[72] M. Weinert, E. Wimmer, and A. J. Freeman. Total-energy all-electron density functional method for bulk solids and surfaces. *Phys. Rev. B*, 26:4571, 1982.

[73] P. E. Blöchl. Projector augmented-wave method. *Phys. Rev. B*, 50:17953, 1994.

[74] N. W. Ashcroft and N. D. Mermin. *Solid State Physics*. Holt-Saunders, Philadelphia, 1976.

[75] W.E. Pickett. Pseudopotential methods in condensed matter applications. *Comp. Phys. Rep.*, 9:115, 1989.

[76] S. G. Louie, S. Froyen, and M. L. Cohen. Nonlinear ionic pseudopotentials in spin-density-functional calculations. *Phys. Rev. B*, 26:1738, 1982.

[77] D.R. Hamann, M. Schlüter, and C. Chiang. Norm-conserving pseudopotentials. *Phys. Rev. Lett.*, 43:1494, 1979.

[78] D. Vanderbilt. Soft self-consistent pseudopotentials in a generalized eigenvalue formalism. *Phys. Rev. B*, 41:7892, 1990.

[79] G. Kresse and D. Joubert. From ultrasoft pseudopotentials to the projector augmented-wave method. *Phys. Rev. B*, 59:1758, 1999.

[80] L. Kleinman and D.M. Bylander. Efficacious form for model pseudopotentials. *Phys. Rev. Lett.*, 48:1425, 1982.

[81] X. Gonze, P. Käckell, and M. Scheffler. Ghost states for separable, norm-conserving, *ab initio* pseudopotentials. *Phys. Rev. B*, 41:12264, 1990.

[82] X. Gonze, R. Stumpf, and M. Scheffler. Analysis of separable potentials. *Phys. Rev. B*, 44:8503, 1991.

[83] G. B. Bachelet, D. R. Hamann, and M. Schlüter. Pseudopotentials that work: From H to Pu. *Phys. Rev. B*, 26:4199, 1982.

[84] G.B. Bachelet and M. Schlüter. Relativistic norm-conserving pseudopotentials. *Phys. Rev. B*, 25:2103, 1982.

[85] L. Hedin. New method for calculating the one-particle Green's function with application to the electron-gas problem. *Phys. Rev.*, 139:A796, 1965.

[86] S. Albretch, L. Reining, R. Del Sole, and G. Onida. *Ab Initio* calculation of excitonic effects in the optical spectra of semiconductors. *Phys. Rev. Lett.*, 80:4510, 1998.

[87] R. van Leeuwen. Causality and symmetry in time-dependent density-functional theory. *Phys. Rev. Lett.*, 80:1280, 1998.

[88] E. K. U. Gross and W. Kohn. Local density-functional theory of frequency-dependent linear response. *Phys. Rev. Lett.*, 55:2850, 1985.

[89] E. K. U. Gross, J. F. Dobson, and M. Petersilka. *Density Functional Theory of Time-Dependent Phenomena*. Topics in Current Chemistry. Springer-Verlag, Berlin, 1996.

[90] R. van Leeuwen. Mapping from densities to potentials in time-dependent density-functional theory. *Phys. Rev. Lett.*, 82:3863, 1999.

[91] K. Burke, J. Werschnik, and E. K. U. Gross. Time-dependent density functional theory: Past, present, and future. *J. Chem. Phys.*, 123:062206, 2005.

[92] S. Botti, A. Schindlmayr, R. D. Sole, and L. Reining. Time-dependent density-functional theory for extended systems. *Rep. Prog. Phys.*, 70:357, 2007.

[93] T. K. Ng and K. S. Singwi. Time-dependent density-functional theory in the linear-response regime. *Phys. Rev. Lett*, 59:2627, 1987.

[94] W. Yang. Dynamic linear response of many-electron systems: An integral formulation of density-functional theory. *Phys. Rev. A*, 38:5512, 1988.

[95] F. A. Parpia and W. R. Johnson. The relativistic time-dependent local-density approximation. *J. Phys. B*, 17:531, 1984.

[96] D. Toffoli, M. Stener, and P. Decleva. Photoionization of mercury: A relativistic time-dependent density-functional-theory approach. *Phys. Rev. A*, 66:012501, 2002.

[97] P. Romaniello. *Time-Dependent Current-Density-Functional Theory for Metals*. PhD thesis, University of Groningen, The Netherlands, 2006.

[98] G. Fronzoni, M. Stener, P. Decleva, F. Wang, T. Ziegler, E. van Lenthe, and E. J. Baerends. Spin-orbit relativistic time dependent density functional theory calculations for the description of core electron excitations: $TiCl_4$ case study. *Chem. Phys. Lett.*, 416:56, 2005.

[99] R. Bast, H. J. AA. Jensen, and T. Saue. Relativistic adiabatic time-dependent density functional theory using hybrid functionals and noncollinear spin magnetization. *Int. J. Quantum Chem.*, 109:2091, 2009.

[100] N. Vast. Some *ab initio* studies of the physical properties of materials. *HDR thesis, Ecole Polytechnique, Palaiseau, France*, 2009.

[101] M. Petersilka, U. J. Gossmann, and E. K. U. Gross. Excitation energies from time-dependent density-functional theory. *Phys. Rev. Lett.*, 76:1212, 1996.

[102] I. G. Gurtubay, J. M. Pitarke, W. Ku, A. G. Eguiluz, B. C. Larson, J. Tischler, P. Zschack, and K. D. Finkelstein. Electron-hole and plasmon excitations in 3*d* transition metals: *Ab initio* calculations and inelastic X-ray scattering measurements. *Phys. Rev. B*, 72:125117, 2005.

[103] S. L. Adler. Quantum theory of the dielectric constant in real solids. *Phys. Rev.*, 126:413, 1962.

[104] N. Wiser. Dielectric constant with local field effects included. *Phys. Rev.*, 129:62, 1963.

[105] I. G. Gurtubay, W. Ku, J. M. Pitarke, A. G. Eguiluz, B. C. Larson, J. Tischler, and P. Zschack. Large crystal local-field effects in the dynamical structure factor of rutile TiO_2. *Phys. Rev. B*, 70:201201(R), 2004.

[106] W.-D. Schöne, D. S. Su, and W. Ekardt. Theoretical and experimental study of the dynamical electronic response of Ag. *Phys. Rev. B*, 68:115102, 2003.

[107] R. Car, E. Tosatti, S. Baroni, and S. Leelaprute. Dielectric band structure of crystals: General properties and calculations for silicon. *Phys. Rev. B*, 24:985, 1981.

[108] M. S. Hybertsen and S. G. Louie. *Ab initio* static dielectric matricies from the density-functional approach. I. formulation and application to semiconductors and insulators. *Phy. Rev. B*, 35:5585, 1987.

[109] F. Sottile, F. Bruneval, A.G Marinopoulos, L. Dash, S. Botti, V. Olevano, N. Vast, A. Rubio, and L. Reining. TDDFT from molecules to solids: the role of long-range interactions. *Int. J. Quant. Chem.*, 102:684, 2005.

[110] P. Nozières and D. Pines. Electron interaction in solids. Characteristic energy loss spectrum. *Phys. Rev.*, 113:1254, 1959.

[111] D. Pines. Electron interaction in solids. *Can. J. Phys.*, 34:1379, 1956.

[112] H. Ehrenreich and M.H. Cohen. Self-consistent field approach to the many-electron problem. *Phys. Rev.*, 115:786, 1959.

[113] H. Ehrenreich and H. R. Philipp. Optical properties of Ag and Cu. *Phys. Rev.*, 128:1622, 1962.

[114] E. G. Maksimov, I. I. Mazin, S. N. Rashkeev, and Yu. A. Uspenski. First-principles calculations of the optical properties of metals. *J. Phys. F: Met. Phys.*, 18:833, 1988.

[115] N. W. Ashcroft and N. D. Mermin. *Solid State Physics*. Holt-Saunders, Philadelphia, 1976.

[116] J. W. Allen and J. C. Mikkelsen. Optical properties of CrSb, MnSb, NiSb, and NiAs. *Phys. Rev. B*, 15:2952, 1977.

[117] M.-L. Thèye. Investigation of the optical properties of Au by means of thin semi-transparent films. *Phys. Rev. B*, 2:3060, 1970.

[118] J. J. Hopfield. Infrared properties of transition metals. *AIP Conf. Proc.*, 4:358, 1972.

[119] M.C. Beard, G.M. Turner, and C.A. Schmuttenmaer. Transient photoconductivity in GaAs as measured by time-resolved terahertz spectroscopy. *Phys. Rev. B*, 62:15764, 2000.

[120] S. R. Nagel and S. E. Schnatterly. Frequency dependence of the Drude relaxation time in metal films. *Phys. Rev. B*, 9:1299, 1974.

[121] N.P. Armitage, R. Tediosi, F. Lévy, E. Giannini, L. Forro, and D. van der Marel. Infrared conductivity of elemental bismuth under pressure: Evidence for an avoided Lifshitz-type semimetal-semiconductor transition. *Phys. Rev. Lett.*, 104:237401, 2010.

[122] A. Marini, G. Onida, and R. Del Sole. Plane-wave DFT-LDA calculation of the electronic structure and absorption spectrum of copper. *Phys. Rev. B*, 64:195125, 2001.

[123] R. Tediosi, N.P. Armitage, E. Giannini, and D. van der Marel. Charge carrier interaction with a purely electronic collective mode: Plasmarons and the infrared response of elemental bismuth. *Phys. Rev. Lett.*, 99:016406, 2007.

[124] V. J. Keast. *Ab initio* calculations of plasmons and interband transitions in the low-loss electron energy-loss spectrum. *J. Electron Spectrosc. Relat. Phenom.*, 143:97, 2005.

[125] S. Waidmann, M. Knupfer, B. Arnold, J. Fink, A. Fleszar, and W. Hanke. Local-field effects and anisotropic plasmon dispersion in diamond. *Phys. Rev. B*, 61:10149, 2000.

[126] L.K. Dash, Fabien Bruneval, Virginie Trinité, Nathalie Vast, and Lucia Reining. Electronic excitations: *ab initio* calculations of electronic spectra and application to zirconia ZrO_2, titania TiO_2 and cuprous oxide Cu_2O. *Comp. Mat. Sci.*, 38:482, 2006.

[127] M. Petersilka, E. K. U. Gross, and K. Burke. Excitation energies from time-dependent density functional theory using exact and approximate potentials. *Int. J. Quantum Chem.*, 80:534, 2000.

[128] Silvana Botti, Francesco Sottile, Nathalie Vast, Valerio Olevano, Lucia Reining, Hans-Christian Weissker, Angel Rubio, Giovanni Onida, Rodolfo Del Sole, and

R. W. Godby. Long-range contribution to the exchange-correlation kernel of time-dependent density functional theory. *Phys. Rev. B*, 69:155112, 2004.

[129] M. Rohlfing and S. Louie. Electron-hole excitations and optical spectra from first principles. *Phys. Rev. B*, 62:4927, 2000.

[130] G. D. Mahan. *Many-particles physics*. Plenum Press, New York, 2nd ed., 1975.

[131] R. F. Egerton. *Electron Energy-Loss Spectroscopy in the Electron Microscope*. Plenum, New York and London, 2nd ed., 1996.

[132] J. A. Soininen, A. L. Ankudinov, and J. J. Rehr. Inelastic scattering from core electrons: A multiple scattering approach. *Phys. Rev. B*, 72:045136, 2005.

[133] Y. Joly. X-ray absorption near-edge structure calculations beyond the muffin-tin approximation. *Phys. Rev. B*, 63:125120, 2001.

[134] L. Van Hove. Correlations in space and time and Born approximation scattering in systems of interacting particles. *Phys. Rev.*, 95:249, 1954.

[135] R. Hambach. *Theory and ab-initio calculations of collective excitations in nanostructures: towards spatially-resolved EELS*. PhD thesis, Ecole Polytechnique, 2010.

[136] R. Kubo. The fluctuation-dissipation theorem. *Rep. Prog. Phys.*, 29:255, 1966.

[137] N. Vast, L. Reining, V. Olevano, P. Schattschneider, and B. Jouffrey. Local field effects and the anisotropy of the electron energy loss spectrum of titanium dioxide TiO_2. *Phys. Rev. Lett.*, 88:37601, 2002.

[138] H.-C. Weissker, J. Serrano, S. Huotari, F. Bruneval, F. Sottile, G. Monaco, G. Krisch, V. Olevano, and L. Reining. Signatures of short-range many-body effects in the dielectric function of silicon for finite momentum transfer. *Phys. Rev. Lett.*, 97:237602, 2006.

[139] V. Olevano and L. Reining. Excitonic effects on the silicon plasmon resonance. *Phys. Rev. Lett.*, 86:5962, 2001.

[140] H.-C. Weissker, J. Serrano, S. Huotari, E. Luppi, M. Cazzaniga, F. Bruneval, F. Sottile, G. Monaco, V. Olevano, and L. Reining. Dynamic structure factor and dielectric function of silicon for finite momentum transfer: Inelastic X-ray scattering experiments and *ab initio* calculations. *Phys. Rev. B*, 81:085104, 2010.

[141] J. A. Berger, L. Reining, and F. Sottile. *Ab initio* calculations of electronic excitations: Collapsing spectral sums. *Phys. Rev. B*, 82:041103(R), 2010.

[142] J. A. Berger, L. Reining, and F. Sottile. Efficient calculation of the polarizability: a simplified effective-energy technique. *Eur. Phys. J. B*, 85:326, 2012.

[143] K. Yabana and G. F. Bertsch. Time-dependent local-density approximation in real time. *Phys. Rev. B*, 54:4484, 1996.

[144] G.F. Bertsch, J.-I. Iwata, A. Rubio, and K. Yabana. Real-space, real-time method for the dielectric function. *Phys. Rev. B*, 62:7998, 2000.

[145] B. Walker and R. Gebauer. Ultrasoft pseudopotentials in time-dependent density-functional theory. *J. Chem. Phys.*, 127:164106, 2007.

[146] M. A. L. Marques, X. Lopez, D. Varsano, A. Castro, and A. Rubio. Time-dependent density-functional approach for biological chromophores: The case of the green fluorescent protein. *Phys. Rev. Lett.*, 90:258101, 2003.

[147] S. K. Ghosh and A. K. Dhara. Density-functional theory of many-electron systems subjected to time-dependent electric and magnetic fields. *Phys. Rev. A*, 38:1149, 1988.

[148] F. Kootstra, P. L. Boeji, and J. G. Snijders. Efficient real-space approach to time-dependent density functional theory for the dielectric response of nonmetallic crystals. *J. Chem. Phys.*, 112:6517, 2000.

[149] B. Walker, A. M. Saitta, R. Gebauer, and S. Baroni. Efficient approach to time-dependent density-functional perturbation theory for optical spectroscopy. *Phys. Rev. Lett.*, 96:11300, 2006.

[150] D. Rocca, D. Lu, and G. Galli. *Ab initio* calculations of optical absorption spectra: Solution of the Bethe-Salpeter equation within density matrix perturbation theory. *J. Chem. Phys.*, 133:164109, 2010.

[151] D. Rocca, Y. Ping, R. Gebauer, and G. Galli. Solution of the Bethe-Salpeter equation without empty electronic states: Application to the absorption spectra of bulk systems. *Phys. Rev. B*, 85:045116, 2012.

[152] Y. Ping, D. Rocca, D. Lu, and G. Galli. *Ab initio* calculations of absorption spectra of semiconducting nanowires within many-body perturbation theory. *Phys. Rev. B*, 85:035316, 2012.

[153] S. Baroni, R. Gebauer, O. Bariş Malcioğlu, Y. Saad, P. Umari, and J. Xian. Hardnessing molecular exited states with Lanczos chains. *J. Phys.: Cond. Matter*, 22:074204, 2010.

[154] O. B. Malcioglu, R. Gebauer, D. Rocca, and S. Baroni. TurboTDDFT - a code for the simulation of molecular spectra using the Liouville-Lanczos approach to time-dependent density-functional perturbation theory. *Comput. Phys. Commun.*, 182:1744, 2011.

[155] R. Car and M. Parrinello. Unified approach for molecular dynamics and density-functional theory. *Phys. Rev. Lett.*, 55:2471, 1985.

[156] D. Rocca, R. Gebauer, F. De Angelis, M. K. Nazeeruddin, and S. Baroni. Time-dependent density functional theory study of squaraine dye-sensitized solar cells. *Chem. Phys. Lett.*, 475:49, 2009.

[157] F. De Angelis, S. Fantacci, and R. Gebauer. Simulating dye-sensitized TiO_2 heterointerfaces in explicit solvent: Absorption spectra, energy levels, and dye desorption. *J. Phys. Chem. Lett.*, 2:813, 2011.

[158] O. B. Malcioglu, A. Calzolari, R. Gebauer, D. Varsano, and S. Baroni. Dielectric and thermal effects on the optical properties of natural dyes: A case study on solvated cyanin. *J. Am. Chem. Soc.*, 133:15425, 2011.

[159] M. E. Casida. *Recent Advances in Density Functional Methods Part I.* World Scientific, Singapore, 1995.

[160] M. E. Casida. Propagator corrections to adiabatic time-dependent density-functional theory linear response theory. *J. Chem. Phys.*, 122:054111, 2005.

[161] E. Tsiper. A classical mechanics technique for quantum linear response. *J. Phys. B*, 34:L401, 2001.

[162] D. Rocca. *Time-Dependent Density Functional Perturbation Theory: New algorithms with applications to molecular spectra.* PhD thesis, SISSA, Trieste, Italy, 2007.

[163] S. Baroni and R. Resta. *Ab initio* calculation of the macroscopic dielectric constant in silicon. *Phys. Rev. B*, 33:7017, 1986.

[164] D. W. Bullet, R. Haydock, V. Heine, and M. Kelly. *Solid State Physics*, vol. 35. Academic, New York, 1980.

[165] Y. Saad. *Iterative Methods for Sparse Linear Systems.* SIAM, Philadelphia, 2nd ed., 2003.

[166] M. Grüning, A. Marini, and X. Gonze. Implementation and testing of Lanczos-based algorithms for random-phase approximation eigenproblems. *Comp. Mater. Sci.*, 50:2148, 2011.

[167] Z. Bai and D. Day. *Templates for the Solution of Algebraic Eigenvalue Problems: A Practical Guide.* SIAM, Philadelphia, 2000.

[168] S. Hirata and M. Head-Gordon. Time-dependent density functional theory within the Tamm-Dancoff approximation. *Chem. Phys. Lett.*, 314:291, 1999.

[169] S. Baroni and R. Gebauer. *Fundamentals of Time-Dependent Density Functional Theory.* Springer, Berlin, 2012.

[170] Y. Hasegawa, M. Murata, D. Nakamura, T. Komine, T. Taguchi, and S. Nakamura. Mobility estimation in microsized bismuth wire arrays. *J. Appl. Phys.*, 105:103715, 2009.

[171] H. Fukuyama and R. Kubo. Interband effects on magnetic susceptibility. II. Diamagnetism of bismuth. *J. Phys. Soc. Jpn.*, 28:570, 1970.

[172] P. H. Craig. The Hall effect in bismuth with low magnetic fields. *Phys. Rev.*, 27:772, 1926.

[173] L. D. Hicks and M. S. Dresselhaus. Thermoelectric figure of merit of a one-dimensional conductor. *Phys. Rev. B*, 47:16631, 1993.

[174] Y.-M. Lin, X. Sun, and M. S. Dresselhaus. Theoretical investigation of thermoelectric transport properties of cylindrical Bi nanowires. *Phys. Rev. B*, 62:4610, 2000.

[175] J. P. Heremans, C. M. Thrush, D. T. Morelli, and W. Ming-Cheng. Thermoelectric power of bismuth nanocomposites. *Phys. Rev. Lett.*, 88:216801, 2002.

[176] J. Kang, J. W. Roh, W. Shim, J. Ham, J.-S. Noh, and W. Lee. Reduction of lattice thermal conductivity in single Bi-Te core/shell nanowires with rough interface. *Adv. Mater.*, 23:3414, 2011.

[177] B. Weitzel and H. Micklitz. Superconductivity in granular systems built from well-defined rhombohedral Bi-clusters: Evidence for Bi-surface superconductivity. *Phys. Rev. Lett.*, 66:385, 1991.

[178] M. Z. Hasan and C. L. Kane. *Colloquium*: Topological insulators. *Rev. Mod. Phys.*, 82:3045, 2010.

[179] X.-L. Qi and S.-C. Zhang. Topological insulators and superconductors. *Rev. Mod. Phys.*, 83:1057, 2011.

[180] K. S. Novoselov, A. K. Geim, S. V. Morozov, D. Jiang, M. I. Katsnelson, I. V. Grigorieva, S. V. Dubonos, and A. A. Firsov. Two-dimensional gas of massless Dirac fermions in graphene. *Nature (London)*, 438:197, 2005.

[181] T. W. Cornelius, J. Brötz, N. Chtanko, D. Dobrev, G. Miehe, R. Neumann, and M. E. Toimil Molares. Controlled fabrication of poly- and single-crystalline bismuth nanowires. *Nanotechnology*, 16:S246, 2005.

[182] R. Peierls. *More surprises in theoretical physics*. Princeton University Press, Princeton, 1991.

[183] D. Fausti, *Phase Transitions and Optically Induced Phenomena in Cooperative Systems*. Facilitair Bedrijf RuG, Groningen, 2008.

[184] K. J. Chang and M. L. Cohen. Rhombohedral phase stability of the group-VA elements. *Phys. Rev. B*, 33:7371, 1986.

[185] R. J. Needs, R. M. Martin, and O. H. Nielsen. Total-energy calculations of the structural properties of the group-V element arsenic. *Phys. Rev. B*, 33:3778, 1986.

[186] X. Gonze, J.-P. Michenaud, and J.-P. Vigneron. *Ab initio* calculations of bismuth properties, including spin-orbit coupling. *Phys. Scr.*, 37:785, 1988.

[187] L.M. Falicov and S. Golin. Electronic band structure of arsenic. I. Pseudopotential approach. *Phys. Rev.*, 137:A871, 1965.

[188] M.H. Cohen. Energy bands in the bismuth structure. I. A nonellipsoidal model for electrons in Bi. *Phys. Rev.*, 121:387, 1961.

[189] D. Schiferl and C.S. Barrett. The crystal structure of arsenic at 4.2, 78 and 299 K. *J. Appl. Crystallogr.*, 2:30, 1969.

[190] N. Vast. *Propriétés vibrationnelles du bore α et du carbure de bore B_4C.* PhD thesis, Université Paris VI, France, 1998.

[191] J.H. Xu, E.G. Wang, C.S. Ting, and W.P. Su. Tight-binding theory of the electronic structures for rhombohedral semimetals. *Phys. Rev. B*, 48:17271, 1993.

[192] G. Gutiérrez, E. Menéndez-Proupin, and A.K. Singh. Elastic properties of the bcc structure of bismuth at high pressure. *J. Appl. Phys.*, 99:103504, 2006.

[193] R. D. Brown, R. L. Hartman, and S. H. Koenig. Tilt of the electron Fermi surface in Bi. *Phys. Rev.*, 172:598, 1968.

[194] Y. Giret. *Etude ab initio de la dynamique des phonons cohérents dans le bismuth.* PhD thesis, Université de Rennes-1, 2010.

[195] S. Mase. Electronic structure of bismuth type crystals. *J. Phys. Soc. Jpn.*, 13:434, 1958.

[196] S. Mase. Electronic structure of bismuth type crystals, II. *J. Phys. Soc. Jpn.*, 14:584, 1959.

[197] P. E. Blöchl, O. Jepsen, and O. K. Andersen. Improved tetrahedron method for Brillouin-zone integrations. *Phys. Rev. B*, 49:16223, 1994.

[198] Yu.M. Koroteev, G. Bihlmayer, J.E. Gayone, E.V. Chulkov, S. Blügel, P.M. Echenique, and Ph. Hofmann. Strong spin-orbit splitting on Bi surfaces. *Phys. Rev. Lett.*, 93:046403, 2004.

[199] C. R. Ast and H. Höchst. Fermi surface of bi(111) measured by photoemission spectroscopy. *Phys. Rev. Lett.*, 87:177602, 2001.

[200] T. Hirahara, T. Nagao, I. Matsuda, G. Bihlmayer, E. V. Chulkov, Yu. M. Koroteev, P. M. Echenique, M. Saito, and S. Hasegawa. Role of spin-orbit coupling and hybridization effects in the electronic structure of ultrathin Bi films. *Phys. Rev. Lett.*, 97:146803, 2006.

[201] C. R. Ast and H. Höchst. Two-dimensional band structure and self-energy of Bi(111) near the $\overline{\Gamma}$ point. *Phys. Rev. B*, 66:125103, 2002.

[202] C. R. Ast and H. Höchst. Electronic structure of a bismuth bilayer. *Phys. Rev. B*, 67:113102, 2003.

[203] T. Hirahara, K. Miyamoto, I. Matsuda, T. Kadono, A. Kimura, T. Nagao, G. Bihlmayer, E. V. Chulkov, S. Qiao, K. Shimada, H. Namatame, M. Taniguchi, and S. Hasegawa. Direct observation of spin splitting in bismuth surface states. *Phys. Rev. B*, 76:153305, 2007.

[204] A. Kimura, E. E. Krasovskii, R. Nishimura, K. Miyamoto, T. Kadono, K. Kanomaru, E. V. Chulkov, G. Bihmayer, K. Shimada, H. Namatame, and M. Taniguchi. Strong Rashba-type spin polarization of the photocurrent from bulk continuum states: Experiment and theory for Bi(111). *Phys. Rev. Lett.*, 105:076804, 2010.

[205] A. Takayama, T. Sato, S. Souma, and T. Takahashi. Giant out-of-plane spin component and the asymmetry of spin polarization in surface Rashba states of bismuth thin film. *Phys. Rev. Lett.*, 106:166401, 2011.

[206] E. D. Murray, S. Fahy, D. Prendergast, T. Ogitsu, D. M. Fritz, and D. A. Reis. Phonon dispersion relations and softening in photoexcited bismuth from first principles. *Phys. Rev. B*, 75:184301, 2007.

[207] J. L. Yarnell, J. L. Warren, R. G. Wenzel, and S. H. Koenig. Phonon dispersion curves in bismuth. *IBM J. Res. Dev.*, 8:234, 1964.

[208] D. B. Smith. *Los Alamos Report 3773*, 1967 (unpublished).

[209] P. Pavone, K. Karch, O. Schütt, W. Windl, D. Strauch, P. Giannozzi, and S. Baroni. *Ab initio* lattice dynamics of diamond. *Phys. Rev. B*, 48:3156, 1993.

[210] W. Windl, P. Pavone, K. Karch, O. Schütt, D. Strauch, P. Giannozzi, and S. Baroni. Second-order Raman spectra of diamond from *ab initio* phonon calculations. *Phys. Rev. B*, 48:3164, 1993.

[211] J. Kulda, H. Kainzmaier, D. Strauch, B. Dorner, M. Lorenzen, M. Krisch. Overbending of the longitudinal optical phonon branch in diamond as evidenced by inelastic neutron and x-ray scattering. *Phys. Rev. B*, 66:241202, 2002.

[212] K. Sokolowski-Tinten, C. Blome, J. Blums, A. Cavalleri, C. Dietrich, A. Tarasevitch, I. Uschmann, E. Förster, M. Kammler, M. Horn von Hoegen, and D. von der Linde. Femtosecond X-ray measurement of coherent lattice vibrations near the Lindemann stability limit. *Nature*, 422:287, 2003.

[213] H.J. Zeiger, J. Vidal, T.K. Cheng, E.P. Ippen, G. Dresselhaus, and M.S. Dresselhaus. Theory for displacive excitation of coherent phonons. *Phys. Rev. B*, 45:768, 1992.

[214] M. F. DeCamp, D. A. Reis, P. H. Bucksbaum, and R. Merlin. Dynamics and coherent control of high-amplitude optical phonons in bismuth. *Phys. Rev. B*, 64:092301, 2001.

[215] A. V. Kuznetsov and C. J. Stanton. Theory of coherent phonon oscillations in semiconductors. *Phys. Rev. Lett.*, 73:3243, 1994.

[216] E. D. Murray, D. M. Fritz, J. K. Wahlstrand, S. Fahy, and D. A. Reis. Effect of lattice anharmonicity on high-amplitude phonon dynamics in photoexcited bismuth. *Phys. Rev. B*, 72:060301(R), 2005.

[217] G. Sciaini, M. Harb, S. G. Kruglik, T. Payer, C. T. Hebeisen, F.-J. Meyer zu Heringdorf, M. Yamaguchi, M. Horn von Hoegen, R. Ernstorfer, and R. J. Dwayne Miller. Electronic acceleration of atomic motions and disordering in bismuth. *Nature*, 458:56, 2009.

[218] T. K. Cheng, J. Vidal, H. J. Zeiger, G. Dresselhaus, M. S. Dresselhaus, and E. P. Ippen. Mechanism for displacive excitation of coherent phonons in Sb, Bi, Te, and Ti_2O_3. *Appl. Phys. Lett.*, 59:1923, 1991.

[219] E.S. Zijlstra, L. L. Tatarinova, and M.E. Garcia. Laser-induced phonon-phonon interactions in bismuth. *Phys. Rev. B*, 74:220301(R), 2006.

[220] S. Fahy and D. A. Reis. Coherent phonons: Electronic softening or anharmonicity? *Phys. Rev. Lett.*, 93:109701, 2004.

[221] C. J. Powell. The origin of the characteristic electron energy losses in ten elements. *Proc. Phys. Soc.*, 76:593, 1960.

[222] C. J. Powell. Differences in the characteristic electron energy-loss spectra of solid and liquid bismuth. *Phys. Rev. Lett.*, 15:852, 1965.

[223] C. J. Powell. Characteristic energy losses of 8-kev electrons in liquid Al, Bi, In, Ga, Hg, and Au. *Phys. Rev.*, 175:972, 1968.

[224] O. Sueoka. Plasma oscillation of electrons in Be, Mg, Al, Si, Ge, Sn, Sb and Bi. *J. Phys. Soc. Japan*, 20:2203, 1965.

[225] P. Zacharias. Bestimmung optischer konctanten von wismut im energiebereich von 2 bis 40 ev aus elektronen-energieverlustmessungen. *Opt. Comm.*, 8:142, 1973.

[226] B. Gauthe and C. Wehenkel. Characteristic electron energy losses in thin bismuth films. *Phys. Lett. A*, 39:171, 1972.

[227] C. Wehenkel and B. Gauthé. Electron energy loss spectra and optical constants of bismuth. *Solid State Commun.*, 15:555, 1974.

[228] Y. W. Wang, J. S. Kim, G. H. Kim, and K. S. Kim. Quantum size effects in the volume plasmon excitation of bismuth nanoparticles investigated by electron energy loss spectroscopy. *Appl. Phys. Lett.*, 88:143106, 2006.

[229] N. Jiang, D. Su, J. C. H. Spence, S. Zhou, and J. Qiu. Volume plasmon of bismuth nanoparticles. *Solid State Commun.*, 149:111, 2009.

[230] M. Li, Z. Wang, R. Q. Zhang, and A. Soon. Size and dimension effect on volume plasmon energy of nanomaterials. *Solid State Commun.*, 152:1564, 2012.

[231] M. S. Sander, R. Gronsky, Y. M. Lin, and M. S. Dresselhaus. Plasmon excitation modes in nanowire arrays. *J. Appl. Phys.*, 89:2733, 2001.

[232] T. W. Cornelius. *Fabrication and characterization of bismuth nanowires.* PhD thesis, Ruperto-Carola University of Heidelberg, Germany, 2006.

[233] Y. Wang, J. S. Kim, J. Y. Lee, G. H. Kim, and K. S. Kim. Diameter- and length-dependent volume plasmon excitation of bismuth nanorods investigated by electron energy loss spectroscopy. *Chem. Mater.*, 19:3912, 2007.

[234] W. R. Hunter, D. W. Angel, and R. Toussey. Thin films and their uses for the extreme ultraviolet. *Appl. Opt.*, 4:891, 1965.

[235] J. A. Bearden and A. F. Burr. Reevaluation of X-ray atomic energy levels. *Rev. Mod. Phys.*, 39:125, 1967.

[236] W. C. Walker. *d*-band transitions in solids. *J. Phys. Chem. Solids*, 24:1667, 1963.

[237] F. Combet-Farnoux. Photoionization of gold and bismuth in the extreme ultraviolet: Calculations including final state correlations. *Phys. Lett. A*, 38:405, 1972.

[238] M. Cardona and D. L. Greenaway. Optical properties and band structure of group IV-VI and group V materials. *Phys. Rev.*, 133:A1685, 1964.

[239] A. P. Lenham, D. M. Treherne, and R. J. Metcalfe. Optical properties of antimony and bismuth crystals. *J. Opt. Soc. Am.*, 55:1072, 1965.

[240] P.Y. Wang and A.L. Jain. Modulated piezoreflectance in bismuth. *Phys. Rev. B*, 2:2978, 1970.

[241] O. Hunderi. Optical properties of crystalline and amorphous bismuth films. *J. Phys. F*, 5:2214, 1975.

[242] J. Toots and L. Marton. Optical properties of antimony and bismuth in the far ultraviolet. *J. Opt. Soc. Am.*, 59:1305, 1969.

[243] R. Fletcher. *Practical methods of optimization.* Wiley, New York, 2nd ed., 1987.

[244] M. Methfessel and A.T. Paxton. High-precision sampling for Brillouin-zone integration in metals. *Phys. Rev. B*, 40:3616, 1989.

[245] I. Timrov, T. Kampfrath, J. Faure, N. Vast, C.R. Ast, C. Frischkorn, M. Wolf, P. Gava, and L. Perfetti. Thermalization of photoexcited carriers in bismuth investigated by time-resolved terahertz spectroscopy and *ab initio* calculations. *Phys. Rev. B*, 85:155139, 2012.

[246] C. Hartwigsen, S. Goedecker, and J. Hutter. Relativistic separable dual-space Gaussian pseudopotentials from H to Rn. *Phys. Rev. B*, 58:3641, 1998.

[247] D. Yu and M. Scheffler. First-principles study of low-index surfaces of lead. *Phys. Rev. B*, 70:155417, 2004.

[248] M. J. Verstraete, M. Torrent, F. Jollet, G. Zérah, and X. Gonze. Density functional perturbation theory with spin-orbit coupling: Phonon band structure of lead. *Phys. Rev. B*, 78:045119, 2008.

[249] A. Dal Corso. *Ab initio* phonon dispersions of face centered cubic Pb: effects of spin-orbit coupling. *J. Phys.: Condens. Matter*, 20:445202, 2008.

[250] R. Heid, K.-P. Bohnen, I. Yu. Sklyadneva, and E. V. Chulkov. Effect of spin-orbit coupling on the electron-phonon interaction of the superconductors Pb and Tl. *Phy. Rev. B*, 81:174527, 2010.

[251] A. Dal Corso. A pseudopotential plane waves program (PWscf) and some case studies. *Lectures Notes in Chemistry*, 67:155, 1996.

[252] R.T. Isaacson and G.A. Williams. Alfvén-wave propagation in solid-state plasmas. III. Quantum oscillations of the Fermi surface of bismuth. *Phys. Rev.*, 185:682, 1969.

[253] G.E. Smith, G.A. Baraff, and J.M. Rowell. Effective g factor of electrons and holes in bismuth. *Phys. Rev.*, 135:A1118, 1964.

[254] R.N. Brown, J.G. Mavroides, and B. Lax. Magnetoreflection in bismuth. *Phys. Rev.*, 129:2055, 1963.

[255] M.P. Vecchi and M.S. Dresselhaus. Temperature dependence of the band parameters of bismuth. *Phys. Rev. B*, 10:771, 1974.

[256] H.R. Verdún and H.D. Drew. Far-infrared magnetospectroscopy of the hole pocket in bismuth. I. Band-structure effects. *Phys. Rev. B*, 14:1370, 1976.

[257] R.T. Bate, N.G. Einspruch, and P.J. May Jr. Galvanomagnetic studies of Sn-doped Bi. II. Negative Fermi energies. *Phys. Rev.*, 186:599, 1969.

[258] J.P. Omaggio, J.R.Meyer, C.A. Hoffman, A. DiVenere, X.J. Yi, C.L. Hou, H.C. Wang, J.B. Ketterson, G.K. Wong, and J.P. Heremans. Magneto-optical determination of the T-poit energy gap in bismuth. *Phys. Rev. B*, 48:11439, 1993.

[259] V. de Renzi, M.G. Betti, and C. Mariani. Electronic and dielectric properties of Bi grown on GaAs(110). *Surf. Sci.*, 287/288:550, 1993.

[260] V. de Renzi, M.G. Betti, and C. Mariani. Quantum size effects and temperature dependence of low-energy electronic excitations in thin Bi crystals. *Phys. Rev. B*, 48:4767, 1993.

[261] L. Ley, R.A. Pollak, S.P. Kowalczyk, R. McFeely, and D.A. Shirley. Evidence for covalent bonding in crystalline and amorphous As, Sb, and Bi from valence-band photoelectron spectra. *Phys. Rev. B*, 8:641, 1973.

[262] C. R. Ast and H. Höchst. High-resolution photoemission mapping of the three-dimensional band structure of Bi(111). *Phys. Rev. B*, 70:245122, 2004.

[263] B. Norin. Temperature and pressure dependence of the band structure in bismuth. *Physica Scripta*, 15:341, 1977.

[264] M. van Schilfgaarde, T. Kotani, and S. Faleev. Quasiparticle Self-Consistent *GW* Theory. *Phys. Rev. Lett.*, 96:226402, 2006.

[265] T.G. Pedersen, P. Modak, K. Pedersen, N.E. Christensen, M.M. Kjeldsen, and A.N. Larsen. *Ab initio* calculation of electronic and optical properties of metallic tin. *J. Phys.: Condens. Matter*, 21:115502, 2009.

[266] V. Tyuterev, S.V. Obukhov, N. Vast, and J. Sjakste. *Ab initio* calculation of electron-phonon scattering time in germanium. *Phys. Rev. B*, 84:035201, 2011.

[267] E. Papalazarou, J. Faure, J. Mauchain, M. Marsi, A. Taleb-Ibrahimi, I. Reshetnyak, A. van Roekeghem, I. Timrov, N. Vast, B. Arnaud, and L. Perfetti. Coherent phonon coupling to individual Bloch states in photoexcited bismuth. *Phys. Rev. Let.*, 108:256808, 2012.

[268] M. Hase, K. Mizoguchi, H. Harima, S. I. Nakashima, and K. Sakai. Dynamics of coherent phonons in bismuth generated by ultrashort laser pulses. *Phys. Rev. B*, 58:5448, 1998.

[269] M. Hase and M. Kitajima. Interaction of coherent phonons with defects and elementary excitations. *J. Phys.: Condens. Matter*, 22:073201, 2010.

[270] F. S. Khan and P. B. Allen. Deformation potentials and electron-phonon scattering: Two new theorems. *Phys. Rev. B*, 29:3341, 1984.

[271] L. Kleinman. Comment on the average potential of a Wigner solid. *Phys. Rev. B*, 24:7412, 1981.

[272] Matteo Calandra and Francesco Mauri. Electron-phonon coupling and electron self-energy in electron-doped graphene: Calculation of angular-resolved photoemission spectra. *Phys. Rev. B*, 76:205411, 2007.

[273] K.-W. Lee and W. E. Pickett. Superconductivity in boron-doped diamond. *Phys. Rev. Lett.*, 93:237003, 2004.

[274] F. Schmitt, P. S. Kirchmann, U. Bovensiepen, R. G. Moore, L. Rettig, M. Krenz, J.-H. Chu, N. Ru, L. Perfetti, D. H. Lu, M. Wolf, I. R. Fisher, and Z.-X. Shen. Transient electronic structure and melting of a charge density wave in TbTe3. *Science*, 321:1649, 2008.

[275] S. Zollner, S. Gopalan, and M. Cardona. Microscopic theory of intervalley scattering in GaAs: k dependence of deformation potentials and scattering rates. *J. Appl. Phys.*, 68:1682, 1990.

[276] S. Zollner, S. Gopalan, and M. Cardona. Short-range deformation-potential interaction and its application to ultrafast processes in semiconductors. *Semicond. Sci. Technol.*, 7:B137, 1992.

[277] J. Sjakste, V. Tyuterev, and N. Vast. *Ab initio* study of $\Gamma - X$ intervalley scattering in GaAs under pressure. *Phys. Rev. B*, 74:235216, 2006.

[278] J. Sjakste, V. Tyuterev, and N. Vast. Intervalley scattering in GaAs: *ab initio* calculation of the effective parameters for Monte Carlo simulations. *Applied Physics A*, 86:301, 2007.

[279] J. Sjakste, N. Vast, and V. Tyuterev. *Ab initio* method for the electron-phonon scattering times in semiconductors: application to GaAs and GaP. *Phys. Rev. Lett.*, 99:236405, 2007.

[280] U. Bovensiepen. Coherent and incoherent excitations of the Gd(0001) surface on ultrafast timescales. *Condens. Matter*, 19:083201, 2007.

[281] S. Faleev, M. van Schilfgaarde, T. Kotani, F. Léonard, and M. P. Desjarlais. Finite-temperature quasiparticle self-consistent GW approximation. *Phys. Rev. B*, 74:033101, 2006.

[282] T. Kampfrath, L. Perfetti, F. Schapper, C. Frischkorn, and M. Wolf. Strongly coupled optical phonons in the ultrafast dynamics of the electronic energy and current relaxation in graphite. *Phys. Rev. Lett.*, 95:187403, 2005.

[283] N. Del Fatti, R. Bouffanais, F. Vallée, and C. Flytzanis. Nonequilibrium electron interactions in metal films. *Phys. Rev. Lett.*, 81:922, 1998.

[284] H. Y. Fan, W. Spitzer, and R. J. Collins. Infrared absorption in n-type germanium. *Phys. Rev.*, 101:566, 1956.

[285] W. P. Dumke. Quantum theory of free carrier absorption. *Phys. Rev.*, 124:1813, 1961.

[286] R. Von Baltz and W. Escher. Quantum theory of free carrier absorption. *Phys. Stat. Sol. (b)*, 51:499, 1972.

[287] A. Wacker, G. Bastard, F. Carosella, R. Ferreira, and E. Dupont. Unraveling of free-carrier absorption for terahertz radiation in heterostructures. *Phys. Rev. B*, 84:205319, 2011.

[288] E. Kioupakis, P. Rinke, A. Schleife, F. Bechstedt, and C. G. Van de Walle. Free-carrier absorption in nitrides from first principles. *Phys. Rev. B*, 81:241201(R), 2010.

[289] A. Y. Liu, I. I. Mazin, and J. Kortus. Beyond Eliashberg superconductivity in MbB_2: Anharmonicity, two-phonon scattering, and multiple gaps. *Phys. Rev. Lett.*, 87:087005, 2001.

[290] A. Stroppa, S. Picozzi, A. Continenza, M. Y. Kim, and A. J. Freeman. Magneto-optical properties of (Ga,Mn)As: An *ab initio* determination. *Phys. Rev. B*, 77:035208, 2008.

[291] L. Perfetti, P. A. Loukakos, M. Lisowski, U. Bovensiepen, H. Berger, S. Biermann, F. S. Cornaglia, A. Georges, and M. Wolf. Time evolution of the electronic structure of 1T-TaS2 through the insulator-metal transition. *Phys. Rev. Lett.*, 97:067402, 2006.

[292] C.-L. Fu and K.-M. Ho. First-principles calculation of the equilibrium ground-state properties of transition metals: Applications to Nb and Mo. *Phys. Rev. B*, 28:5480, 1983.

[293] N. Marzari, D. Vanderbilt, A. De Vita, and M. C. Payne. Thermal contraction and disordering of the Al(110) surface. *Phys. Rev. Lett.*, 82:3296, 1999.

[294] R. Del Sole and R. Girlanda. Optical properties of semiconductors within the independent-quasiparticle approximation. *Phys. Rev. B*, 48:11789, 1993.

[295] P. Gava, M. Lazzeri, A. M. Saitta, and F. Mauri. *Ab initio* study of gap opening and screening effects in gated bilayer graphene. *Phys. Rev. B*, 79:165431, 2009.

[296] V. S. Édelman. Electrons in bismuth. *Advances in Physics*, 25:555, 1976.

[297] V. S. Édelman. Properties of electrons in bismuth. *Usp. Fiz. Nauk*, 123:257, 1977.

[298] B. Lax and J. G. Mavroides. *Solid State Physics*, vol. 11, p. 368. Academic, New York, 1960.

[299] R.T. Isaacson and G.A. Williams. Alfvén-wave propagation in solid-state plasmas. II. Bismuth. *Phys. Rev.*, 177:738, 1969.

[300] M. van Exter and D. Grischkowsky. Carrier dynamics of electrons and holes in moderately doped silicon. *Phys. Rev. B*, 41:12140, 1990.

[301] Z. Zhu, B. Fauqué, Y. Fuseya, and K. Benhia. Angle-resolved Landau spectrum of electrons and holes in bismuth. *Phys. Rev. B*, 84:115137, 2011.

[302] A. A. Lopez. Electron-hole recombination in bismuth. *Phys. Rev.*, 175:823, 1968.

[303] M.H. Cohen. Optical constants, heat capacity and the Fermi surface. *Phil. Mag.*, 3:762, 1958.

[304] N. V. Smith. Optical constants of sodium and potassium from 0.5 to 4.0 eV by split-beam ellipsometry. *Phys. Rev.*, 183:634, 1969.

[305] C. S. Wang and J. Callaway. Band structure of nickel: Spin-orbit coupling, the Fermi surface, and the optical conductivity. *Phys. Rev. B*, 9:4897, 1974.

[306] K. Ishioka, M. Kitajima, and O.V. Misochko. Temperature dependence of coherent A_{1g} and E_g phonons of bismuth. *J. Appl. Phys.*, 100:093501, 2006.

[307] A. S. Vengurlekar and S. S. Jha. Picosecond time evolution of photoexcited hot-electron mobility in GaAs and the speed of photoresponse. *J. Appl. Phys.*, 65:3189, 1989.

[308] C. J. Stanton and D. W. Bailey. Rate equations for the study of femtosecond intervalley scattering in compound semiconductors. *Phys. Rev. B*, 45:8369, 1991.

[309] T. Winzer, A. Knorr, and E. Malic. Carrier multiplication in graphene. *Nano Letters*, 10:4839, 2010.

[310] J.J.H. Pijpers, R. Ulbricht, K.J. Tielrooij, A. Osherov, Y. Golan, C. Delerue, G. Allan, and M. Bonn. Assessment of carrier-multiplication efficiency in bulk PbSe and PbS. *Nature Physics*, 5:811, 2009.

[311] J.W. Cockburn, J.J. Finley, M.S. Skolnick, P. Wisniewski, R. Grey, G. Hill, and M.A. Pate. Determination of intervalley scattering times in GaAs from electroluminescence spectroscopy of single barrier tunneling devices. *Appl. Phys. Lett.*, 70:622, 1997.

[312] S. Wu, P. Geiser, J. Jun, J. Karpinski, D. Wang, and R. Sobolewski. Time-resolved intervalley transitions in GaN single crystals. *J. Appl. Phys.*, 101:043701, 2007.

[313] D. Kim and P. Y. Yu. Hot-electron relaxations and hot phonons in GaAs studied by subpicosecond Raman scattering. *Phys. Rev. B*, 43:4158, 1991.

[314] J. Faure, J. Mauchain, E. Papalazarou, M. Marsi, D. Boschetto, I. Timrov, N. Vast, Y. Ohtsubo, B. Arnaud, and L. Perfetti. Direct observation of electron thermalization and electron-phonon coupling in photoexcited bismuth. (submitted).

[315] B. Arnaud and Y. Giret. Electron Cooling and Debye-Waller Effect in Photoexcited Bismuth. *Phys. Rev. Lett.*, 110:016405, 2013.

[316] A. Dal Corso. Density functional perturbation theory for lattice dynamics. *Lecture notes Cork 2010*, 2010.

[317] S. de Gironcoli. Lattice dynamics of metals from density-functional perturbation theory. *Phys. Rev. B*, 51:6773, 1995.

[318] M. Grüning, A. Marini, and X. Gonze. Exciton-plasmon states in nanoscale materials: Breakdown of the Tamm-Dancoff approximation. *Nano Lett.*, 9:2820, 2009.

[319] W. Schülke, J. R. Schmitz, H. Schulte-Schrepping, and A. Kaprolat. Dynamic and static structure factor of electrons in Si: Inelastic X-ray scattering results. *Phys. Rev. B*, 52:11721, 1995.

[320] M. Cazzaniga, H.-C. Weissker, S. Huotari, T. Pylkkänen, P. Salvestrini, G. Monaco, G. Onida, and L. Reining. Dynamical response function in sodium and aluminum from time-dependent density-functional theory. *Phys. Rev. B*, 84:075109, 2011.

[321] Y. Takada and H. Yasuhara. Dynamical structure factor of the homogeneous electron liquid: Its accurate shape and the interpretation of experiments on aluminum. *Phys. Rev. Lett.*, 89:216402, 2002.

[322] W. Schülke, H. Schulte-Schrepping, and J. R. Schmitz. Dynamic structure of electrons in Al metal studied by inelastic X-ray scattering. *Phys. Rev. B*, 47:12426, 1993.

[323] O.H. Nielsen and R.M.Martin. First-principles calculation of stress. *Phys. Rev. Lett*, 50:697, 1983.

[324] H.J. Monkhorst and J.D. Pack. Special points for Brillouin-zone integrations. *Phys. Rev. B*, 13:5188, 1976.

[325] D. R. Hamann. Generalized norm-conserving pseudopotentials. *Phys. Rev. B*, 40:2980, 1989.

[326] A. A. Quong and B. M. Klein. Self-consistent-screening calculation of interatomic force constants and phonon dispersion curves from first principles: Application to aluminum. *Phys. Rev. B*, 46:10734, 1992.

[327] Y. Wang, E.W. Plummer, and K. Kempa. Foundations of plasmonics. *Advances in Physics*, 60:799, 2011.

[328] J.M. Pitarke, V.M. Silkin, E.V. Chulkov, and P.M. Echenique. Theory of surface plasmons and surface-plasmon polaritons. *Rep. Prog. Phys.*, 70:1, 2007.

[329] C. Herring. Theory of the thermoelectric power of semiconductors. *Phys. Rev.*, 96:1163, 1955.

[330] M. Matsuo, A. Endo, N. Hatano, H. Nakamura, R. Shirasaki, and K. Sugihara. Quantum Nernst effect in a bismuth single crystal. *Phys. Rev. B*, 80:075313, 2009.

[331] T.-R. T. Han, Z. Tao, S. D. Mahanti, K. Chang, C.-Y. Ruan, C. D. Malliakas, and M. G. Kanatzidis. Structural dynamics of two-dimensional charge-density waves in $CeTe_3$ investigated by ultrafast electron crystallography. *Phys. Rev. B*, 86:075145, 2012.

[332] M. D. Johannes and I. I. Mazin. Fermi surface nesting and the origin of charge density waves in metals. *Phys. Rev. B*, 77:165135, 2012.

[333] M. Calandra and F. Mauri. Charge-density wave and superconducting dome in $TiSe_2$ from electron-phonon interaction. *Phys. Rev. Lett.*, 106:196406, 2011.

[334] N. Troullier and J. L. Martins. Efficient pseudopotentials for plane-wave calculations. *Phys. Rev. B*, 43:1993, 1991.

[335] D.A. Young. *Phase Diagrams of the Elements*. University of California Press, Berkley/Los Angeles/Oxford, 1991.

[336] C. G. Homan. Phase diagram of Bi up to 140 kbars. *J. Phys. Chem. Solids*, 36:1249, 1975.

[337] C. C. Yang, J. C. Li, and Q. Jiang. Temperature-pressure phase diagram of silicon determined by Clapeyron equation. *Solid State Commun.*, 129:437, 2004.

[338] S. Sankaralingam, G. Subramoniam, S. Pauline, and R. Asokamani. Pressure induced superconductivity in bismuth. *High Pressure Research*, 6:219, 1991.

[339] S. Hüfner, *Photoelectron Spectroscopy*. Springer, Berlin, 1995.

[340] A. Damascelli, Z. Hussain, and Z.-X. Shen. Angle-resolved photoemission studies of the cuprate superconductors. *Rev. Mod. Phys.*, 75:473, 2003.

[341] A. Damascelli. Probing the electronic structure of complex systems by ARPES. *Physica Scripta*, T109:61, 2004.

[342] M.C. Beard, G.M. Turner, and C.A. Schmuttenmaer. Terahertz spectroscopy. *J. Phys. Chem. B*, 106:7146, 2002.

[343] C. A. Schmuttenmaer. Exploring dynamics in the far-infrared with terahertz spectroscopy. *Chem. Rev.*, 104:1759, 2004.

[344] J.B. Baxter and G.W. Guglietta. Terahertz spectroscopy. *Anal. Chem.*, 83:4342, 2011.

[345] E. Anderson, Z. Bai, C. Bischof, S. Blackford, J. Demmel, J. Dongarra, J. Du Croz, A. Greenbaum, S. Hammarling, A. McKenney, and D. Sorensen, editors. *LAPACK Users' Guide*. Philadelphia, PA: Society for Industrial and Applied Mathematics, 3rd edition, 1999.

[346] M. Frigo and S. G. Johnson. The design and implementation of FFTW3. *Proc. IEEE*, 93:216, 2005.

[347] Message passing interface forum. *Int. J. Supercomput. Appl.*, 8:159, 1994.